

**FORWARD CALORIMETRY IN ALICE AND HIGH  
MULTIPLICITY PHYSICS IN PROTON-PROTON  
COLLISIONS AT THE LARGE HADRON COLLIDER**

*By*

**SANJIB MUHURI**

**Enrolment No. PHYS04201404002**

**CI Name; VARIABLE ENERGY CYCLOTRON CENTRE,  
KOLKATA**

*A thesis submitted to*

*The Board of Studies in Physical Sciences*

*In partial fulfillment of requirements*

*For the Degree of*

**DOCTOR OF PHILOSOPHY**

*Of*

**HOMI BHABHA NATIONAL INSTITUTE**



**June, 2019**



# Homi Bhabha National Institute<sup>1</sup>

## Recommendations of the Viva Voce Committee

As members of the Viva Voce Committee, we certify that we have read the dissertation prepared by Mr. Sanjib Muhuri entitled "FORWARD CALORIMETRY IN ALICE AND HIGH MULTIPLICITY PHYSICS IN PROTON-PROTON COLLISIONS AT THE LARGE HADRON COLLIDER" and recommend that it may be accepted as fulfilling the thesis requirement for the award of Degree of Doctor of Philosophy.

|                    |                              |   |
|--------------------|------------------------------|---|
| Chairman -         | Prof. Asis Kumar Chaudhuri   | <i>Asis Kumar Chaudhuri</i> 19/6/2019   |
| Guide / Convener - | Prof. Tapan Kumar Nayak      | <i>Tapan Kumar Nayak</i> 19/6/2019      |
| Co-guide -         | Not applicable               |   |
| Examiner -         | Prof. Tatsuya Chujo          | <i>Tatsuya Chujo</i> 19/6/2019          |
| Member 1-          | Prof. Subhasis Chattopadhyay | <i>Subhasis Chattopadhyay</i> 19/6/2019 |
| Member 2-          | Prof. Prashant Shukla        | <i>Prashant Shukla</i> 19/6/2019        |

Final approval and acceptance of this thesis is contingent upon the candidate's submission of the final copies of the thesis to HBNI.

I/We hereby certify that I/we have read this thesis prepared under my/our direction and recommend that it may be accepted as fulfilling the thesis requirement.

Date: 19/6/2019

Place: Kolhata

Signature

Co-guide (if any)

Signature

Guide

<sup>1</sup> This page is to be included only for final submission after successful completion of viva voce.



## **STATEMENT BY AUTHOR**

This dissertation has been submitted in partial fulfillment of requirements for an advanced degree at Homi Bhabha National Institute (HBNI) and is deposited in the Library to be made available to borrowers under rules of the HBNI.

Brief quotations from this dissertation are allowable without special permission, provided that accurate acknowledgment of source is made. Requests for permission for extended quotation from or reproduction of this manuscript in whole or in part may be granted by the Competent Authority of HBNI when in his or her judgment the proposed use of the material is in the interests of scholarship. In all other instances, however, permission must be obtained from the author.

SANJIB MUHURI



## **DECLARATION**

I, hereby declare that the investigation presented in the thesis has been carried out by me. The work is original and has not been submitted earlier as a whole or in part for a degree / diploma at this or any other Institution / University.

**SANJIB MUHURI**



---

## List of Publications arising from the thesis

### Journal

1. "Dynamic fuzzy c-means (dFCM) clustering and its application to calorimetric data reconstruction in high-energy physics"; Radha Pyari Sandhir, Sanjib Muhuri, Tapan K. Nayak; Nuclear Instruments and Methods in Physics Research A 681 (2012) 34–43.
2. "Multiplicity distributions in the forward rapidity region in proton-proton collisions at the Large Hadron Collider"; Premomoy Ghosh and Sanjib Muhuri; Physical Review D 87, 094020 (2013).
3. "Test and characterization of a prototype silicon–tungsten electromagnetic calorimeter"; Sanjib Muhuri, Sourav Mukhopadhyay, Vinay B. Chandratre, Menka Sukhwani, Satyajit Jena, Shuaib Ahmad Khan, Tapan K. Nayak, Jogender Saini, Rama Narayana Singaraju, Nuclear Instruments and Methods in Physics Research A 764 (2014) 24–29.
4. "Indication of transverse radial flow in high-multiplicity proton–proton collisions at the Large Hadron Collider"; Premomoy Ghosh, Sanjib Muhuri, Jajati K Nayak and Raghava Varma; J. Phys. G: Nucl. Part. Phys. 41 (2014) 035106 (14pp).

### Communicated.

1. "Do we see change of phase in proton-proton collision at the Large Hadron Collider", Premomoy Ghosh, Sanjib Muhuri, A. K. Choudhuri.
2. "Fabrication and beam test of a silicon-tungsten electromagnetic calorimeter", Sanjib Muhuri et. al..

### Conferences proceedings.

1. "Feasibility Study of a Forward Calorimeter in the ALICE Experiment at CERN"; Sanjib Muhuri and T. K. Nayak; Proceedings of the DAE Symp.on Nucl. Phys. 55 (2010).

2. **"A Fuzzy Clustering Technique for Calorimetric Data Reconstruction"**; Radha Pyari Sandhir, Sanjib Muhuri, and Tapan K. Nayak; Proceedings of the DAE Symp.on Nucl. Phys. 55 (2010).
3. **"A Forward Calorimeter (FoCal) as upgrade for the ALICE Experiment at CERN"**; Dr NOOREN, Gerardus, Mr REICHER Martijn, Mr MUHURI Sanjib, Dr GUNJI, Taku, Mr TSUJI, Tomoya, and Tapan K. Nayak; QM 2011.
4. **"Physics and Design Studies for a Silicon-Tungsten Calorimeter for the ALICE experiment at CERN"**; Sanjib Muhuri, and Tapan K. Nayak; Proceedings of the DAE Symp.on Nucl. Phys. 56 (2011).
5. **"Low-x Forward Physics With ALICE"**; Sanjib Muhuri; QGP Meet - 2012.
6. **"Simulation and design studies of ALICE Forward Calorimeter"**; Sanjib Muhuri, T. K. Nayak; Proceedings of the DAE Symp.on Nucl. Phys. 57 (2012).
7. **"Silicon Pad Detectors for ALICE Forward Calorimeter"**; S.R. Narayan, S.A. Khan, J. Saini, P. Bhaskar, Sanjib Muhuri, T.K. Nayak, Y.P. Viyogi, Y.P. Prabhakara Rao, Y. Rejeena Rani, S. Mukhopadhyay, V.B.Chandratre, M. Sukhwani and C.K.Pithawa; Proceedings of the DAE Symp.on Nucl. Phys. 57 (2012).
8. **"Development and Characterization of Prototype Electromagnetic Calorimeter"**; Sanjib Muhuri, Tapan. K. Nayak, S. R. Singaraju, Sourav Muhkopadhyay, Shuaib A. Khan, J. Saini, V.B. Chandratre; Proceedings of the DAE Symp.on Nucl. Phys. 58 (2013).
9. **"Test and Characterization of a Prototype Silicon-Tungsten Electromagnetic Calorimeter"**; Sanjib Muhuri; IWAD - 2014.
10. **"Do we see change of phase in proton-proton collisions at the Large Hadron Collider"**; Sanjib Muhuri; ICPAQGP - 2015.
11. **"Prototype tests of full-depth Si-W electromagnetic calorimeter for ALICE upgrade at CERN"**; Sanjib Muhuri, Sourav Mukhopadhyay, Sumit Saha, Sanchari Thakur, V.B. Chandratre, Shuaib A. Khan, T. K. Nayak, Jogender Saini, R.N. Singaraju, Menka Sukhwani;

---

Proceedings of the DAE Symp.on Nucl. Phys. 61 (2016).

12. **"Test of prototype electromagnetic calorimeter (FOCAL) using large dynamic range ASIC ANUINDRA at CERN-SPS"**; Sanjib Muhuri, Sinjini Chandra, Sourav Mukhopadhyay, Jogender Saini, V.B. Chandratre, R.N. Singaraju, T.K. Nayak, Ton van den Brink, S. Chattopadhyay; Proceedings of the DAE Symp.on Nucl. Phys. 62 (2017).

## Conferences presentations.

1. **"ALICE Upgrade: Forward Calorimeter Design Studies"**, 4-6 Aug, ALICE-INDIA Meeting, VECC, 2011.

2. **"A Forward Calorimeter (FoCal) as upgrade for the ALICE Experiment at CERN"**, Gerardus Nooren, Taku Gunji, Sanjib Muhuri, Martijn Reicher, Tomoya Tsuji, Quark Matter 2011.

3. **"Low-x Forward Physics with ALICE"**, 3-6 July, QGP MEET 2012, Quark Gluon Plasma, Narosa Publishing House.

4. **"Forward Physics with ALICE FOCAL"**, 27-28 April, 2013, IIT-B, Mumbai.

5. **"Forward Calorimeter for ALICE"**, 12-14 Jan, 2014, ALICE-India Meeting. VECC, Kolkata.

6. **"Data taking with ALICE PMD at 13TeV pp collision and QA analysis"**, 22-24 July, 2015, ALICE-India Meeting, IOP, Bhubaneswar.

7. **"Forward Calorimetry in ALICE"**, 22-24 July, 2015, ALICE-India Meeting, IOP, Bhubaneswar.

8. **"Test results from the Si-W calorimeter for FOCAL"**, 6-7Jan, 2016, ALICE-India Meeting, SINP, Kolkata.

9. **"Data taking with PMD for PbPb collision in RUN-II"**, 6-7Jan, 2016, ALICE-India Meeting, SINP, Kolkata.

10. **"Invited talk on "Collectivity in small system"**, Contemporary issues in High Energy Physics, North Bengal University, Siliguri, 21-22 March, 2016.

## **Other Publications**

### **(A) Refereed journals**

**"Multiple parton interactions and production of charged particles up to the intermediate- $p_T$  range in high-multiplicity pp events at the LHC"**; Somnath Kar, Subikash Choudhury, Sanjib Muhuri, and Premomoy Ghosh; PHYSICAL REVIEW D 95, 014016 (2017).

### **(B) Conferences**

**"Test of a triple GEM chamber with neutrons using alpha beam at VECC cyclotron"**; A. K. Dubey, J. Saini, R. Ravishankar, T. Bandopadhyay, P.P. Bhaduri, R. Adak, S. Samanta, S. Chattopadhyay, G.S.N. Murthy, Z. Ahammed, S.A. Khan, S. Ramnarayan, Sanjib Muhuri, P. Ghosh, S.K. Pal, T.K. Nayak and Y.P. Viyogi; Proceedings of the DAE Symp.on Nucl. Phys. 58 (2013).

SANJIB MUHURI

## **DEDICATIONS**

*Dedicated to All my "TEACHERS ....."*

*From my Grandfather*

*To my daughter*



## Acknowledgements

I am extremely honored, at this occasion, to avow all those people and their unconditional blessings and guidance, without what, probably I could not achieve the present stage of my research activity. I would like to begin with my wholehearted gratitude to my supervisor Prof. Tapan Kumar Nayak for his immutable encouragement and patient guidance and protecting me from any unfavourable annoyances in so cool and calm way. I should begin once more with my unending obligation to Dr. Premomoy Ghosh, a person you approach and forget feeling alone in any circumstances, for his immense support and nurture for doing research work with his extraordinary human qualities.

I would like to recapitulate reverentially the making of my childhood learnings (Barnaporichay to master of Tense) by my dear **Dadu Late Shyamapada Muhuri and my younger Uncle Late Joydeb Muhuri** so rigorously each and every step irrespective of any specific importance. I will remain respectful to my Thakuma - Late Debola Muhuri, Dida - and grandfather - Bhiswa Ranjan Biswas for being philanthropically protective and extremely careful irrespective even for a misdeed. It's my immense pleasure to respect and gratitude all my teachers and friends of my primary school (Kalipur Nimnobuniyadi primary School) where I was brought up with in a so naturely and friendly ambience. I would also like to cherish my school "Shikarpur Vivekananda High School" for providing all necessary support with excellent teachers. I should admit my fortune being blessed by Mr. Muktaram Howli, my science teacher and bit more..., who taught me so parently and gave the initial boost to my life. I would like to acknowledge the guidance from Mr. Haraprashad Maitra, my chemistry teacher during +2 years in Bapuji Vidyamandir at Chakdaha. I am greatly obliged to Mr. Anish Ghosh, an excellent teacher I was gifted in my life who build lot of confidence in me. I am very much delighted to be a student of Mr. Shambhu Manthony, who consistently encouraged and protected me from any kind of misdeed during my school days and made me a bit comfortable with english literature. I would also like to acknowledge all my school friends specifically, Mr. Arun Biswas, Mr. Soumen Ghosh, Mr. Pranab Khan, Mrs. Pampa Biswas, Mrs. Rakhi Ghosh and others for proving me memorising school days without any rat-racing bitterness.

I must acknowledge my gratifying experiences that I have earned from my university life

at University of Kalyani. It was a heavenly fortune that I could learn physics from some of the best teachers specifically Prof. Padmanabha Dasgupta, Late Prof. Prasanta Kumar Rudra, Prof. Sidhartha Roy, Prof. Satyabrata Biswas, Prof. Somnath Chakraborty, Prof. Chirantan Neogy, Prof. Nandita Rudra and others. It was only my teachers from the department of physics, K.U., because of whom I started understanding the glimpse of physics and could dare to carry forward further in physics. On this occasion, I would also like to express a lot of thanks to my friends Mr. Anirban Banerjee, Mr. Kunal Mukherjee, Mr. Shubhendu Nandi, Mr. Avijit Maitra, Mr. Prasanta Jana, Mr. Biswasjit Mondal and others for their constant encouragement and support either this way or other.

I would also like to express my sincere respect to Dr. Joydeep Ghosh of Institute of Plasma Research for being so kind to me in carrying a project under him and encouragement to take a decision always in favor of me in my IPR-days. It would be incomplete without appreciating my dear friend and well-wisher Dr. Deepak Sangwan for his so protecting behavior towards me and facing a hard time in correcting my Hindi. I would also like to thank Dr. Kshitish Barada and Dr. Prabal Singh for their immense support and togetherness during post M.Sc. course-work at IPR.

I would like to recollect my Training days at BARC-Training school which gave me a different avenue in furthering my research work and helped me a lot in starting my research in High Energy Physics at Variable Energy Cyclotron Centre afterwards. I was blessed with some precious teachers like Dr. Prashant Shukla, Dr. Lalit Mohan Panth, Dr. I would also like to gratefully thank my friends Mr. Sandip Bhowmik, Mr. Arya Das, Mr. Debes Roy, Mr. Sanat Kumar Pandit for so brotherly behaviour and constant encouragement at each and every moment during my training days. I would like to thank a lot for being a part of my life for ever.

I would like to express my indebtedness to Mr. Ramanarayan Singaraju for teaching me each and every step of doing experiments so patiently and explaining in details repeatedly without getting annoyed. I must recognise his enormous effort to all the test beam without which it would have not got success at all. I must also be very much thankful to Mr. Jogender Saini, who always appeared more as a friend than a colleague, who always enthusiastically approached to any kind of issue with "N" number of solutions, had it been technical or personal. It's my pleasure to accept the contribution of Mr. Shuaib Ahmad Khan in many occasions in doing experiments.

I would like to express my wholehearted gratitude to Dr. V. Chandratre of Bhabha Atomic Research Centre for being so kind in encouraging me blindly in pursuing my research activity. I am always overwhelmed by his so outspread knowledge in any relevant topics. I must also admit my gratification because of his pampering sometimes!

I am delighted to specify the contribution of Mr. Sourav Mukhopadhyay of BARC for each

and every step of detector and electronics development for the forward calorimeter. Not only academically, he brings lots of enrichments with his so pleasant bothership in our personal relation which has been extended far beyond our professional life.

I am very much grateful to Prof. Subhasis Chattopadhyay, Head, EHEPAG, VECC, for his indubitable help for any kind of need, had it been physics discussion, difficulties in simulation or related to research facilities. I would also like to recapitulate the needful assistance of Dr. Tapashi Ghosh in learning GEANT4 during my early days of detector simulations. It's my pleasure to mention Dr. Sidharth K. Prasad, Dr. Saikat Biswas, Dr. Mriganka Mondal for valuable discussions many times.

I would also like to commemorate intense help from Dr. Partha Pratim Bhaduri and Dr. Prithwish Trivedy for sharing valuable physics inputs in an effortless manner. I am also thankful to Dr. Nihar Ranjan Sahoo, Dr. Sudipan De, Dr. Subhash Singha and other PhD students of EHEPAG group for sharing many useful discussions.

I would like to express my wholehearted respect to Dr. Y. P. Viyogi, former Director, IOP and Group-Head, EHEPAG, VECC, for his encouraging supports and suggestions in pursuing the research activity smoothly. I would feel delighted to express my respect to Prof. D. K. Srivastava for his careful guidance and suggestions in need.

It's my pleasure to mention unflappable nature of my senior colleagues of EHEPAG, specifically, Dr. Anand Dubey and Dr. Bedangadas Mohanty, which help me a lot in many hard times with their useful suggestions. I would like to express my owe to Mr. Vikas Singhal for helping with an excellent grid computing facility and for his very helping nature in any need. It's my glad to acknowledge Dr. Koushik Mukherjee for being so nice and helpful in all scientific and personal difficulties during my research work. I would also like to thank all those people of PMD and electronics lab for helping so immediately without expecting any return. I would like to mention Dr. Zubayer Ahmad for his ease approach during discussion. It's my immense pleasure to recognise Swagata Mallick, Sabir Ali, Dipta Pratim Dutta, Debashis Banerjee, Tapan Kumar Mandi for being so much supportive and heartwarming association during the tedious research period. I would like to recall the amiable presence of Dr. Pintu Bandyopadhyay and Dr. Ritu Banerjee for proving me so caring ambience during early days of my research work. It's my pleasure to memorize Mr. Saroj K. Biswas and Sudip Sikdar for their constant encouragement and affectionate words.

At this point, I would like to admire few precious friends - Mr. Amlan Ghosh, Mr. Koushik Bose, Mr. Santanu Mondal, Mr. Selim Mollah, Mrs. Antara Roy Choudhury, Mr. Debal kole,

Mr. Mithun Sarkar for their immoderate assistance, warmth and inspiration. I would also like to accede the cooperation and favor of my cousin brother Mr. Biplab Biswas for all his unconditional anticipation.

I can not forget the endless support I am rewarded from my younger sister Mrs. Mithu Mondal without what my journey could have been a mess. Moreover I can not forget the affectionate moments that I have spent with my niece Swastika Mondal and nephew Saptasha Mondal which kept me fresh always in stress. I should also be thankful having Gopal, Sampa as my dearest brother and sister for being so supportive.

Last not the least, I should be thankful for being fortunate having Moumita as my soul mate for ever who made my life charming and took away all other pain for carrying my research work smooth going. At last to complete the loop, I would like go back to the beginning to dedicate my wholehearted devotion and obligation to my parents Mr. Sunil Kumar Muhuri and Mrs. Sabita Muhuri, without whom the journey would have remained unidentified.

Finally I must confess being blessed with the heavenly gift, My Daughter **Tua**, who made me so enthusiastic and made me never tired to set for a new aim. I would like to express my courtesy to facilities at VECC and helps from Department of Atomic Energy and Department of Science and Technology regarding funding for the project without which it would have not started at all. I would end with all my relatives, friends, neighbours and colleagues for their geniality and providing a harmonious working environment.

---

## Synopsis

### Introduction:

Calorimetry, a unique science to measure heat (energy in the wider sense), provides an excellent method to detect and characterize particles of different nature (mass, charge, structure) in collision experiments from low (few hundred MeV) energy to today's ultra-relativistic high (many TeV) energies. With the increase of collision energy, the number of particles increases along with their energies. This results in growing complexities in particle detection, requiring state of the art technological advancement in calorimetric physics. Silicon, among different possible choices as the detector, has lots of advantages over others because of its very good signal to noise ratio, insensitiveness to magnetic fields, enriched technologies to achieve very high granularity, and etc. Measurement of each individual particle produced in proton-proton (pp), proton-lead (p-Pb) and lead-lead (Pb-Pb) collisions at the CERN Large Hadron Collider (LHC) gets more complicated in forward rapidities because of the increase in particle density. This requires for a finely segmented and precise calorimeter. An optimized sampling type (both in longitudinal and transverse direction) silicon (detecting medium) - Tungsten (converter/absorbing medium) calorimeter has been proposed as an upgrade proposal for the ALICE experiment at CERN to widen its physics goals. A rigorous study for the design, fabrication, and characterization with prototype calorimeters both with radioactive source and CERN beam facilities have been carried out, which shows encouraging results in favour of the feasible and acceptable upgrade. A new proposal for a forward calorimeter (FOCAL) has been prepared to be submitted to ALICE for a possible upgrade of the detector.

A phenomenological study with presently available data for the proton-proton collision at LHC energies has been pursued, which is complementing the physics motivation behind building the calorimeter. So far, particle production in proton-proton collision used to be explained as fundamental interaction between partons which results in only a few particles (3 to 5) in the final state. With the increase in collision energies, proton-proton collisions produce events with comparatively high multiplicity (more than one hundred) which need more fundamental introspection towards particle production mechanisms, such as initial state effects, multi-partonic interaction, medium formation, etc. In the present scenario, the formation of medium (mostly partonic) draws a lot of attention as a strong reason for production of high multiplicity in the proton-proton collisions. A successful explanation with Double negative binomial distribution (NBD) model for particle production in pp collisions shows that there exists another mechanism of particle production apart from hard scattering. A phenomenological Blast wave model has been used to characterize these high multiplicity pp events assuming a miniature version of the medium produced in heavy ion collisions. A satisfactory explanation of the medium formation in pp collision encourages us to further

investigate its nature of the medium formed in these collisions. Study of the variation in degrees of freedom as a function of mean transverse momentum (representation of the temperature of the system) shows a possible existence of partonic medium in pp collision. These aspects are discussed below in more detail.

### **Design and optimization of the Forward Calorimeter:**

Limited capability in the forward rapidity region of the ALICE experiment has inspired us to investigate the feasibility of instrumenting a new calorimeter to aid a wide range of physics interests starting from initial conditions, gluon saturation, parton energy loss and much more. The calorimeter has been designed to cover a pseudorapidity region of 2.5 to 5.5 with full azimuthal coverage at 400 cm away from the interaction point. The Geant4 package was used to simulate the geometry and the performance of the calorimeter. The thickness of the calorimeter needs to be properly optimized to obtain optimum energy resolution. It is found that 25 radiation length ( $X_R$ ) material depth is sufficient for full energy containment along the beam direction for gamma or photons of energy ranging from 1 GeV to 200 GeV. Silicon as detector and tungsten as converter/absorber are chosen taking both physics requirements and practical limitations into account. Multilayer sampling type calorimeter with highly segmented detectors of sizes  $1\text{ cm}^2$  in most of the layers and  $1\text{ mm}^2$  in some high-resolution layers are essential to handle a large number of particles produced in pp, p-Pb and Pb-Pb collisions at LHC energies. Two types of detector layers (three high-granular with  $1\text{ mm}^2$  pixels) and rest all layers with  $1\text{ cm}^2$  pads) have been used as an optimization between physics requirements and cost estimation. Tungsten as converter is a precise choice because of its high-Z and compact structure which will effectively make the electromagnetic shower confined within a comparatively narrow cone. In this study, a configuration with 20 layers of the absorber (Tungsten of  $1 X_R$  thick) and sensors with associated electronics have been accommodated. A detailed simulation shows satisfactory results for longitudinal and cumulative energy deposition profile for the energy range of interest. Electron to photon discrimination as well as direct to decayed photon discrimination efficiency has been investigated for this configuration. To find the clusters (hit patch) produced by the electromagnetic showers, soft computing techniques using fuzzy logics have been developed as cluster finders. These have been used and found to differentiate clusters separated by as low as 3 mm apart.

As a part of the calorimeter response to incident particles, minimum ionizing particles (MIP), mostly created by very high energy particles (with kinetic energy larger than the rest mass) have been simulated. The most probable value (MPV) of the energy loss for

---

MIP is found to be 89 KeV. Responses of photons with a wide range of incident energies have been simulated to study electromagnetic shower characteristics. The Geant4 package along with Fuzzy c-means (FCM) and dynamic FCM clustering algorithms show that the configuration is quite efficient in discriminating the photons from up to 200 GeV neutral pions. The transverse profile has been studied which effectively explain the compactness of the shower produced. Moreover, the primary requirement for a calorimeter is to work reliably in linear region for a wide range of incident energies. The energy resolution of the calorimeter has been simulated and found to be about 19%. As the physics performance study, reconstruction of neutral pion (Invariant Mass) from its decayed photons has been done rigorously up to 200 GeV for neutral pions.

### **Fabrication and characterization of FOCAL prototype**

After detailed simulations for designing and optimizing, the next effort was put to fabricate a prototype calorimeter. Two generations of detector prototypes were constructed. First one is a mini-prototype with 4 layers of silicon pad detectors and tungsten absorbers. The second one was made with full length (20 layers) of silicon detectors and tungsten absorbers, which is a more realistic design, resembling the actual configuration. The silicon detectors were fabricated on <111> FZ n-type wafers with 3→5 k-Ω resistivities. Each of the silicon pad detector was tested in the laboratory with 60 V as the operating voltage, which affirms reasonably good signal to noise ratio with full depletion. These detectors are characterized with very few nA leakage current and are surrounded by a guard ring. Being physically isolated, the probability of having a cross-talk among the silicon pads is ideally zero. Two different kinds of ASICs, namely, MANAS and ANUSANSKAR were used as readout electronics.

Detailed characterization of the calorimeter was made using the PS and SPS facilities at CERN. First test was with the mini-prototype with  $5 \times 5$  arrays of  $1 \text{ cm}^2$  pads and tungsten absorbers. A devoted trigger system consisting of two pairs of scintillator paddles, a finger scintillator, and a Cherenkov detector was used in the experiment which helped both in proper positioning of the beam as well as selecting electron or hadron beams. The silicon pad arrays, along with backplane PCBs are properly shielded against EMI and ambient light for better signal to noise ratio. The detector signals are readout by using a FEE board and further processed by MARC ASIC, which communicates with the Cluster Read Out Concentrator Unit System (CROCUS). Finally, the CROCUS interfaces to the data acquisition system via

fiber optic cable.

Inspired by the performance of the mini-prototype, the full-length prototype was constructed with 20 layers of tungsten plates and silicon pad sensors of dimension  $1\text{ cm}^2$  area (with  $6 \times 6$  arrays on a single wafer for this time). Exhaustive tests both in the laboratory and with SPS beam at CERN have been carried out. A devoted flexible mechanical arrangement with four movable segments have been made for the experimental setup in which all the three sides (left, top, bottom) are kept open for taking out connections of readout electronics. Options were kept for position adjustment to make either a continuous full depth calorimeter with pad detectors only all through or provision to insert two or more high granular layers ( $1\text{ mm}^2$ ). Front-end-electronics, read-out-electronics, and data acquisition system used for the test were same as was used in its earlier mini-version. Like in mini-prototype, a devoted triggering unit consisting of x-y scintillators, a finger scintillator, and a Cherenkov counter was used. Operating voltage for the silicon detector for this set-up was fixed at 45 V with full depletion. The response of the detectors to  $\text{Sr}^{90}$   $\beta$ -source shows clearly distinguished peaks corresponds to beta-spectrum and the noise elucidating the good functionality of each element of the silicon detector array. To understand the performances of the detector, detailed tests with mini-prototype at T10 beamline at CERN-PS followed by full-length prototype test at H6 beam line at SPS were done for incident energy range 1 to 6 GeV and 5 to 60 GeV electrons respectively. A thorough check and critical analysis have been performed with both set of data taken in Mini-Prototype and Full-length prototype test. A good MIP response found with MPV about 17 ADC both for mini-prototype and full-length prototype, respectively. The variation of total ADC (Experimental measure) with Edep (simulation) shows a good linear behaviour of the mini-prototype. Moreover, partial (only up to  $6 X_R$ ) longitudinal profile of the electron shower also have been extracted and compared with simulation and found to be quite promising. This study with Mini-prototype test has been published in NIM.

The test for full length prototype have been performed and data have been analyzed. After checking the MIP signal, electron responses for different incident energies have been analyzed and found distinctively separated from each other. The response of electrons (ADC) at each layer for particular incident energy shows a rise initially and falls after a certain depth as expected. Longitudinal profile has been obtained and fitted with a phenomenological profile which shows a nice shift of the shower maximum with an increase in incident energy towards deeper along the depth. Calibration, response of output ADC to incident energy, of the prototype shows a very good linear relationship which is must for accurate energy

measurement. The resolution has been found to be 22%, which is close to the simulated expectation. The detailed analyses have been completed and documented as a part of the present study.

### **Study of High Multiplicity events in proton-proton collision with NBD and Blast-Wave model**

With the increase in the center of mass energy, the proton-proton collision has now brought much more challenges to both experimentalists and theorists. Previously at comparatively lower energies, pp collision used to be explained with more fundamental two-particle scattering and used as the reference for the system with the higher order of complicity. Among various physics capabilities with the proposed FOCAL as explained in the previous section, particle production in pp collisions has the most fundamental and impressive expectations for initial state phenomenon, gluon saturation and existence of medium like signatures. In this study, an effort has been made to better understand the particle production in pp collisions at the LHC energies in terms of global variables like multiplicity ( $n$ ), transverse momentum ( $PT$ ), etc. Multiplicity, the number of particles produced in each individual collision, can be used as the first primary global observable for characterizing the collision. Presence of various mechanisms responsible for particle production in a collision is supposed to be reflected in multiplicity distribution. In the present study, a two-source model (superposition of two NBDs) has been adopted to explain multiplicity distribution in proton-proton collision at LHC energies. Surprisingly, reasonings other than so far understood hard scattering has been found to explain the particle production trend quite effectively. A two-component model was studied to better describe particle production at forward rapidities in the small window for LHCb experimental data relying on the event selection criterion used by them which has the limitation in explaining for large rapidity intervals. This study has been reported and published in the refereed journal. We analyze the measured spectra of pions, kaons, protons in pp collisions at 0.9, 2.76 and 7 TeV in the light of blast-wave model to extract the transverse radial flow velocity and kinetic temperature at freeze-out for the system formed in p-p collisions. The dependence of the blast-wave parameters on average charged particle multiplicity of event sample or the ‘centrality’ of collisions has been studied and compared with results of a similar analysis in the nucleus-nucleus (AA) and proton–nucleus (p-A) collisions. We analyze the spectra of  $K_S^0$  and other strange particles to see the dependence of blast-wave description on the species of produced particles. Within the framework of the blast-wave model, the study reveals an indication of collective behavior for high-multiplicity

events in p-p collisions at LHC. Strong transverse radial flow in high-multiplicity p-p collisions and its comparison with that in p-A and A-A collisions match with predictions from recent theoretical works (Shuryak and Zahed 2013 arXiv:hep-ph/1301.4470) that addresses the conditions for applicability of hydrodynamics in pp and pA collisions. After finding non-zero collectivity, advocating presence of some medium, an effort was spent to understand the nature of system produced in HM pp events using simplistic one-dimensional Bjorken Hydrodynamic model as well as with more recent 3D hydrodynamic model calculation. The study shows there is indeed a chance of having partonic medium even in pp collision with high multiplicity events at LHC energies.

### **Bibliography**

1. L. Evans and P. Bryant, JINST 3, S08001 (2008).
2. K. Aamodt et al. (ALICE Collaboration), Eur. Phys. J. C 68, 345 (2010).
3. V. Khachatryan et al. (CMS Collaboration), J. High Energy Phys. 01 (2011) 079
4. K. Aamodt et al. (ALICE Collaboration), Eur. Phys. J. C
5. A. Giovannini and R. Ugoccioni, Phys. Rev. D 68, 034009 68
6. D. Acosta et al. (CDF Collaboration), Phys. Rev. D 65.
7. G. Aad et al. (ATLAS Collaboration), New J. Phys. 13, 072005 (2002).
8. I. M. Dremin and V. A. Nechitailo, Phys. Rev. D 84, 1947 (2012).
9. R. Aaij et al. (LHCb Collaboration), Eur. Phys. J. C 72, 034026 (2011).
10. M. Praszalowicz, Phys. Lett. B 704, 566 (2011).
11. R. E. Ansorge et al. (UA5 Collaboration), Z. Phys. C 43.
12. I. M. Dremin and V. A. Nechitailo, Phys. Rev. D 70, 357 (1989).
13. G. N. Fowler, R. M. Friedlander, R. Weiner, and G. Will, Phys. Rev. Lett. 57, 2119 (1986).
14. A. B. Kaidalov and K. A. Ter-Martirosyan, Phys. Lett. 117B, 247 (1982).
15. A. Giovannini and R. Ugoccioni, Phys. Rev. D 59, 094020 (1999). 034022 (1999).
16. Alexopoulos, Phys. Lett. B 435, 453 (1998).
17. A. Capella and E. G. Ferreira, arXiv:1301.3339.
18. Collins J C and Perry M J 1975 Phys. Rev. Lett. 34 1353
19. Shuryak E V 1980 Phys. Rep. 61 71
20. Arsene I et al (BRAHMS Collaboration) 2005 Nucl. Phys. A 757 1.
21. Adcox K et al (PHENIX Collaboration) 2005 Nucl. Phys. A 757 184.
22. Back B B et al (PHOBOS Collaboration) 2005 Nucl. Phys. A 757 28.
23. Adams J et al (STAR Collaboration) 2005 Nucl. Phys. A 757 102.

24. Adams J et al (STAR Collaboration) 2005 Phys. Rev. Lett. 95 152301.
25. Adams J et al (STAR Collaboration) 2005 Phys. Rev. C 71 044906.
26. Floris M et al (ALICE Collaboration) 2011 J. Phys.: Conf. Ser. 270 012046.
27. Khachatryan V et al (CMS Collaboration) 2011 J. High Energy Phys. JHEP05(2011)064.
28. Dumitru A et al 2011 Phys. Lett. B 697 21.
29. McLerran L 2001 arXiv:hep-ph/0104285v2.
30. Shuryak E and Zahed I 2013 Phys. Rev. C 88 044915.
31. Abelev B et al (ALICE Collaboration) 2012 Phys. Lett. B 719 29.
32. Chatrchyan S et al (CMS Collaboration) 2013 Phys. Lett. B 718 795.
33. Aad G et al (ATLAS Collaboration) 2013 Phys. Rev. Lett. 110 182302.
34. Chatrchyan S et al (CMS Collaboration) 2013 arXiv:hep-ex/1307.3442.
35. The Durham HepData Project <http://hepdata.cedar.ac.uk/view/ins1123117>.
36. The Durham HepData Project <http://hepdata.cedar.ac.uk/view/ins890166>.
37. L.A. Zadeh, Communications of the ACM 37 (3) (1994) 77.
38. A. Engelbrecht, in: Computational Intelligence: An Introduction, Wiley Sons, 2007. ISBN 0-470-84870-7.
39. S.K. Pal, S. Chattopadhyay, Y.P. Viyogi, Nuclear Instruments and Methods in Physics research Section A 626 (2011) 105.
40. S. Chattopadhyaya, Z. Ahammed, Y.P. Viyogi, Nuclear Instruments and Methods in Physics Research Section A 421 (1999) 558.
41. M. Ambriolaa, R. Bellottia, M. Castellanoa, G. De Cataldo, C. De Marzo, Nuclear Instruments and Methods in Physics Research Section A 387 (1997) 83.
42. S. Whiteson, D. Whiteson, Engineering Applications of Artificial Intelligence 22 (2009) 1203.
43. Christian W. Fabjan, Fabiola Gianotti, Reviews of Modern Physics 75 (2003) 1243.
44. P.G. Rancoita, Journal of Physics G 10 (1984) 299.
45. P.G. Rancoita, A. Seidman, Nuclear Instruments and Methods in Physics Research Section A 263 (1988) 84.
46. G. Barbiellini, G. Cecchet, J.Y. Hemery, F. Lemeilleur, C. Leroy, G. Levman, P.G. Rancoita, A. Seidman, Nuclear Instruments and Methods in Physics Research Section A 235(1985)55.
47. G. Barbiellini, G. Cecchet, J.Y. Hemery, F. Lemeilleur, C. Leroy, G. Levman, P.G. Rancoita, A. Seidman, Nuclear Instruments and Methods in Physics Research Section A 236(1985) 316.
48. G. Ferri, F. Groppi, F. Lemeilleur, S. Pensotti, P.G. Rancoita, A. Seidman, L. Vismara, Nuclear Instruments and Methods in Physics Research Section A 273 (1988) 123.

49. M. Bocciolini, et al., WIZARD Collaboration, Nuclear Instruments and Methods in Physics Research Section A 370 (1996) 403.
50. G. Abbiendi, et al., OPAL Collaboration, European Physical Journal C 14 (2000) 373.
51. Jeremy Rouene, et al., CALICE Collaboration, Nuclear Instruments and Methods in Physics Research Section A 732 (2013) 470.
52. Remi Cornat, et al., CALICE Collaboration, Journal of Physics: Conference Series 160 (2009) 012067.
53. E. Kistenev, et al., PHENIX Forward Calorimeter Collaboration, Czechoslovak Journal of Physics 55 (2005) 1659.
54. V. Bonvicini, et al., IEEE Transactions on Nuclear Science NS-52 (2005) 874.
55. D. Strom, et al., IEEE Transactions on Nuclear Science NS-52 (2005) 868.
56. T. Peitzmann, et al., ALICE FoCal Collaboration, arXiv:1308.2585 [physics.ins-det].
57. S. Agostinelli, et al., Nuclear Instruments and Methods in Physics Research Section A 506 (2013) 250.
58. J. Allison, et al., IEEE Transactions on Nuclear Science NS-53 (2006) 270.
59. P. Courtat, et al., The electronics of the Alice Dimuon Tracking Chambers, ALICE Internal Note, ALICE-INT-2004-026, 2004, <http://cds.cern.ch/record/1158633/files/p242.pdf>.

## Key Finding of the Thesis

The Large Hadron Collider (LHC) at CERN, world's largest particle accelerator, designed to explore the fundamental particles and their interactions in terms of the Standard Model and beyond. The design goals are to have proton on proton (pp), proton on lead (p-Pb), lead on lead (Pb-Pb) collisions at centre-of-mass energies of 14 TeV, 8.8 TeV and 5.5 TeV (per nucleon), respectively. ALICE, one among four large scale experiments at CERN, are instrumented to explore especially the early stage of matter (partonic matter) when the universe was microsecond old. The aim of this thesis work is to study the state of the matter at initial states in case of heavy-ion collisions which is dominated by gluon dynamics. A research and development of a new silicon-tungsten sampling calorimeter, measures photons from different sources, have been undertaken as the first part of the thesis work. The study includes an extensive simulation work for geometry and physics performances followed by fabrication and test of a series of prototype calorimeter both with radioactive source and CERN beam facility. The results were found to be encouraging for building the full size calorimeter. The energy resolution was found for the prototype test to be  $\frac{\sigma}{E} = 0.22 \oplus \frac{0.02}{\sqrt{E_0}}$  for energy range 5 to 60 GeV as is shown in figure-1.

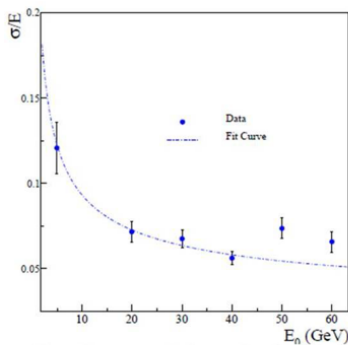


Figure-1: Energy resolution as a function of incident energy for the prototype calorimeter

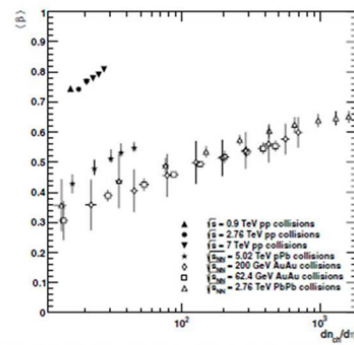


Figure-2: Average transverse radial flow as a function of multiplicity for proton-proton, proton-lead and lead-lead collision.

On the other hand, the second part of the thesis is dedicated to the study of particle production in proton-proton (pp) collisions using different phenomenological models at LHC energies. The pp collision at LHC energies have produced events with comparatively high multiplicity which needs more fundamental introspection towards particle production mechanisms, such as initial state effects, medium formation and etc. A Double Negative Binomial distribution (NBD) model found to explain particle production in pp collisions which shows existence of mechanisms other than hard scattering. The study with a phenomenological Blast wave model indicates the existence of a collectivity in high multiplicity pp events, resulted a larger flow velocity compare to lead-lead and proton-lead collision as is shown in figure-2. A study of degrees of freedom as a function of mean transverse momentum (representing temperature) shows a possible existence of partonic medium in pp collision which might be responsible for the collectivity found.



# Table of contents

|  |             |
|--|-------------|
| <b>List of figures</b>   | <b>xxix</b> |
| <b>List of tables</b>  | <b>xli</b>  |
| <b>1 Introduction</b>  | <b>1</b>    |
| 1.1 Preamble . . . . .   | 2           |
| 1.2 Quark-Gluon-Plasma . . . . .                                 | 7           |
| 1.3 Relativistic high energy collisions . . . . .                | 11          |
| 1.3.1 Aim of high energy collisions . . . . .                    | 12          |
| 1.3.2 Initial conditions . . . . .                               | 14          |
| 1.3.3 Kinematics . . . . .                                       | 16          |
| 1.3.4 Collision parameters . . . . .                             | 18          |
| 1.3.5 Experimental observables . . . . .                         | 19          |
| 1.3.6 Signatures of Quark Gluon Plasma . . . . .                 | 27          |
| 1.4 Motivation and skeleton of the thesis work . . . . .         | 29          |
| <b>2 Interaction and Detection of particles</b>                  | <b>31</b>   |
| 2.1 Introduction . . . . .                                       | 31          |
| 2.2 Interaction of charged particle with matter . . . . .        | 31          |
| 2.2.1 Interaction of heavy charged particles . . . . .           | 32          |
| 2.2.2 Interaction of electron . . . . .                          | 33          |
| 2.3 Interaction of neutral particle . . . . .                    | 36          |
| 2.3.1 Interaction of photon . . . . .                            | 36          |
| 2.3.2 Interaction of neutral particle ( $m \neq 0$ ) . . . . .   | 38          |
| 2.4 Basic measurements . . . . .                                 | 40          |
| 2.4.1 Vertex detection . . . . .                                 | 44          |
| 2.4.2 Particle identification and momentum measurement . . . . . | 45          |
| 2.4.3 Energy measurement . . . . .                               | 47          |

|          |  |            |
|----------|--|------------|
| 2.5      | Physics of calorimetry . . . . .                                 | 48         |
| 2.6      | Summary . . . . .  | 52         |
| <b>3</b> | <b>Large Hadron Collider and The ALICE Experiment</b>            | <b>53</b>  |
| 3.1      | Introduction . . . . .   | 53         |
| 3.2      | Large Hadron Collider (LHC) . . . . .                            | 54         |
| 3.3      | A Large Ion Collider Experiment (ALICE) . . . . .                | 56         |
| 3.4      | Central detectors . . . . .                                      | 59         |
| 3.5      | Forward detectors . . . . .                                      | 60         |
| 3.6      | Photon Multiplicity Detector . . . . .                           | 62         |
| 3.7      | Summary . . . . .  | 65         |
| <b>4</b> | <b>Forward Physics and Calorimetry in ALICE</b>                  | <b>67</b>  |
| 4.1      | Introduction . . . . .   | 67         |
| 4.2      | Physics motivation . . . . .                                     | 68         |
| 4.3      | Calorimetry in high energy physics . . . . .                     | 74         |
| 4.4      | Summary . . . . .  | 75         |
| <b>5</b> | <b>FOCAL: Design and Simulation</b>                              | <b>77</b>  |
| 5.1      | Introduction and pre-requisites . . . . .                        | 77         |
| 5.2      | Geometry optimisation . . . . .                                  | 85         |
| 5.3      | Shower reconstruction . . . . .                                  | 90         |
| 5.4      | Response of calorimeter . . . . .                                | 97         |
| 5.4.1    | Minimum Ionising particle . . . . .                              | 98         |
| 5.4.2    | Electromagnetic shower . . . . .                                 | 98         |
| 5.5      | Summary and scope . . . . .                                      | 105        |
| <b>6</b> | <b>FOCAL: Detector Development, Fabrication and Tests</b>        | <b>107</b> |
| 6.1      | Introduction . . . . .   | 107        |
| 6.2      | Test of Si-detector with $\beta$ -source ( $Sr^{90}$ ) . . . . . | 108        |
| 6.2.1    | Experimental set-up . . . . .                                    | 108        |
| 6.2.2    | Discussion of laboratory test results . . . . .                  | 109        |
| 6.3      | Mini-Prototype . . . . .   | 111        |
| 6.3.1    | Construction and test at CERN-PS . . . . .                       | 111        |
| 6.3.2    | Test beam results and discussion . . . . .                       | 115        |
| 6.4      | Full-Depth prototype . . . . .                                   | 121        |
| 6.4.1    | Fabrication and beam test . . . . .                              | 122        |

---

|          |   |            |
|----------|---|------------|
| 6.4.2    | Data analysis and performances . . . . .                            | 126        |
| 6.5      | Summary and Scope . . . . .   | 135        |
| <b>7</b> | <b>High Multiplicity Proton-Proton Physics</b>                      | <b>139</b> |
| 7.1      | Introduction . . . . .  | 139        |
| 7.2      | Review and motivation of proton-proton physics . . . . .            | 140        |
| 7.3      | Framework and models used for pp physics . . . . .                  | 147        |
| 7.3.1    | Negative Binomial Distribution (NBD) . . . . .                      | 147        |
| 7.3.2    | Blast Wave formalism (BW) . . . . .                                 | 149        |
| 7.3.3    | Estimation of energy density . . . . .                              | 152        |
| 7.4      | Particle production in pp-collision with NBD and BW model . . . . . | 155        |
| 7.4.1    | Particle multiplicity and NBD approach . . . . .                    | 155        |
| 7.4.2    | Analysis and discussion . . . . .                                   | 156        |
| 7.4.3    | Collectivity in pp-collisions and Blast Wave Model . . . . .        | 163        |
| 7.4.4    | Results and discussion . . . . .                                    | 166        |
| 7.5      | Source of collectivity in pp collision. . . . .                     | 178        |
| 7.5.1    | Search for signal of phase change . . . . .                         | 179        |
| 7.5.2    | Analysis, results and discussion . . . . .                          | 181        |
| 7.6      | Summary . . . . .   | 190        |
| <b>8</b> | <b>Summary</b>  | <b>191</b> |
| 8.1      | Summary and Future Scope . . . . .                                  | 191        |
| 8.1.1    | Forward Calrimetry . . . . .  | 191        |
| 8.1.2    | Phenomenology with HM pp physics . . . . .                          | 194        |
|          | <b>Bibliography</b>   | <b>197</b> |



# List of figures

|     |   |    |
|-----|---|----|
| 1.1 | The variation of running coupling constant as a function of momentum transfer, helps in understanding the phenomenon like colour confinement and asymptotic freedom [9] for strongly interacting quarks and gluons. . . .   | 6  |
| 1.2 | The chart shows the list of fundamental particles like quarks, leptons, gauge bosons (gluon, photon, W and Z particles) etc. as predicted by the Standard Model [12]. . . . .   | 8  |
| 1.3 | The picture shows different possible stages of an relativistic high energy collision [25]. . . . .  | 12 |
| 1.4 | Schematic of the QCD-phase diagram [26] which explains the phase transition between partonic to hadronic matter. The phase diagram explain the aim of the relativistic heavy-ion collision which is to explore the different part of the phase diagram in detail to understand the evolution of the universe starting from Big-Bang or the core of the neutron star which are made of high density partonic matter. . . . . | 13 |
| 1.5 | Parton Distribution Functions (PDF) for different type of quarks and gluon are shown in the picture. The distributions are represented as the variation of $x f(x)$ as function of <i>Bjorken-x</i> as published by CTEQ collaboration for momentum transfer $Q^2=10$ GeV/c. . . . .  | 15 |
| 1.6 | Variation of Charged particle multiplicity a function of centre of mass energy $\sqrt{S}$ for proton-proton and heavy ion collision. The plot has been generated taking data from different experiments at different centre of mass energies [52]. It shows the difference in dependence of particle production on centre of mass energy for pp and heavy ion collision. . . . .  | 21 |
| 1.7 | Rapidity distribution for net proton for AGS, SPS, RHIC energies together with an extrapolation for LHC energies. The figure describes how the shape of the rapidity distribution changes with increase of centre of mass energy [54].  | 23 |

|     |   |    |
|-----|---|----|
| 2.1 | The figure represents energy loss per unit length as a function of particle momentum, following Bethe-Bloch formulation [60]. The formulation found to describe the energy loss due to collision and radiation over a wide region of $0.1 < \beta\gamma < 100$ . . . . .  | 33 |
| 2.2 | Energy loss per unit length as a function of particle momentum for different particle following Bethe-Bloch formulation [60]. It illustrates the region for which particles can be identified from their energy deposition profile. . . . .   | 34 |
| 2.3 | Relative cross-sections for photoelectric, Compton and pair production as a function of photon energy for copper, which express the dominance of a particular process for a specific photon energy range. . . . .   | 39 |
| 2.4 | Cross sections for Photoelectric, Compton and Pair production as function of material-Z and incident energy of particle, illustrates which process is relevant for a photon of particular energy interacting with a specific material. . . . .  | 40 |
| 2.5 | Cross sectional view of a complex experiment (ALICE for example) which explains how different sub-detectors are stacked into an anoin like structure to measure particles of wide range in mass, type, energy for almost full $4\pi$ coverage. . . . .  | 44 |
| 2.6 | Sketch of the electromagnetic shower formation following a simplistic Heitler model [64], which illustrates the the number of secondaries produced with in an absorber/converter material as a function of depth in units of radiation length. . . . .  | 50 |
| 3.1 | Schematic representation of the the ALICE experiment at the CERN LHC, embedded in a solenoid with magnetic field $B = 0.5$ T. It has an excellent measurement capability at mid rapidity with ITS, TPC, TRD, TOF, PHOS, EMCal, and HMPID for various type of particles over a wide transverse momentum range. It can also measure cosmic events with the help of ACORDE. Forward detectors like PMD, FMD, V0, T0, MCH and ZDC are used for triggering, event characterisation, and multiplicity studies [68]. . . . . | 56 |
| 3.2 | The figure shows the rapidity coverage of each individual detector of ALICE. ALICE has an excellent mid-rapidity coverage, whereas forward rapidity measurement is restricted by the limited number of detectors and acceptance [69]. . . . .   | 58 |
| 3.3 | The photograph represents the actual PMD, installed at ALICE experiment at a 360 cm away from the interaction point. . . . .  | 63 |
| 3.4 | The figure shows the schematic representation of the working principle of PMD. It explains how it responds to charged particles and photons. . . . .  | 64 |

- 4.1 PDFs inside a hadron as a function of longitudinal momentum fraction ( $x = \frac{Q^2}{2p \cdot q}$ ) with  $Q^2 = -q^2 = 10 \text{ GeV}$  for the struck parton from CTEQ6 collaboration. (*Red : Gluon, Green : Up quark, Blue : Down quark, Pink : Strange quark*). A continuous rise in gluon distribution function is of prime interest in the Bjorken- $x$  sector which might lead to gluon-saturation phenomenon [40–45]. 69
- 4.2 Contribution of prompt photons from different partonic scattering processes. Leading order isolated photons from quark-gluon Compton Scattering, and quark-antiquark annihilation process can be isolated with proper selection criterion from that next to leading order contributions like bremsstrahlung and fragmentation. The figure, indeed, show such an estimation by JETPHOX for prompt photon production applying isolation cuts [87]. . . . . 71
- 4.3 Feynman diagrams for different QCD processes responsible for prompt photon production. Leading order isolated photons (electromagnetic probe) are mostly produced from a) quark-gluon Compton Scattering, and b) quark-antiquark annihilation process. On the other hand, non-isolated photons from next-to-leading order processes like c) bremsstrahlung from a quark, and d) emission during the gluon fragmentation [87] are involved parton-to-hadron fragmentation processes [87]. . . . . 72
- 4.4 Sensitive regions as function of  $x$  and  $Q^2$  for different existing experiments with detectors for hardonic measurements. The expected saturation scale ( $Q_s$ ) is indicated in the figure. Specific acceptance in this schematic diagram, covered by FOCAL, is also shown [87]. . . . . 73
- 5.1 Density of Photons ( $/\text{cm}^2$ ) in proton-proton, proton-Lead, Lead-proton and minimum bias Lead-Lead collisions at LHC energies. . . . . 82
- 5.2 Opening angle of two  $\gamma$ 's coming from symmetric decay of  $\pi^0$ , which help in deciding the design parameter like granularity of the detector to start with. 82
- 5.3 Pseudo-Rapidity Distribution for photons produced in proton-proton, proton-Lead, Lead-proton and minimum bias Lead-Lead collisions at LHC energies using standalone HIJING event generator. It helps in estimating expected particle density for particular  $\eta$ -acceptance. . . . . 83
- 5.4 Sketch of the Calorimeter with Tungsten as absorber and Silicon as a sensitive medium (Not in scale). There are three high granular layers (HGL) and 17 coarse layers (LGL) with sensor dimensions (1 mm\*1 mm) and (1 cm\*1 cm) respectively. . . . . 86

- 
- 5.5 Response of a single 1cm \* 1cm silicon pad detector at 8<sup>th</sup> layer of the calorimeter to an electromagnetic shower produced by a 10 GeV photon. Gaussian fitting to the simulated data is shown by the solid line. The error bars are representing the statistical error. . . . . 88
- 5.6 Cumulative energy deposition profile exhibits the development of "layer added energy deposition" as a function of "layer-number" for EM-showers over a wide range of incident energies. It demonstrates qualitatively an estimation of longitudinal leakage incurred in the calorimeter using its saturation trend (non-saturation) at a depth depending on incoming photon energy. . . 89
- 5.7 A snap from GEANT4 event display for electromagnetic showers, produced by decayed photons from 10 GeV  $\pi^0$ , with corresponding tracks shown by the solid lines which have been reconstructed using clustering technique for clusters formed at 4<sup>th</sup>, 8<sup>th</sup>, 12<sup>th</sup> layers respectively. . . . . 90
- 5.8 The flow chart of the dynamic FCM (dFCM) algorithm. . . . . 93
- 5.9 Reconstruction of neutral pion of energy 10 GeV (top), 50 GeV (middle), and 100 GeV (bottom) decaying to two photons. GEANT4 event display for Longitudinal shower profiles are shown along with clusters found by the FCM algorithm on the 4th, 8th and 12th layers, which are used to find photon tracks. XY-hit distributions, representing the lateral spread of shower at a particular depth (8<sup>th</sup> layer) with cluster centres superimposed. It shows the effectiveness of the FCM even for substantially overlapped clusters, found by the FCM algorithm. . . . . 95
- 5.10 Invariant Mass ( $M_{\gamma-\gamma}$ ) reconstruction from two decayed photons using FCM clustering technique for the proposed FOCAL. The left panel shows for 10 GeV, whereas, the right panel is for 30 GeV  $\pi^0$ . The error bars in both cases represents statistical errors only. . . . . 96
- 5.11 The left panel shown reconstruction of invariant mass ( $M_{\gamma-\gamma}$ ) for 100 GeV  $\pi^0$ , resulting 162 MeV for  $M_{\pi^0}$ , little more compare to its actual value. The right panel summarises the reconstructed invariant masses, calculated for  $\pi^0$  with varying incident energies using FCM, from two decayed photon as a function of  $E_{\pi^0}$ . The errors bars are indicating statistical error. . . . . 96
- 5.12 The plot illustrates the variation of opening angle (top) and minimum distance (bottom) between two photons, decayed from  $\pi^0$ , as a function of  $E_{\pi^0}^{incident}$ . Both the opening angle and the distance decreases with the increase in incident  $\pi^0$  energy. The results are matching satisfactorily with theoretical prediction as shown by the dashed curves. The error is within the marker size. 97

- 5.13 Response to a Minimum Ionising Particle  $\pi^+$  for single pad detector of dimension  $1\text{cm} * 1\text{cm}$  of a particular layer of the calorimeter. The curve represents fit to simulated data with Landau distribution. . . . . 99
- 5.14 Longitudinal profile of an EM-Shower from incoming photons with different incident energies. It represents the variation of energy deposition at a particular layer with a depth of the calorimeter (layer number). The profile shows first rising and then followed by a falling trend with a shower maximum decided by the calorimeter and the incident energy of the incoming particle. 100
- 5.15 The plot represents the position of shower maximum ( $t_{max}$ ) as a function of incident energy for incoming photon. The position of shower maximum ( $t_{max}$ ), expressed in units of radiation length, varies linearly with the logarithmic of the incident energy. Importantly it hints about the depth of the calorimeter and the probable position of the highly granular layers for a specified energy range in designing a calorimeter. . . . . 101
- 5.16 Calibration shows variation of total deposited Energy by the EM-shower triggered by inflowing Gamma with that of incident energy. It assures the the calorimeter is working in liner region indeed. . . . . 102
- 5.17 Energy resolution: represents the efficiency of the calorimeter in measuring the energy precisely of an inflowing particle. It is represented in terms of percentage of the incident energy that has been measured. Lesser the resolution ( $\frac{\sigma}{E_{in}}$ ) better will be the calorimeter. The dashed curve represents two-term resolution formula. The parameter associated with  $\frac{1}{\sqrt{E}}$  used to quote the resolution which is  $\approx 19\%$  in this case. . . . . 104
- 6.1 Experimental arrangement used to test the silicon detectors at VECC laboratory with the  $\text{Sr}^{90}$   $\beta$  source. . . . . 108
- 6.2 Photograph of a single  $1\text{ cm}^2$  silicon pad detector mounted on a PCB board. 109
- 6.3 (Colour online). Response of a single silicon pad detector to  $\text{Sr}^{90}$ - $\beta$  source. A clear peak has been detected corresponding to  $\beta$  spectrum of with end point energy 0.546 MeV. The signal is well dispersed from the noise peak which is around the channel number 20. . . . . 110
- 6.4 Sketch of the silicon detector array of dimension  $5 \times 5$  made of  $1\text{ cm}^2$  physically isolated silicon pad detectors which are mounted on the detector PCB. . . . . 112
- 6.5 (Colour online) The figures represent sketches of two different setups of the Mini-prototype which had been used for the beam test at CERN-PS. . . . . 112

|      |  |     |
|------|--|-----|
| 6.6  | (Colour online) The figure represents the schematic of the mini-prototype with all different components in sequence as was arranged during the experiment. . . . .   | 113 |
| 6.7  | (Colour online) Photograph of the actual experimental set-up which was used at T10 PS Beam Line facility at CERN for the mini prototype test. . . . .  | 115 |
| 6.8  | (Colour online).Response of silicon pad detector arrays to pions, showing the distribution similar to the minimum ionizing particles. The plot is shown in units of ADC. . . . .   | 116 |
| 6.9  | Response of silicon pad detector arrays, placed at the depth of $2X_0$ of the mini-prototype, for electrons at three different energies. . . . .   | 118 |
| 6.10 | (Colour online) The plots represent the longitudinal shower profile which has been reconstructed from data using layer wise energy deposition of the incoming particle over a wide range of energy. . . . .  | 119 |
| 6.11 | (Colour online) The plot shows longitudinal shower profile which has been reconstructed using simulated data with all details of mini-prototype set-up included in simulation package. . . . .   | 120 |
| 6.12 | (Colour online) Conversion curve which compare between energy depositions within the calorimeter prototype which were reconstructed using experimental data (ADC) and the energy deposition from simulated data (MeV). . . . .   | 121 |
| 6.13 | Experimental arrangement for the full-length Prototype with 19 layers of silicon pad detector arrays and tungsten plates along with all associated electronics for the test at CERN-SPS. . . . .   | 122 |
| 6.14 | (Colour online) Sketch of the silicon detector array of dimension $6 \times 6$ made of $1 \text{ cm}^2$ silicon pad detectors which are fabricated on a single wafer and mounted on a detector PCB. . . . .  | 123 |
| 6.15 | Schematic of the mechanical frame, designed and developed for the FOCAL prototype, is made of stainless steel. There are four movable segments, each of which can accommodate five detector and absorber layers. Option for electrical connections are kept both from either side or the top of the frame. . . . . | 125 |
| 6.16 | Schematic of the experimental setup for the full-depth prototype calorimeter which has been used at CERN-SPS. Different components of the experimental set -up are shown in the figure in a hierarchical order as positioned during the experiment. . . . .  | 126 |

- 6.17 (Colour online). The figures show response of silicon pad detector in terms of the mean (upper) and RMS (lower) values of the pedestal as a function of electronic channel. Each 32 channels corresponds to one layer of the prototype calorimeter. In RMS plot, sharp drop to zero represent dead channels which was taken care during offline analysis. . . . . 127
- 6.18 (Colour online). The plot shows the ADC distribution for pions as reconstructed from the prototype test data. The distribution reproduce the minimum ionising particles response. . . . . 128
- 6.19 (Colour online). Energy deposition in unit of ADC at the 7th layer of the Si-W calorimeter prototype for incoming electrons of different energies (5, 20, 30, 40, 50 and 60 GeV). Gaussian fits to the curves give the mean ADC value of the spectra which are shifting to right gradually with the increase of incident energy. . . . . 130
- 6.20 (Colour online) The figure illustrates the longitudinal shower profile which has been reconstructed using experimental data from full depth prototype test at CERN-SPS. . . . . 131
- 6.21 (Colour online). The plot shows the distribution of total energy deposition as measured by the full depth prototype calorimeter. The energy is expressed in unit of ADC as shown in the X-axis of the figure. . . . . 132
- 6.22 (Colour online) Calibration Curve from experimental data (ADC) to Incident energy of incoming particles (GeV). . . . . 133
- 6.23 (Colour online) The figure presents the energy resolution as a function of incident energy of incoming electrons from experimental data. The data resulted resolution expressed with  $a = 0.053 \pm 0.005$  and  $b = 0.221 \pm 0.036$  which has been obtained from the fitting with  $\frac{\sigma}{E_{dep}} = a \oplus \frac{b}{\sqrt{E_0}}$  over the incident energy range of  $5 \rightarrow 60$  GeV . . . . . 134
- 6.24 A series of detector development starting from the  $1 \text{ cm}^2$  physically isolated detectors to  $6 \times 6$  array of  $1 \text{ cm}^2$  on a single 4 inch wafer shown. The proposed final requirement for detector also shown in the sketch. . . . . 137
- 7.1 (Colour online). The plot shows the measured multiplicity density both by ALICE [154] and CMS [155] for proton-proton collision at  $\sqrt{S} = 7$  TeV. The value for the multiplicity density for pp collision reach to a limit where the possibility of medium formation is predicted energetically. . . . . 142

- 7.2 (Colour online). Ridge, structure found for particle correlation in  $\Delta\eta - \Delta\phi$  plane, attributed to hydrodynamical description in case of heavy-ion collision, has been found also in proton-proton collision recently. . . . . 143
- 7.3 (Colour online). HBT radius ( $R_G$ ) of the fireball, produced in proton-proton collision at LHC energy, is shown as a function of charged particle multiplicity density  $\frac{dN_c}{d\eta}$  [71]. The dimension of fireball for high multiplicity proton-proton collision is quite indicative about the existence of a collective medium. . . . . 144
- 7.4 (Colour online). Theoretical prediction for initial energy density ( $\epsilon_{ini}$ ), temperature ( $T_{ini}$ ) and pressure ( $p_{ini}$ ) as a function of multiplicity of produced particles in pp collision [178] at 7 TeV centre of mass energy. . . . . 145
- 7.5 (Colour online). Theoretical prediction for the temperature of the fireball formed in small system like in proton-proton as a function of the size of the fireball [186]. . . . . 146
- 7.6 (Colour online). Primary charged particle multiplicity distributions for minimum bias events in pp collisions at  $\sqrt{S}=7$  TeV for five different  $\eta$ -windows of width  $\Delta\eta=0.5$  within the range  $2.0 < \eta < 4.5$ . The solid lines represent single NBD fitting along with the data points, while the dotted lines are for two-NBD fits. The error bars include both the statistical and the systematic uncertainties [213]. . . . . 158
- 7.7 (Colour online). Primary charged particle multiplicity distributions for Hard-QCD events in pp collisions at  $\sqrt{S}=7$  TeV for five different  $\eta$ -windows of width  $\Delta\eta=0.5$  within the range  $2.0 < \eta < 4.5$ . The solid lines represent single NBD fitting along the data points, while the dotted lines are for two-NBD fits. The error bars include both the statistical and the systematic uncertainties [213]. . . . . 159
- 7.8 (Colour online). Primary charged particle multiplicity distributions for minimum bias and Hard-QCD events in pp collisions at  $\sqrt{S}=7$  TeV for the entire  $\eta$ -range  $2.0 < \eta < 4.5$ . The solid and dotted lines are representing single and double NBD fitting respectively. The error bars include both the statistical and the systematic uncertainties [213]. . . . . 160
- 7.9 (Colour online). Mass ordering, variation of the inverse slope parameter as a function of particle species (mass  $m$ ), found for pPb collision at 5.02 TeV by CMS collaboration which is explained as a signature for collectivity of the system produced in the collision [217]. . . . . 164

- 7.10 (Colour online). Variation of inverse slope parameter ( $T_{effective}$ ) as a function of particle mass, following almost same trend as has been found in pPb and PbPb collision which indicate the scope of applying hydrodynamic model to system produced in proton-proton collision as well [218]. . . . . 165
- 7.11 (Colour online). Transverse momentum ( $p_T$ ) spectra for  $\pi^\pm$ ,  $K^\pm$ ,  $p(\bar{p})$  within rapidity range  $|y| < 1$  for minimum bias pp collisions and for  $K_S^0$ ,  $\Lambda$  and  $\Xi$  within rapidity range  $|y| < 2$  for the non-single diffractive (NSD) events of pp collisions at  $\sqrt{S} = 7$  TeV as measured by CMS collaboration [219, 220]) at LHC. Uncertainties shown, are obtained by adding statistical and systematic errors in quadrature [223]. . . . . 168
- 7.12 (Colour online). Transverse momentum spectra for  $\pi^\pm$ ,  $K^\pm$ ,  $p(\bar{p})$  as measured by CMS collaboration for proton-proton collision at centre of mass energy 7 TeV for multiplicity class 131 (highest multiplicity measure at 7 TeV) [223]. The solid lines represents the simultaneous blast-wave fitting to the data. . . 169
- 7.13 (Colour online). Transverse momentum spectra for  $\pi^\pm$ ,  $K^\pm$ ,  $p(\bar{p})$  as measured by CMS collaboration for proton-proton collision at centre of mass energy 2.76 TeV for multiplicity class 98 (highest multiplicity measure at 2.76 TeV) [223]. The solid lines represents the simultaneous blast-wave fitting to the data. . . . . 170
- 7.14 (Colour online). Transverse momentum spectra for  $\pi^\pm$ ,  $K^\pm$ ,  $p(\bar{p})$  as measured by CMS collaboration for proton-proton collision at centre of mass energy 0.9 TeV for multiplicity class 75 (highest multiplicity measure at 0.9 TeV) [223]. The solid lines represents the simultaneous blast-wave fitting to the data. . . . . 171
- 7.15 (Colour online). Transverse radial flow velocity as a function of charged particle multiplicity density ( $\frac{dn_{ch}}{d\eta}$ ) for different centre of mass energies ( $\sqrt{S}$ ) as obtained from simultaneous blast wave fit to  $\pi^\pm$ ,  $K^\pm$ ,  $p(\bar{p})$  data for pp, pPb, and heavy ion collisions at LHC energies [223]. The system formed in pp collision found to flow with higher velocity compare to that in pPb and PbPb collision. . . . . 174
- 7.16 (Inverse slope parameter ( $T_{kin}$ : combined effect from flow and temperature) as a function of charged particle multiplicity density ( $\frac{dN_{ch}}{d\eta}$ ) for different centre of mass energies ( $\sqrt{S}$ ) as obtained from simultaneous blast wave fit to  $\pi^\pm$ ,  $K^\pm$ ,  $p(\bar{p})$  data for pp, pPb, and heavy ion collisions at LHC energies [223]. 175

- 7.17 (Colour online). Transverse momentum spectra for strange particles  $K_S^0$ ,  $\Lambda$  and  $\Xi$  as measured by CMS collaboration for minimum bias proton-proton collision at 7 TeV centre of mass energy [223]. The solid lines are representing simultaneous blast-wave fitting to the family of strange particles. 176
- 7.18 (Colour online). Transverse momentum spectra for strange particles  $K_S^0$ ,  $\Lambda$  and  $\Xi$  as measured by CMS collaboration for minimum bias proton-proton collision at 0.9 TeV centre of mass energy [223]. The solid lines are representing simultaneous blast-wave fitting to the data. . . . . 177
- 7.19 (Colour online). The figure represents the variation of entropy scaled with cube of transverse momentum ( $\frac{\sigma}{\langle p_T \rangle^3}$ ) as a function of average transverse momentum ( $\langle p_T \rangle$ ). Effectively, the figure shows the variation of degrees of freedom (DOF) for pions, obtained from the published pion-spectra data from CMS collaboration. The trend towards saturation at larger  $\langle p_T \rangle$  has been observed. The solid lines, joining data points, are to guide the eye. The error bars include both the statistical and systematic uncertainties [244]. . . 183
- 7.20 (Colour online). The figure represents the variation of entropy scaled with cube of transverse momentum ( $\frac{\sigma}{\langle p_T \rangle^3}$ ) as a function of average transverse momentum ( $\langle p_T \rangle$ ). Effectively, the figure shows the variation of degrees of freedom (DOF) for kaons, obtained from the published pion-spectra data from CMS collaboration. The trend towards saturation at larger  $\langle p_T \rangle$  has been observed. The solid lines, joining data points, are to guide the eye. The error bars include both the statistical and systematic uncertainties [244]. . . 185
- 7.21 (Colour online). The figure shows average transverse momentum ( $\langle p_T \rangle$ ) as a function of charged particle multiplicity ( $N_{ch}$ ) for the  $p_T$ -range  $0 \rightarrow 10$  GeV and pseudo-rapidity range  $\pm 0.3$ . The data (solid red circle) has been taken from ALICE collaboration and was compared with the simulated events using PYTHIA8 Tune 4C event generator both with and without Colour Reconnection (CR) for pp collisions at 7 TeV. The error bars include both the statistical and systematic uncertainties [244]. . . . . 186

- 7.22 (Colour online). The figure shows the variation of average transverse momentum ( $\langle p_T \rangle$ ) as a function of charged particle multiplicity ( $N_{ch}$ ) for kaon (upper panel) and pion (lower panel) for proton-proton collisions at 7 TeV. The data from was taken from ALICE collaboration and compared with the simulated events using PYTHIA8 Tune-4C both for colour reconnection on and off. The plots had been generated for the  $p_T$ -range up to 2 GeV both for kaon and pion. The error bars include both the statistical and systematic uncertainties [244]. . . . . 187
- 7.23 (Colour online). The figure shows the variation of  $\frac{\sigma}{\langle p_T \rangle^3}$  as a function of the mean transverse momentum ( $\langle p_T \rangle$ ) for pions (upper panel) and kaons (lower panel) for proton-proton collision at 7 TeV. The open squares represents simulated data from PYTHIA Tune-4C, whereas, solid squares are obtained from the measured [217] spectra data by CMS collaboration. The figures clearly shows differences between simulation and experiment as was expected. The error bars include both the statistical and systematic uncertainties [244]. . . . . 188
- 7.24 (Colour online).The figure illustrates the behaviour of  $\frac{\sigma}{\langle p_T \rangle^3}$ , extracted for proton-Lead collision at 5.02 TeV, as a function of the average transverse momentum ( $\langle p_T \rangle$ ) pion (upper) and kaon (lower). The open circles represents data from PYTHIA Tune-4C simulation, whereas, solid circles are obtained from the CMS collaboration [217]. The error bars include both the statistical and systematic uncertainties [244]. . . . . 189



# List of tables

|     |  |     |
|-----|--|-----|
| 1.1 | Three generation of quarks are presented in the table along with their relevant quantum numbers. . . . .   | 4   |
| 3.1 | The table illustrates the excellent capability of LHC in providing collision for different systems like proton-proton, proton-Lead, Lead-Lead and Xenon-Xenon. Moreover, the centre of mass energy varies for different colliding systems starting from 900 GeV to 14 TeV. . . . . | 55  |
| 3.2 | Coverages of each individual detector of ALICE experiment in $\eta - \phi$ plane   | 57  |
| 5.1 | Pseudo-rapidity coverage for the proposed FOCAL with a comparison with existing experiments at the LHC. . . . .  | 77  |
| 5.2 | Comparative properties for optimized absorber/converter of a calorimeter. .  | 84  |
| 6.1 | Specifications of the readout ASICS (MANAS and ANUSANSKAR) used in the mini-tower set-up and tests. . . . .  | 114 |
| 7.1 | An overview of the dimension that can be probed with proton and electron of different beam energies using de’Broglie hypothesis. . . . .   | 141 |
| 7.2 | Parameters as extracted from fitting with NBD functions to the multiplicity distributions for the primary charged particles for minimum bias events in pp collisions at $\sqrt{S}=7$ TeV for five small $\eta$ -windows. . . . .   | 157 |
| 7.3 | Parameters extracted from two NBDs fitting to the multiplicity distributions for the primary charged particles in minimum bias events in pp collisions at $\sqrt{S}=7$ TeV for five $\eta$ -windows, and shown in the table in the same order as in table 7.2. . . . .             | 161 |
| 7.4 | Parameters as extracted from fitting with single NBD function to the multiplicity distributions for the primary charged particles for Hard QCD events in pp collisions at $\sqrt{S}=7$ TeV for five small $\eta$ -windows. . . . .   | 161 |

|     |  |     |
|-----|--|-----|
| 7.5 | Parameters extracted from single NBD fitting to the multiplicity distributions for the primary charged particles in pp collisions at $\sqrt{S}=7$ TeV for $\eta$ -range 2.5 ( $2.0<\eta<4.5$ ) both for minimum bias and "Hard-QCD" events. . . . .  | 162 |
| 7.6 | Parameters extracted from two NBD fitting to the multiplicity distributions for the primary charged particles in pp collisions at $\sqrt{S}=7$ TeV for $\eta$ -range 2.5 ( $2.0<\eta<4.5$ ) both for minimum bias and "Hard-QCD" events. . . . .   | 162 |
| 7.7 | Parameters of BGBW, $T_{kin}$ , $\beta$ and n, have been extracted from the simultaneous fit to the published [53] spectra of $\pi^\pm$ , $K^\pm$ and $p(\bar{p})$ for pp collisions at $\sqrt{S}=0.9, 2.76$ and 7 TeV for different event classes depending on average multiplicity, $N_{ch}$ , in the pseudo-rapidity range $\eta<2.4$ . . . . . | 172 |
| 7.8 | Parameters of BGBW, $T_{kin}$ , $\beta$ and n, have been extracted from the simultaneous fit to the published [31-54] spectra of strange mesons, $K_S^0$ , $\Lambda$ and $\Xi$ for pp collisions at $\sqrt{S}=0.9$ and 7 TeV. . . . .  | 178 |

# Chapter 1

## Introduction

The Large Hadron Collider (LHC) at CERN is the world's largest particle accelerator, designed to explore the fundamental particles and their interactions in terms of the Standard Model and beyond. It has the capability to accelerate particles at ultra-relativistic energies. The design goals are to have proton on proton (pp), proton on lead (p-Pb), lead on lead (Pb-Pb) collisions at center-of-mass energies of 14 TeV, 8.8 TeV and 5.5 TeV (per nucleon), respectively. Four large scale experiments, ALICE, ATLAS, CMS and LHCb, are instrumented to explore different physics goals. ATLAS and CMS experiments are dedicated to the study of Higgs particles and exploring new particles. LHCb explores the new physics through a precise test of the heavy-flavour sector of the Standard Model. ALICE is specifically designed for the study of quark-gluon plasma (QGP), formed in heavy-ion (such as Pb-Pb) collisions.

The aim of the thesis work is to study the state of the matter at initial states in case of heavy-ion collisions which is dominated by gluon dynamics. These conditions can be well studied by measuring high-energy photons at forward rapidities in ALICE. For this purpose, research and development of a new silicon-tungsten calorimeter have been undertaken as a part of the thesis work. After extensive simulation work, the design of the calorimeter was finalised. The silicon pad detectors are designed and fabricated according to our specifications. A series of dedicated tests using high-energy electrons were made at CERN PS and SPS. The test results have shown that the silicon-tungsten calorimeter is suitable for achieving the desired physics goals of ALICE for probing gluon saturation and related physics. The second part of my thesis is dedicated to the study of QGP in proton-proton collisions using different phenomenological models.

In this Chapter, I will first give a preamble to fundamental physics and discoveries leading to the revelation of quark structure as the building block of matter. Then I briefly discuss quantum chromodynamics (QCD) and QGP phase transition and its signatures. At the end of this Chapter, I will briefly outline the organisation of the thesis.

## 1.1 Preamble

The quest of knowing matter down to its tiniest possible constituent has strong philosophical and scientific history. It probably started long back in 460 BC from the great Greek philosopher Democritus with his curiosity about "what happens if you break a matter in halves and halves and so on". The search, indeed, gave birth to the concept of *the particle* [1], thought as smallest possible bit of matter and *named as atom* which can not be either created or destroyed. Interestingly, Maharshi Kanada, a Great Sage and philosopher of ancient India, independently brought similar kind of concept about existence of *atoms* [2] with different variants relying on perception and realism at around 600 BC. It is long after conceiving the concept about structural constituents which went through lot of ups and down over centuries until the great English chemist John Dalton came up with his experimental results in 1800. The results indicate about the existence of tiny, lumpy and fundamental unit of matter called "atom". It took about 100 years to realise that atom can further be decomposed when J. J. Thomson discovered the electron and subsequently the *plum-pudding* model in 1897. In fact, the study about knowing deeper in structure of matter got accelerated after this leap and resulted the discovery of positively charged "proton" by Eugen Goldstein in 1900 in his anode ray experiment. The most important breakthrough experiment in physics, however, came in 1911 with Rutherford Scattering [3] of positively charged alpha particle ( $\alpha : He_2^4$  ion) on thin gold foil which explored for the first time a clean schematic about how the atom looks like with its positively charged massive centroid (nucleus) surrounded by negatively charged electrons. Paralelly, the discovery of natural and artificial radioactivity opens up a new avenue in probing the structure of matter in controlled experiment. However, the limit on the highest available energy for the probing particle imposes the dimension of the smallest structure that can be explored. The need for an accelerator was immediately perceived and the first effort was materialised in 1929 by Ernest O. Lawrence with a cyclic accelerator. In the meantime, the details about the structure of atom has been postulated by Neils Bhor in 1912 and successively tuned by Sommerfield and successors to make it more realistically precise. Moreover, the historic invention of relativity by Albert Einstein came into the picture and thus the famous  $E = mc^2$  withhold the boundary between mass and energy and interpreted the conversion of mass into energy and vice versa. The atomic

structure however, remain incomplete until 1933 when Chadwick [4] discovered neutron, a proton like but neutral particle, equally responsible in building the atomic nucleus. For next few decades, the research was directed in developing theoretical framework and relevant experiments in understanding strong interaction and strongly interacting matter which led to many important discoveries regarding new particles like antimatter ( $e^-$ ), muon, pion, neutrino etc. and breakthrough phenomenon like uncertainty principle, expanding universe, nuclear fission, parity violation, superconductivity and so on. The next boost in understanding the constituents of matter came up from Murray Gell-Mann [5] and George Zweig [6] in 1964 with their independent research on quarks as building blocks for hadron. However, the first experimental proof in support of the structure for hadron (proton) established in 1968 with the results from Deep Inelastic Scattering at Stanford Linear Accelerator Center (SLAC) [7]. A more comprehensive study about the partonic structure of hadron came little later by Feynmann in 1971 [8]. At the beginning, Gellmann's model started with two types of quarks (up and down) as constituents of hadron either as quark-antiquark combination (mesons) or three quarks combination (baryons). However, for complete description of partonic structure of matter at subatomic level, two more generations of quarks of different properties were postulated and discovered in experiments subsequently. So, the partonic picture essentially came up with three generations or six types (six different flavours more precisely) of quarks along with their corresponding anti-partner as the fundamental building block of matter. Characteristically, quarks of individual flavours, possesses different properties like mass, electric charge, spin etc. Moreover properties like baryon number, strangeness, charm, beauty etc. which are relevant for strongly interacting particles following corresponding conserved quantities. In addition, explanations of triple quark combinations found difficulties in accommodating spin-statistics theorem, Pauli exclusion principle to be specific, which was rescued by Bogoliubov, Struminsky and Tavkhelidze, Han and Nambu and Miyamoto independently in the year 1965 with the introduction of an internal quantum number which was named colour by Gellmann. Following the concept of colour quantum number, as is formulated in Quantum Chromodynamics, the quarks are ascribed three different colours, red, green and blue, to make them coexist and form colourless particles like proton, neutron etc. Basically, the concept of colour established quarks as real physical entity from Gellmann's mathematical concept. The different identifying properties for all three generations of quark are summarised as is shown in table 1.1

On the other hand, the theory of strong interaction, *Quantum Chromo Dynamics (QCD)*, can be explained, like other three forces, by a  $SU(3)$  gauge group which is the colour symmetry group obeyed by quarks, following the Yang-Mills principle of local invariance and quantisation of chromodynamics fields. However, to understand the interaction among

Table 1.1: Three generation of quarks are presented in the table along with their relevant quantum numbers.

| Generation      | Quark-Type (Symbol) | Baryon Number | Charge          | Strangeness | Charm | Bottom | Top | Mass (MeV)  |
|-----------------|---------------------|---------------|-----------------|-------------|-------|--------|-----|-------------|
| 1 <sup>st</sup> | Up (u)              | $\frac{1}{3}$ | $+\frac{2}{3}e$ | 0           | 0     | 0      | 0   | 2 → 8       |
| 1 <sup>st</sup> | Down (d)            | $\frac{1}{3}$ | $-\frac{1}{3}e$ | 0           | 0     | 0      | 0   | 5 → 15      |
| 2 <sup>nd</sup> | Strange (s)         | $\frac{1}{3}$ | $-\frac{1}{3}e$ | -1          | 0     | 0      | 0   | 100 → 300   |
| 2 <sup>nd</sup> | Charm (c)           | $\frac{1}{3}$ | $+\frac{2}{3}e$ | 0           | 1     | 0      | 0   | 1000 → 1600 |
| 3 <sup>rd</sup> | Bottom (b)          | $\frac{1}{3}$ | $-\frac{1}{3}e$ | 0           | 0     | -1     | 0   | 4100 → 4500 |
| 3 <sup>rd</sup> | Top (t)             | $\frac{1}{3}$ | $+\frac{2}{3}e$ | 0           | 0     | 0      | 1   | 180000      |

quarks, the QCD potential needs to be understood. The lack of existence of coloured particles in nature imposes some special properties in quark-quark interaction unlike quantum electrodynamics, an electromagnetic counterpart of QCD. In QCD, the interaction among quarks is mediated by gluons (g), a gauge boson in QCD. Gluons, having colour charge unlike photon in QED, can interact among themselves which makes the QCD potential to be of short range in nature. The QCD contribution to the quark-quark potential can be represented by a simple expression as is shown in equation 1.1

$$V_{q-q} = V_{QCD}(r) + V_{QED}(r), \quad (1.1)$$

$$V_{QCD}(r) = -\frac{4}{3} \frac{\alpha_S}{r} + kr,$$

where the  $V_{QED}(r)$  is contribution due to electromagnetic interaction (QED) and coulombic in nature. On the other hand, the QCD, dominantly characterises the properties of interaction, have two contributions.

a)  $-\frac{4}{3} \frac{\alpha_S}{r}$  is Coulombic counterpart of QED in case of strongly interacting particles which behave like QED at short distances ( $r < 0.1$  fm). The contribution, being negative, act as an attractive potential and held the quarks to be tightly bound because of the large value of the strong coupling constant  $\alpha_S$  (0.2).

b)  $kr$  represents string tension, increases linearly at large distances ( $r \geq 1$  fm) which is responsible for the colour confinement and thus restrict free coloured quarks. The string constant

"k" has values  $1\text{GeV}/\text{fm}$ , resulted in large value for the interaction potential between two quarks when separated apart from each other.

The running coupling constant  $\alpha_s$  determines the strength of strong interaction. Unlike in QED, QCD running coupling constant varies significantly with the distance between two quarks. Depending on the types of quarks, their colours and the momentum scale involved in the coupling constant can be represented by equation 1.2

$$\alpha_s(Q^2) = \frac{\alpha_s(\mu)}{1 + \frac{\alpha_s(\mu)}{12\pi}(11N_C - 2N_f)\ln\left(\frac{Q^2}{\mu^2}\right)}. \quad (1.2)$$

In the above equation,  $\alpha_s$  decreases with increase in  $Q^2$  (momentum transfer) which makes the QCD to be oppositely behaved compare to QED. Pictorially, the variation of  $\alpha_s$  can be explained with the figure 1.1 The behaviour of  $\alpha_s$  at large distances and low energy scale, the self-interacting nature of gluons makes the strong interaction anti-screening in nature instead of screening the effect of colour charge like in QED, resulted confinement of colour charges where perturbation technique fails to explain. On the other hand, at small distances and higher energy scale, the quarks can roam around freely since the QCD reach the limit of asymptotic freedom. Essentially, when two quarks are trying to move apart, the force between them increases and the string (gluon) binding them is excited. In the limit when  $E_{string} \geq 2m_q$ , it breaks up and new quark-antiquark pair produced which render in getting a free colour charge. However, approaching towards asymptotic freedom can lead to form a free coloured quark in a confined region. The limit of asymptotic freedom can be achieved either with pumping very high energy (relativistic heavy ion collision) or compressing matter to such extent so that constituent nucleon loose individual boundaries and parton become close enough to behave like free particles.

The process of phase change from the confined colourless system to a deconfined partonic medium is called deconfinement phase transition. The deconfinement QCD phase transition can be well understood with the schematic diagram in  $T - \mu$ -plane as shown in figure 1.4. It is to be noted at this point, that the phase transition, which the system undergoes at such extreme condition is not only the "confinement  $\Leftrightarrow$  deconfinement phase transition associated with iso-spin symmetry of QCD" but is described along with chiral phase transition associated with "breaking/restoration of chiral symmetry", an approximate QCD symmetry in the limit of vanishing quark masses. At small distances and large energy scale (Temperature,  $T > T_C$ ),

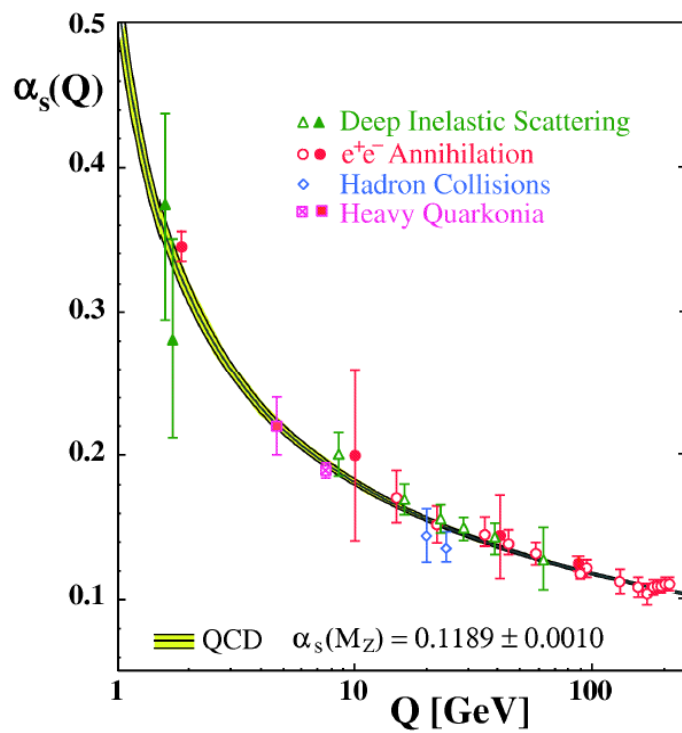


Figure 1.1: The variation of running coupling constant as a function of momentum transfer, helps in understanding the phenomenon like colour confinement and asymptotic freedom [9] for strongly interacting quarks and gluons.

the system undergoes a phase transition with partons as degrees of freedom. Beyond the transition temperature, the chiral symmetry is expected to be restored. Usually, with vanishing quark masses, the chiral phase transition is expected to be of either 1<sup>st</sup> or 2<sup>nd</sup> order, however, the introduction of physical quark masses describe the phase transition either of 1<sup>st</sup> order or of crossover type. The availability of relativistic colliders across the world facilitate in probing the partonic matter, that might have formed just after the collision, mimicking the big-bang in small scale. Quark-Gluon-Plasma (QGP), a special state of the partonic medium has been experimentally established which will be discussed in more details in the subsequent section.

There were several experimental attempts in proving the existence of partons (quarks and gluon) and their characterisation since its prediction at different experiments like SLAC, Alternating Gradient Synchrotron (AGS), Super Proton Synchrotron (SPS), Relativistic Heavy Ion Collider (RHIC) and very recently Large Hadron Collider (LHC). In fact, the motivation behind a colliding system like electron-proton, proton-proton, proton-heavy ion, heavy ion-heavy ion for a wide range of centre of mass energy starting from 1 GeV to few TeV, was to study the properties of fundamental parton-parton scattering to the complicated partonic system (QGP for example). The most recent discovery regarding the search for a fundamental particle is "Higgs" boson [10, 11], responsible for the mass of quarks, in 2012 was explained, a rare parton-parton scattering process which is experimentally verified by ATLAS and CMS independently at LHC. This in some sense completes the list of particles, as depicted in figure 1.2, as constituents of standard model prediction.

*ALICE* (A Large Ion Collider Experiment [13]) at LHC, among many other large scale experiments, is a unique experiment addressing the physics of strongly interacting matter at extreme energy densities and temperature, known as Quark-Gluon-Plasma [14–17]. QGP can be produced in relativistic heavy ion collision between nucleus-nucleus and recently even in small systems, formed in proton-nucleus and proton-proton collisions.

However, for the present thesis work, a formal introduction to the field of strongly interacting partonic matter (Quark Gluon Plasma) and the relativistic high energy collision will be discussed in brief in the subsequent sections.

## 1.2 Quark-Gluon-Plasma

Quark Gluon Plasma, a deconfined partonic mater constituted with quarks and gluons, is one of the main aims behind the study of relativistic high energy collisions. It helps in revealing different stages of evolution of the system, starting from the initial partonic matter to finally created hadronic phase. Plenty of experimental signatures have confirmed the creation of

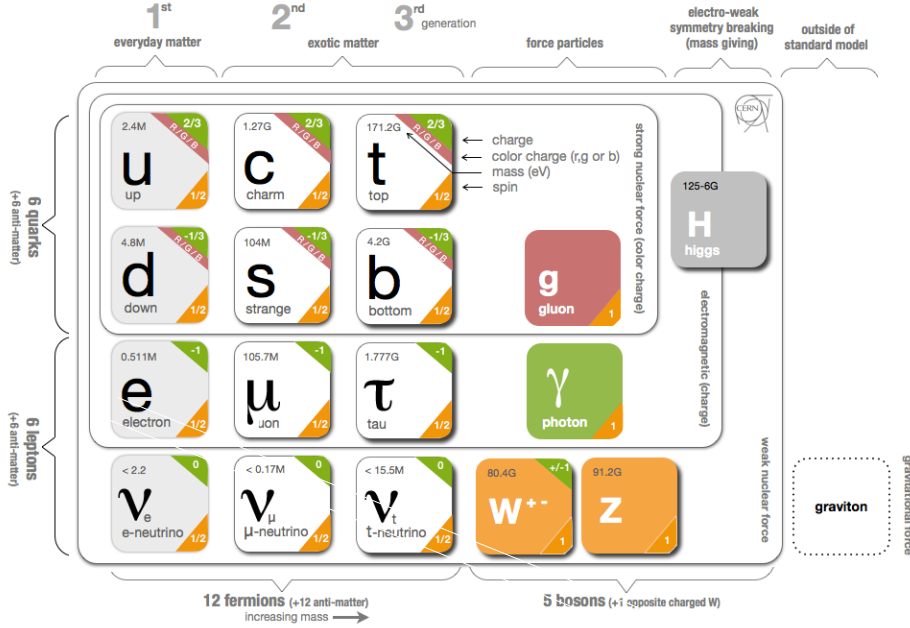


Figure 1.2: The chart shows the list of fundamental particles like quarks, leptons, gauge bosons (gluon, photon, W and Z particles) etc. as predicted by the Standard Model [12].

deconfined parton. However, understanding the details of the partonic phase has become one of the main focus of relativistic heavy ion collision. Several theoretical and phenomenological studies explored that the partons created in extremely high energy collision likely to be in a plasmatic state, governed by the theory of strong interaction. Quark-Gluon-Plasma, a partonic soup and a phase of quantum chromodynamics, can be created under extremely high energy and/or density if the temperature of the partonic system is above a critical temperature  $T_C$  ( 160 GeV). To be in QGP phase, the system must possess plasmatic characteristics like

**a.) Plasma Approximation ( $N_D \gg 1$ )** - Signifies the number of particles within the Debye sphere, determined by the screening of colour charge, should be large to make the Debye shielding a statistically valid concept and ensures collective nature of the system to dominate over single one-to-one interaction.

**b.) Existence of Bulk Interaction ( $\Lambda_D \ll L$ )** - Imposes the properties to be controlled by the bulk of the system rather than the surface/edge effects and so helps in achieving quasi-neutrality for the system.

**c.) Existence of Plasma Frequency ( $\omega\tau > 1$ )** - Ensures the plasma frequency to be larger compared to the hard sphere collisional frequency. In turns, it will result the strong interaction to govern the kinematics and the dynamics of the system.

The plasmas, in general, could be gases, liquids, or solids depending on the plasma parameter  $\Gamma(\frac{E_{interaction}}{E_{Kinetic}})$ , which take values  $\geq 1$  for strongly coupled plasmas and deviate more for the ideal gas characteristics. For example, QGP at just  $T > T_C (\approx 200 \text{ GeV})$ , with  $\alpha_S = 0.3 \rightarrow 0.5$ , take values  $1.5 \rightarrow 6$  for  $\Gamma(\frac{2C\alpha_S}{aT^2})$  with  $C$  and  $a$  are Casimir invariant and inter-parton distance respectively which let the plasma to behave like as strongly interacting [18]. Moreover, strongly- coupled QGP (sQGP) has interesting property of shear viscosity-to-entropy density ( $\frac{\eta}{s}$ ), characterising the fluid being a perfect liquid, which get negligible values ( $\approx 0.4$ ). The life of a deconfined QGP, produced in high energy heavy ion collision, evolved through many stages like expansion, cooling down, parton fragmentation before finally hadronises to final colourless hadrons. Though the details of all individual stages can not be observed experimentally, but what is measured are time-integrated final state observables like momentum spectra of hadrons/photons/leptons, particle multiplicities, system size, flow, energy density and etc. Signatures like final state particle multiplicity have direct consequence with the entropy of the system whereas high  $p_T$  particles, expected to come from early stage high- $p_T$  partons or heavy flavours. They carry information about the initial stages of the partonic system produced in high energy collisions. The  $p_T$ -spectra of produced particles and their yields carries important information like strong radial flow, arises due to the large internal pressure of the partonic medium. Usually, in any experiments, there are few first-day results like charged particle multiplicity density ( $\frac{dN_{ch}}{d\eta}$ ) and their dependence on centrality and centre of mass energy of collision. Simple phenomenological models like Bjorken model can help in estimating the energy density of the partonic medium using  $\frac{dN_{ch}}{d\eta}$  at mid-rapidity. The properties, collectivity in specific, of the partonic medium can be directly probed studying the evolution of anisotropic flow in terms of different flow coefficients which can be directly correlated to the physical properties like viscosity, initial geometrical anisotropy, thermodynamical nature and etc. Lattice QCD, a non perturbative QCD approach and used to study properties partonic system with quarks and gluons, has predicted the critical values for energy density ( $\epsilon_C \approx (0.34 \pm 0.16) \text{ GeV}/fm^3$ ), temperature ( $T_C = (154 \pm 9) \text{ MeV}$ ) at which the matter become de-confined and form QGP. The predictions are quite consistent with results from other model calculations like Hadron Resonance Gas (HRG) model below  $T < T_C$ . The first circumstantial evidence about the creation of partonic state of matter in Pb + Pb collisions was announced in 2000 by SPS at CERN [19] followed by the official discovery of QGP in Au + Au collisions in 2005 by four experimental collaborations at the Relativistic Heavy Ion Collider [20–22]. The formation of quark-gluon-plasma and their characterisation was studied in relativistic heavy ion collision (HIC) where the predicted thresholds for parameters off QGP can be achieved easily. On

the other hand, proton-proton (pp) collision, assumed to produce very few particles through basic hard scattering among strongly interacting partons, are used as the reference for results from HIC. However, with the increase of the central of mass energy such as 7 TeV and above, pp collision has shown to produce a special class of a comparatively large number of particles which has potential in terms of energy density and temperature to produce partonic collective system! A brief discussion about HI and pp collision in respect of quark gluon plasma formation and their properties will be followed in the next subsections.

In view of creating a partonic medium, the relativistic collision between heavy ions (HI) had been always preferable to attain the required threshold energy density. Collision b/w large nuclei like Au (RHIC) and Pb (LHC) results head-on collision of Lorentz contracted discs (pancake) of thickness  $\approx \frac{14}{\gamma}$  fm with  $\gamma$ 's 100 and 2500 at highest beam energies at RHIC and LHC respectively. The volume between two receding pancakes contains a medium which might have created because of soft/hard interactions among constituent partons of two incoming nuclei with an energy density  $\approx 0.5$  GeV/fm<sup>3</sup>, substantially large compared to usual energy density inside hadron 0.13 GeV/fm<sup>3</sup>. A naive estimation shows PbPb collision at the centre of mass energy of 2.76 TeV at LHC can lead to an energy density of 12 GeV/fm<sup>3</sup>, an order of magnitude larger than the threshold energy density for partonic medium production [23] which corresponds to QCD based thermal medium of temperature 300 MeV. Interesting to note, in HI collision, an enormous amount of entropy is produced which resulted  $\approx 10^4$  (LHC) particles from almost initially zero entropy (two directed disc before collision). The lifetime ( $\tau$ ) of partonic medium plays a vital role for partonic medium to achieve the thermodynamic equilibrium to be in a plasmatic state. Measurement shows lifetime of the partonic medium for RHIC and LHC at 200 and 2760 GeV are 8.4 fm/c and 10.6 fm/c respectively which assures the condition for thermalisation to be a reasonable assumption. Apart from a head-on collision, there is plenty of occasion in HI-collisions, where two nucleon interact in an off-centric manner which leads to special anisotropy, turned into momentum anisotropy in final go, which can be measured experimentally in terms of coefficients of flow.

In contrast, the proton-proton (pp) collision are used to serve the baseline to study QGP properties in HI collision until the results from CMS collaboration at LHC came up with a very special class of events in pp collision, called high multiplicity (HM) events. These HM events with an unusually large number of charged particles ( $N_{ch} \approx 10^2$ ) where spatial correlations resembling those, attributed to QGP in heavy-ion collisions. With the increase in the centre of mass energy available at LHC, the HM event classes become more frequent. ALICE and ATLAS collaborations at LHC confirmed the discovery of collectivity

even in small systems like in pp collision which was hardly anticipated by the community earlier. Strangeness enhancement, a special and hallmark signature for QGP, was reported immediately for pp collision by ALICE experiment [24]. These results, though not yet decisive, but shown potential to find QGP in a smaller system which has become a milestone in the study of QGP. More detail discussion will be followed in this regards in chapter 7.

### 1.3 Relativistic high energy collisions

The beginning of modern-day experiments at different colliders around the globe might have started with the discovery of "atomic structure" from Rutherford scattering back in 1911 [3]. However, with the continuous advancement of the particle accelerator and detection techniques, the aim of such experiments have shifted from atomic to nucleonic to the quarkonic structure of matter. After the discovery of proton and neutron as constituents of the nucleus, it took long to discover the structure of proton's (hadrons in general) in "Deep Inelastic Scattering" at HERA at SLAC facility in 1968 [7]. The depth of a structure of matter which can be probed in a scattering experiment depend on the particle itself and its energy following de Broglie hypothesis. In general, a scattering experiment has three different adjoint aspects, *before - during and after* the collision respectively, which need to be regarded accordingly to explore the relevant physics potential. To start with, there could be two ways, collisions can be made either in *Fixed Target Mode* or in *Collider mode*, both having their own advantages and disadvantages. Along with state of art technological requirements, to achieve the same available useful energy of collision (centre of mass energy:  $\sqrt{S}$ ), collider experiments are always preferable by a factor of

$$\frac{E^{fixed\ target}}{E^{collider}} = \frac{(E_{CM}^2 - 2m^2)/2m}{E_{CM}/2},$$

for a particle of mass  $m$ , however, fixed target experiments are more beneficial for higher luminosity and larger interaction cross-section which are more desirable for investigating rare physics phenomenon. The need for more and more energies for the collision to probe deeper details of partonic structure of matter and their properties came up with experimental facilities like SLAC, SPS, RHIC and LHC and efforts for future colliders like ILC, FCC etc. In the present discussion, a brief review of different aspects of relativistic collisions, like kinematics, initial conditions, collisional parameters, final observables and etc., will be explored. Quantitatively, particle production in a relativistic high energy collision can be expressed, assuming QCD factorisation theorem, as

$$\text{Particle production} = \text{PartonDistributionFunction} \otimes \text{CrossSection} \otimes \text{Fragmentation}$$

and can be pictorially represented with contribution from stages of evolution from initial to final state particles as following the figure 1.3 .

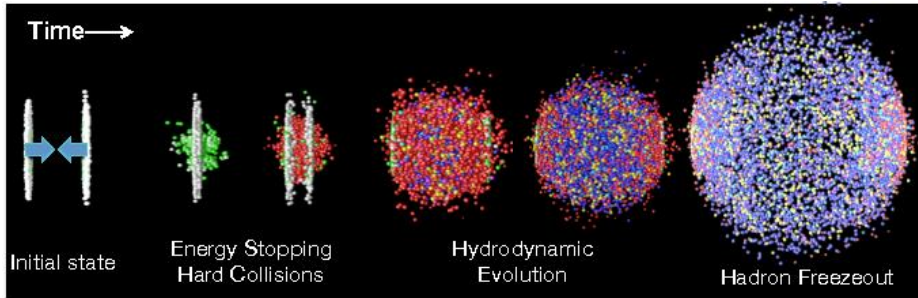


Figure 1.3: The picture shows different possible stages of an relativistic high energy collision [25].

### 1.3.1 Aim of high energy collisions

Starting from the first relativistic heavy-ion collision experiment at BNL and CERN in 1986 with energy 10 GeV per nucleon, the physics goal roams around the understanding of formation and evolution of deconfined partonic matter which advances in steps and reaches to a stage of finer details with latest inputs from LHC experiments. The main goal of the relativistic heavy-ion collision, however, is to explore the phase diagram as shown in 1.4, representing the details of partonic-to-hadronic phase transition and vice versa in  $\mu_B$ -T plane. Heavy-ion collision at relativistic energies is supposed to create a deconfined matter at the extreme condition of temperature and energy density coming from "Little Bang", a small scale laboratory version for "Big Bang", responsible for the creation of the universe. The purposes of high energy collision can be categorised naively as following-

**Properties of matter under extreme energy and density:-** Recreating the matter that had been there just when the universe was microsecond old or present in the stellar object like neutron stars [27, 28]. The matter was supposed to be completely different from stable nuclear matter and is governed by the partonic degrees of freedom.

**Study of hadronic  $\Leftrightarrow$  partonic phase transition:-** The deconfinement phase transition, responsible to create the state where partons (quarks and gluons) are free due to asymptotic freedom, can be studied in details along with the nature of transition such as the order of phase transition and etc. Moreover, The chiral symmetry restoration, where hadrons are found

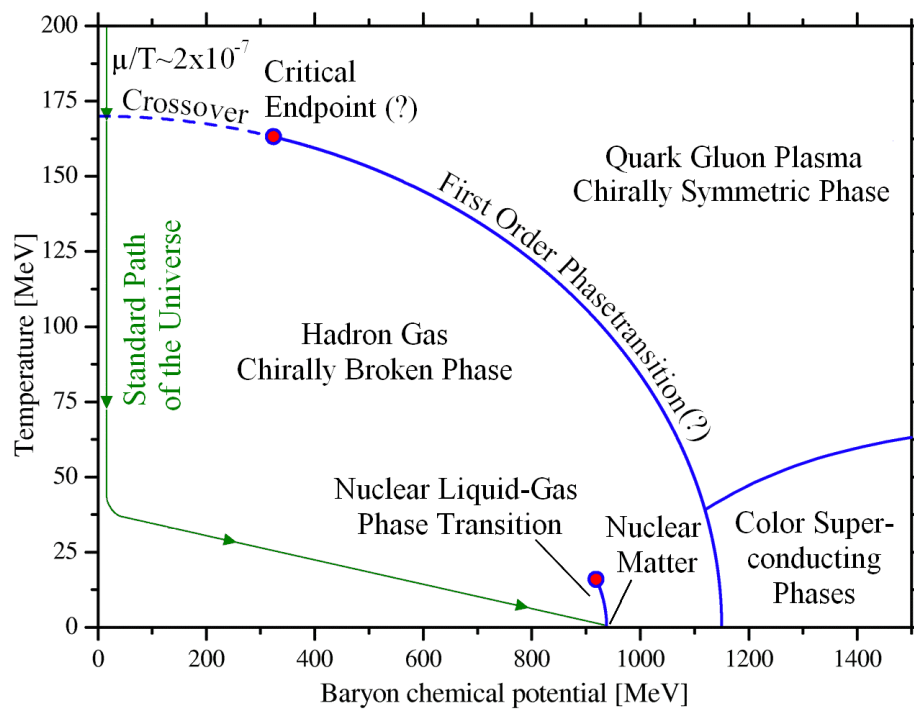


Figure 1.4: Schematic of the QCD-phase diagram [26] which explains the phase transition between partonic to hadronic matter. The phase diagram explain the aim of the relativistic heavy-ion collision which is to explore the different part of the phase diagram in detail to understand the evolution of the universe starting from Big-Bang or the core of the neutron star which are made of high density partonic matter.

with the same mass which otherwise came up differently when symmetry is broken. Study of relativistic high energy collision can also reveal the possible interconnection between deconfinement and chiral phase transition.

**QCD and QGP:-** The Quantum Chromodynamics, a non-abelian gauge theory of strongly interacting particles (quarks and gluons) and an important ingredient for the standard model, can describe the interaction and dynamics of the system with partonic degrees of freedom. Relativistic high energy collision gives unique opportunity to test the success of QCD in terms of particle production and their properties. Moreover, Quark Gluon Plasma (QGP), a primordial state of matter with quarks and gluons as constituents, is expected to be formed in heavy-ion collision at RHIC or LHC energies. The details of QGP properties and their evolution can be explored with the help of high energy collision. There are several QCD based theoretical and phenomenological models which can estimate the signals like energy density (particle density), momentum distributions and etc. which can be verified using experimental results from high energy collision between hadron/nucleus.

**Parton distribution function:-** Exploring parton distribution (PDF) function for both nucleon and nucleus are other important objectives which can be probed for a wide range of energies using high energy collision. As is shown in figure 1.5, contribution to particle production in high energy collision among hadron or nucleus depends on the centre of mass energy of the collision which in turn decide the relative significance of a particular type of parton (quark/gluon). Inputs from experimental results have enriched the understanding of partons distributed inside hadron/nucleus. Results from RHIC and LHC has opened a new regime of parton distribution, mostly dominated by gluon, became one of the most discussed physics potentials of today's high energy collision. Moreover, not only PDFs, fragmentation functions (FF), responsible to create colourless particles from the coloured partons, can also be probed in relativistic high energy collision using QCD based theoretical calculations.

So, in brief, the aim behind experiments with high energy collision is to explore and reconstruct the deconfined matter under extreme condition of temperature and density in terms of particle multiplicity, momentum distribution, angular correlations among produced particles and etc. It will help in revealing the knowledge of transport properties, the structure of the phase diagram, in-medium properties of partons and hadrons and etc.

### 1.3.2 Initial conditions

For a collision experiment, initial condition refers to the kinetic state of the participating particles. In case of low energy collision, the momentum and the mass of the particle are enough to specify the kinematic state. However, with increase in energy, the definition of kinetic states get modified. Specifically, in relativistic high energy collision among nuclei

or proton-nuclei and so on, the initial condition includes information about the distribution of parton inside the nucleon/nucleus which is actually taking part during the collision. The importance of parton distribution, however, was understood little later after the discovery of partonic medium in a nucleus-nucleus collision. There are several model predictions about parton distribution [29–35], tuned with experimental inputs, which successfully explain the effect of the initial state of participants of the collision as well as the particle production after the collision. Usually, parton distribution function (PDF) is expressed in term of *Bjorken-x*, longitudinal momentum fraction of the parent nucleon that is carried by the parton, and behave differently depending on their flavour. PDFs are, in general, universal in nature, can describe the structure of hadrons/nuclei and evolve according to DGLAP equation [36–39] as is shown in figure 1.5 from the CTEQ collaboration. At LHC energies, the PDFs, with

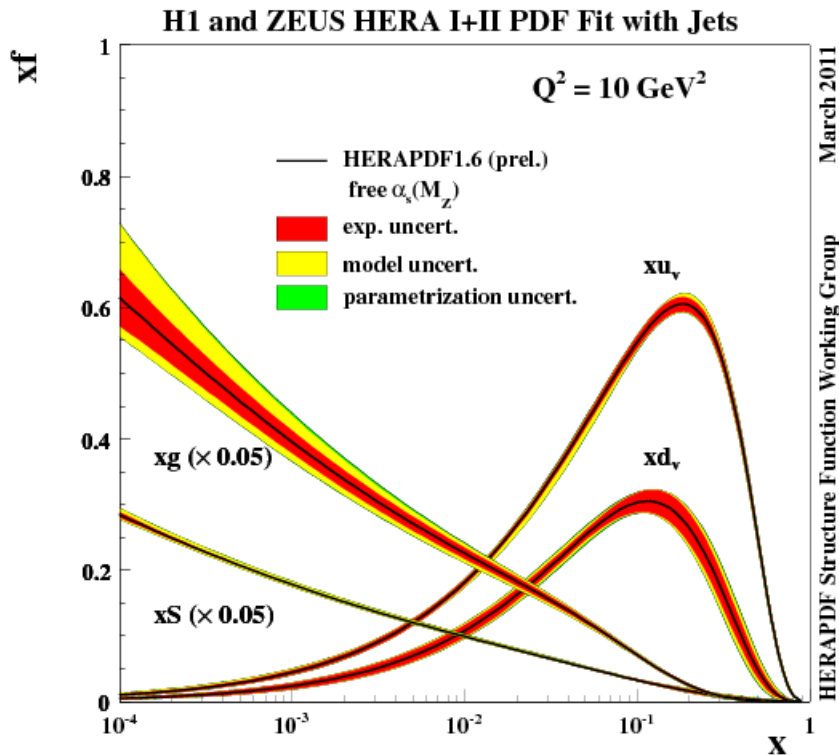


Figure 1.5: Parton Distribution Functions (PDF) for different type of quarks and gluon are shown in the picture. The distributions are represented as the variation of  $xf(x)$  as function of *Bjorken-x* as published by CTEQ collaboration for momentum transfer  $Q^2=10 \text{ GeV}/c$ .

substantially small *bjorken-x* and with ability in probing a novel and so far unexplored QCD regime with ( $x < 10^{-3}$ ), has drawn lots of attraction because of the increasing trend of "Gluon" in particular which is predicted to reach a saturation scale and might form a system

called colour glass condensate (CGC) [40–46]. The particle production, in turn, will be dominated by gluonic interaction rather than quarks unlike in AGS, SPS and even in RHIC energies. On the other hand, Cold Nuclear Effects (CNM) [47] are also considered as initial state effects which are mainly attributed to the nuclear parton distribution function and makes it different from that of the proton.

### 1.3.3 Kinematics

Before going into details about the different aspects of the relativistic heavy ion collision, it is important to understand different variables and notation those are used to describe the particle interaction in the relativistic domain. It is relevant to adopt the relativistic kinematics and four vector approaches in understanding the physical interpretation of the results in high energy collision. In this section, we will briefly discuss variables which should be Lorentz invariant in nature.

To start with, the most basic variable is the particle position and momentum in four dimension space, which can be represented as following

$$x^\mu = (x^0, x^1, x^2, x^3) = (ct, x, y, z),$$

$$p^\mu = (p^0, p^1, p^2, p^3) = \left( \frac{E}{c}, p_x, p_y, p_z \right) = mu^\mu \gamma(1, \vec{v}),$$

where,  $x^\mu$  and  $p^\mu$  represents four vectors for position and momentum respectively with  $\mu$  runs from  $0 \rightarrow 3$ , while  $\vec{v}$  is the three velocity of the particle. However, the four component for position and momentum can be reduced to three component assuming the azimuthal angle negligible (relevant for relativistically high energy particle) and can be represented as  $(t, x_T, z)$  and  $(E, p_T, p_z)$  respectively in natural unit ( $\hbar = c = \mu_0 = \epsilon_0 = 1$ ) and  $x_T = \sqrt{x^2 + y^2}$  and so for momentum. The invariant quantity in this formalism is the scalar product of two four vector. It can be represented as

$$x^\mu x_\mu = g^{\mu\nu} x^\nu x^\mu = \tau^2$$

$$p^\mu p_\mu = g^{\mu\nu} p^\nu p^\mu = m^2$$

$$x^\mu p_\mu = g^{\mu\nu} x^\nu p^\mu = Et - \vec{p} \cdot \vec{r}$$

where,  $\tau^2$  and  $m^2$  are Lorentz invariant quantity and can be related to the proper time, rest mass and phase of the particle.

Knowing fundamental variables, the next step is to describe the physics in terms of Lorentz invariant formulation. *Mandelstam variable*, a numerical notation which carries informations regarding energy, momentum and scattering angle in a scattering experiment.

It can be used to derive Lorentz invariant quantities such as cross-section of an interaction. Mandelstam variables can be represented for two particle scattering (1,2  $\rightarrow$  3,4) phenomenon as following,

$$\begin{aligned} s &= (p_1 + p_2)^2 = (p_3 + p_4)^2 \\ t &= (p_1 - p_3)^2 = (p_2 - p_4)^2 \\ u &= (p_1 - p_4)^2 = (p_2 - p_3)^2 \end{aligned}$$

with,  $p_i$ 's are four-momenta of the  $i^{th}$  particle. Here, (1,2) and (3,4) represents the incoming and the outgoing channels of the scattering respectively. Physically, s and t represents the square of centre of mass energy and momentum transfer. Being derived from the scalar product of four vectors, Mandelstam variables and other physical entities (e.g. decay width, differential and total cross-section as shown in equation 1.3) expressed in terms of Mandelstam variables are always Lorentz invariant.

$$\begin{aligned} \Gamma &= \frac{\vec{p}^*}{32\pi^2 m_i^2} \int M_{fi}^2 d\Omega \\ \frac{d\sigma}{dt} &= \frac{1}{64\pi s \vec{p}_i^2} M_{fi}^2 \\ \sigma &= \frac{1}{64\pi^2 s} \frac{\vec{p}_f^2}{\vec{p}_i^2} \int M_{fi}^2 d\Omega^* \end{aligned} \tag{1.3}$$

Apart from so far discussed fundamentals of relativistic kinematics, there are physical quantities which make the physics interpretations more straight forward under Lorentz transformation. Rapidity represents particle distribution in a Lorentz invariant way and shows only a shift (additive) by an amount, determined by the boost of the frame. In the non-relativistic limit, it is reduced to the velocity. Moreover, in collider type of experiments, the transverse momentum component, perpendicular to boost along beam direction (z), is an invariant quantity. In practice, the differential cross-section for a particle produced in the relativistic collision are expressed in terms of rapidity, transverse momentum and the azimuthal angle which can be represented as

$$E \frac{d^3\sigma}{dp^3} = \frac{E d^3\sigma}{p_T dp_T dp_L d\phi} = \frac{d^3N}{p_T dp_T dy d\phi} = \frac{1}{2\pi} \frac{d^2N}{dp_T dy}$$

This way of representing the cross-section helps in extracting yield in a Lorentz invariant way as well as in terms of experimentally measurable variables. More details about the experimental observables in understanding particle production in the relativistic collision will be discussed in the following sections.

### 1.3.4 Collision parameters

Once the initial kinematic states of the colliding particle are known or modelled, the next important step would be to understand the parameters, defining the collision, to reveal the properties of the system produced during the collision. Most important parameters are *Impact parameter* (corresponding experimental observable is *Centrality*) and the *Luminosity* which affect the particle production at the final stage.

**Impact parameter (b)**, taken as zero for most central collisions and sum of the radii of the participants for extreme peripheral, is considered to be important for the participants with extended structure. Theoretical calculations invoke the initial geometry of the collision through impact parameter "b" and obtain prediction as a function of it. However, in experiments, there is no such direct way to measure the impact parameter of the collision and thus required some indirect methods, like produced particle multiplicity, Forward energy ( $E_F$ ) from spectator of the collision, number of participants etc., which results "*Centrality*" as the observable inheriting initial geometry of the collision. It has been found that the impact parameter holds a direct relationship with centrality which decreases with a decrease in multiplicity and participants of the collision. It will be relevant to mention that the experimental results for relativistic heavy ion collision are always published as a function of centrality classes because of the fact that the initial geometry of the collision zone get tampered and the symmetry lost as we move away from central to peripheral collisions. Usually, the relationships between centrality and the impact parameter are extracted using Global model calculations [48–50]. For a particular impact parameter, the number of wounded participants or binary collisions are calculated and subsequently related to the particle multiplicities which will help in determining the centrality of the collision and thus comparing theoretical predictions with the experimental observations. By definition, centrality can be defined as a percentage of the total nuclear interaction (particle production in experiment) cross-section as  $c = \int_0^b \frac{d\sigma}{dx} dx$ . As discussed, global model calculation can effectively support for centrality measurement in a nucleus-nucleus collision. But for proton-proton collision, there is a lack of such effort to include the initial geometry in the collision. However, as the particle multiplicity has an impact parameter (centrality) dependence, particle production in pp collision at LHC energies (with comparatively large particles) are studied for classes defined by the multiplicity itself.

**Luminosity (L)** is, on the other hand, measures the ability of a particle accelerator to deliver the desired number of interactions and connect between experimental observation (particle production) with that of theoretical prediction (cross-section) and can be expressed as expressed in equation 1.4

$$\frac{dR}{dt} = L \cdot \sigma. \quad (1.4)$$

with  $L$  as luminosity in units of  $cm^{-2}s^{-1}$ ,  $\sigma$  being the cross section for a particular interaction and  $\frac{dR}{dt}$  represents the rate of interaction. Calculation for luminosity differs depending on whether it is a fixed target or collider type experiment and can be represented by the equations 1.5

$$\begin{aligned} L &= \Phi \rho_T l \quad \text{for fixed target experiment,} \\ &= \frac{N_1 N_2 f N_b}{4\pi \sigma_x \sigma_y} \quad \text{for collider experiment.} \end{aligned} \quad (1.5)$$

where,  $\Phi$  is the incident particle flux,  $\rho_T$  and  $l$  are the target density and length respectively in case of fixed target experiment. And for collider experiment,  $N_1$ ,  $N_2$  are intensities of two colliding bunches with  $N_b$  as the number of bunches in one beam while  $f$  and  $\sigma_i$  are the revolution frequency and beam sizes respectively.

### 1.3.5 Experimental observables

Knowing initial state and collision parameters, the system formed in a high energy collision among hadron and (or) nucleus is characterised with the help of experimentally measured observables at the end. There could be different type of measured observables depending on a particular experiment but all are related to primary measurements like the number of particles (particle multiplicity "N"), energy (momentum) spectrum of produced particles, particle identity, (Pseudo-)Rapidity distribution, the angular correlation among produced particles and etc. In this section, we will discuss commonly measured experimental observables in high energy collision and their importance in brief.

#### Particle multiplicity(N)

Particle multiplicity in high energy collision is the primary measurement which, however, contribute most about the particle production mechanisms and serves the basic input for relevant Monte Carlo calculations and theoretical formulations. Measuring the number of particles, produced in a collision and averaged over a large number of events, might explore possibilities of different particle production mechanisms and any possible correlation if exist at the source level. Usually, the multiplicity distribution represents the probability of finding

a particular number of particles in a collision as a function of multiplicity ( $P(n)$  vs  $n$ ) either for full or for a specified phase-space. In a collision, if the particles are produced from an independent and identical point-like scattering centres, the particle multiplicity follows Poisson distribution which might get smeared or modified for correlated sources. In the beginning, for  $e^-e^-$  scattering or proton-proton scattering at comparatively low energies (at 29 and 62 GeV), multiplicity distribution could be illustrated assuming sources are either point-like and identical or super-position of many such sources. However, with the discovery of KNO [51]-scaling, the importance of the multiplicity distribution was enlightened again. With the increase of available centre of mass energy, the particle multiplicity got different perspectives about production mechanisms starting from QCD hard scattering to non-perturbative soft production processes. Recently, at LHC energies, multiplicity distribution exhibiting profile, comprised of two or even more type of particle sources and can be explained by single or convoluted Negative Binomial distributions. As the integrated multiplicity should depend on the number of participants and so on the initial energy density of the collision, it increases with the increase of centre of mass energy of the collision. However, dependencies of multiplicities on the centre of mass energy behave differently for proton-proton and nucleus-nucleus collisions [52] as shown in figure 1.6. Noticeably, particle production increases more rapidly with centre of mass energy in case of heavy ion collision than that of proton-proton collision and can be explained by power law as  $s^{0.15}$  and  $s^{0.11}$  for heavy ion and pp collision respectively, which shows a deviation from logarithmic behaviour for proton-proton collision earlier for comparatively low energies.

Beside integrated multiplicities, identified particle multiplicity have different perspectives in probing the hot and dense matter produced in high energy collision. With the increase in  $E_{CM}$  off collision, the increased yield for identified particles brings the scope to study the relative abundances of different particles in terms of particle ratios such as Baryon-to-meson, strange-to-non strange etc. Identified particle yields can give important information about the properties of the strongly interacting system like about degrees of freedom, collectivity, quark coalescence etc.

### **Rapidity distribution**

The introduction of rapidity become essential in case of relativistic high energy particles where variables transform according to Lorentz prescription and take complicated form in going from one frame to other. The rapidity, as expressed by the equation 1.6, distribution becomes invariant and associated with a shift in the whole distribution under transformation.

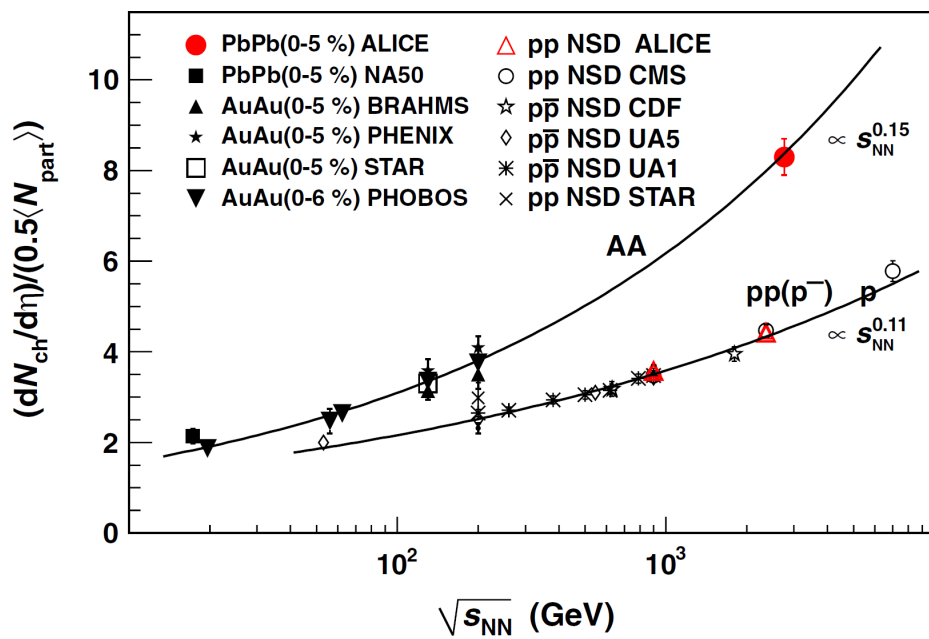


Figure 1.6: Variation of Charged particle multiplicity a function of centre of mass energy  $\sqrt{s}$  for proton-proton and heavy ion collision. The plot has been generated taking data from different experiments at different centre of mass energies [52]. It shows the difference in dependence of particle production on centre of mass energy for pp and heavy ion collision.

$$y = \frac{1}{2} \ln \left( \frac{E + p_z}{E - p_z} \right). \quad (1.6)$$

There can be two extreme limits for the rapidity, (a.) for particles moving perpendicular to the beam have  $y = 0$  and on the other hand, (b.) for particles moving along the beam will have  $y = \pm\infty$ . So, briefly, the rapidity is related to the angle between particle and beam direction. Experimentally, rapidity is hard to calculate as one need both the particle identity as well as the momentum, however, with the introduction of Pseudo-Rapidity ( $\eta$ ), the distribution can be reconstructed easily as it doesn't require any particle identity and which can be expressed by equation 1.7

$$\eta = \frac{1}{2} \ln \left( \frac{p + p_z}{p - p_z} \right) = -\ln \left( \tan \left( \frac{\theta}{2} \right) \right). \quad (1.7)$$

Of course, knowing pseudo-rapidity distribution for some identified particles, one can always transform it to the rapidity distribution using a Jacobian ( $J = \sqrt{1 - \frac{m^2}{m_T^2 \cosh^2 y}}$ ) and vice versa. However, both the distribution merged in the limit of massless particle ( $m = 0$ ) or ultra-relativistic particles ( $pc \gg mc^2$ ).

One of the successful form for rapidity distribution came from "Landau Hydrodynamical Model" back in 1953 [53] and had been experimentally confirmed for AGS to RHIC energies. Following Landau prescription, the rapidity distribution can be expressed as shown in equation 1.8

$$\frac{dN}{dy} \propto \exp \left( \frac{-y^2}{2 \ln(\gamma)} \right), \quad (1.8)$$

where,  $\gamma$  is the Lorentz contraction factor ( $\gamma = \frac{\sqrt{s_{NN}}}{2m_N}$ ). The gaussian rapidity distribution can explain data for central AuAu collision up to RHIC energies. However, there is an ambiguity with the original landau description (with  $\exp(\sqrt{L^2 - \lambda^2})$ ) about, whether the variable ( $\lambda$ ) should be taken as rapidity or pseudo-rapidity. The typical rapidity distribution can be represented by the figure 1.7 with two peaks corresponding to two fragmentation regions which are moving away with the increase in the centre of mass energy, indicating baryon depleted (almost no stopping power) system is expected at LHC energy. Approximately, the

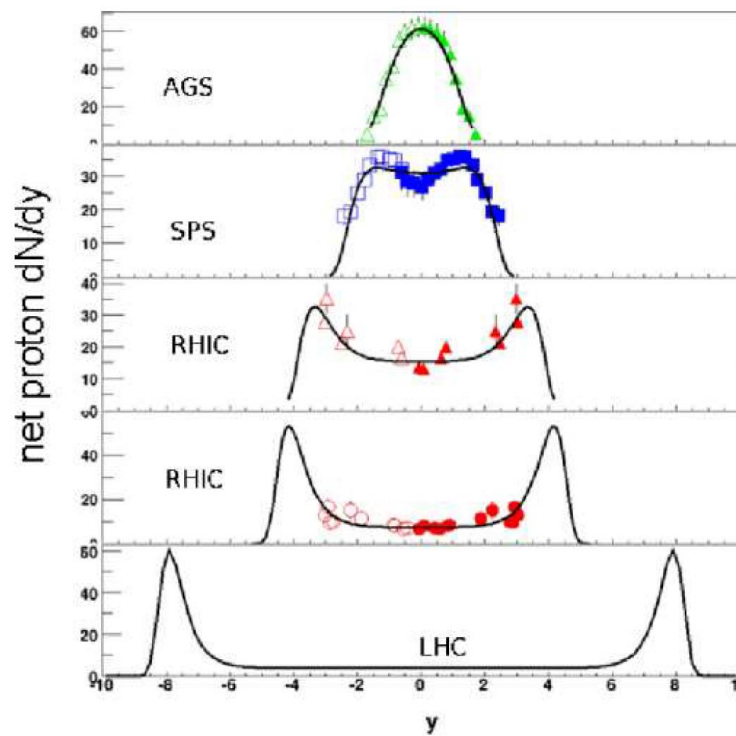


Figure 1.7: Rapidity distribution for net proton for AGS, SPS, RHIC energies together with an extrapolation for LHC energies. The figure describes how the shape of the rapidity distribution changes with increase of centre of mass energy [54].

spread in the rapidity can be taken as the difference between two beam rapidities (projectile and target rapidity in case of fixed target experiment) in case of a collider type experiment and can be taken as  $\Delta y = 2 \times \ln\left(\frac{2E}{m}\right)$ . In a collider experiment, naively, the system formed after collision may have two different regions, central rapidity and fragmentation regions respectively. The particles with large rapidity are emerging from the fragmentation regions whereas, particles with intermediate rapidity are coming from the central rapidity zone. With the increase of the  $E_{CM}$ , the stretch of the rapidity interval become more and more prominent and can further be classified into even smaller  $y$ -windows which can reflect the details of particles production mechanism in the collision. (Pseudo-) Rapidity distribution for produced particles in high energy collisions usually refers to the global properties of the created system. Being simple, (Pseudo-) Rapidity measurement is considered as a first-day observables in any complex high energy experiment, however, many physics issues can be addressed with it. The most commonly measured region for rapidity is mid-rapidity region which is sensitive to the hadron-production mechanism and may vary depending on the available centre of mass energies such as baryon-rich system at SPS to baryon-free at LHC energies. Moreover, assuming boost invariant central plateau in rapidity distribution, the energy density can be calculated using Bjorken prescription from rapidity distribution according to the following 1-dimension equation 1.9

$$\varepsilon_{BJ} \simeq \frac{\frac{dN_{ch}}{d\eta} * \frac{3}{2} \langle P_T \rangle}{V}. \quad (1.9)$$

Where,  $\frac{dN_{ch}}{d\eta}$  is the number of charged particles per unit pseudorapidity,  $P_T$  is transverse momentum and  $V$  is the volume of the fireball, created during the collision. The details of the energy estimation will be described in more details in 5<sup>th</sup> chapter in the context of understanding particle production in the proton-proton collision at LHC energies. On the other hand, the stretch of the rapidity distribution contains the longitudinal expansion of the produced system which illustrates the stopping power (transparency) of the medium formed. Also, particles produced with forward and backward rapidities (fragmentation region) can be used to study the "limiting fragmentation" phenomenon for particle production. The variation of the particle rapidity density as a function of centrality (impact parameter) of collision inherit important information about the contribution of the soft ( $\propto N_{part}$ ) and hard ( $\propto N_{collision}$ ) processes in particle production mechanisms

### Transverse momentum $p_T$ -Spectra

Transverse momentum ( $p_T = \sqrt{p_x^2 + p_y^2}$ ) of a produced particle is the momentum component transverse to the beam axis and has the property of Lorentz invariance for particles produced in relativistic high energy collision experiments. In any collision, since there is no net transverse momentum at the beginning, the final state particle must be produced obeying the same. However,  $P_T$  distribution for produced particles follow a particular profile, which illustrates information regarding different type of interactions that those particles might have experienced. It also illustrates the thermal property of the system as well as the exploding nature of the system. In high energy heavy-ion collision,  $p_T$ -spectra might get affected by collision dynamics as well as by the final state hadronisation processes, which might be folded together in the final profile. The particle production mechanisms can be categorized in broad classes, soft parton scattering followed by string fragmentation and hard parton scattering followed by transverse fragmentation respectively. Usually, the transverse momentum profile can be considered as the convolution of an exponential ("corresponding to thermal part") and a power law ("hard scattering") contribution [55]. Though the hard component of the spectra is well understood in terms of pQCD calculation followed by fragmentation, however, the soft part is still required conclusive understanding about its origin. The importance of transverse momentum spectra lies in explaining the particle production mechanisms in the proton-proton collision which differs in case of heavy ion collisions and can contribute in understanding the collective flow, recombination, jet quenching etc. [56]. There is various theoretical/phenomenological model which can explain the transverse momentum spectra in most of the cases. Following are such few frequently used description for transverse momentum spectra for produced particles in high energy collisions.

**Maxwell-Juettner distribution:** The model is the relativistic generalisation of the Maxwell-Boltzmann distribution, that explain particle spectra assuming thermal models, introduced back in 1911 by Juettner [57]. The simplistic model can be expressed as shown in equation 1.10 following [58] and does not include the collectivity of the system which resulted in overestimation in temperature.

$$f(p_T) = \frac{1}{4\pi m^2 T K_2(m/T)} e^{\left[-\frac{\gamma p_T m}{T}\right]} \quad (1.10)$$

with,  $\gamma(p_T) = \sqrt{1 + \left(\frac{p_T}{m}\right)^2}$ ,

where  $T$  and  $m$  are freeze-out temperature and mass respectively. As expected, the distribution can explain the low- $P_T$  ( $\leq 0.5$  GeV) part of the whole spectra. However, its major drawback is the absence of the collectivity in the formulation which does present in the produced system. Interestingly, an effort to invoke the collective nature in the model is done through the temperature as  $T^* = T + km \langle v_T \rangle^2$  [59], where  $\langle v_T \rangle$  is average velocity at-freeze-out and is function of centrality.

**Tsallis Distribution:** The distribution represents a more generalised form of statistical approach which can be applied to a system away from the equilibrium. The distribution can be represented in terms of transverse mass and temperature as shown in equation 1.11

$$E \frac{d^3N}{dp^3} = C_n m_T \left( 1 + (q-1) \frac{m_T}{T} \right)^{-n}, \quad (1.11)$$

where,  $T$  represents the temperature at freeze-out (to be noted that the one to one correspondence of the parameter "T" to temperature in thermodynamical sense needs to be carefully used.) and the "n" represents the real power index (however, making it complex, extend the Tsallis distribution in more wider region of application) and can be taken as  $\frac{1}{q-1}$ , with "q" measure the non-extensivity of the statistical approach. Tsallis distribution, being more general, can lead to an exponential distribution in the limit  $m \rightarrow \infty$ . Moreover, Tsallis distribution can describe the  $P_T$ -spectra from an exponential ( $\exp(-m_T/T)$ ) form to power law distribution ( $\propto (p_T/nT)^{-n}$ ) with the limit  $p_T \rightarrow 0$  and  $p_T \rightarrow \infty$ . So in general, with the increase of centre of mass energy, produced particles have larger  $P_T$  which can not be explained by soft particle production mechanism and need pQCD based calculation for hard scattering phenomenon which can be taken care by default with Tsallis distribution.

**Blast-wave approach:** However, There are phenomenological models like "Blast-Wave model", inspired with the hydrodynamical approach, which can address the  $P_T$ -spectra including both the collective expansion and the thermal nature of the system. This model assumes local thermal equilibrium at freeze-out ( $T$ ) and the existence of both transverse and longitudinal expansion. Adopting a flow profile, defined by  $\beta_T(r) = \beta_s \left(\frac{r}{R}\right)^\alpha$ , the particle spectra can be expressed as shown in equation 1.12

$$\frac{dN}{p_T dp_T} \approx \int_0^R r dr m_T I_0 \left( \frac{p_T \sinh \rho}{T} \right) K_1 \left( \frac{p_T \cosh \rho}{T} \right). \quad (1.12)$$

Though the blast wave model describes the collectivity within the system in terms of temperature, collective velocity and the flow profile parameter, the application is restricted to the softer part of the spectra only. The details of the model description and its application to particle production will be illustrated in details in 7<sup>th</sup> chapter.

### 1.3.6 Signatures of Quark Gluon Plasma

The deconfined partonic medium, expected to be produced in HI (HM pp) collision, need to be characterised using measurable experimental observables. As the QGP exists only for a few microseconds, it is practically impossible to probe the system with direct measurements. However, particles produced before, during or after the formation of QGP carry important information which collectively can be used both to confirm and characterisation of the QGP. Undoubtedly, there can not be a unique signal which alone can be considered as the smoking gun identification for quark gluon plasma. Rather there are a number of different signals, both differential and global, which together may be treated as signatures for QGP. Different bookmark signatures for QGP can be listed as following -

**a) Photons and Dileptons** - Either of these signals, once produced, can traverse through the whole evolution of the QGP undisturbed as they only interact electromagnetically not through strong interaction. Moreover, photons, produced at different stages like at the very beginning, during pre-equilibrium, from thermalised or even after hadronisation, carries the full history of QGP and serve as a cleanest signature. Differentiation of photons from different sources can be treated as a good thermometer for QGP. On the other hand, dileptons (lepton-antilepton pair), produced by initial quark-antiquark annihilations and from hadronic medium later during evolution, can also be treated as a clean probe for studying QGP as they also remain undisturbed by the strongly interacting medium.

**b) Strangeness enhancement** - Enhanced strange particle production can be treated as a good signature for QGP medium. For an equilibrated QGP with  $T > m_S$ , strange quarks and antiquarks can be abundantly produced. Since the threshold energy for strange particle production in hadronic phase is much higher (almost by a factor of two) than that of QGP, strange can be produced during QGP phases easily. This enhanced strange production is reflected in the production of strange and multi-strange particles in the final stage which can be treated as an indication for the formation of deconfined phase.

**c)  $J/\Psi$  suppression** -  $J/\Psi$ , an  $c\bar{c}$  bound state, formed at the beginning of the medium formation in relativistic HI (pp) collision. The suppression of  $J/\Psi$ , an artefact of Debye screening attributed specifically to plasma formation, can identify the formation of QGP. The presence of QGP is essentially dilute the bonding between  $c\bar{c}$  pair and hence melt the  $J/\Psi$ .

**d) Jet Quenching** - The phenomenon of Jet in relativistic heavy ion collision is ascribed to the

hard probes, characterised with large momentum transfer and associated with hard scattering in the initial stage just after the collision. When two partons from two incoming nucleons interact and a large momentum transfer occurs, the particles (maybe quarks, gluons or photons) in the outward channel carries large momentum. Being either quarks or gluon, they can interact with coloured medium if produced and lose substantial amount of energy which directly reflected in the final state hadron production. Usually, partons with large momentum fragment into partons till their energy become critical for further parton production and followed by hadronisation which resulted in a spray of particles in the final stage within a very narrow cone. If there are two partons in the hard scattering, two oppositely directed jet will be produced, however for a parton along with gamma in the output channel will produce a jet along with a photon moving exactly in opposite direction. The two oppositely directed jet are similar unless the jet producing partons traverse through a strongly interacting matter like QGP. In the presence of QGP, the jet structure gets modified for the away side and become diffused whereas the near one remains intact.

**e) Elliptic flow** - Elliptic flow is one the most important observables in the field of relativistic heavy ion collision. A large values for elliptic flow indicates the applicability of an ideal (i.e., equilibrium) hydrodynamics which justify the formation of almost perfect fluid at RHIC. The non-zero impact parameter (non-central) for collision between two nucleon coming from opposite direction can vary both in magnitude and direction which led to an initial asymmetry in the geometry of the overlapped zone (interaction zone). To understand the effect of such asymmetry, the distribution of final state particles ( $E \frac{d^3N}{dp^3}$ ) can be Fourier-decomposed as following

$$\frac{d^3N}{p_T dp_T dy d\phi} = \frac{d^2N}{p_T dp_T dy} \frac{1}{2\pi} [1 + \sum_{n=1}^{\infty} 2v_n \cos n(\phi - \phi_R)],$$

with each terms carrying their usual meaning. The first term in the square bracket is called the radial flow whereas, the  $v_1$  and  $v_2$  are called directed and elliptic flow respectively. The information about the different flow coefficients brings important insights regarding the hydrodynamics of the produced partonic medium and can serve a good signal for the QGP.

None the less, there are many signals like Constituent quark number scaling, Ratios of particle yields, quarkonia, the study of heavy flavour and etc. which have their own significance in characterising the partonic medium formed in relativistic heavy ion collision. The remark about the signal of QGP lies in the fact that not a single signal but all relevant indications need to be critically investigated to confirm the creation of QGP.

## 1.4 Motivation and skeleton of the thesis work

The present thesis work comprises of two major parts - *a. Forward Calorimetry for ALICE experiment* and *b. High Multiplicity Proton-Proton Physics* respectively. The main physics motivation behind the 1<sup>st</sup> part of the thesis is to probe a so far unrevealed domain of small *Bjorken-x* regime  $\leq 10^{-4}$ , dominated by gluon dynamics for particle production. From theoretical predictions, there are possibilities of achieving such small-x at forward rapidity with ALICE experiment at LHC energies. However, limited capability of ALICE experiment in forward rapidity, leave scope for a proposal of a calorimeter which can measure high energy photons from different sources over a wide range of incident energy (up to 200 GeV). The thesis is starting with a general introduction about the field of relativistic high energy collision (1<sup>st</sup> chapter) and followed by an overall discussion about the particle interaction with matter (2<sup>nd</sup> chapter). The first two chapters basically contain general relevant information regarding the thesis work which have been collected from different references. The main thesis work started with a brief discussion about the LHC and ALICE. The discussion was aimed to explore the usability of forward rapidity measurement which has been described in brief in chapter 1.

A general discussion about the particle interaction with matter will be introduced in chapter 2. Different techniques of particle detection over a wide range of particle types, their incident energies, momentum and etc. will also be covered in chapter 2 which is indeed important to understand the detector designing, fabrication and its uses.

A formal introduction to the Large Hadron Collider experiment will be presented in chapter 3. Since the present study involves mainly the ALICE detector in specific, a general introduction will be discussed in this chapter. A brief discussion about different sub-systems of ALICE and their importance will also be discussed. It will essentially help in understanding the need for a new calorimeter which will come in the next chapter.

The major part (1<sup>st</sup> part) of the thesis is devoted to the design, performance simulation, fabrication and testing of forward calorimeter (FOCAL) which is distributed over chapters **4, 5 and 6** of this thesis. It started with the description of the calorimetry in ALICE experiment. A brief description of the physics motivation along with its relevance in the high energy physics measurement behind building the calorimeter has been discussed in chapter 4.

The design and simulation details, which I have carried out during for the thesis work, are explained to study the feasibility of the calorimeter, both technically and physics wise, with the help of Geant4 toolkit in chapter-5. The study aimed to achieve optimal design and performances for the calorimeter.

In continuation of my thesis work, the next chapter (6) mainly addresses the hardware de-

velopment for fabricating prototype sampling calorimeters with  $1 \text{ cm}^2$  pad detectors and tungsten absorbers. A series of prototype design, development, fabrication and their test, aiming for the final goal of the full calorimeter, were presented. The details of results from the prototype test at laboratory, PS and SPS beamline facilities at CERN-LHC have been presented and discussed. The 1<sup>st</sup>-chapter ends with a short discussion about the future work and scope for building the calorimeter.

As has been discussed, the main aim behind relativistic high energy collision is to understand particle production and their subsequent evolution for system produced in proton-proton (pp), proton-nucleus (pA) or nucleus-nucleus (AA) collisions at extreme temperature and densities. My work regarding particle production in pp collision has been documented in the 2<sup>nd</sup>-part (chapter-7) of the thesis work. The particle production in proton-proton collisions at LHC energies, which earlier used as the reference to understand a more complex system like in pA and AA collisions, was studied using a different phenomenological model with published data. The chapter was started with a brief history and importance of proton-proton collisions from low to ultra-relativistic high energy collision, followed by a discussion about different phenomenological frameworks (two source model with NBD, Blast-wave approach and etc.), used in this study. The chapter has three sub-sections - firstly understanding the multiplicity distribution in pp collision at LHC energies with NBD model, secondly applying BW-approach to search for collectivity in pp collision for very special high-multiplicity classes and their consequences, and lastly understanding the nature of the collectivity in pp collision, an anomalous signal, with the help of simple Bjorken one dimensional prescription for energy density calculation. In this study, both collectivity and the energy density (thus the Degree of freedom) was studied as a function of multiplicity classes of proton-proton events. In the end, the outlook and future scope of the study has been illustrated.

# Chapter 2

## Interaction and Detection of particles

### 2.1 Introduction

Understanding of experimental results, in general, need a close look on "how particles interact with matter and thus deposit energy". Then the rest part will be to collect the deposited energy either in forms of light or electrical signal and processed it accordingly. In this chapter, we will discuss the interaction of particles with the matter. Primarily, interaction of particle can be divided into two broad categories, **a)** Interaction of charged particles and **b)** Interaction of neutral particles. The type and intensity of interactions depend both on particle type (mass, charge, energy etc) and the matter (density, elements, structure etc) through which the particles are moving. The electromagnetic force is the one which is mostly responsible for particle interaction with matter in connection to particle detection. However, there is scope for strong and weak interaction as well for particles like neutrons and neutrinos.

### 2.2 Interaction of charged particle with matter

The interaction of the charged particle with matter can further be divided into two broad categories **1) Interaction of electrons ( $e^-$ ) and other charged particles** and **2) Heavy charged particle**. Electron, being lighter mass, become relativistic very quickly and dominated by radiation loses mostly while heavy charged particles undergo both collisional and radiational losses depending on the energy of the particle. In general, energy loss by a charged particle

can be represented as following 2.1

$$\begin{aligned}
 -\left(\frac{dE}{dx}\right)_{Total} = & -\left(\frac{dE}{dx}\right)_{collision} - \left(\frac{dE}{dx}\right)_{Radiation(brems/cher)} - \left(\frac{dE}{dx}\right)_{pair} \\
 & - \left(\frac{dE}{dx}\right)_{compton} - \left(\frac{dE}{dx}\right)_{Photo} - \left(\frac{dE}{dx}\right)_{had} + O(Other\ mechanisms),
 \end{aligned} \tag{2.1}$$

where,  $-\left(\frac{dE}{dx}\right)$  represents the energy loss by the particle per unit path length travelled. The subscripts collision, radiation and etc stands for the corresponding underlying processes of energy loss mechanisms.  $O(Other\ mechanisms)$  represents other relatively less contributing processes to the total energy loss of the particle. However, the relevance of a particular term in the expression depends on the incident particle and the material medium.

### 2.2.1 Interaction of heavy charged particles

Heavy charged particles, usually, are those with atomic mass number unity or more by definition. Though muons, pions and kaons are not in that sense a heavy charged particle, however, they behave similarly when passing through a material medium and differ from proton and all because of their small mass and different interaction probability. Primarily, all charged particle loses energy in a matter through collisional/ionisation processes during its passage through matter. The specific energy loss, energy Loss per unit path length travelled:  $-\left(\frac{dE}{dx}\right)$ , can be expressed quantitatively using Bethe-Bloch formula, as is shown in equation 2.2

$$-\frac{dE}{dx} = \frac{4\pi k^2 e^4}{m_e c^2} \frac{z^2}{\beta^2} \frac{\rho Z N_A}{A} B(v) \quad \text{with ,} \tag{2.2}$$

$$B(v) = \frac{1}{2} \ln \left( \frac{2m_e \gamma^2 v^2 T_{max}}{I^2} \right) - \beta^2 - \frac{\delta(\beta\gamma)}{2} - \frac{C(I, \beta\gamma)}{Z}.$$

Where,  $T_{max} = \left( \frac{2m_e c^2 \beta^2 \gamma^2}{1 + \frac{2\gamma m_e}{M} + \frac{m_e}{M}} \right)^2$ , represents maximum energy transfer in single collision and "I" represents mean excitation energy of medium.  $m_e$  and M are mass of electron and the incoming particle, whereas  $\gamma = (1 - \beta^2)^{-1/2}$  with  $\beta$  being the scaled velocity  $\left(\frac{v}{c}\right)$  of the particle.  $\rho, Z, A$  stands for mass density, atomic number and mass number

of the target material. A typical graph for the energy loss by a charged particle is shown in the figure 2.1 for  $\mu^+$ , which illustrates fall in energy loss with the increase in incident energy due to collision and then followed by a comparatively slow rise of energy deposition because of radiational losses. The plot also presents a shoulder like structure at very low energy due to Coulomb scattering. However, complete energy loss profile has a minimum where loss due to ionisation and radiation balances each other found to be at  $\beta\gamma = 3.5$ , which is independent of the particle. Though, depending on the particle mass, the energy loss profile can shift either to the right or to left but all will merge at the point of minimum energy loss, know as minimum ionisation potential as is shown in figure 2.2, which put a restriction for identifying particle experimentally by measuring  $-\frac{dE}{dx}$  for particle momentum corresponds to  $\beta\gamma = 3.5$ . nevertheless, it must be noted that the value for minimum ionisation potential could be different for different material medium.

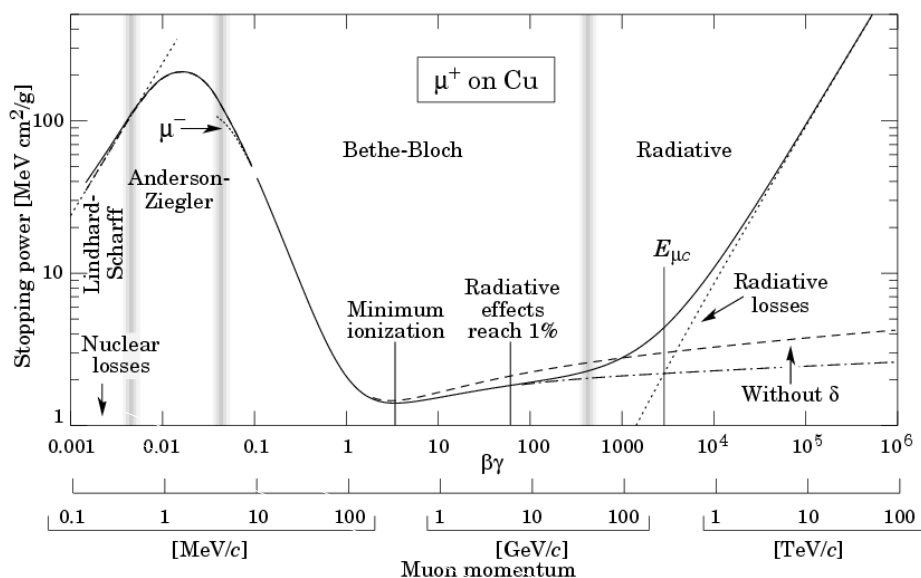


Figure 2.1: The figure represents energy loss per unit length as a function of particle momentum, following Bethe-Bloch formulation [60]. The formulation found to describe the energy loss due to collision and radiation over a wide region of  $0.1 < \beta\gamma < 100$ .

## 2.2.2 Interaction of electron

Electrons can interact with matter in a plenty of different ways depending on the incident energy of the electron itself. Being lighter mass ( $m_{e^-} = 0.511 \text{ MeV}$ ), it becomes relativistic at nuclear energy scale, where radiative losses become equal important as of inelastic collisional

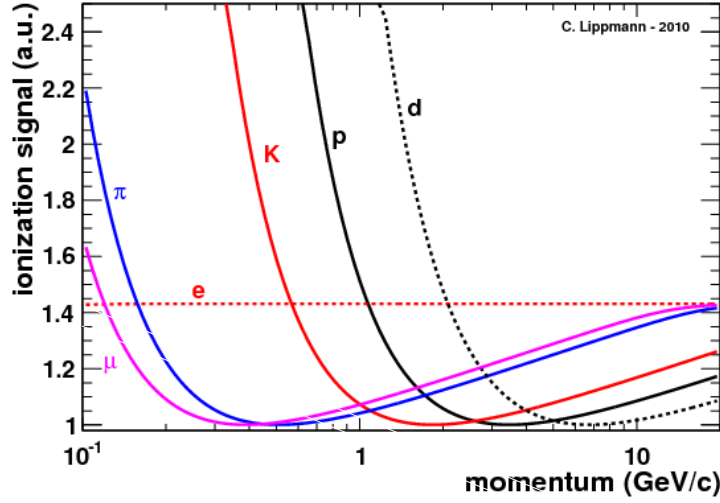


Figure 2.2: Energy loss per unit length as a function of particle momentum for different particle following Bethe-Bloch formulation [60]. It illustrates the region for which particles can be identified from their energy deposition profile.

energy loss mechanism. The inelastic process which is responsible for electron energy loss, can be represented by modified **Bethe-Bloch Formula**. The expression is different from normal Bethe-Bloch form because of fact that electron experience "large angle multiple scattering", "large energy loss possible b/w electron on electron scattering", "indistinguishability of incident and matter electron", "relativistic in nature at nuclear energies". Taking all these anomalous effects into account, electron energy loss can be expressed by the following equation 2.3

$$-\frac{dE}{dx} = \frac{4\pi k^2 e^4}{m_e c^2} \frac{z^2}{\beta^2} \frac{\rho Z N_A}{A} B(v) \quad ,$$

$$\text{where, } B(v) = \frac{1}{2} \ln \left( \frac{\tau^2(\tau+2)}{2 \left( \frac{I}{m_e c^2} \right)^2} \right) + \frac{F(\tau)}{2} - \frac{\delta(\beta)}{2} - \frac{C(I,\beta)}{Z} \quad , \quad (2.3)$$

$$\text{with, } F(\tau) = 1 - \beta^2 + \frac{\tau^2}{8} - \frac{(2\tau+1)\ln 2}{(\tau+1)^2} \text{ for electron.}$$

As the energy loss of any particle during passage through matter is a stochastic process, the energy deposition, even for a mono-energetic incident beam, spread (straggling) over a

certain energy window instead of being a delta function. Usually, the straggling for electron is more compare to heavier charged particle. However, for a thin material, electron can still results a landau distribution which looks like a minimum ionisation particle but with value higher than usual.

Apart from collisional losses, there are two major radiational losses, **Bremstrahlung and Cherenkov radiation** respectively, for relativistically energetic electrons. A charged particle, moving faster than the speed of light in a medium, emits **cherenkov radiation** which is a result of collective effect (polarisation) of the medium to the fast moving particle. The spectrum of the Cherenkov radiation can be expressed by Frank-Tamm's formula as shown equation 2.4

$$\frac{dE}{dx} = \frac{Z^2 e^2}{c^2} \left( 1 - \frac{1}{\beta^2 n(w)^2} \right) \Theta \left( v - \frac{c}{n(w)} \right) \omega d\omega, \quad (2.4)$$

where,  $\Theta$  is Heaviside step function

$\frac{dE}{dx}$  is the energy emitted per unit distance traveled by a particle of charge  $Ze$  for a frequency range  $d\omega$ . On the other hand, an energetic electron can emit **Bremstrahlung**, radiation under influence of an electric field. Mostly when an electron passes by a strong nuclear electric field, the amount of bremsstrahlung become significant. However, electron bremsstrahlung is also possible but the contribution is suppressed by the nuclear part. The spectrum of the bremsstrahlung radiation can be illustrated using equation 2.5

$$P(\omega) \approx \frac{8}{2\pi} \frac{e^6}{m_e^2 c^3 v^2 b^2}, \text{ for } \omega \ll \frac{v}{2b}, \quad (2.5)$$

$$P(\omega) \approx \frac{8}{2\pi} \frac{e^6}{m_e^2 c^3 v^2 b^2} e^{-\frac{\omega b}{v}}, \text{ for } \omega \gg \frac{v}{2b},$$

Where,  $P(\omega)$  represents energy emitted per second by a particle of charge  $ze$ . However, the energy loss by the bremsstrahlung by a charged particle can be represented by equation 2.6

$$-\frac{dE}{dX} = 4\alpha N_A \frac{Z^2}{A} z^2 \left( \frac{1}{4\pi\epsilon_0} \frac{e^2}{mc^2} \right) E \ln \left( \frac{183}{Z^{1/3}} \right). \quad (2.6)$$

where,  $Z$  and  $A$  are atomic number and mass number of the medium. Important to note, that the bremsstrahlung radiation loss by an incoming charged particle varies inversely with fourth power of the mass, which itself explain why electron is so crucial compare to other heavy charged particle in this case. In brief, electron loses energy through **ionization**, varies

linearly with "E" and with  $Z_{material}^2$ , and **radiational**, varies logarithmically with "E" and linearly with Z. As is evident, electron will loss energy through radiation at high incident energies, while with decrease in energy, ionisation losses will take over. At some particular incident energy (known as critical energy:  $E_C$ ), however, there will be an balance between two processes, resulting a critical energy:  $E_C$ , and can be defined as shown in equation 2.7

$$\left(\frac{dE}{dx}\right)_{radiation} = \left(\frac{dE}{dx}\right)_{collision}, \text{ for } E = E_C, \quad (2.7)$$

$$\text{where, } E_C = \frac{1600m_e c^2}{Z},$$

The expression for  $E_C$ , as shown, can be approximated using Bethe and Heitler prescription. For the  $E > E_C$ , the energy of the electron can be expressed in terms of incident energy and

the distance travelled within the medium as  $E(x) = E_0 e^{-\left(\frac{x}{X_R}\right)}$ , where  $X_R$  is the radiation length and depend on the material as  $X_R = \frac{1}{N\sigma_{rad}}$  with N as number of scattering centre inside the material.

Apart from these two major mechanisms of energy loses by electrons, there are other important elastic process, like multiple scattering which plays important role by increasing the effective distance of the path inside matter. Usually, the angular distribution for deflection by multiple scattering can be approximated to a Gaussian distribution.

## 2.3 Interaction of neutral particle

Primarily, neutral particle can interact with matter either through strong or weak interaction. However, photon, even being neutral, can interact with matter quite differently from other charged particles. In the following sub-section, we will mainly concentrate on interaction of photons with matter and discuss about other neutral particle like neutron and neutrinos.

### 2.3.1 Interaction of photon

Like in case of charged particles, photon can interact with matter both by **Elastic and Inelastic** scattering processes. In elastic scattering, photon energy remains unchanged apart from a negligible amount which appears as recoiling momentum to the target particle which is required for momentum conservation. There are two type of elastic scattering, that a photon can experience namely Thomson's scattering and Rayleigh scattering respectively. When a photon interact with a free electron or nucleus, it undergoes Thomson scattering which can

be quantitatively expressed as

$$\sigma_{Thomson} = \frac{8\pi}{3} \left( \frac{e^2}{4\pi\epsilon_0 m_e c^2} \right)^2 \quad (2.8)$$

where  $\sigma$  represents the cross section for the scattering process. On the other hand, if the photon get scattered from a bound electron, it will encounter Rayleigh scattering which can be expressed as shown in equation 2.9 for cross-section

$$\sigma_{Rayleigh} = \frac{2\pi^5}{3} \left( \frac{d^6}{\lambda^4} \right) \left( \frac{(n^2 - 1)}{(n^2 + 2)} \right)^2. \quad (2.9)$$

Where,  $n$  is refractive index of the material,  $d$  is the diameter of the particle. Photon, although the cross-section is small, might undergo nuclear resonance scattering as an another possible interaction channel, where the photon get absorbed by the nucleus and go to a higher excited state and subsequently come down to the ground state by emitting a photon. In this case, the energy of the photon hardly changed except by a negligible amount for momentum conservation. The cross-section can quantitatively be expressed as shown in equation 2.10

$$\sigma_{NR} = \frac{\lambda^2 \Gamma \Gamma_\gamma}{4\pi \left( (E_0 - E)^2 + \left( \frac{\Gamma}{2} \right)^2 \right)}. \quad (2.10)$$

Here,  $\Gamma$  is the total width of the nuclear level,  $\Gamma_\gamma$  is the partial width for gamma decay. Nonetheless, as far as the energy loss of a photon inside a matter is considered, it is the inelastic processes which are relevant. Photon, depending on the energy and the atomic number of the material, can loss energy through either among **photoelectric effect, Compton scattering and pair-production**. In a photoelectric effect, an incoming photon interact with a bound atomic electron and get absorbed completely within the matter and the energy appeared as the kinetic energy of an atomic electron, resulting ionisation of the medium. Approximately, The cross-section for photoelectric effect, away from the characteristic energy peaks, can be approximately expressed by the equation 2.11 in terms of particle energy and medium- $Z$ , makes it dominant for incident energies  $E_\gamma < 0.1 \text{ MeV}$

$$\sigma_{photoelectric} \propto \frac{Z^5 \alpha^4}{E_\gamma}. \quad (2.11)$$

In the intermediate energy, photon-energy loss is dominated by another inelastic scattering, **Compton scattering**, in which an incoming photon get scattered by an electron and

transferred part of its energy to the electron which essentially produce ionisation with in the medium. The cross-section, as a function of incident photon energy ( $E_\gamma$ ) and material properties, can be represented by an approximated formula 2.12

$$\sigma_{compton} \propto Z \left( \frac{E'_\gamma}{E_\gamma} \right)^2 \left( \frac{E'_\gamma}{E_\gamma} + \frac{E_\gamma}{E'_\gamma} - \sin^2 \theta \right). \quad (2.12)$$

The contribution of Compton scattering to photon energy loss is a dominant process for incident energy range of  $0.1 \text{ MeV} \leq E_\gamma \leq 10 \text{ MeV}$ . However, in case of very high energy photon, relevant in relativistic heavy ion collision and particle physics, photons loses their energy by **pair production** in which get converted into matter by creating particle-anti-particle pair. Unlike other two processes, pair production has energy threshold  $E_\gamma^{th} > 1.02 \text{ MeV}$  and become practically energy independent for  $E_\gamma > \frac{70}{Z^{1/3}} \text{ MeV}$ , as the cross section for pair production reach a plateau region which can be represented by 2.13

$$\sigma_{pair} \approx \frac{7}{9} (4\alpha r_e^2 Z^2) \ln \left( \frac{183}{Z^{1/3}} \right). \quad (2.13)$$

The expression for radiation length, as derived from this equation will become  $\lambda_{pair} \approx \left( \frac{9}{7} \right) X_R$ , which is slightly higher compare to electron, reflected as photon is neutral and will start interacting with matter little later relative to charged electron.

However, to understand the importance of all three processes with respect to photon interaction, it will be more explicit by expressing the cross section as a function of both photon energy ( $E_\gamma$ ) and material properties as is shown in figure 2.3 and 2.4 respectively which explains the domain of dominance for Pair production, Compton scattering and photoelectric effect. For relativistic (beyond 1 MeV) energy, the most important process is the pair production whereas photoelectric effects is most dominant in the low energy limit. However, there is an interplay among photoelectric, Compton and pair production at intermediate energies (0.5 MeV to 500 MeV) which is taken over by Compton process around 1 MeV. On the other hand, these processes have strong material dependence ( $f(Z)$ ) as well which is described in the figure 2.4.

### 2.3.2 Interaction of neutral particle ( $m \neq 0$ )

Apart from photon, other neutral particles, like neutron and neutrinos, interact with matter through strong and weak interaction. Interaction of neutron has a strong dependence on the

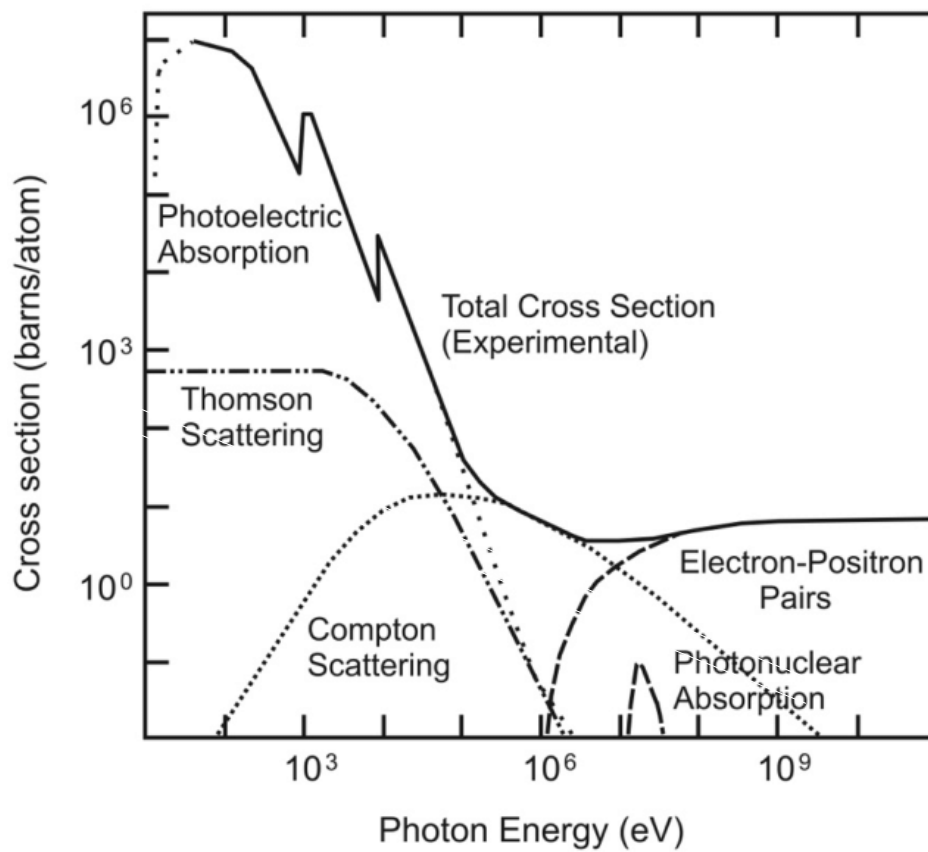


Figure 2.3: Relative cross-sections for photoelectric, Compton and pair production as a function of photon energy for copper, which express the dominance of a particular process for a specific photon energy range.

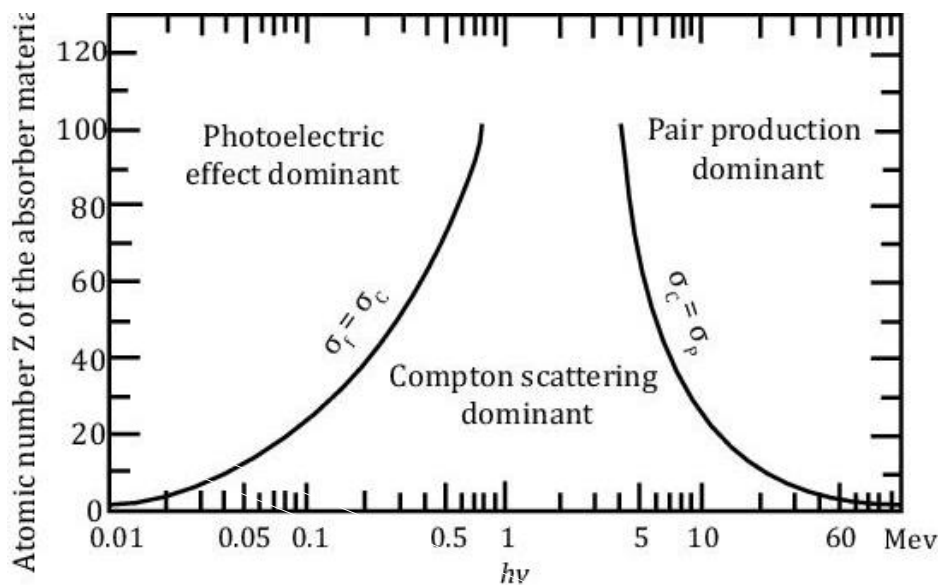


Figure 2.4: Cross sections for Photoelectric, Compton and Pair production as function of material- $Z$  and incident energy of particle, illustrates which process is relevant for a photon of particular energy interacting with a specific material.

energy of the particle. In both the cases primarily the interaction results a secondary particle which went through electromagnetic interaction and produce ionisation in the medium. However, if the energy of the particle is high enough to create further particles, it might lead to shower of hadron and thus a hadronic shower. Within the present scope, we will restrict our discussion without going in detail about the hadronic shower formation and their characterisation. On the other hand, neutrinos interact with matter weakly either by a charged-current or a neutral-current. As the cross-sections for either with electrons and/or the nuclei within matter are small, comparatively large matter is required to produce measurable amount of secondary charged particles. There are another important mechanism, such as **transition radiation**, come into the picture when a relativistic particle with large- $\gamma$  crosses the boundary between two medium with different refractive indices. The radiation, thus emitted, is strongly forward peaked and varies logarithmically with  $\gamma$ .

## 2.4 Basic measurements

The discussion so far, regarding the interaction of particles, was intended to understand the working principle of different particle detection and measurement techniques, used in

the different field of physics. In this section, we will discuss particle detection techniques and thus detectors in brief, commonly used in the field of relativistic high energy collisions. Historically, probably the concept of modern detector brought to the field back in 1895 with the discovery of x-ray by W. C. Röntgen. Since then, the technology of particle detection has advanced in close connection with particle physics and vice versa. The development of detectors can be divided naively into three ages of technologies, *Image tradition*, *Logic tradition* and *Electronic images*. In the early days of *Cloud chamber*, *Emulsion method* and *Bubble chamber*, each and every event was imaged by producing ionisation which surrounded by condensed vapour molecules. The picture, so formed, are left as an image for analysis afterwards. The simplistic and innovative approach, however, is restricted with very slow count rate (few tens/second) and no choice for triggering. The detection techniques changed over to logic tradition in the 1970's with the invention of *Geiger counter*, *Scintillators with a photomultiplier*, *Spark chambers* and *etc.* The incident particle, although, can not be seen, but their presence and characteristics can be reconstructed using logics like coincidences, triggers and decay kinematics. The inherent amplification of the signal and high rate handling capability makes the detection techniques robust and appropriate even today. However, with the boost in available energy of the collision, physics of detection techniques enter a new horizon, where the complexities in experiments folded by many times. Multi-dimensional requirements, like tracking, particle identification, energy measurements, handling the huge amount of data, reconstruction etc, took the detection techniques to electronic imaging with *Wire chamber*, *Silicon detector* and *so on*. In general, a detecting medium can be made of either solid, liquid or gas with each having their own advantages and disadvantages.

**Gas detector** - In the field of nuclear and particle physics, broadly used detecting mediums are usually gas and solid because of their abundances and ease of use. In case of gas detectors, it can be divided into many categories like Ionisation chamber, Spark Chamber, Geiger-Muller counter and the proportional counter which are different mostly in terms of applied voltage across two electrodes and differ in working principle. The multi-wire chamber can work with both Geiger-Muller counter and proportional counter in principle, however, the region of working principle depend on the requirement of either only counting of particles or more. Drift chambers and more advanced time projection chamber fall into the categories of proportional counter. The most interesting part of gas detector is, though it creates less amount of charge in primary interaction it can be multiplied to a large value with external electric field which let the output signal to be substantially large and well separated from the noise. The main disadvantage of gas detector is the comparatively large dead time which

restricts it to be used in high rate measurements. However, with the advancement of modern gas detector technology, the time resolution (resulting less dead time) can be achieved at about few nanoseconds with Gas Electron Multiplier (GEM). GEMs, in comparison to other gas detectors, produce an intense electric field in small holes in a thin polymer sheet (instead of a metal mesh or wire) which resulted in large electrons to come out through avalanches within these holes. Moreover, a separate electrode is used to collect the electrons followed by the readout.

**solid state detector** - On the other hand, the use of solid as detecting medium has several advantages over gas because of its high density, the possibility of achieving higher granularity, less ionisation energy for charge pair creation and fast signal processing (low dead time). There are two broad categories of solid state detectors namely Scintillator and Semiconductor.

A scintillator, by definition, is a material which absorbs part of the incident particle and emits in the form of light (called scintillation). Usually, the materials which are capable of exhibiting such phenomenon is called Luminescent materials. Depending on the transition from the excited (resulted because of absorption of energy from the incoming particle) to the ground state, the energy/frequency of the outgoing light is decided. Among many, high density, fast operation speed, low cost, radiation hardness, photon conversion capability, stability are the basic general required properties for a scintillator to be used as a detector. Scintillators can be broadly divided into three categories such as a) organic, b) plastic and c) inorganic scintillators. Organic scintillators are made from "aromatic hydrocarbon" having a benzene ring in it and have luminescence of the order of few nanoseconds. Most common scintillators are crystalline in nature like anthracene  $C_{14}H_{10}$  and stilbene  $C_{14}H_{12}$ . However, there are liquid organic scintillators which are organic solvent like toluene, xylene, benzene etc in which fluors (solutes) like p-terphenyl, PBD, butyl PBD etc are admixed. On the other hand, plastic scintillators are a combination of a fluor (solute) suspended in bases such as aromatic plastics, polymers etc. The advantages of plastic scintillators are high light output, fast signal generation (decay time  $\approx 2 \rightarrow 4$ ) and most importantly it can be shaped according to the requirement with a high degree of durability. In contrast, inorganic scintillators are crystals, grown in high temperature furnaces, such as alkali metal halides with a small amount of activator impurity (NaI(Tl), CsI(Tl), CsI and etc. There are also non-alkali scintillator crystals like  $BaF_2$ ,  $CaF_2(Eu)$ ,  $ZnS(Ag)$ ,  $CaWO_4$ . The most attractive property of inorganic scintillator is the large photon output ( $\approx 50000$  per MeV) in comparison to organic scintillators. However, the main disadvantages of inorganic scintillators are they are hygroscopic in

nature and comparatively slow compared to organic one.

On the other hand, the use of semiconductor p-n junction as a particle detection tool was first realised back in 1950. With technological advancement, the solid state detectors, silicon in specific, was found to fulfil the requirement of very fine granularity up to few microns which helps in achieving very good position resolution. Comparatively less amount of ionisation energy ( $\approx 3 \rightarrow 4$  eV) for e-h pairs creation in comparison to gas detectors ( $\approx 30$  eV) make it attractive which leads to very good energy resolution. Fast charge collection ( $\delta t \approx 10ns$ ) is an inherent property of silicon due to its high mobility of charge carriers. Radiation hardness of semiconductor detectors makes it widely acceptable for experiments with high radiation environments. Naively, solid state detectors can be subdivided into two types depending on their working principle like **Photo resistors** which shows the change in resistance with irradiation and *Photo diode* which is a depleted semiconductor with large electric fields. Silicon, among commonly used semiconductor material like Si, Ge, GaAs, Diamond, found most optimised and suitable candidate due to characteristics like comparatively low cost can operate in room temperature, optimised energy and position resolution and widely used in commercial fields make its technological advancement faster.

Conventionally the classification of a detector in a complex experiment can be done depending on the use into four categories as Vertex detector, Tracking detector, Particle identification detector and Calorimeter, driven by the requirement of measuring the position, particle identity, momentum and energy. The primary objective of particle detection is to characterise an unknown incoming particle by knowing its position and direction, mass (identity), momentum, energy, lifetime, spin and etc. The techniques, commonly used, are tracking (with or without magnetic field), spectroscopy and PID, Cherenkov radiation, calorimeters, Time of Flight measurement and etc. The basic concerns associated with any measurement are the type and the specific property of the particle, the maximum number of particle expected (rate) and etc. In large experimental facilities like RHIC, LHC, FAIR, as the spectrum of particle type, energy, momentum is spread over a wide range, a single detector can never accomplish the purpose of complete measurement. Hence, a cluster of detectors with diverse capabilities are assembled in an order accordingly, which might differ for fixed target and collider experiments. Fixed target experiments are populated with detectors mainly in the forward direction after the target, while collider experiments are occupied with detectors, arranged in a cylindrical geometry covering the interaction point. The end cap of the cylindrical coverage can also be used for measurements which, thus, provide a  $\approx 4\pi$  detector coverage for collider experiment. As is shown, for example, in the picture 2.5, the

detectors are stacked in an onion-like structure such that low momentum and more sensitive particles can be detected first. Usually, calorimeters, which absorb the particle, are placed at the outer layer not to affect other measurements. In the following section, a brief discussion about the generic schematic of the detection technique of a complex experiment will be presented along with the relevant working principle.

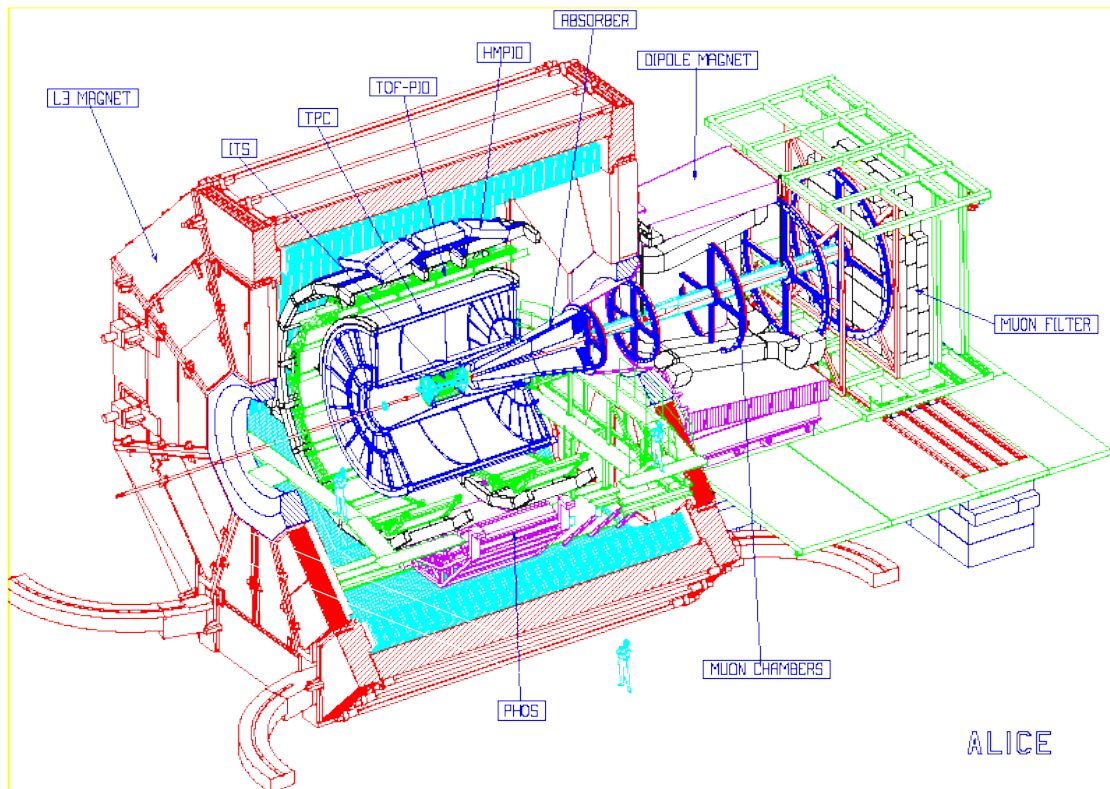


Figure 2.5: Cross sectional view of a complex experiment (ALICE for example) which explains how different sub-detectors are stacked into an onion-like structure to measure particles of wide range in mass, type, energy for almost full  $4\pi$  coverage.

### 2.4.1 Vertex detection

The purpose of a Vertex detector is to find the point of interaction or the source of particle emission and so it must be placed immediately next to the interaction point. The vertex detector is usually composed of a number of layers with desired pixel dimension so that it can handle a large density of particles coming from either a primary or secondary vertex in an experiment. Primarily, the vertex detector serves the purpose of measuring the position and

angles off any charged particle to a sufficient precision so that different tracks, specifically, primary to secondary (coming from the decay of some other particle) can be disentangled. For a good vertex detector, it must be radiation hard (to handle extreme high multiplicity density), highly granular, of excellent position resolution ( about few  $\mu\text{m}$ ), and has high rate handling capability (charge collection time: tens of ns). Silicon detector, segmented into strips, pads or pixels, are commonly used as vertex detector as the necessary requirements can be easily achieved. As an example, ALICE experiment at CERN has vertex detector, namely Inner Tracking System, composed of 6 layers of silicon detectors with 2 layers each for pixel, pad and strip.

## 2.4.2 Particle identification and momentum measurement

**Time projection chamber:** Time projection chambers (TPC), invented by David Nygren in 1974, are considered as the heart of any complex experiment which provides both the tracks and momentum of charged particles traversing through it. TPC, usually cylindrical in geometry, consists of large gas-filled sensitive volume with the central cathode at high potential and two anodes with readouts at both the end. Time projection chambers are commonly placed coaxially with the beam line with interaction point as its centre. Depending on the length along the beam line, there is a number of field cages which are placed to make the electric field inside the drift volume homogeneous. An additional magnetic field parallel to the electric field applied to bend the charged particle tracks which are used to reconstruct the momentum of the corresponding particles. However, the sensitivity and range of momentum measurement completely depend on the energy of the particles passing through the detector and the applied magnetic field. The TPC works according to the energy loss of charged particle and the ionisation produced by it inside the gaseous medium. The three dimensional reconstruction of the charged particle track is done by reconstructing  $r - \phi$  from projection on the pad plane and the z-position (parallel to beam axis) from the drift time ( $t_{drift} = t_{in\ passing\ through\ TPC\ volume} - t_{measured\ signal\ on\ the\ pad}$ ). The momentum of the particle can be calculated using simple kinematics of a moving charged particle in a combination of electric and magnetic field and can be expressed as following 2.14

$$m \frac{dv}{dt} = eE + e[v \times B] - Kv$$

with,  $K$  as viscosity of the medium,

$$s = R - R \cos \frac{\phi}{2} \approx \frac{L^2}{8R} \quad , \quad (2.14)$$

$$\frac{\Delta p}{p} = \frac{\Delta R}{R} \approx \frac{\Delta s}{s} \quad .$$

where,  $m \frac{dv}{dt}$  represents the force experienced by a charged particle with  $K$  as the frictional force constant arising due to interaction with gas, momentum  $p = eBR$ , with  $R$  being the radius of curvature of the track. The error in both Sagitta and momentum expressed above, thus depend on Length of TPC, Magnetic field applied and the momentum range to be measured.

**Time of Flight method:** In general, "Time of Flight (TOF)" is measured taking difference between two detectors with good time resolution, placed at a certain gap ( $L$ ). Usually, for TOF measurement either scintillator or resistive plate chambers are preferred because of their excellent time resolution ( ns and ps respectively). Specifically, TOF is very much useful in discriminating two particles with different masses but of same momentum. The time of flight difference ( $\Delta t$ ) can be expressed in terms off difference in TOF for two particle of masses  $m_1, m_2$  and energies  $E_1, E_2$  as shown in equation 2.15

$$\Delta t = \tau_1 - \tau_2 = \frac{L}{c} \left( \frac{1}{\beta_1} - \frac{1}{\beta_2} \right),$$

$$\text{where, } \beta = \frac{pc}{E} \quad ,$$

$$m^2 = p^2 \left( \frac{\tau^2}{L^2} - 1 \right) \quad (2.15)$$

$$\text{with, momentum } p = \beta \gamma m \text{ and } \beta = \frac{L}{\tau}.$$

In an extreme case, when two particles are of same momentum with  $pc \gg m_0c^2$ , time difference becomes

$$\Delta t = \frac{Lc}{2p^2} (m_1^2 - m_2^2).$$

However, at moderate momentum when particles become relativistic, expression for mass as a funtion of time of flight can be expressed as

$$\delta(m^2) = 2m^2 \frac{\delta p}{p} + 2E^2 \frac{\delta \tau}{\tau} + 2E^2 \frac{\delta L}{L},$$

The measurement of mass is contributed by three terms, momentum, time of flight and the length travelled respectively. The measurement in mass reconstruction can be expressed as following

$$\sigma(m^2) = 2 \left( m^4 \left( \frac{\sigma_p}{p} \right)^2 + E^4 \left( \frac{\sigma_\tau}{\tau} \right)^2 + E^4 \left( \frac{\sigma_L}{L} \right)^2 \right)^{\frac{1}{2}}.$$

Neglecting momentum and the length term, the error in mass measurement can be approximated as

$$\sigma(m^2) \approx 2E^2 \frac{\sigma_\tau}{\tau}$$

Although, geometrically the TOF detector can be of any shape, for collider type experiment, it is cylindrical and placed coaxially with TPC.

**Transition Radiation detection:** when the particles become ultra-relativistic ( $\gamma \geq 1000$ ), neither TPC or TOF can individually differentiate particle of different masses effectively, whereas, with the transition radiation can help as has been already discussed earlier. Specifically, the detection of electron get augmented with inclusion of transition radiation detector to the experiment. An electron emits an X-ray when crossing an interface between two medium which is introduced by including a radiant in the TRD [61]. The radiated energy spectra can be expressed by 2.16

$$\frac{d^2w}{d\omega d\Omega} = \frac{\alpha}{\pi^2} \left( \frac{\theta}{\gamma^{-2} + \theta^2 + \zeta_1^2} - \frac{\theta}{\gamma^{-2} + \theta^2 + \zeta_2^2} \right)^2, \quad (2.16)$$

where,  $\gamma \gg 1$ ,  $\zeta_i^2 = \frac{\omega_{pi}^2}{\omega^2} = 1 - \epsilon_i(\omega)$ . Like in other cases, TRD also placed coaxially with TPC and TRD in a collider experiment, centred at the interaction point itself.

### 2.4.3 Energy measurement

Apart from particle identification and momentum measurement, another important part of a complex experimental set up is the calorimeter, a means of energy measurement in which the particle will be lost either partially or fully. Depending on the type of the particle, the calorimeter design might change accordingly but the basic requirements are more or less similar. In an experiment, calorimeter can be of two types *hadronic and electromagnetic*

*calorimeter*. Hadronic calorimeter is commonly placed at the outermost layers of the onion structure of the detector assembly. However, electromagnetic calorimeter is placed one step ahead and meant for electron or photon energy (momentum) measurement. There is a number of advantages, like compactness (size varies logarithmically with energy), optimised energy and position resolution and etc. The calorimeter can be placed both for central part (with common coverage as other detectors) or at the end of the cylindrical central part of the experiment. A more detail discussion about the physics of calorimeter, design issues, performances etc. will be taken up in the next section and subsequent chapters of this thesis. Moreover, there could be options for measuring muons and neutrinos which will make the particle detection complete in a sense. Commonly, muons are also measures using tracker/calorimeter and placed in the end of the detector assembly. As the interaction probability is very less, it requires a lot of material budget which might affect other measurement if otherwise placed.

## 2.5 Physics of calorimetry

In this section, we will discuss the physics of calorimetry such as mechanisms of electromagnetic shower formation, the propagation of shower inside calorimeters and etc. However, to start, the interaction of a high energy particle (except  $e^-$  or  $\gamma$ ) need to be described. It deposits energy through either collisional or ionisation processes and behaves mostly like a minimum ionising particle at sufficiently high energies. The energy loss profile can be described by a landau distribution, as shown in equation 2.17, following the bethe-block energy loss formula which has been described in detail in section 2.2.1.

$$f(\lambda) = \frac{1}{\sqrt{2\pi}} e^{-\frac{1}{2}(\lambda+e^{-\lambda})} \text{ with,} \quad (2.17)$$

$$\lambda = \frac{\Delta E - \bar{\Delta E}}{C \frac{m_e c^2}{\beta^2} \frac{Zz}{A} \Delta x}$$

The minimum ionisation potential is described by Landau-Vavilov taking the proper upper limit for the energy deposition in a thin material medium. Heavier charged particles are unlikely to produce the electromagnetic shower during their passage in the matter. However, for sufficiently high incident energy, they can induce hadronic shower within a larger depth

of material as an outcome of strong interaction with matter. The depth of the calorimeter needs to be an order of magnitude larger compared to its EM-counterpart (e.g.  $\frac{9.946}{0.35} \approx 28$  for tungsten 5.2) for significant contribution to hadronic shower. The relevant length scale in case of hadronic shower formation and propagation in the medium is the interaction length ( $\lambda_I$ ) which is ( $\approx 20\times$  higher than the radiation length  $X_R$ ).

The physics of an EM-calorimeter is, however, more involved in case of electron or photons which produce secondary particles in the form of showers within the calorimeter depth. An electromagnetic shower is produced by an electron or photon with energy ( $E > E_C$ ) when interacting with matter through either pair production (for  $\gamma$ ) or Bremsstrahlung (for electrons). Theoretical calculations [62] show that the probability for energy loss through bremsstrahlung process decreases rapidly with increase in particle mass according to the expression for "Total Radiated Power" as shown in equation 2.18

$$\begin{aligned} \text{Perpendicular component: } P_{a_{\perp v}} &= \frac{q^2 \gamma^4 a^2}{\pi \epsilon_0 c^3}, \\ \text{And Parallel component: } P_{a_{\parallel v}} &= \frac{q^2 \gamma^4 a^2}{\pi \epsilon_0 c^3}, \end{aligned} \tag{2.18}$$

where  $q \rightarrow$  charge,  $a \rightarrow$  acceleration and  $\gamma \rightarrow$  Lorentz factor. Since Energy  $E$ , ( $E = \gamma mc^2$ ), radiated by bremsstrahlung process is found to vary either with  $m^{-4}$  or  $m^{-6}$  as shown in equation 2.18. It is preferable for an electron to lose more energy compared to other heavier particles like proton, neutron,  $\pi$  etc. Electrons produce EM shower [63] because of its lighter mass and electromagnetic nature. The shower propagates through the calorimeter block and leaves its footprints at consecutive detector layers which can be reconstructed afterwards. In contrary, photons can trigger EM-shower by pair production in the presence of the calorimeter medium following equation 2.13 even if they are not charged in nature. However, because of neutrality, photons will start showering little later compare to the electron which is otherwise identical as far as shower properties and propagation are concerned. Concurrent nature of EM-showers produced either by electron or photons might invite inaccuracy in photon measurements and need proper discrimination technique in an actual experiment.

The energy lost by an electron of initial energy  $E_0$  in the form of photon through bremsstrahlung after travelling a distance of  $1 X_R$  on average can be calculated using Heitler cascade model. In this simplistic model, the energy of the emitted bremsstrahlung photon and the remaining electron is assumed as half of the initial energy of the primary electron  $\left(\frac{E_0}{2}\right)$ . In the next step, as the cross-section for pair production for high energy photons is

dominant, it might undergo electron-positron pair creation again after a path length of  $1 X_R$  on average with the photon energy shared equally among two particles. So effectively at a depth of  $2 X_R$ , there will be four particles of about same energy (simplified). This process of cascading will continue until the energy of the particle at a particular step reach the critical energy ( $E_C$ ). The energy loss afterwards will be dominated by multiple scattering which results in soft particle (photon or electron) production.

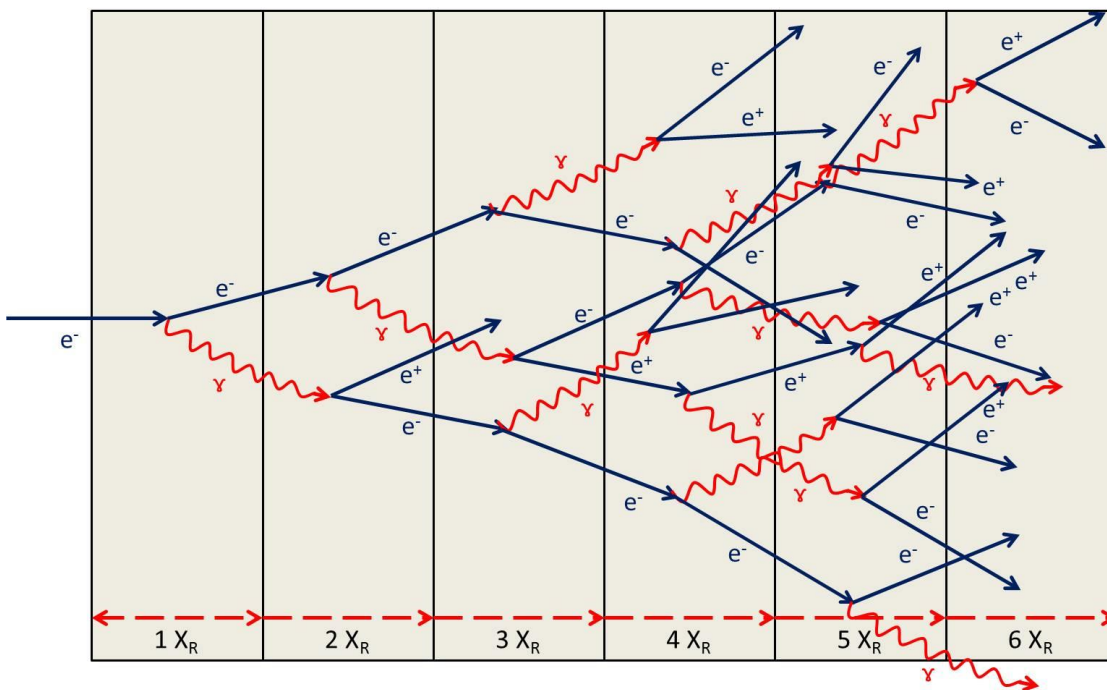


Figure 2.6: Sketch of the electromagnetic shower formation following a simplistic Heitler model [64], which illustrates the the number of secondaries produced with in an absorber/convertor material as a function of depth in units of radiation length.

The electromagnetic shower, as illustrated by the simplistic cascade model, can describe most of the global properties of the EM shower. However, the details of the shower structure need more involved theoretical calculation, including asymmetric energy sharing and accurate cross-section for the bremsstrahlung and pair-production implemented. The properties of the

shower, in terms of initial energy, the path length in  $X_R$ , can be expressed as following-

$$\begin{aligned}
 \text{Number of particles after traveling } t X_R: & \quad N(t) = 2^t. \\
 \text{Energy of each particles at } t X_R \text{ depth:} & \quad E(t) = \frac{E_0}{2^t}. \\
 \text{Number of particles after reaching } E = E_C: & \quad N(t_{max}) = 2^{t_{max}} = \frac{E_0}{E_C}. \quad (2.19) \\
 t_{max} \text{ is distance in } X_R \text{ when energy become critical } E_C: & \quad t_{max} = X_R \ln \left( \frac{E_0}{E_C} \right).
 \end{aligned}$$

In brief, the predictions from the cascade model can be listed as:-

- The number of particles at a particular depth for the shower is proportional to the incident energy of the particle ( $N(t) \propto E_0$ ), resulting linearity between the output (energy deposition) -to - input (incident energy).
- The depth with maximum shower particles varies with incident energy logarithmically ( $t_{max} \propto \ln(E_0)$ ).
- The shower development is independent of the material, expressing length in  $X_R$  and energy in units of  $E_C$ .
- The angular spread of particles till shower maximum is small, defined by small opening angle of bremsstrahlung and pair production of high energy particles.

However, a detailed calculation of electromagnetic shower came later from Longo in 1975 [65] with a modification to more exact form which describes the profile along the depth of the shower propagation according to the expression as shown in equation 2.20

$$\frac{dE}{dt} = \frac{E_0 \times \beta \times (\beta t)^{\alpha-1} e^{-\beta t}}{\Gamma(\alpha)} \approx E_0 t^\alpha e^{-\beta t}, \quad (2.20)$$

with

$$t_{max} = \frac{\alpha - 1}{\beta} = \ln \left( \frac{E_0}{E_C} \right) + C_{e\gamma},$$

with  $t$  as the path length in units of radiation length and  $C_{e\gamma}$  -0.5 and -1.0 for  $\gamma$  and e-induced shower respectively. Where,  $\frac{dE}{dt}$  represents the energy deposition by the shower per unit depth in the unit of radiation length.  $\alpha$  and  $\beta$  are profile parameters of the shower. The term  $(\beta t)^{\alpha-1}$  with power law dependence explains the fast increase of the profile at the beginning of shower development due to secondary particle production, whereas,  $e^{-\beta t}$  took over for later part of the profile after the shower maximum.

Although, the shower is mostly dominated by radiational loss upto shower maximum, there is still some probability for soft particle production which might not be able to create further secondaries and undergo multiple scattering with a comparatively large opening angle. On the other hand, the transverse profile of energy deposition by the EM-shower at a particular depth illustrates the variation of energy deposition as a function of distance from the shower axis (direction of shower propagation) which can be expressed by equation 2.21

$$\frac{dE}{dr} = \alpha e^{-\left(\frac{r}{R_M}\right)} + \beta e^{-\left(\frac{r}{\lambda_{min}}\right)}. \quad (2.21)$$

Here,  $\frac{dE}{dr}$  is energy deposition per unit radial distance ( $r$ ) from the shower axis.  $R_M$  and  $\lambda_{min}$  are Moliere radius and the range of low energy photons respectively. There are two concentric parts of the transverse profile, inner-part mostly dominated by coulomb scattering where  $e^\pm$  move away from the shower axis due to multiple scattering. The outer-part is populated with low energy photon and electrons which are produced because of isotropic processes like Compton scattering, photo-electric effect and etc. which become more important after shower maximum.

## 2.6 Summary

The discussion about the particle interaction and measurement is undoubtedly significant in understanding experimental results. However, at the end, the aim for building and experimenting with a complex set of detectors in relativistic high energy collisions is to extract the properties the system formed in the collision from a different collisional system like pp pA, AA and etc at various collision energies. In the next section, we will discuss briefly the Large Hadron Collider and ALICE experiment in specific, in relevance to the present study along with different sub-detectors.

# Chapter 3

## Large Hadron Collider and The ALICE Experiment

### 3.1 Introduction

The phenomenal Rutherford experiment opened a new domain of generalised scattering experiment to probe the innermost structure of matter. The need for accelerated high energy beam was felt immediately after few years and the discovery of accelerator was done by Lawrence. During the same period, de-Broglie hypothesis ( $\lambda = \frac{h\pi}{p}$ ) sets guidance for the energy of a particle to probe a particular dimension. At a glance, the development of accelerators and particle physics are very much entangled and had advanced fulfilling the need of the other. In general, the accelerator can be defined as a device which accelerates particles and thus produces an energetic beam in a controllable manner. Properties of the beam such as intensity, energy, energy spread, transverse size, angular spread and etc can be well controlled in an accelerator. The development of accelerator has passed through a long journey starting from the early stage Cockroft Walton to Van de Graaff to Tandem to cyclotron and finally to today's state of the art extremely big accelerators like Relativistic Heavy Ion Collider (RHIC) or Large Hadron Collider (LHC). There are almost 30,000 operational accelerators exist around the world. Though it would have been interesting to have details of different accelerators and their uses, for the present study, we will restrict ourselves to the world's most powerful accelerator Large Hadron Collider and its different experiments.

## 3.2 Large Hadron Collider (LHC)

Large Hadron Collider, world's largest and most powerful accelerator, was made operational in 2008 after an enormous effort of 14 years. The uniqueness of LHC is lies in many ways not only in deliverable physics issues but also regarding the state of art technological achievements and their successful implementation. Following are some of the unique and distinctive features of LHC [66] -

**a) Giant accelerator** - The accelerator is 27 km long along the circumference and located in France and Switzerland. The 4 meter wide circular tunnel has been buried around 50 m to 175 m (100 m on average) underground.

**b) Practically absolute vacuum** - Extreme (ultra high) vacuum - air pressure of  $\approx 10^{-13}$  atm. This level of vacuum is maintained over a huge volume of about  $9,000 m^3$  (total volume of the LHC's major vacuum systems)s.

**d) world's largest fridge** - It operates at the temperature ( $\approx 1.9^o K$ ) colder than the deep outer space. It is required to operate superconducting coils, meant to produce a huge magnetic field of 8.3 Tesla (top field strength of each of the LHC's 1232 superconducting dipole magnets). Beams are kept in the path by superconducting magnets.

**e) Producing and handling the massive amount of data** - LHC produces an enormous amount of data with all its big experiments which are enough to fill about  $5 * 10^4$  TB hard disks per years.

**f) Extremely high energy production** - LHC can boost proton to a speed close to that of light ( $0.999999991 * c$  and only about 300mph less than light), which corresponds to collective energy of LHC's protons at the top speed of about 362 mega joules.

**c) Highest temperature known to mankind-** Huge amount of energy generation which led the temperature for proton-proton collision is  $\approx 10^{16}c$  in comparison to the core of sun  $\approx 10^{6}c$ .

**g) Collider with high intensity** - At any time, there are 0.00000000047 grams of protons which are circulating the LHC ring 11000 times per second.

However, the extremely high energy imparted to the particle by LHC is not a single state mechanism. Rather the boost in the energy of the particle happens in stages. In the beginning, when the energy of proton reaches 50 MeV it fed to PS Booster from the Linac 2. Proton energised to 1.4 GeV at PS Booster before the feed to Proton Synchrotron where it achieves the energy of about 25 GeV. In the next step, the protons are feed to Super Proton Synchrotron to lift the energy to 450 GeV. At the final stage, The particles are injected to LHC ring where it split into two which are circulated oppositely and achieve the highest energy of 6.5 TeV (designed for 7 TeV) each. LHC is capable of colliding different types of particles apart from proton. Proton, Lead, and Xe have collided at the different centre of mass

energies with various combinations. The details of different colliding system at the different centre of mass energies at LHC can be better understood from the following table 3.1

Table 3.1: The table illustrates the excellent capability of LHC in providing collision for different systems like proton-proton, proton-Lead, Lead-Lead and Xenon-Xenon. Moreover, the centre of mass energy varies for different colliding systems starting from 900 GeV to 14 TeV.

| Colliding system | Centre of mass energy (TeV)               |
|------------------|---|
| proton-proton    | 0.9, 2.36, 2.76, 5.02, 5.44, 7, 8, 13, 14 |
| proton-Lead      | 5.02                                      |
| Lead-proton      | 5.02                                      |
| Lead-Lead        | 2.76, 5.02                                |
| Xenon-Xenon      | 5.44                                      |

As is explained, being an extremely complex and precision machine, LHC can not be a single purpose facility. Indeed, it has several experiments which cover a wide range of physics starting from fundamental particle physics to the physics of quark gluon plasma. It has seven experiments, each with a distinct feature and characterised with the devoted detector(s). The four major experiments are ATLAS, CMS, ALICE and LHCb respectively. ATLAS and CMS are the general-purpose detectors to investigate the largest range of physics possible, starting from precision measurements of Higgs boson to searches for new physics beyond the Standard Model. Though both the experiments are meant to address same physics issues which are absolutely necessary to cross confirm any discovery. However, the basic difference between them lies in different technical solutions towards the problem and detector design. On the other hand, LHCb is a specialised experiment to measure the matter-antimatter asymmetry expected to be there in interactions of B-particles. The primary purpose of the experiment is to answer “the reason behind survival of matter world”. The LHCb experiment is composed of a number of sub-detectors to detect and measure particles in one of the beam directions. The ALICE experiment is designed to study the properties of quark-gluon plasma, a state of matter comprised of quarks and gluons, under extremely high temperature and density, in which partons become asymptotically free. Such a state of matter, QGP, is supposed to be existed just after the Big Bang, when our universe was only a microsecond old. Unlike other major experiments, ALICE’s main focus is to study the relativistic heavy ion collision and investigate QGP. Apart from these four main experiments, there are few more purpose motivated and small scale experiments exist in LHC - namely TOTEM, LHCf and MOEDAL respectively. TOTEM and LHCf are to measure forward particles, produced in proton-proton or heavy ions collisions. TOTEM is basically coupled with CMS and positioned on either side of the CMS interaction point. On the other hand,

LHCf has two detectors which are placed along the LHC beam-line, at 140 metres either side of the ATLAS interaction point. MOEDAL has been installed near LHCb to search for the hypothetical particle called the magnetic monopole. In the next section, we will focus on ALICE experiment, in particular, keeping the relevance about the scope of the Thesis work in mind.

### 3.3 A Large Ion Collider Experiment (ALICE)

The ALICE [67] experiment, composed of many individual sub-detectors as shown in figure 3.1, has dimensions of  $16 \times 16 \times 26 \text{ m}^3$  and of total weight of  $10^3$  ton. ALICE is

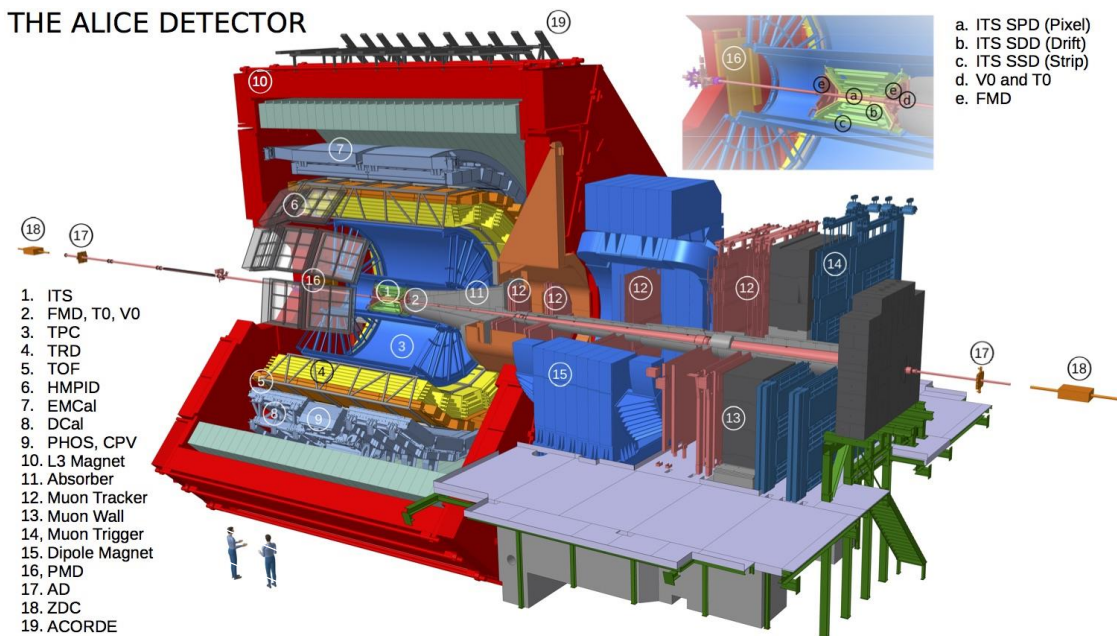


Figure 3.1: Schematic representation of the the ALICE experiment at the CERN LHC, embedded in a solenoid with magnetic field  $B = 0.5 \text{ T}$ . It has an excellent measurement capability at mid rapidity with ITS, TPC, TRD, TOF, PHOS, EMCal, and HMPID for various type of particles over a wide transverse momentum range. It can also measure cosmic events with the help of ACORDE. Forward detectors like PMD, FMD, V0, T0, MCH and ZDC are used for triggering, event characterisation, and multiplicity studies [68].

specifically designed to handle high particle density, produced in central Lead-Lead collision at the highest LHC energy. It has a unique feature of low transverse momentum threshold as  $p_{min} \approx 0.15 \text{ GeV}/c$  while it can identify particles up to  $20 \text{ GeV}/c$ . Naively, the ALICE

detectors can be divided into two categories depending on the the detector acceptance as is shown in table 3.2 and in rapidity plot 3.2 - 1) **central-barrel detectors** and 2) **forward detectors** respectively.

Table 3.2: Coverages of each individual detector of ALICE experiment in  $\eta - \phi$  plane

| Category         |         | Detector  | Acceptance (polar: $\phi$ )                          |   |
|------------------|---------|---|--|---|
| Central Barrel   | ITS-SPD | $ \eta  \leq 2.0$ (at $r = 3.9$ cm)                               | Full   |   |
|                  |         | $ \eta  \leq 1.4$ (at $r = 7.6$ cm)                               | Full   |   |
|                  | ITS-SDD | $ \eta  \leq 0.9$ (at $r = 15$ cm)                                | Full   |   |
|                  |         | $ \eta  \leq 0.9$ (at $r = 23.9$ cm)                              | Full   |   |
|                  | ITS-SSD | $ \eta  \leq 1.0$ (at $r = 38$ cm)                                | Full   |   |
|                  |         | $ \eta  \leq 1.0$ (at $r = 43$ cm)                                | Full   |   |
|                  | TPC     | $ \eta  \leq 0.9$ (at $85$ cm $\leq r \leq 247$ cm)               | Full   |   |
|                  |         | TRD   | $ \eta  \leq 0.8$ (at $290$ cm $\leq r \leq 368$ cm) | Full  |
|                  |         |   | TOF  | $ \eta  \leq 0.9$ (at $370$ cm $\leq r \leq 399$ cm)  |
|                  |         | PHOS  |  | $ \eta  \leq 0.12$ (at $460$ cm $\leq r \leq 478$ cm) |
|                  |         |   | EMCal  | $ \eta  \leq 0.7$ (at $430$ cm $\leq r \leq 455$ cm)  |
|                  |         | HMPID   |  | $ \eta  \leq 0.6$ (at $r = 490$ cm)                   |
|                  |         |   | ACORDE   | $ \eta  \leq 1.3$ (at $r = 850$ cm)                   |
| Forward Rapidity | PMD     | $6.5 \leq  \eta  \leq 7.5$ (at $r = 367$ cm)                      | Full   |   |
|                  |         | FMD   | $3.6 \leq  \eta  \leq 5.0$ (at $r = 320$ cm)         | Full  |
|                  | V0      |   | $1.7 \leq  \eta  \leq 3.7$ (at $r = 80$ cm)          | Full  |
|                  |         | $-3.4 \leq  \eta  \leq -1.7$ (at $r = 70$ cm)                     | Full   |   |
|                  |         | $2.8 \leq  \eta  \leq 5.1$ (at $r = 329$ cm)                      | Full   |   |
|                  |         | $3.7 \leq  \eta  \leq -1.7$ (at $r = -88$ cm)                     | Full   |   |
|                  | T0      | $4.6 \leq  \eta  \leq 4.9$ (at $r = 370$ cm)                      | Full   |   |
|                  |         | $-3.3 \leq  \eta  \leq -3.0$ (at $r = -70$ cm)                    | Full   |   |
|                  | ZDC     | $ \eta  \leq 8.8$ (at $r = \pm 113$ m)                            | Full   |   |
|                  |         | $6.5 \leq  \eta  \leq 7.5$ (at $r = \pm 113$ m)                   | $ \phi  \leq 10^\circ$                               |   |
|                  |         | $4.8 \leq  \eta  \leq 5.7$ (at $r = 730$ m)                       | $ \phi  \leq 16^\circ$                               |   |
|                  | MCH     | $-4.0 \leq  \eta  \leq -2.5$ (at $-142$ cm $\leq r \leq -540$ cm) | Full   |   |
|                  | MTR     | $-4.0 \leq  \eta  \leq -2.5$ (at $-171$ cm $\leq r \leq -161$ cm) | Full   |   |

ALICE has significantly contributed to the understanding of the strongly interacting matter. The centre of mass energy at LHC is 30 times higher than that at RHIC and produces a system with 10 times higher energy density. According to QCD prediction, a phase transition from confined (hadronic) to de-confined state (partonic) occurs at temperature  $T_C \geq 160$ - $190$  GeV which corresponds to an energy density of about  $0.7$ - $1.0$  GeV/fm<sup>3</sup>. At the start of LHC, experimental results from RHIC already confirmed the formation of a partonic matter (QGP), independently established by STAR, PHENIX and BHRAMS experiments. As the main focus of ALICE experiment is to find the details of the phase diagram in  $T - \mu$  plane specifically around zero chemical potential region, where a baryon-free partonic matter is expected to be formed in the collision. The understanding of parton distribution both inside nucleon and nuclei are equally important to understand the particle production in terms of either perturbative-QCD (hard particle) or non-perturbative QCD based phenomenological

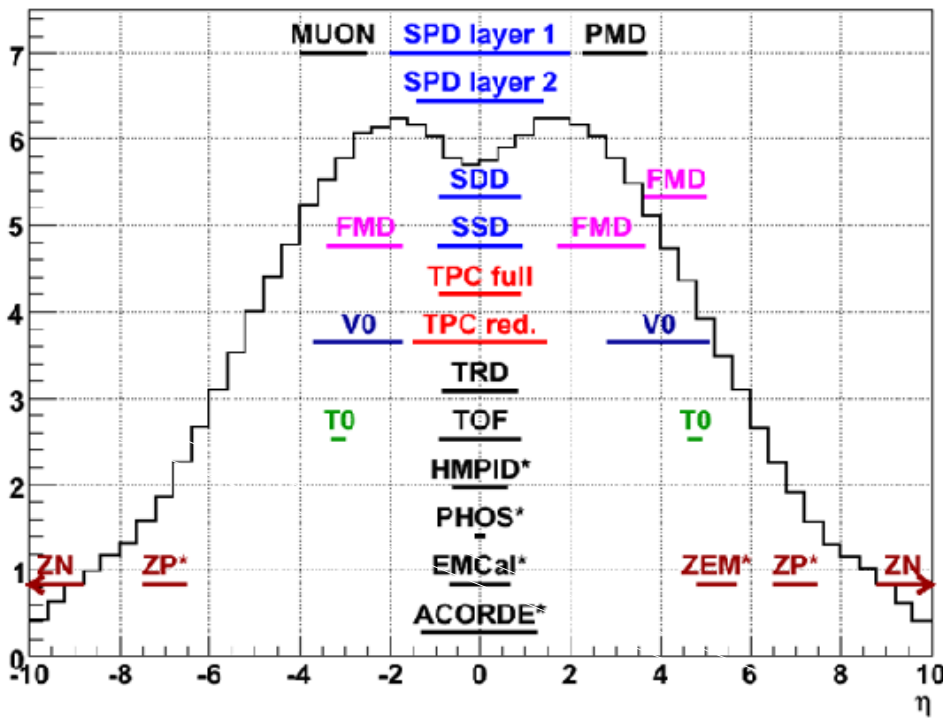


Figure 3.2: The figure shows the rapidity coverage of each individual detector of ALICE. ALICE has an excellent mid-rapidity coverage, whereas forward rapidity measurement is restricted by the limited number of detectors and acceptance [69].

model prediction (soft particles) at such large centre of mass energy. Expectedly, ALICE puts shades in characterising the partonic medium formed in collision in terms of finding the **Thermal Radiation** (estimation of initial temperature [70]), **HBT correlation**(system size and life time [71]), **Low- $p_T$  Hadron production** (to probe hydrodynamical/Thermal properties of the system), **measurement of initial anisotropy**, **p-QCD predictions**(partonic energy loss, suppression of charmed quarks, characterisation of heavy flavour particles) and **anti-matter and Hypernuclei search** etc. But recently, there has been path-breaking results from ALICE in proton-proton collisions. Multiplicity dependent proton-proton collision indicates the formation of heavy-ion like partonic medium for high multiplicity event classes [72] which draws pp collisions to be reviewed more rigorously than just simple hard scattering among partons at LHC energies. The far-ranging physics objectives for strongly interacting matter can thus be explored with ALICE experiment because of its state of art detector technologies adopted for the different sub-detectors.

### 3.4 Central detectors

As has been discussed, any experiment, in high energy physics, is composed of onion-like multi-layered detection system around the collision (vertex) point. As illustrated by the figure 3.2, ALICE has excellent coverages in the central region. It consisted of Inner Tracking System (ITS), Time Projection Chamber (TPC), Time of Flight Detector (TOF), Transition Radiation Detector (TRD), ElectroMagnetic CALorimeter (EMCAL), PHOton Spectrometer (PHOS), High Momentum Particle Identification Detector (HMPID) which are placed in a concentric manner with full azimuthal coverages except EMCAL and PHOS.

ITS, consisted of six cylindrical layers of silicon detectors, is located at a distance between 4 cm to 43 cm from the beamline along the radius. It has a rapidity coverage of  $|\eta| < 0.9$ . There are three different silicon detectors, Silicon Pixel Detectors (SPD), Silicon Drift Detectors (SDD) and Silicon Strip Detectors (SSD) for each consecutive two layers respectively. Since it is placed very much next to the interaction point, the particle density can vary from 1 to 50 per  $cm^2$ . It is to measure the track of each individual particle with a special resolution better than 100  $\mu m$ .

TPC, the main tracking detector of the central barrel and is considered as the heart of ALICE experiment, is used for charged-particle momentum measurements, particle identification, vertex determination with good two-track separation efficiency. Like ITS, TPC has also full azimuthal coverages along with pseudo-rapidity  $|\eta| < 0.9$  for tracks with full radial track length and  $|\eta| < 1.5$  for reduced track length. TPC is capable of measuring

a wide range of transverse momentum starting from 0.1 GeV/c to 100 GeV/c with good momentum resolution.

Transition Radiation Detector (TRD), on the other hand, is devoted mainly for electron identification in the central barrel for momentum range above 1 GeV/c. Light and heavy vector-meson resonances and di-lepton both for pp and AA collisions can be studied using TRD along with ITS and TPC. It has very good pion rejection capability of factor 100 for momentum beyond 100 GeV. TRD has a good momentum resolution of 3.5 (4.7)% at 5 GeV/c [73]. An optimised tracking efficiency of 90% has been achieved with the detector granularity of  $6 \text{ cm}^2$ . It has an extent of 2.90 m to 3.68 m along the radius and 7.8 m along the beam (7 m is active region).

The Time-Of-Flight detector, a large area array MRPC gas detector with  $|\eta| < 0.9$  in the central barrel in ALICE, is meant for Particle Identification (PID) in the intermediate momentum range ( $< 2.5 \text{ GeV/c}$  for  $\pi$  and k and up to  $4 \text{ GeV/c}$  for protons). The detector has a polar acceptance of  $|\theta - 90^\circ| < 45^\circ$  and has modular structure distributed over 18 sectors along  $\phi$  and 5 segments along z-direction respectively. The TOF detector unit is made of 10-gap double-stack MRPC strip of 122 cm long and 13 cm width leading to an active area of  $120 \times 7.4 \text{ cm}^2$ .

The PHOS, meant to measure photons from different sources in the central barrel of ALICE, is placed just below interaction point at a distance of 4.60 m from the beam axis. Unlike ITS, TPC and all, PHOS has only limited azimuthal coverage of 100 deg and pseudo-rapidity of between -0.12 and 0.12. The PHOS is made of  $\text{PbWO}_4$  (PWO) (known for the fast signal and good energy resolution) crystals and Avalanche Photon Diodes (APD). There are altogether 17920 channels each of dimension  $22 \times 22 \times 180 \text{ mm}$ .

ElectroMagnetic Calorimeter (EMCal), on the other hand, was designed to explore the details of jet quenching (high-pt physics) over a large kinematic range. The building blocks of EMCal is large Pb-scintillator and has very limited phase space acceptance with 107 deg in azimuth above the TPC and adjacent to HMPID and pseudo-rapidity of  $< 0.7$ . Moreover, EMCal, a sampling type calorimeter with cylindrical geometry, is located at 4.5 m away from the beam line and adjacent to ALICE magnet coil which is approximately opposite in azimuth to PHOS.

### 3.5 Forward detectors

Apart from very rich mid-rapidity measurements, ALICE is also populated with detectors in forward rapidity which can be used to measure muons, photons, centrality and can serve triggers for other detectors. There are few crucial detectors, namely muon spectrometer

(MCH and MTR), forward multiplicity detector (FMD), zero degree calorimeter (ZDC), T0, V0 and photon multiplicity detector (PMD), which are used to measure centrality, multiplicity apart from main forward measurement of muon and photons. Moreover these detectors are used to provide triggers for other detectors.

**Muon spectrometer** - It has a phase space coverage with pseudo-rapidity of  $-4.0 < \eta < -2.5$  and polar angular range of  $171 \rightarrow 178$  deg and extended along the beam direction of  $-5030 \text{ mm} \leq z \leq -900 \text{ mm}$ . The components of muon spectrometer are a passive front absorber (absorb hadrons and photons from the vertex), 10 detectors planes with a high-granularity, a large dipole magnet, a passive muon-filter wall, four planes of trigger chambers, an inner beam shield (to protect from primary and secondary particles at large rapidities). The main focus of the detector is to measure the muons of momentum  $\geq 4 \text{ GeV}/c$ . However, entangled with the mid rapidity, it can probe the  $e^- - \mu$  measurements as well with a reduced rapidity window.

On the other hand, the multiplicity of charged particle in forward rapidity is measured by Forward Multiplicity Detector (FMD), which has the pseudo-rapidity coverage of  $-3.4 < \eta < -1.7$  and  $1.7 < \eta < 5.0$  and placed at both side of the interaction vertex. The most important is the overlap between the FMD and the ITS layers which provides redundancy and cross-checks among sub-detectors and extend the  $\eta$ -coverages for particle distribution as has been shown in figure 3.2. The optimised design of FMD was achieved by compromising the required multiplicity resolution and the cost and complexity of the detector. Comparatively large readout time ( $> 1.2 \mu\text{s}$ ) restrict it to be used as a multiplicity trigger unit and thus provides for offline analysis only. FMD, consisted of three sectors FMD1, FMD2 and FMD3 - among which FMD2 and FMD3 are evenly placed across the IP, is annular in shape which composed of 10 (inner ring - size is constrained by beam pipe) and 20 (outer ring - constrained by the inner wall of TPC) silicon detectors. Inner sensors (radii from 4.2 cm to 17.2 cm) consist of 512 silicon strips, whereas, outer sensors (radii from 15.4 cm to 28.4 cm) are with 256 silicon strips, lead to total 51200 readout channels for full FMD.

The centrality measurement in ALICE for heavy ion collision is provided by zero degree calorimeter (ZDC) placed at 116 m on either side of the Interaction Point. The centrality is estimated by measuring the energy carried in forward direction by the spectator (non-interacting) nucleons of the collision. The centrality information is used as L1 trigger for the whole experiment. Moreover, being position sensitive, ZDC can provide a good estimate for the reaction plane of nuclear collision. ZDC has two distinct detectors, ZP (dim:  $7.04 \text{ cm} * 7.04 \text{ cm} * 100 \text{ cm}$ ) and ZN (dim:  $12 \text{ cm} * 22.4 \text{ cm} * 150 \text{ cm}$ ) for proton and neutron respectively. Spectator protons are made separated from that of the neutron by the magnetic

field. In addition, a small electromagnetic calorimeter with  $4.8 < \eta < 5.7$  in eta (ZEM: (dim: 7 cm\*7 cm\*20.4 cm)) is placed at 7 m away from IP on both sides. Different materials tungsten alloy, brass and lead have been used as absorbers for ZN, ZP, ZEM respectively. Quartz fibre of core diameter 365  $\mu\text{m}$  (ZN), 550  $\mu\text{m}$  (ZP, ZEP) was used to collect the signals. Physics performance of ZDC depends on the resolution of the detectors which are 11.4% and 13 % for Zn and ZP respectively. V0 detector consists of two planes of scintillator counters V0A and V0C respectively, which placed on either side of the ALICE interaction point. The pseudo-rapidity coverages of V0A (at 340 cm) and V0C (at 98 cm) are  $2.8 < \eta < 5.1$  (V0A) and  $-3.7 < \eta < -1.7$  respectively. Both the counters are segmented into 32 individual counters, distributed in four rings and eight sectors of 45 deg. As far as functionality is concerned, first of all, it gives the minimum bias trigger for central barrel detectors for all collision systems like pp, pA and AA. It measures the centrality in terms of multiplicity, recorded in an event.

In complement to V0, another trigger detector, called T0 detector, is also there in ALICE both to generate a start time (T0) for the TOF detector and to set a fixed time delay which is independent of the vertex position with a precision of 50 ps. Moreover, it can provide the vertex position with a precision of  $\pm 1.5$  cm. A wake-up signal to the TRD, prior to L0 is also delivered by T0. Finally, it is also used to generate minimum bias and multiplicity triggers for ALICE.

The detector is a combination of two arrays (T0A and T0C) of Cherenkov counters each having 12 counters. Each Cherenkov counter consisted of a fine-mesh photomultiplier tube (diameter 30 mm and length 45 mm) which are coupled to a quartz radiator off dimension (diameter: 20 mm and thickness 20 mm). Two arrays are placed at 375 cm and -72.7 cm away from the vertex (both side of the IP). The pseudo-rapidity coverages for T0A and T0C are  $4.61 \leq \eta \leq 4.92$  and  $-3.28 \leq \eta \leq -2.97$  respectively. The desired time resolution of T0 detector is about 50  $\mu\text{s}$ .

Apart from above discussed muon spectrometer and different trigger detectors, there is a devoted photon detector, called photon multiplicity detector, which is placed at A side of IP in forward rapidity and adjacent to V0A. The details of PMD will be discussed separately in the next section in view of relevance to the present study.

### 3.6 Photon Multiplicity Detector

The measurement of photons in forward rapidity by ALICE is done with the photon multiplicity detector (PMD), placed opposite to muon spectrometer at a distance of 360 cm away from interaction vertex. The main purpose of PMD is to measure the multiplicity and spatial  $\eta - \phi$  distribution of photons in forward pseudo-rapidity coverage of  $2.3 \leq \eta \leq 3.7$ . The

estimation of transverse electromagnetic energy and the reaction plane can also be performed with the help of PMD on an event-by-event basis. Photon multiplicity gives important physics information regarding limiting fragmentation, QGP phase transition, and the disoriented chiral condensates.

figure 3.4 The PMD consists of two detector (PRE and CPV) planes separated by a three

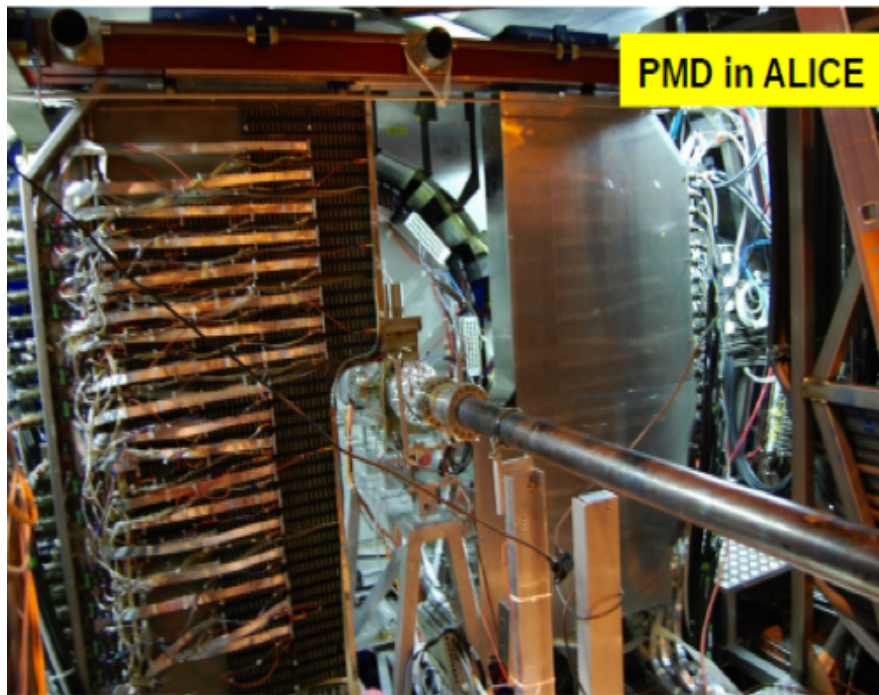


Figure 3.3: The photograph represents the actual PMD, installed at ALICE experiment at a 360 cm away from the interaction point.

radiation ( $\approx 1.5$  cm) length thick lead converter as shown in picture 3.3. Both the detector planes are identical in nature apart from their functionality. The first plane, called charged particle veto plane (CPV), is facing incoming particles directly and is used to discriminate hadrons and electrons from that of photons. On the other hand, the second plane, called pre-shower detector plane, is to detect electromagnetic shower signal (a patch of hit in multiple detectors), produced either by electron or photons, at pre-shower (before shower maximum is achieved) position. To cope with very high particle density, both the detector planes are made up of highly granular hexagonal proportional gas detector of dimension  $0.22$  cm<sup>2</sup> for the area and 0.5 cm for the depth along the beam. The working principle of the detector explained schematically in figure 3.4 As is pointed out, PMD has performed excellently in data taking since the beginning of LHC started giving data. At the end of LHC

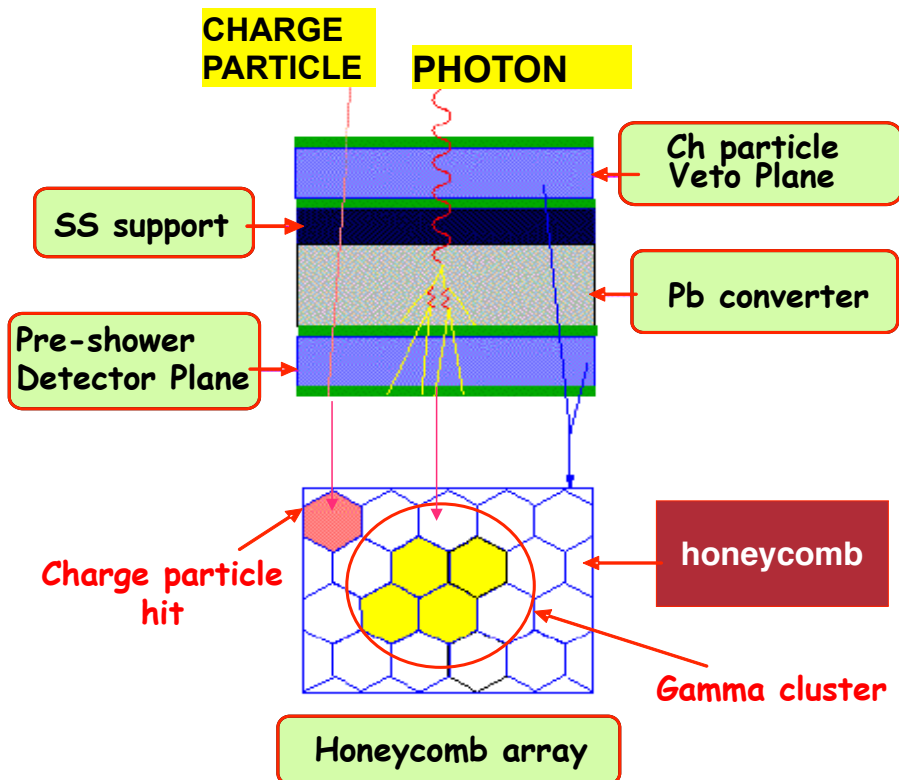


Figure 3.4: The figure shows the schematic representation of the working principle of PMD. It explains how it responds to charged particles and photons.

RUN 2, PMD is will be dismantled. The ALICE forward rapidity region will have a scope to introduce a new detector which can extend the photon measurement in forward rapidity to a full extent (both the energy and momentum). A rather unrevealed domain of small Bjorken- $x$  can be explored if such an extensive photon measurement of different origin can be done which has brought the discussion of a new electromagnetic calorimeter.

### 3.7 Summary

We have discussed the Large Hadron Collider and the ALICE experiment in details. Specifically, we have dicussed the relevance of introducing a forward calorimeter. The fact that ALICE has limited forward measurement capability let the possibility to augment the photon measurements in forward rapidity. It has great physics implications in the domain of low *Bjorken- $x$*  regiem which is expected to be dominated by the gluon dynamics. In the next chapter forward calorimetry in ALICE will be presented.



# Chapter 4

## Forward Physics and Calorimetry in ALICE

### 4.1 Introduction

A Large Ion Collider Experiment (ALICE) at LHC has 17 detectors stacked into an onion structure, following the general scheme of the collider experiment. Ideally, a full- $4\pi$  coverage for an experiment is desired to capture the full snap of the collision. However, because of geometrical constraints, ALICE has almost closed coverage around the interaction point which can be divided into two parts - central barrel and forward region. In a collider experiment, detector acceptance is primarily dominated by the central part (mid-rapidity) with forward (backward) part along the beam direction restricted with limited coverages. ALICE has an excellent mid-rapidity detector coverage which enables measuring different particles for a wide range of incident energies. On the other hand, forward rapidity measurement is limited to mostly muon detection and photon counting. Moreover, as far as the photon detection is concerned, ALICE can measure only for a very limited region in mid-rapidity with EMCAL and PHOS. The measurement of direct photons can contribute to the understanding of initial stages of the primordial matter in a more cleaner way. In this context, the inclusion of a calorimeter to measure photon in forward rapidity, can extend the existing physics reach of ALICE to a new regime of small- $x$ , which is now accessible with LHC energies. Feasibility of a calorimeter at forward rapidity in ALICE experiment has been considered in this thesis work. A general discussion about the importance of calorimetry and the relevance physics aspects in small *Bjorken-x* will be discussed in the subsequent sections.

## 4.2 Physics motivation

A detailed study of QGP, formed in heavy ion collision has been front-line interest with the available ultra-high centre of mass energy available at LHC. ALICE is precisely to enlighten the current understanding and dig deeper in this area [74]. Even with the existing excellent physics capabilities as discussed in chapter-3, ALICE with its present configuration is inadequate to address a number of important issues both in QGP and baseline physics, specifically, in low Bjorken-x domain where gluon dominated dynamics is expected. There are several up-gradation proposals regarding central ( $-1 \leq y \leq +1$ ) detectors at mid-rapidity like Inner Tracking System, Time Projection Chambers etc. But, this up-gradation are meant to elevate measurements with the high rate of interactions planned by LHC during RUN-3. As an important complement to the QGP physics at mid-rapidity, an ardent plan for enhancement in forward-rapidity (muon arm) has also been adopted. Complete interpretation for the matter produced in these collisions taking both in mid and forward rapidities together is quite entangled and complicated as they are causally disconnected throughout most of the evolution of the system. As an obvious effect, the properties of the QGP in the two regions are expected to be significantly different. Though forward measurements with only muons are undoubtedly powerful but have limited scope and are inadequate in framing all the relevant properties of the produced matter at LHC energies. To bridge the gap between an excellent mid-rapidity measurement capability and restricted forward-rapidity measurement, ALICE collaboration has proposed an upgrade to its present detector configurations such that the unravelled area of low-x for parton distribution and their contribution can be better understand.

Partons, responsible degrees of freedom for a de-confined matter, are the relevant participants in collisions for relativistic high energy collision. Understanding of partons inside hadron/nucleus is extremely important for studying particle production and their mechanism (cross-section) which vary with the centre of mass energy of the collision. Parton distribution function (PDF), probability of finding a parton inside hadron/nucleus as a function of longitudinal momentum fraction "x" ( $x = \frac{p_L^{parton}}{p_L^{hadron}}$ ), behave differently for different type of partons (up, down, strange, charm, bottom, top and gluon). There are several effort in formulating the parton distribution function [29–35], taking input from existing experiment. Figure 4.1 shows parton distributions for up, down, strange and gluons, as formulated by CTEQ-collaboration. Quarks contribute more at large-x with a maximum value around 1/3 of the parent hadron. However, with the decrease in x and thus with the increase of centre

of mass energy ( $x = \frac{2P_T}{\sqrt{S}} e^{\pm y}$ :  $\sqrt{S}$  and  $y$  are centre of mass energy and rapidity), the quark contribution decreases and gluons starts dominating with an increasing trend.

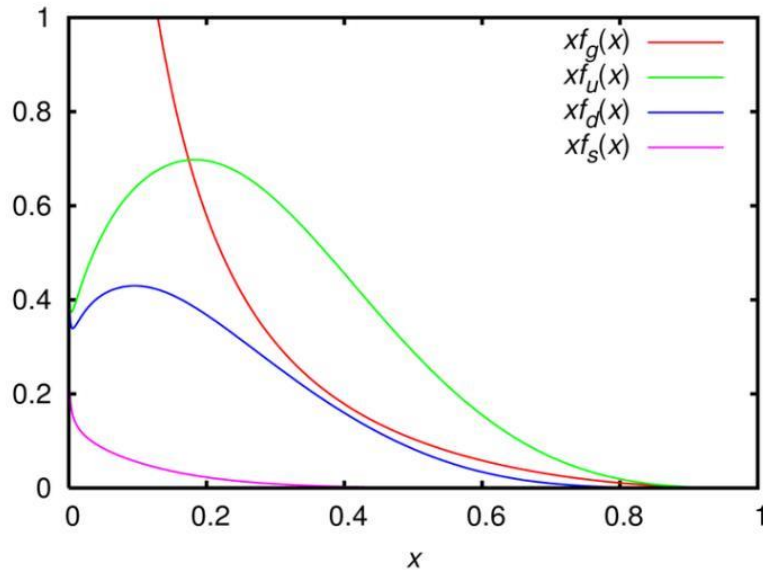


Figure 4.1: PDFs inside a hadron as a function of longitudinal momentum fraction ( $x = \frac{Q^2}{2p \cdot q}$  with  $Q^2 = -q^2 = 10 \text{ GeV}$  for the struck parton from CTEQ6 collaboration. (Red : Gluon, Green : Up quark, Blue : Down quark, Pink : Strange quark). A continuous rise in gluon distribution function is of prime interest in the Bjorken- $x$  sector which might lead to gluon-saturation phenomenon [40–45].

Theoretically, the evolution of parton distribution as a function of  $x$  and  $Q^2$ , can be described by perturbative quantum chromodynamics with DGLAP [36–39] and BFKL [75–77] equation which is established with experimental supports. This QCD evolution leads to a strong rise in the parton-density distributions, particularly for the gluons at very small- $x$  and has been argued to lead to unitarity violation. The evolution equations, however, are linear in contrary and should not be applicable to high gluon density. Non-linear evolution equations, like JIMWLK [78–84] and the BK equations, have been adopted for the understanding gluon-rich dense regime which might result in saturation phenomenon. There are plenty of theoretical predictions against gluon saturation and a number of phenomenon in hadron production which are consistent with saturation models as explained in [40–46]. Moreover, though Parton Distribution functions (PDF) [29–35] in protons are well established both experimentally and theoretically for intermediate Bjorken- $x$ , they need more attention in small Bjorken- $x$  limit to probe the gluon rich domain.

The universality of factorisation for **the parton distribution functions (PDFs)** can be used in any calculation involving parton-parton scattering which might have been obtained from an independent particular measurement. Scaling of the PDFs, as has been predicted by different parton model and established by experiments, predicts that the dependence is only on the longitudinal momentum fraction of the struck parton ( $x = \frac{Q^2}{2p \cdot q}$  with  $Q^2 = -q^2 =$  momentum transfer). Experiments, like deep inelastic scattering [85, 86], have contributed a lot in obtaining parametrisation of the PDFs for hadron which has been applied successfully in explaining results from different experiments. However, because of limited kinematic coverage, no single experiment can explore the complete range of PDFs and thus leaves unconstrained regions of the  $(x - Q^2)$  phase space. A wide set of experiments starting from HERA, SPS, RHIC to LHC has contributed substantially in understanding PDFs, specifically in digging gluon contribution in *small-x* part. As of today, at the highest LHC beam energies, partons distribution reach to a regime with small-x of the order of  $10^{-4}$  to  $10^{-5}$  at the mid rapidity region and which can be extended to as low as  $10^{-6}$  considering the forward rapidity into account. As discussed, the regime of small-x is effectively dominated by gluons which evolve linearly and increases dramatically for  $x \rightarrow 0$ . However, to respect the unitarity, it can not increase infinitely and as a result, nonlinear processes like gluon recombination will start growing which can be described by JIMWLK equation [78–84]. This non-linear effect will make the PDF for gluon to grow until it balances gluon splitting and achieves a dynamic equilibrium value, known as gluon saturation with a characteristic scale ( $Q_s$ ), defined as  $Q_s^2 \approx \frac{xG_A(x, Q^2)}{\pi R_A^2} \propto A^{\frac{1}{3}} x^{-\lambda}$  with A is nuclear mass number and  $\lambda$  to be 0.3. There are many non-perturbative QCD based model calculation which takes the gluon saturation effect into account for particle production in relativistic heavy ion collision. **Colour-Glass Condensate (CGC)** [40], is one among most discussed models in describing particle production incorporating gluon saturation phenomenon.

To search for competent and experimentally measurable observables, which contain the information about gluon distribution at small-x, electromagnetic probes (e.g. photons) are found more convenient in reducing the uncertainties compare to hadronic counterpart. The dominant leading order partonic scattering processes as shown in figure 4.3, such as quark-gluon Compton scattering, quark-anti-quark annihilation, contribute most at the large-x region where the photon is coming out directly from the parton interaction vertex without fragmentation. On the other hand, there are next-to-leading order contributions for photons, produced in quark bremsstrahlung or by fragmentation of out-going partons 4.3. However, The later contributions are involved with "parton-to-photon" fragmentation distributions  $D_{\gamma k}(z)$  which are partly known from existing measurements. At LHC energies, the contribution of prompt

photons is dominated by next-to-leading order processes involving fragmentation which complicate the reconstruction of participant partons. Since the prompt photons from fragmentation will lie within the jet of hadron, they can be suppressed substantially by proper isolation cuts, as shown in figure 4.2 to disentangle the photons from quark-gluon Compton scattering which might contain more prominent gluon PDF information. So in brief, measurement of

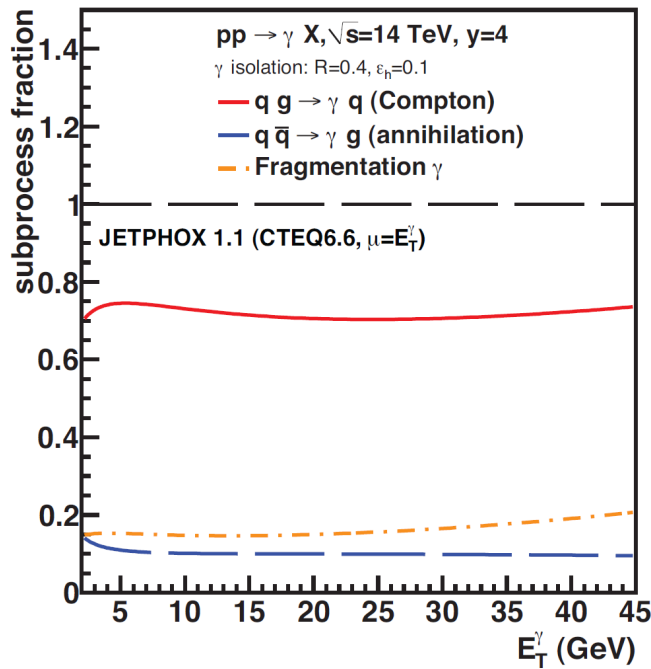


Figure 4.2: Contribution of prompt photons from different partonic scattering processes. Leading order isolated photons from quark-gluon Compton Scattering, and quark-antiquark annihilation process can be isolated with proper selection criterion from that next to leading order contributions like bremsstrahlung and fragmentation. The figure, indeed, show such an estimation by JETPHOX for prompt photon production applying isolation cuts [87].

prompt photons with proper selection criterion on the production process can serve as the potential clean candidate for the small- $x$  effect of parton distribution. Apart from prompt photon measurements, there are a number of other observables which can shade light in understanding the physics of large gluon density regime. Parton induced Jet, e.g., as one of the established and important probe, in either pp or pA or AA collisions which can provide a good amount of details of large gluon distribution as there is a number of direct contributions to jet from processes like  $gg \rightarrow gg \rightarrow Jet$ ,  $qg \rightarrow qg \rightarrow Jet$ . Hadron production at forward rapidity in terms of nuclear modification factor  $R_{AA}$  has been measured which should be unity for an incoherent superposition of a given number of nucleon-nucleon collisions and otherwise get modified. So, though there are uncertainties, still light hadron production in

forward direction can also contribute to understanding the medium produced and thus the relevant PDFs.

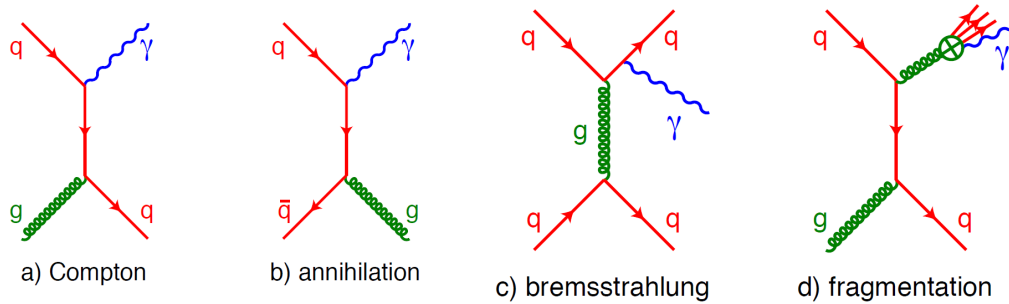


Figure 4.3: Feynman diagrams for different QCD processes responsible for prompt photon production. Leading order isolated photons (electromagnetic probe) are mostly produced from a) quark-gluon Compton Scattering, and b) quark-antiquark annihilation process. On the other hand, non-isolated photons from next-to-leading order processes like c) bremsstrahlung from a quark, and d) emission during the gluon fragmentation [87] are involved parton-to-hadron fragmentation processes [87].

However, with existing experimental facilities, it is impossible to probe the desired *bjorken-x* to such a regime where gluon saturation effects contribute significantly which in turn results in the lack of a smoking gun observables. This, indeed, brings the opportunity to measure observables (photons) at forward rapidity in ALICE experiment at LHC, which can navigate to probe small-*x* domain in a most effective experimental way which might lead to the study of gluon saturation and its effects on particle productions. Hence a proposal for the addition of a **F**ORWARD **C**ALorimeter to the ALICE experiment is very much timely and subjective which will enhance the ALICE capability in many ways like

- perform unique measurements for prompt isolated photons to prove or refute the existence of gluon saturation.
- complement the forward QGP measurements of the Muon Spectrometer with other important probes of the QGP, in particular via studies of jet quenching, and
- constraint underlying physics mechanisms of new features recently observed in p-Pb and high multiplicity pp collisions, like the so-called ridge.

Moreover, the possibility of accessing more forward rapidity in ALICE experiment, make  $P_T$  measurement more flexible in the higher side without compromising the desired Bjorken-*x* regime, which assertion the application of pQCD calculations. Important to mention, that with different experiments and measurements available presently, the regions in  $x - Q^2$  plane which can be probed both for photons and hadron are shown in figure 4.4. The left

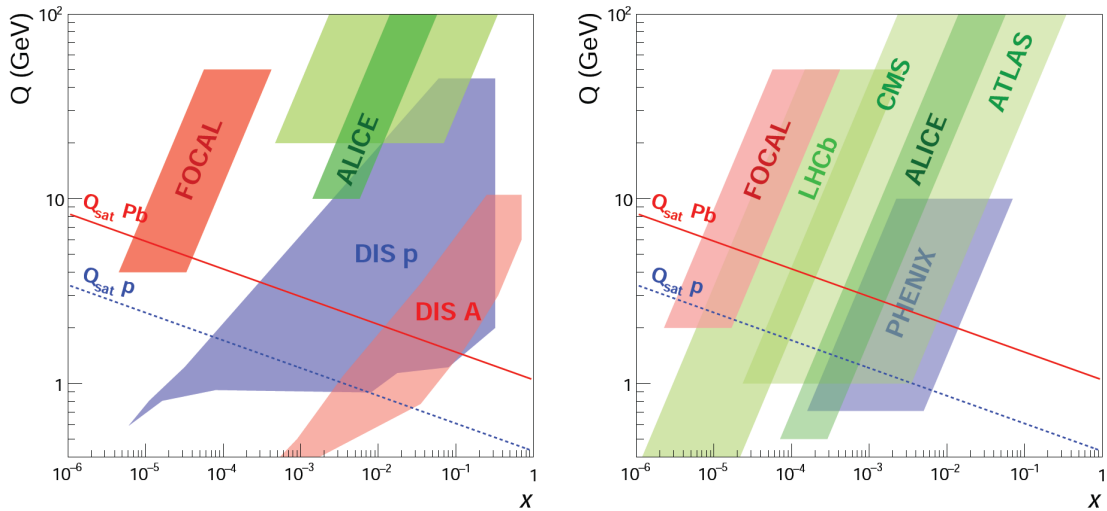


Figure 4.4: Sensitive regions as function of  $x$  and  $Q^2$  for different existing experiments with detectors for hardonic measurements. The expected saturation scale ( $Q_s$ ) is indicated in the figure. Specific acceptance in this schematic diagram, covered by FOCAL, is also shown [87].

panel shows coverages achieved by DIS measurements and the photon measurements by different experiments at LHC. The extent of the region in terms of photons measurement with the inclusion of FOCAL is also shown which surely extend smaller- $x$  part compare to the existing measurements. On the other hand, hadron measurements from RHIC and LHC in terms of  $x - Q^2$ -reach are also presented where LHCb has coverage competing the FOCAL. Though not exact, this calculation can be taken as a first approximation of the actual regions, specifically for hadron production, which get affected by fragmentation. Whatsoever, the introduction of FOCAL might aid neutral pion ( $\pi^0$ ) measurement and the effect of the medium on the spectra which will help in understanding the hot and dense strongly interacting matter away from the mid-rapidity, complementing existing results from ALICE. None the less, there are some more recent discoveries like Cold Nuclear Matter effects [47, 88–95], ridge structure ( $\Delta\phi - \Delta\eta$  correlation) in pp and pA collision [96–101], effect of colour reconnection [102–104], possibilities of medium formation in smaller system etc could be better understood in terms of photons and  $\pi^0$  production at forward rapidity at LHC energies.

### 4.3 Calorimetry in high energy physics

Calorimetry, a unique science to measure Heat (Energy in the wider sense), delivers remarkable answers in detecting and characterising particles of different nature (mass, charge, structure) right from low energy to today's ultra-relativistic high energy limit [105]. Growing complexities with an increase in available energy of physical processes, in counting and measuring particles evolve the calorimetric techniques to a state of art height. Historically, detection of charged particles started with early days hodoscope (Started by Thomas H. Johnson and E.C.Stevensonrefback in 1933), and passed through the ages of cloud chambers, emulsion tracks, bubble and streamer chambers and to more sophisticated techniques like magnetic spectrometers. Besides these conventional "non-destructive" methods of measurement, partial/total absorption techniques like calorimetry were also developed in parallel to ease-handling high multiplicity environment with greater precession. Conceptually, a calorimeter is a block(s) of materials (active and passive) with optimised dimension to absorb total energy of the incident particles and its secondaries, produced due to interaction with the calorimeter block. Only a small fraction (depending on active and passive block combination) of the absorbed energy is convertible into a detectable signal to investigate the kinematic state (mass, energy and direction) of particles. In high energy experiments, linearity between the calorimeter signals (generated by ionisation charge, scintillation/Cherenkov light, etc) and the incident kinematic state of the incoming particle, need to hold over the desired range of measurement. The first large scale calorimeter was used in cosmic ray experiment [106](Murzin, 1967) and was followed with fast improvements to fulfil the requirements of complex experiments in CERN-ISR, FNAL, CERN-SPS in the 1960's and 1970's. Unlike the conventional non-destructive methods, a calorimeter has features like

1. **Capability** of measuring both charged and neutral particles.
2. **Dimension** of the calorimeter is comparatively an order of magnitude less ( $\approx \log E$ ) compare to a spectrometer which makes it compact.
3. **Insensitivity to magnetic field** by choosing proper active medium.
4. **Four-momentum** ( $P_x, P_y, P_z, E$ ) measurement with desired precession is possible.
5. **Particle identification** can be done for some selected particle like hadron, electron, muon, neutrino by analysing the shower.
5. **Proper segmentation** with high granularity make it usable in high multiplicity environments.
5. **Low Response time** ( $\approx$  or  $\leq$  100 ns) make it fast and compatible with high event rates.
5. **Energy Resolution** ( $\frac{\sigma}{E}$ ) improves with increase in "E".

Depending on the nature and type of interaction of particles, to be measured, calorimeters can be classified into two broad categories

**(i). Electromagnetic and (ii). Hadronic.**

Mostly for detection of photons and electrons, the electromagnetic calorimeter is un-paralally used, whereas, for high energy hadron (capable of producing new particle through strong interactions within the limit of the calorimeter depth) hadron calorimeter needs to be adopted. The dimension of the hadronic calorimeter is, however, larger by an order defined by the ratio of the Interaction length to Radiation length ( $\frac{\lambda_I}{X_R}$ ). Electromagnetic calorimeters are widely known to the high energy experimental community for precession measurement of photons and leptons.

Moreover depending on the design and technology adopted, calorimeters can be categorised into two types namely

**(a) Homogeneous. and (b) Heterogeneous/Sampling type.**

The same material is used both as a detector as well as the absorber in case of Homogeneous calorimeter. A medium like NaI, BGO,  $PbWO_4$ , Glass etc. are used in this type of calorimeter. On the other hand, sampling electromagnetic calorimeters, having segmentation either or both in the transverse and longitudinal direction, comprising of alternating layers of high-density absorber layer and detector layer. Depending on the experimental constraints and requirements, a choice for the detector medium among possible Gaseous, Liquid, Solid option can be adopted. Segmented sampling calorimeters with alternate passive and active mediums have great advantages as can be optimised for suitable energy and position resolutions [105, 107–121]. In the present era of large-scale experiments like Large Hadron Collider (LHC), Relativistic Heavy Ion Collider (RHIC), Japan Proton Accelerator Research Complex (J-PARC), Anti-proton and Ion Research (FAIR) etc., the necessity for precision measurements of emitted particles and thus underlying physics understanding got manifold. As the collision energy and beam luminosity increases at a steady pace, experimental techniques including calorimetry are also getting upgraded continuously to cope up with the emerging demand.

## 4.4 Summary

A Sampling type electromagnetic calorimeter, using silicon as detector and tungsten as converters/absorbers, has been considered as a feasible solution for photon (direct/decay) measurement in ALICE experiment. A general overview of the calorimetry has been discussed in brief. The physics motivation of probing small-x regime of parton distribution functions and their consequences on particle productions was reviewed in the context of measurement in ALICE experiment. The new regime of unexplored small-x physics motivated to study for a calorimeter in forward rapidity which potentially extends the physics reach of

ALICE experiment along with present set-up. The details of configurations and calorimetric performances will be discussed in the next chapter.

# Chapter 5

## FOCAL: Design and Simulation

### 5.1 Introduction and pre-requisites

Pre-requisites to start for the design of a calorimeter need careful observations with desired physics goals and practical limitations optimised with position and acceptance, materials with proper choice, cost estimation and etc. For the present thesis work, the calorimeter was designed, keeping in mind its usability at forward rapidity in the ALICE experiment at CERN. Presently ALICE has an excellent mid-rapidity coverage ( $-1.0 \leq \eta \leq 1.0$ ), as illustrated in table 3.2, with variety of state-of-art detectors which have contributed in exploring physics problems. However limited detector acceptance in the forward rapidity regions inspired to investigate the feasibility of introducing a new electromagnetic calorimeter which will extend physics reach at *small*  $x$ . Forward Electromagnetic Calorimeter (FOCAL) has been found to be a timely and complementary candidate in forward rapidity ( $2.5 \leq \eta \leq 4.5$ ) of ALICE experiment which can extend the search for Gluon saturation, parton energy loss and many more in terms of photon measurement. According to the present proposal, FOCAL was expected to be placed (considered 3.5 m in the beginning) at 7 m along z-direction from the primary vertex among available possible position with pseudo-rapidity coverages as is illustrated in table 5.1 along with a comparison to other existing experiments at LHC.

Table 5.1: Pseudo-rapidity coverage for the proposed FOCAL with a comparison with existing experiments at the LHC.

|                  | ALICE FoCal@3.5 m | ALICE FoCal@7 m | ATLAS Inner Wheel | CMS EndCap | LHCb ECAL |
|------------------|-------------------|-----------------|-------------------|------------|-----------|
| $\eta$ -coverage | 2.5→4.5           | 3.5→5.1         | 2.5→3.2           | 1.5→3.0    | 1.8→4.3   |

In the beginning, FOCAL was considered at 3.5 m position and proposed to replace the existing photon multiplicity detector (PMD) at forward rapidity in ALICE. However, 7 m

distance evolved as a more suitable position for FOCAL along with the pseudo-rapidity coverage extended in forward direction by 1 unit. However, A detailed study for the geometry optimisation for FOCAL has been carried out using GEANT4 [122, 123] simulation package for a position at 3.5 m away from the primary vertex within the scope of the present thesis work. As obvious, the design and simulation were started with essential design requirements as primary guidelines which are discussed below.

**Rapidity coverage -** The rapidity of the calorimeter, as estimated for the desired *bjorken-x* limit, was intended as  $2.5 \leq \eta \leq 5.5$  which essentially defines its transverse dimension within the detector acceptance. To achieve the desired  $\eta$ -range, the calorimeter must have full azimuthal coverage with inner ( $r_{in}$ ) and outer ( $r_{out}$ ) radii 6 cm and 60 cm respectively. The outer radius is defined by the lower limit of the  $\eta$ -range, whereas, the inner radius is restricted by the radius of the beam pipe of LHC. But for the sake of convenience, the design adopted was square shape instead of circular, which can always be transferred to a circular shape just by making corner part of detector inactive in the transverse direction.

**Depth of the calorimeter -** The length of the calorimeter along beamline should be optimised, guided by full energy deposition for the incident energy range of incoming particles. As the observables will be high energy photons (up to 200 GeV), coming from relativistic heavy ion collision at LHC energies, the calorimeter should be capable of containing photon (electron) energy deposition with ideally no loss along the depth. High energy photons or electrons propagate through the calorimeter in the form of electromagnetic shower [124] which has been calculated to be contained in an extent of 25 radiation-length thick material block. The radiation length  $X_R$ , a material independent way of expressing the length for particle interaction, and can be expressed according to the equation 5.1.

$$X_R \approx \frac{A * 716.4}{Z(Z+1) \ln \left( \frac{287}{\sqrt{Z}} \right)} (gm - cm^{-2}) \approx \frac{180 * A}{Z^2} (gm - cm^{-2}). \quad (5.1)$$

Where A is the atomic number of the material. However, the thickness in an absolute unit can vary depending upon the properties of atomic weight and density ( $Z, \rho$ ) of the materials.

The depth (L) of the calorimeter can be quantified, using electromagnetic shower propagation model [64], as a function of the energy of an incoming particle and the material of the calorimeter according to 5.2

$$L(95\%) = t_{max} + 0.08 + 9.6 * X_R, \quad (5.2)$$

with shower maximum

$$t_{max} = 3.9 + \ln(E) \quad ,$$

where  $t_{max}$  is number of radiation length where the electromagnetic shower reaches its maximum value and E is the incident particle energy in GeV.

As discussed, it is extremely important to ensure full energy containment as much as possible to minimise longitudinal leakage which, otherwise, might affect the energy measurement more seriously than other factors like lateral leakage, noise and etc. So for deciding the depth of the calorimeter, the equation 5.2 provides a crucial input, which explains the depth in which 95% of deposited energy will be contained.

**Choice of detector** - The most important part, however, is the choice of active material (detecting medium) for the calorimeter. Primarily, the choice of the detector should not dilute the effective density ( $\rho_{eff}$ ) of the calorimeter which will otherwise diffuse the transverse shower profile. It guides to choose a relatively high-Z detecting medium among available options for detectors like gas, liquid, Scintillator, semiconductor (Si, Ge, Diamond) etc. Moreover, it must be able to provide the desired energy and position resolution. Acceptance of a particular detector should have both established technological availabilities and associated electronics. So, choosing a proper detector medium is a wise and sensitive decision, which balances the physics, technological requirements and cost estimation.

There are two broad class of calorimeter, commonly used in high energy particle physics, namely **Homogeneous and Sampling** respectively. Inhomogeneous calorimeter, a single block of material, made either with scintillating crystal or  $PbWO_4$  or noble gas, liquids fetched with photo-multiplier or avalanche photo-diode or silicon photo diode [125] read-out. The same material block, in case of the homogeneous calorimeter, is used both to produce EM-shower and absorb the energy from the incident photon. A part of deposited energy is converted into a detectable signal (light converted into electrical pulse) afterwards. As a matter of fact, the whole block will serve the purpose of both passive and active medium for the calorimeter simultaneously. Excellent energy resolution is one of the main advantages for homogeneous calorimeter, whereas, disadvantages like "lack of direct longitudinal shower information", "highly expensive Crystals", "non-linearity for hadrons measurement" etc. restrict its use in large scale experiments.

On the other hand, Sampling type electromagnetic calorimeter has its own advantages and disadvantages as well. Here absorbers/converters and the sensors (active mediums) can be chosen with wider freedom with respect to dimension, volume, density, compactness etc. In the scope of the present study, Tungsten, a material with high-Z and high-density, has been chosen as absorber/converter, whereas, silicon sensors was adopted as the detecting (active) medium for the calorimeter. There are plenty of advantages using silicon as the detector which are listed below

**Large  $\Delta E$ :**- Being comparatively high-Z detecting medium, large energy is deposited within very thin detector depth.

**Small diffusion effect:**- Helps in achieving better position resolution  $\approx 10 \mu\text{m}$  in comparison to other gas or liquid detecting medium.

**Small  $I_p$  for  $e^-$ -h pair production:**- Only few eV ( $\approx 3 \text{ eV}$ ), in comparison to gas ( $\approx 25$ - $30 \text{ eV}$ ) or scintillators ( $\approx (4 \rightarrow 10) \times 10^2 \text{ eV}$ ) to produce electron-hole pairs, make it convenient even though there is no internal amplification.

**Insentiveness to magnetic field** make silicon detector smooth working in complex experiments with large magnetics filed like ALICE at LHC.

**Segmentation** to a small scale is technologically available which is required in high-particle-density environment.

**Silicon detectors can be operated at room temperature** with reasonably good signal-to-noise ratio, unlike germanium (Ge) detectors.

**Synergies with electronics industry** make it availability easier compare to other semiconductor detectors like Ge or diamond.

**Detector Granularity** - The calorimeter under consideration will measure high energy photon of any type irrespective of their source (Direct, Decay or Thermal). In relativistic heavy ion collisions at LHC energies, most of the photons are expected to be decayed photons (coming mainly from  $\pi^0$ ) which has its own physics importance. Apart from these decayed photons, prompt photons contribute substantially which need to be detected as precisely as possible. It will carry novel physics information folded in it specifically for the low-x regime. In this context, discrimination of direct photons from that of decayed photons should be precisely measured. The calorimeter must be efficient to reconstruct  $\pi^0$  from it's two decayed photons ( $\pi^0 \rightarrow \gamma + \gamma$ ) over the desired energy range. Analytically it can be shown that the separation between two decayed photons decreases with an increase in energy of the incident  $\pi^0$  and can be represented in terms of opening angle and energies of delayed photons as is shown in equation 5.3.

$$\begin{aligned} \sin^2\left(\frac{\Theta}{2}\right) &= \frac{m_\pi^2}{4E_{\gamma 1}E_{\gamma 2}} \quad \text{with,} \\ \sin\left(\frac{\Theta_{min}}{2}\right) &= \frac{m_\pi}{E_\pi} = \frac{1}{\gamma} \quad , \end{aligned} \quad (5.3)$$

However, the distance between two photons depend on the distance of the detector from the interaction point as well and can be expressed by equation 5.4

$$d_{\gamma_1\gamma_2} = D * \Theta, \quad (5.4)$$

where D is the distance where the decayed photons are measured. The expression is for  $\pi^0$  decayed into two-photons with  $\Theta$  as the opening angle and  $E_{\gamma 1}$  and  $E_{\gamma 2}$  are energies of the photons respectively. The two photon separation is represented pictorially in figure 5.2 which illustrates the average distance between two photons at 350 cm away from the interaction point (IP), which shows the minimum separation between two photons for highest energy (200 GeV)  $\pi^0$  is  $\approx 3$  mm ( $\Theta_{\gamma\gamma} \times$  Distance from IP) using equation 5.4. So a simplistic guess about the transverse segmentation for the calorimeter for detecting each and every single photon, irrespective of how close they are, should be  $\approx 3$  mm or less than that.

The segmentation (granularity) of detectors are indispensable for the proposed calorimeter as it aimed for forward rapidity region of ALICE experiment, which expects a large number of incoming particles (0.2 for PbPb, 0.04 for Pb-p, 0.02 for pPb and 0.01 per  $cm^2$ ) even for the proton-proton collision at top LHC energy. The particle density for photons, expected at proposed calorimeter coverage, has been estimated using HIJING event generator [126] for p-p, p-Pb, Pb-p and Pb-Pb collisions at 14, 8, 8 and 5.5 TeV centre of mass energies respectively and shown in figure 5.1.

The figure 5.1 illustrates how the particle density decreases with the distance from the beam line. The plot shows the number of particles, passing through the FOCAL coverages, for p-p collision is order of magnitude less compared to Pb-Pb collision. However, since the physics objectives include both the Pb-Pb and p-p collision, inputs were considered from Pb-Pb particle density estimation for the distances (radius for calorimeter) considered for FOCAL during designing. Moreover, the pseudo-rapidity ( $\eta$ ) distribution, as is measured as one of the primary observables in a HEP experiment, is reconstructed for photons only from simulated data using HIJING, as shown in figure 5.3. The distribution is characterised with two distinct zones, mid-rapidity with plateau region and forward-rapidity with falling trend respectively. The profiles show symmetric nature for Pb-Pb and p-p collision, whereas, it

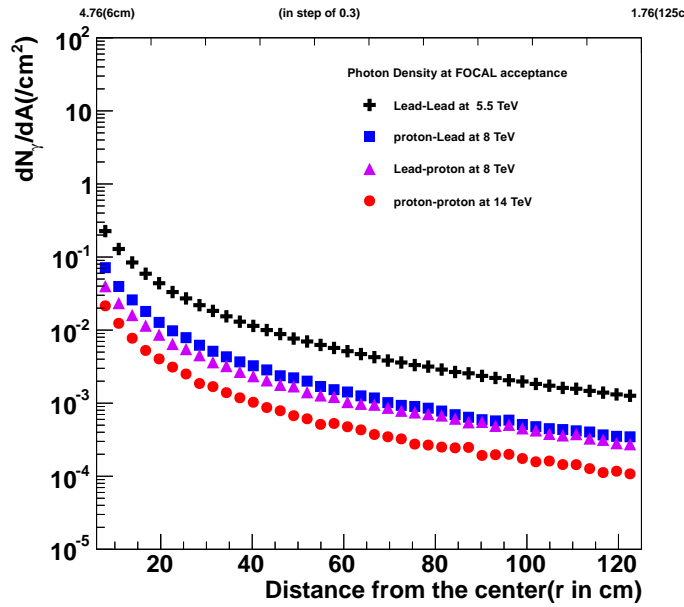


Figure 5.1: Density of Photons ( $/cm^2$ ) in proton-proton, proton-Lead, Lead-proton and minimum bias Lead-Lead collisions at LHC energies.

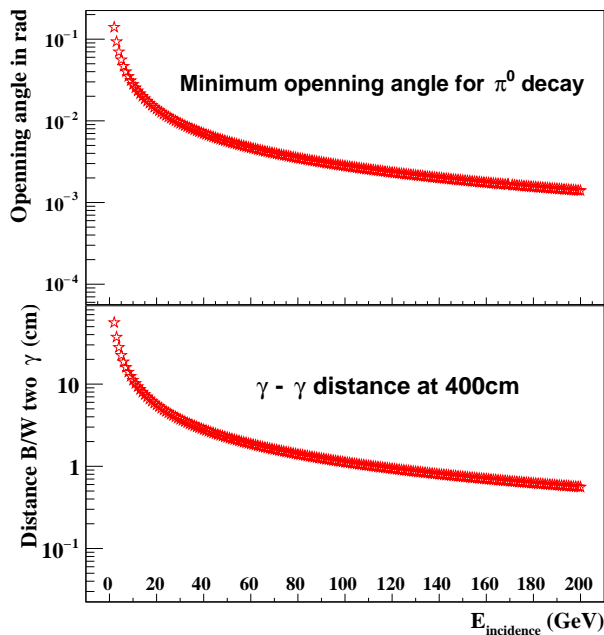


Figure 5.2: Opening angle of two  $\gamma$ 's coming from symmetric decay of  $\pi^0$ , which help in deciding the design parameter like granularity of the detector to start with.

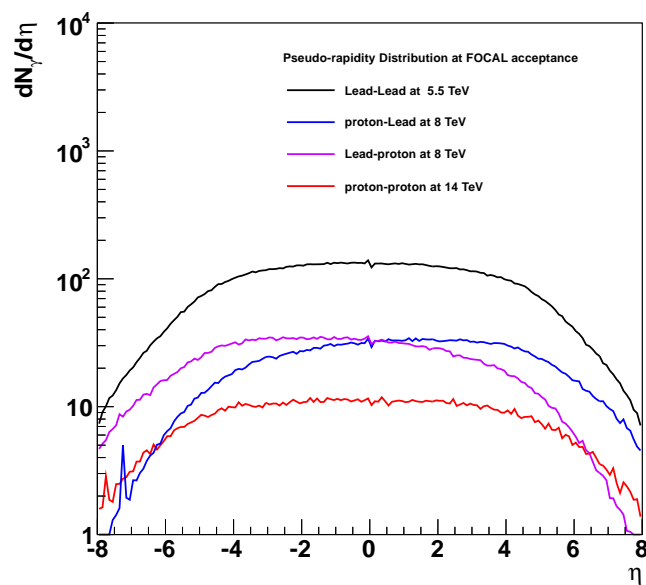


Figure 5.3: Pseudo-Rapidity Distribution for photons produced in proton-proton, proton-Lead, Lead-proton and minimum bias Lead-Lead collisions at LHC energies using standalone HIJING event generator. It helps in estimating expected particle density for particular  $\eta$ -acceptance.

becomes smeared oppositely for the asymmetric collision of p-Pb and Pb-p systems. However, the density of particle, as detected by the calorimeter at a particular depth, will vary according to the incident energy of the incoming photons due to electromagnetic shower formation which will be combined reflected at final particle density as seen by the different layers of the calorimeter. Since the detection of incoming photons will be done by reconstructing the EM-shower (hits patch at layers), every particle (incoming individual photons and its shower particles) need to be detected which ideally require finer granularity compare to as estimated from the opening angle of  $\pi^0$ -decay as shown in figure- 5.2. It has been found that detector of granularity  $1 \text{ mm}^2$  can satisfactorily reconstruct the shower, however, making all the layers with such high granularity is both cost and technically not possible because of huge number of detector channels. An optimisation with two types of detector granularities, High granular layer (HGL) and Low granular layer (LGL: $1 \text{ cm}^2$ ) respectively, could be an acceptable solution.

**absorber/converter** - For each individual detection of photons, the EM-shower should be compact and the transverse spread should be limited within a very small transverse extent. This can be possible with a material of very high-Z as well as of high density simultaneously. In this respect, there could be a different choice among Iron, Lead, Tungsten, Uranium and etc. for the absorber medium of the calorimeter. Important to note, though Lead has high-Z ( $Z_{Pb} = 82$ ) as compared to Tungsten ( $Z_W = 74$ ) because of higher density for Tungsten it is more preferable in very high multiplicity density environments where many simultaneous incidents of EM-shower will be expected. Uranium ( $Z_U = 92$ ), on the other hand, could have been the best for this purpose but because of its radioactive nature, it will bring a higher degree of complexities in the experiment. For better clarity of choosing proper absorbing material, a comparison among relevant candidates for absorber is shown in the following table 5.2.

Table 5.2: Comparative properties for optimized absorber/converter of a calorimeter.

| Material(Z) | Density( $\text{g/cm}^3$ ) | $X_R$ (cm) | $R_M$ (cm) | $\lambda_I$ (cm) | $(\frac{dE}{dx})_{mip}$ (Mev/cm) |
|-------------|----------------------------|------------|------------|------------------|----------------------------------|
| Fe(26)      | 7.774                      | 1.757      | 1.719      | 16.77            | 11                               |
| Cu(29)      | 8.92                       | 1.436      | 1.568      | 18.79            | 13                               |
| Pb(82)      | 11.34                      | 0.56       | 1.60       | 17.59            | 13                               |
| W(74)       | 19.25                      | 0.35       | 0.93       | 9.946            | 22                               |
| U(92)       | 19.05                      | 0.31       | 1.009      | 11.03            | 21                               |

As is illustrated, tungsten could be considered as a natural choice because of high  $Z$  and density, compact structure, availability with desired purity and reasonable price. However, the most important property is its smaller Moliere radius, shown in equation 5.5 (0.93 cm for tungsten), which restrict the transverse-shower spread and thus help in disentangling closely spaced hits patch, formed by EM-showers. Having all these pre-requisites, the physics of calorimeter will be discussed in brief in the next section to understand the calorimeter performances.

$$R_M \approx \frac{21X_R \text{ MeV}}{E_C}, \quad (5.5)$$

where  $E_C|_{\text{SolidorLiquid}} = \frac{610\text{MeV}}{Z+1.24}$ ,  $E_C|_{\text{Gas}} = \frac{710\text{MeV}}{Z+0.92}$  is the critical energy of the particle where it stops producing any further secondary particle and starts losing energy through collisional processes only. Physically, Moliere radius signifies that lateral extent of the shower which contains 90% of the shower energy.

## 5.2 Geometry optimisation

Here we will focus on deciding the design specification of the proposed FOCAL, **Sampling type electromagnetic calorimeter**, which has energy degradation with the depth (layers) along the direction of EM-shower propagation. Considering the above design issues, regarding every individual component, the calorimeter has been opted with silicon sensors as an active medium and high purity (99.9%) tungsten plate as absorber/converter. GEANT4 tool-kit [122, 123], meant for geometry simulation and tracking inside the detector, was used to study the effect of detector geometry and performances. The primary objective of the geometry simulation was to search for an optimised design with adequate energy and position resolutions which can handle extreme high particle density environment as represented by figure 5.1 and is expected in ALICE experiment. Since the energy deposition is measured by accumulating all the deposited energy samples, collected from each and every active segments and layer. It has been found that only a very little fraction ( $\approx 2\%$  for Si-W), depending on the active-passive combination, of the total energy is deposited in the active medium by an incident particle. As both the shower formation and the energy deposition are statistical in nature, more the energy samples collected - more will be the accuracy in the energy measurement. As a result, more the number of alternative absorbing and detecting layers, better will be the detector geometry. However, due to low- $Z$  of the detector material, the equivalent " $Z$ " of the calorimeter, ( $Z_{\text{equi}}$ ), will be certainly decreased and might dilute

the compactness of the configuration which will extend both the depth and the transverse dimension to have same energy containment and shower compactness. Altogether, increasing the number of layers, though have better energy resolution from a statistical point of view, but will invite a loose and extended geometry which will worsen the geometry in other way around. Moreover, being sampling calorimeter with small segmentation along the transverse direction which will be read individually, an increase in layer numbers will multiply the cost for readout electronics measurably. An optimised 25 ( $X_R$ ) length thick calorimeter was found reasonable with the help of geant4 simulation for the incident energy range 1→200 GeV with an optimised longitudinal leakage. However, a **Twenty-Layers** configuration for the calorimeter, comprising of silicon pad detector arrays and tungsten absorbers, alternately placed, has been adopted with proper balance for cost and calorimeter performances. A schematic of the calorimeter, FOCAL, is shown in figure 5.4 with different parts (detectors, absorber, and readout) pointed. As is explained in the figure 5.4, each layer consisted of

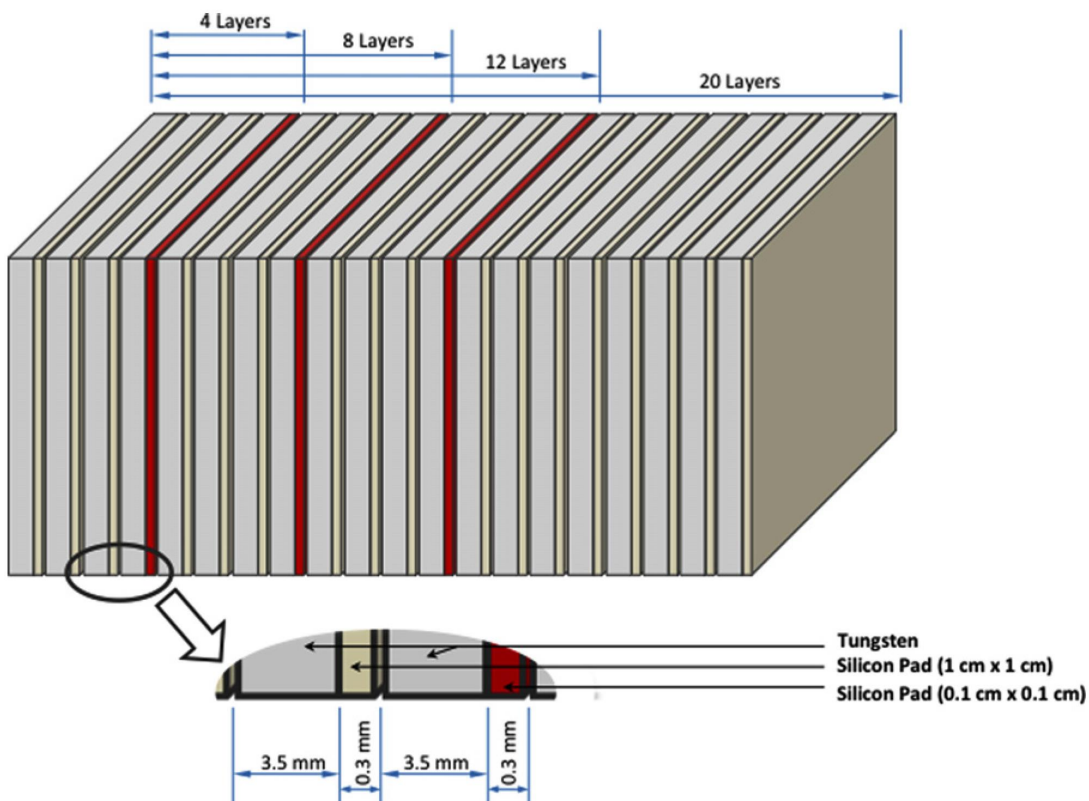


Figure 5.4: Sketch of the Calorimeter with Tungsten as absorber and Silicon as a sensitive medium (Not in scale). There are three high granular layers (HGL) and 17 coarse layers (LGL) with sensor dimensions (1 mm\*1 mm) and (1 cm\*1 cm) respectively.

a 0.35 cm ( $1 X_R$ ) thick tungsten plate followed by a 0.03 cm thin silicon sensors. During simulation with GEANT4, pure tungsten of density of  $19.3 \text{ gm/cm}^3$ , has been implemented. Because of high-Z and high density, tungsten converts high energy photons or electrons into comparatively compact electromagnetic showers, which mostly contained within a circular patch of radius 1 cm. As is discussed, the primary objective of FOCAL, is to reconstruct photon, mostly decayed from  $\pi^0$ -mesons, energy and tracks from their electromagnetic shower profiles. Typically for tungsten, clusters at each layer, as produced by EM-shower, for two close-by photons, just touch each other when centre-to-centre distance is about 2 cm ( $2 \times R_M$ ). So the design must be able to find the details of cluster (energy of the cluster:  $E_{clus}$ , centroid of the cluster:  $r_{clus}$ ) structure for precise tracking of individual incident photon or electron which can be done if detecting sensors are of dimension about 1 mm or less. But constructing a calorimeter with such high segmentation for the full configuration along with all associated stuff throughout is technically difficult and costly beyond the feasible limit. Considering these, a suitable practical optimisation was assumed with a hybrid configuration with a combination of few high-granular layers (HGL:  $\approx 1 \text{ mm}$  or less) and all rest are of comparatively coarse layers (LGL:  $\approx 1 \text{ cm}$ ) [87]). These HGL-part will help precise tracking by shower reconstruction, while the coarse layers will do the rest like 'energy calculation' and etc. Proper arrangement for HGL and LGL is equally important as a next step for the configuration. The placement of the HGL was done depending on the position of the maximum of shower profiles for the incident energy range  $1 \rightarrow 200 \text{ GeV}$ , as calculated using equation 5.2, which varies from  $4^{th}$ -Layer (each of  $1 X_R$ ) to  $12^{th}$ -Layer. As for an incoming photon/electron with particular incident energy, shower-maximum has the maximum number of secondary particles along the shower propagation which in turn give maximum energy deposition. So, a wise distribution for HGLs over the range for shower max, will help the reconstruction of shower clusters even with maximum simultaneous particle incidences and results in positive impact on tracking and improve the position resolution. In the present configuration, there are three high granular layers, placed at  $4^{th}$ ,  $8^{th}$  and  $12^{th}$  layers respectively, to cover the whole shower-maximum range for incident energy  $1 \text{ GeV} \rightarrow 200 \text{ GeV}$  evenly. All the rest layers are occupied with LGL which improve the energy measurements. So, effectively, with the addition of HGLs, there will be four points (Primary vertex along with other three from cluster centroids at three HGL) to reconstruct the whole track for the propagating  $\gamma$  or  $e^-$ -shower.

As a first result for performance of the designed calorimeter, we have studied the response of a minimum ionisation particle, as served by pion, by an individual detector as shown in figure 5.13 which will be discussed later in more details in this chapter. However, the most important is the response of an EM-shower, produced by a 10 GeV photon e.g. in a

single detector segment of  $1 \text{ cm}^2$  size at  $8^{\text{th}}$ -layers (HGL), as shown in figure 5.5, is nicely developed to a Gaussian shape as is expected from energy deposition by a large number of shower secondaries. On the other hand, the feasibility of the calorimeter in containing

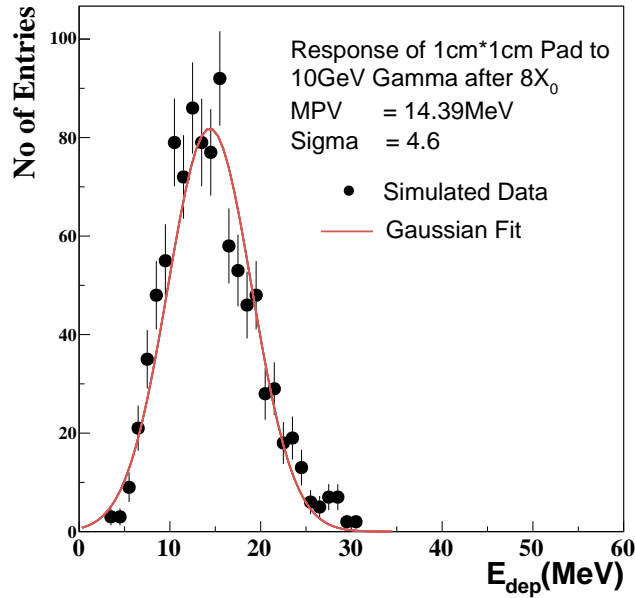


Figure 5.5: Response of a single  $1 \text{ cm} \times 1 \text{ cm}$  silicon pad detector at  $8^{\text{th}}$  layer of the calorimeter to an electromagnetic shower produced by a 10 GeV photon. Gaussian fitting to the simulated data is shown by the solid line. The error bars are representing the statistical error.

the highest desired incident energy photon can be understood by studying the **cumulative energy deposition profile** along the depth of the shower propagation. The layer-added energy deposition profile as a function of depth in units of layer number is shown in figure 5.6 which can be quantitatively expressed as

$$E_{\text{cumulative deposition}}^{n^{\text{th}}\text{-layer}} = \sum^i E_{\text{deposition}},$$

where  $i$  runs from 1 to  $n$ . For the design configuration under study, the profile shows saturation, obtained as a function of layer number, differ for different incident energies. However, the longitudinal depth of the calorimeter can be decided by the profile for the highest desired photon energy. As is illustrated by the figure 5.6,  $20 X_R$  depth could serve the purpose of full energy containment for the highest 200 GeV incident photon energy without any significant longitudinal loss. For the lower end of the energy range, saturation is well obtained even before  $12^{\text{th}}$  layer, whereas, for the higher energies, it reaches almost  $18^{\text{th}}$  layers onward

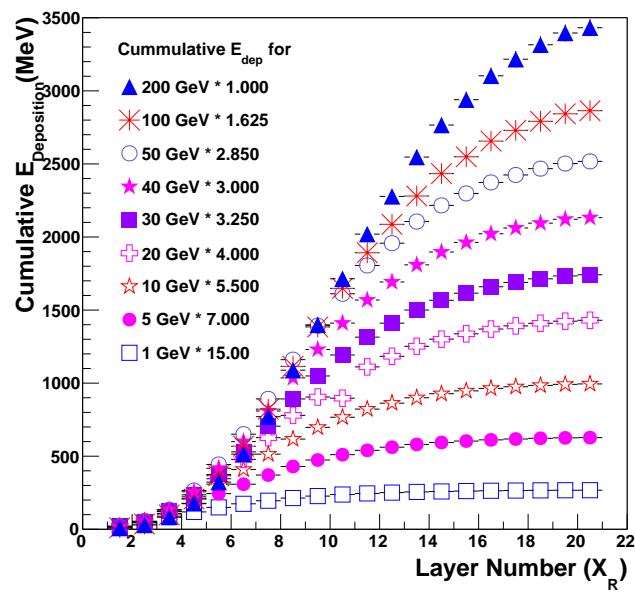


Figure 5.6: Cumulative energy deposition profile exhibits the development of "layer added energy deposition" as a function of "layer-number" for EM-showers over a wide range of incident energies. It demonstrates qualitatively an estimation of longitudinal leakage incurred in the calorimeter using its saturation trend (non-saturation) at a depth depending on incoming photon energy.

to achieve the saturation. As the energy deposition by EM-shower at larger depth dies down to zero asymptotically, the leakage can only be optimised rather than minimised for a calorimeter with a fixed number of layers.

As the final goal of the calorimeter, is to discriminate the prompt photons from decayed photons, it must disentangle two photon-induced showers for highest energy neutral pion incidence. The details of shower reconstruction will be discussed in the subsequent section, however, a snap of geant4 event display is shown in figure 5.7, for two photons, decayed from 10 GeV  $\pi^0$ , with their distinct tracks and shower spreads along the depth of the calorimeter. To be noted, two distinct shower profiles can not be seen so easily for higher energies of

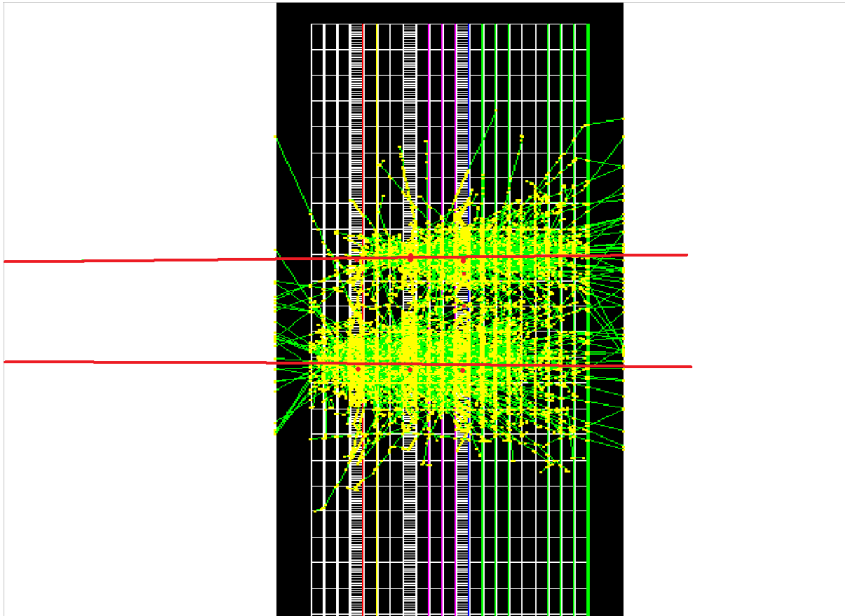


Figure 5.7: A snap from GEANT4 event display for electromagnetic showers, produced by decayed photons from 10 GeV  $\pi^0$ , with corresponding tracks shown by the solid lines which have been reconstructed using clustering technique for clusters formed at 4<sup>th</sup>, 8<sup>th</sup>, 12<sup>th</sup> layers respectively.

incident  $\pi^0$  as they start overlapping which need improved-shower-reconstruction technique to disentangling each other.

### 5.3 Shower reconstruction

Two clusters at a particular layer of the calorimeter, as produced by EM-shower of decayed photon from  $\pi^0$ , are separated by a distance depending on the incident  $\pi^0$ -energy ( $E_{\pi^0}$ ).

Although clusters are well separated for low- $E_{\pi^0}$ , with an increase in incident energy, the clusters start coming closer and at some point, they will start overlapping. For precise reconstruction of cluster information, we need to adopt "a cluster finding algorithm", which can efficiently disentangle cluster even if they are overlapped to a certain extent. For this study, we have used fuzzy clustering technique, which treats data points from their degree of memberships to one or more clusters simultaneously, as is often the case for overlapping clusters. It is important to note that, there are several clustering algorithms available in the literature such as contiguity method, cellular automata, search neighbourhood of cells, deterministic annealing, local maxima search, connected-cell search, k-means and etc. However, their effectiveness in case of overlapping cluster either restricted or depend strongly on the pattern of the clusters, which brings the fuzzy clustering more useful. Fuzzy C-Means (FCM) [127–129], type of k-means algorithm, which incorporates fuzzy logic in addition such that each point is assigned with either weak or strong association to a cluster, defined by the inverse distance to the centre of the cluster. The FCM algorithm can be characterised by an "objective function: ( $J_m(U, V, X)$ )", as expressed by the equation 5.6, which weight within groups sum of squared errors  $J_m$ .

$$J_m(U, V, X) = \sum_{k=1}^n \sum_{i=1}^C (u_{ik})^m \|x_k - v_i\|^2, \quad (5.6)$$

with,  $V = (v_1, v_2, \dots, v_C)$  is a set of unknown cluster centres or centres,  $U$  consists of the memberships of the  $k^{th}$  point to the  $i^{th}$  cluster and  $\|x\| = \sqrt{x^T x}$  is the inner product norm. The fuzzy factor "m" normalises the summed memberships to 1. The objective of finding a set of cluster by FCM is done by optimising  $J_m(U, V, X)$ . The membership 5.7 and cluster centres 5.8 can be found following the FCM Theorem, for  $D_{ik} = \|x_k - v_i\| > 0 \forall i$  and  $k$ , ( $U, V$ ) may minimise  $J_m$  only if,  $m > 1$ ,

$$u_{ik} = \left[ \sum_{j=1}^C \left( \frac{D_{ik}}{D_{jk}} \right)^{\frac{2}{m-1}} \right]^{-1}, \quad (5.7)$$

where,  $1 \leq i \leq C$ ,  $1 \leq k \leq n$ , and

$$v_i = \frac{\sum_{k=1}^n (u_{ik})^m x_k}{\sum_{k=1}^n (u_{ik})^m}. \quad (5.8)$$

Determination of a particular data point as a part of a cluster is done by checking the memberships of the point associated with each cluster. A point is considered as a part of a cluster if the membership to the particular cluster is maximum out of all existing point's memberships to all clusters. The best representation of the results to a data is finally determined by the validity index, which is Xie–Beni index for this particular case which depends on both memberships and geometric distances of data points.

However, there are drawbacks of FCM algorithm such that it depends on the fuzzy factor which may vary for different data sets and the fact that it treats outliers in the same way as the data points within the bulk. To get rid of such effects, FCM algorithm has been modified to a new form, called dynamic fuzzy c-means (dFCM), which finds clusters dynamically as data streams by either deleting or generating clusters as per requirement. The final results for finding valid clusters is made through satisfying the criterion for validity index. Moreover, there is no need to set the upper limit for the maximum number of clusters to start with (meets practical requirement more reasonably), rather it needs only a minimum. The dFCM algorithm can be illustrated by the flow-chart as expressed by 5.8 The subsequent steps of the algorithm can be described as following:

- The algorithm starts assuming a few of the incoming data points a priori which might help to estimate the range of the incoming data. At the beginning, a few parameters, like membership threshold, the FCM error criteria, the bounds of the variable "C", the number of clusters etc are specified. Usually, the initial number of points is taken to be low to give the algorithm to have a brief idea about the data set.

- initially, the number of cluster centres, generated uniformly within the input space, is defined by the minimum value of the variable C is  $C_{min}$  which must be greater than or equal to 2. Once the initial cluster centres are defined, the memberships for data points to the clusters are found using equation 5.7

- For further data point streaming in, its memberships with present clusters calculated. For maximum membership greater than or equal to the membership threshold  $\mu$ , simple Alternating optimisation takes place so that the data point can be assigned to at least one of the clusters such that matches or exceeds  $\mu$ .

- At a given instance, if maximum membership falls below  $\mu$  for "C" clusters, then the validity of the present set of clusters is checked for a range C-2 to C+2 (can be relaxed

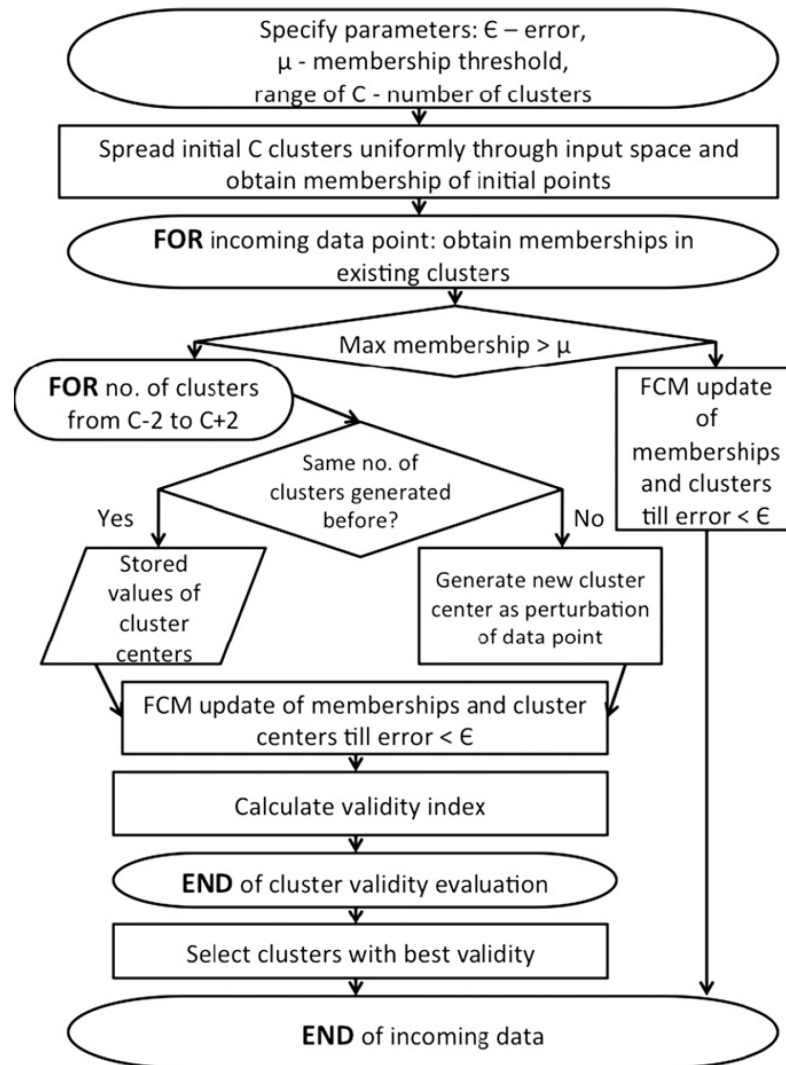


Figure 5.8: The flow chart of the dynamic FCM (dFCM) algorithm.

depending on the requirement) with following steps,

1. Firstly, cluster centres are checked whether they have been updated/generated at a previous time or not. For yes, the old values are updated using the FCM and thus the validity index is evaluated.
2. Otherwise, cluster centres for C-1 are used, and an  $C^{th}$  center is generated by perturbing the data point. Alternating optimisation performed again and the validity index is evaluated.
3. The cluster centres with the best value for validity index are accepted finally.
  - The above described procedure continues till data points stop streaming in.

**Application to simulated data:** The usability of the FCM algorithm along with its modified version has been checked for data, obtained from GEANT4 simulation with the proposed FOCAL detector. Since the algorithm is primarily developed to reconstruct the  $\pi^0$  from its decayed photon showers, we have taken single  $\pi^0$  of different incident energies which decayed to two photons and forming their corresponding showers within the calorimeter. As a first step, the algorithm was applied to find clusters information ( $R_{cluster}$  and  $E_{cluster}$ ) at three HGL layers of the calorimeter to reconstruct the path of the shower propagation and thus the decayed photons. Figure 5.9 explain the shower profiles of decayed photons and their reconstruction for three different incident energies, 10, 50 and 100 GeV respectively [107]. The GEANT4 displays are to show the extent of overlapping off showers, increases with an increase in incident  $\pi^0$  energy, which illustrates the need for applying clustering technique. The xy-hits distribution for the shower at different layers are actually fed to the clustering algorithm for finding the cluster centres and cluster energies.

The results obtained using the clustering for layer 8, in terms of lateral shower spread are shown in the right column of figure 5.9. The photon track (red solid lines) is reconstructed joining three cluster centres at  $4^{th}$ ,  $8^{th}$ ,  $12^{th}$  layers, obtained from FCM clustering. The FCM algorithm can satisfactorily reconstruct the photons tracks despite the large extent of overlap among themselves.

The invariant mass ( $M_{\gamma\gamma}$ ) of the incident  $\pi^0$  is then calculated using individual decayed photon (energy and direction) information. The quality of reconstruction of  $M_{\gamma\gamma}$  is shown in figure 5.10 and figure 5.11 for three different  $\pi^0$  energies [107].

The performance of the clustering, however, was done for a wide range of  $\pi^0$  energy 10 GeV→170 GeV which is shown at the right panel of figure 5.11. The plot shows

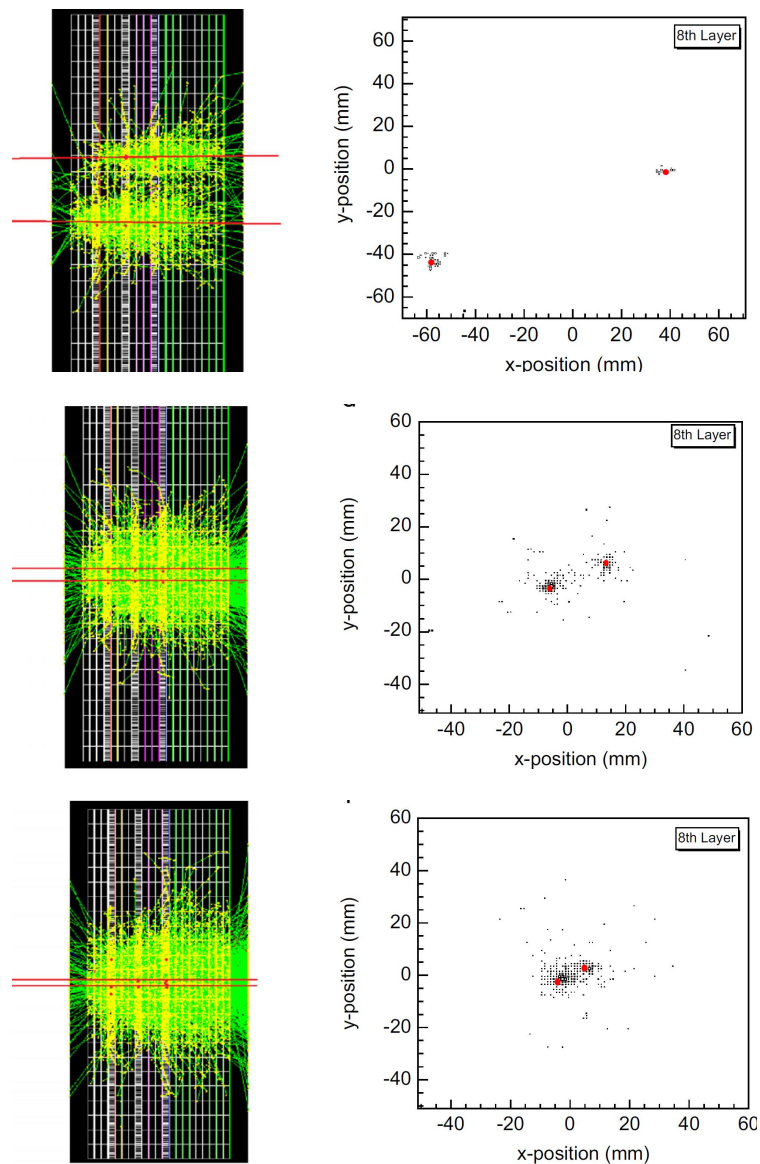


Figure 5.9: Reconstruction of neutral pion of energy 10 GeV (top), 50 GeV (middle), and 100 GeV (bottom) decaying to two photons. GEANT4 event display for Longitudinal shower profiles are shown along with clusters found by the FCM algorithm on the 4th, 8th and 12th layers, which are used to find photon tracks. XY-hit distributions, representing the lateral spread of shower at a particular depth (8<sup>th</sup> layer) with cluster centres superimposed. It shows the effectiveness of the FCM even for substantially overlapped clusters, found by the FCM algorithm.

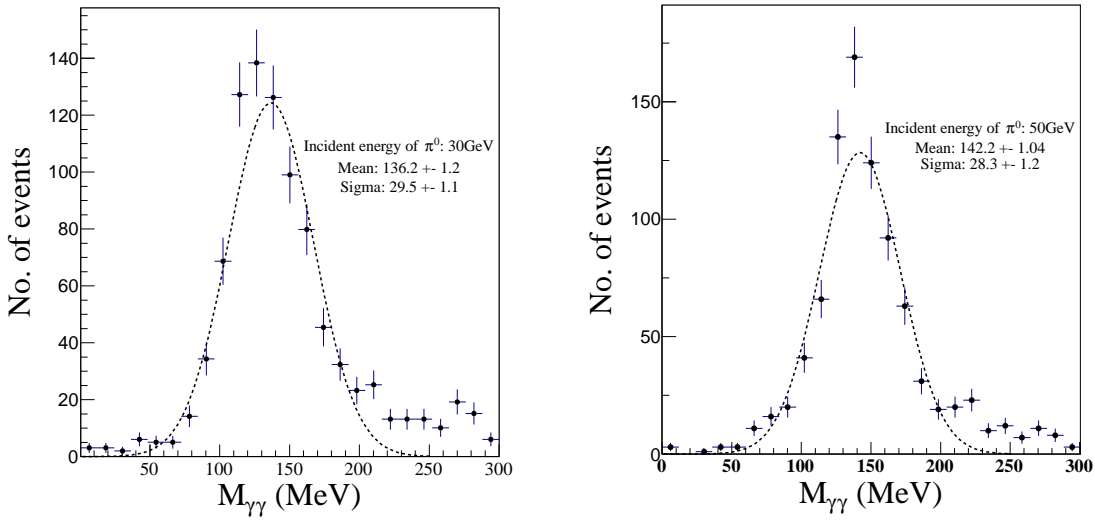


Figure 5.10: Invariant Mass ( $M_{\gamma-\gamma}$ ) reconstruction from two decayed photons using FCM clustering technique for the proposed FOCAL. The left panel shows for 10 GeV, whereas, the right panel is for 30 GeV  $\pi^0$ . The error bars in both cases represents statistical errors only.

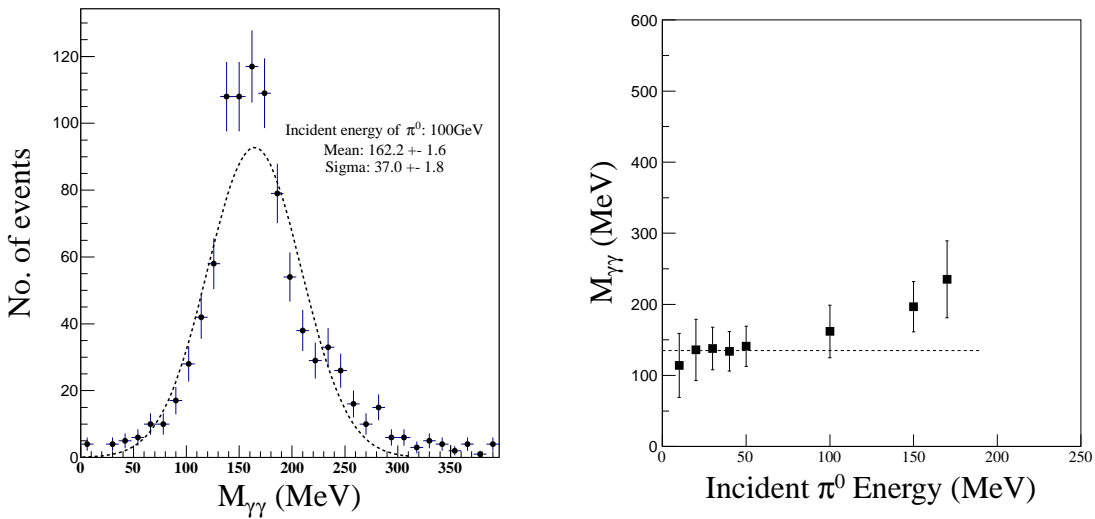


Figure 5.11: The left panel shown reconstruction of invariant mass ( $M_{\gamma-\gamma}$ ) for 100 GeV  $\pi^0$ , resulting 162 MeV for  $M_{\pi^0}$ , little more compare to its actual value. The right panel summarises the reconstructed invariant masses, calculated for  $\pi^0$  with varying incident energies using FCM, from two decayed photon as a function of  $E_{\pi^0}$ . The errors bars are indicating statistical error.

the variation of  $M_{\gamma\gamma}$  as function of incident  $\pi^0$  energy ( $E_{\pi^0}$ ). The statistical errors are calculated from the rms values of the invariant mass distributions. For almost all the cases of incident energies of  $\pi^0$ , the invariant mass distribution shows a peak around the  $\pi^0$ -mass

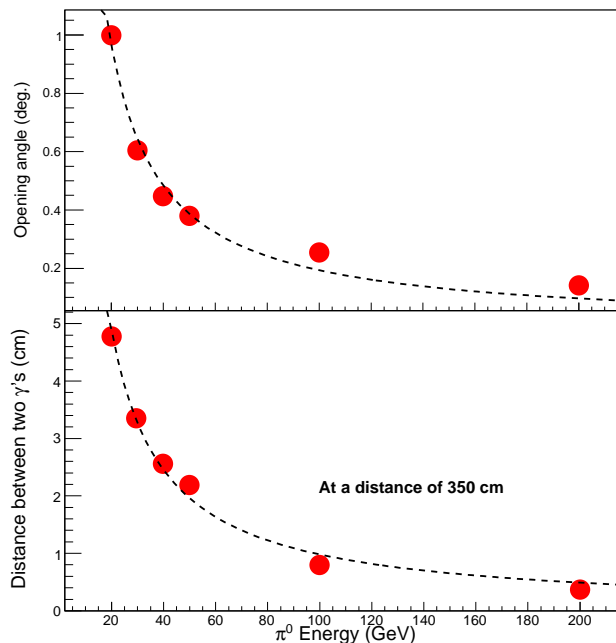


Figure 5.12: The plot illustrates the variation of opening angle (top) and minimum distance (bottom) between two photons, decayed from  $\pi^0$ , as a function of  $E_{\pi^0}^{incident}$ . Both the opening angle and the distance decreases with the increase in incident  $\pi^0$  energy. The results are matching satisfactorily with theoretical prediction as shown by the dashed curves. The error is within the marker size.

( $135MeV/c^2$ ). As is shown, however, the reconstruction of  $M_{\gamma\gamma}$  start deviating at 100 GeV onwards [107]. However, the effect can be attributed to both the detector configuration and the limitations of the clustering routine together which leaves scope for further improvement.

Finally, the opening angle and the distance between the two decayed photons at a distance of 350 cm away from the vertex was reconstructed using FCM clustering results about photon tracks and direction, as shown in figure 5.12.

The results for two photon separation, using clustering, from simulated data are in good agreement with the theoretical prediction. The success of shower reconstruction algorithm, however, leave a scope in furthering the study about the calorimeter performances which will be discussed in detail in the next section.

## 5.4 Response of calorimeter

In this section, the details of the responses of the proposed calorimeter to different particles will be discussed for a wide range of incident energy. Moreover, typical calorimeter performances like linearity b/w input-to-output, energy resolution etc. will be explored with the

simulated data. The study, especially, is to investigate the feasibility of the calorimeter in terms of its basic calorimetric performances.

### 5.4.1 Minimum Ionising particle

As has been discussed in section 2.2.2, below critical energy, particle loses energy in the matter through collision processes. Usually, for the relativistic particle, energy losses become independent of particle type and energy, as is illustrated by the figure 2.2. Pion, being the lowest mass hadron, become relativistic quickly and can be used to study the response of minimum ionising particle (MIP). The study of MIP is extremely important since it defines the sensibility of the sensors to detect any minimum level of signal over noise. To be a good detector, the MIP-signal should be well above the noise profile which makes the  $\frac{S}{N}$  ratio better. During simulation, we have taken  $\pi^+$  to characterise the MIP-response of the detector, as shown in figure 5.13. The profile is for an energy deposition by  $\pi^+$  in a single  $1\text{ cm}^2$  silicon pad detector. As is seen, the energy deposition profile in a  $300\ \mu\text{m}$  thin silicon detector can be well described by a truncated Landau distribution (to be more precise it must be Vavilob-Landau distribution). The most probable value for the energy deposition comes out to be  $\approx 90\text{ KeV}$  which is obvious from the prediction in literature [130]. It is important to note that  $\pi^+$ , with sufficiently high relativistic energy, can produce hadronic shower but at deeper in depth of the calorimeter. To avoid the contamination from the hadronic shower, it is always preferable to study the MIP-response for earlier layers of the calorimeter. However, interpretation of total energy deposition profile within the entire calorimeter by a MIP-particle need special attention which included both MIP-signal convoluted with hadronic shower contribution.

### 5.4.2 Electromagnetic shower

On the other hand, high energy photons create EM-shower and propagate through the calorimeter. Naturally, during the passage of photons through a calorimeter, it is energy deposition by shower secondaries instead of by a single incident particle as is illustrated in figure 5.5. The energy deposition profile by EM-shower, triggered by a  $10\text{ GeV}$  photon, is extracted using simulated data. The signal is a response of a  $1\text{ cm} * 1\text{ cm} * 0.3\text{ mm}$  silicon pad at  $8^{\text{th}}$  layer where shower max is expected for  $10\text{ GeV}$  Gamma. A simplistic Heitler model [64] calculation, as used to understand the EM-shower propagation and global properties, shows the number of secondary particles, produced at a single pad at  $8^{\text{th}}$ -layer, is  $\approx (14.39\text{ MeV} / 90\text{ KeV}) \approx 160$ . However, for the calculation of the total number of secondaries need contribution from others nearby pads along with the central pad which

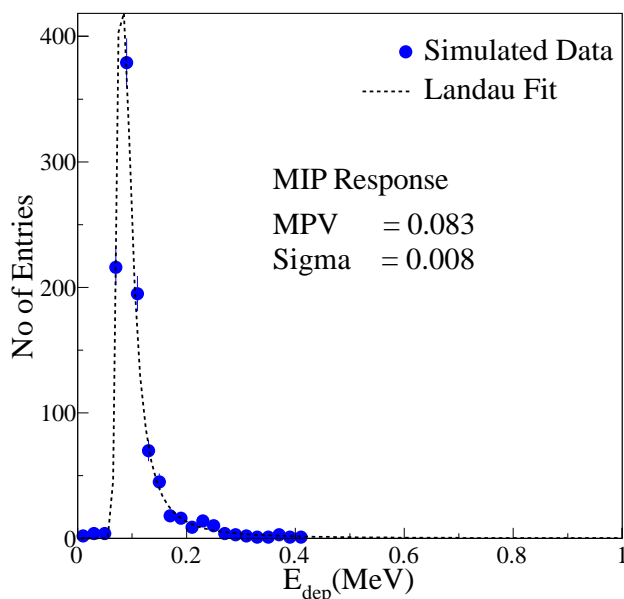


Figure 5.13: Response to a Minimum Ionising Particle  $\pi^+$  for single pad detector of dimension  $1\text{cm} * 1\text{cm}$  of a particular layer of the calorimeter. The curve represents fit to simulated data with Landau distribution.

contributes most. As the main aim for this simulation is to characterise FOCAL with optimised geometry and components, the basic calorimetric performances were reconstructed from the simulated data both to qualify and quantify its good design and functionality. In the remaining part of the chapter, we will discuss the capability of the calorimeter in recreating the shower properties like longitudinal profile, shower maximum as a function of depth and other more general properties like energy calibration, resolution and etc.

**Longitudinal shower profile:** Differential energy deposition as a function of depth (layer) by an EM-shower within the calorimeter, known as longitudinal shower profile, contains information like the required depth of calorimeter, maximum energy deposition at a particular layer and etc. During simulation, the response of high energy photons for a wide range of incident energy ( $1\text{ GeV} \rightarrow 200\text{ GeV}$ ) have been studied. The longitudinal profile, as shown in figure 5.14, get shifted to the right and become more broadened with an an increased area for increase in incident energy. The profile as a function of layer number can be explained using theoretical model prediction (line shown in figure) by Longo and as expressed in equation 2.20. As is expected for a  $e/\gamma$ -triggered EM-showers, the energy deposition first increases with the depth of calorimeter and reaches a maximum called shower-

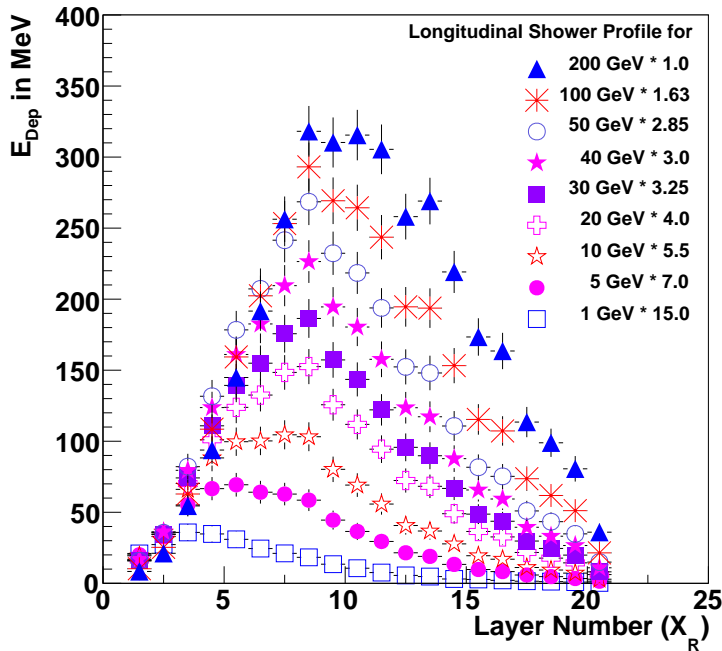


Figure 5.14: Longitudinal profile of an EM-Shower from incoming photons with different incident energies. It represents the variation of energy deposition at a particular layer with a depth of the calorimeter (layer number). The profile shows first rising and then followed by a falling trend with a shower maximum decided by the calorimeter and the incident energy of the incoming particle.

maximum. At the shower maximum, the energy of the shower particles degraded to the critical value ( $E_C$ ), where no further secondary particles are produced. With further increase in depth, the shower profile shows a falling trend representing the losses mostly dominated by ionisation/collisional mechanisms by the shower particles till the end. For a good design of a calorimeter, the longitudinal profile for the desired energy range must be closed or reach approximately zero deposition within the extent of the calorimeter. The shift in profile with increase in incident energy can be quantified by plotting the position of the shower maximum as a function of depth of the calorimeter which is shown in figure 5.15. The plot shows the data points from simulation along with the theoretical prediction, as expressed by  $t_{max} = \frac{(\alpha-1)}{\beta} = \ln \frac{E_0}{E_C} + C_{e^-/\gamma}$ . The parameter  $C_{e^-/\gamma}$  takes different values for electron and photons. The variation, indeed, shows a linearity for shower maximum for the desired energy range.

Apart from the longitudinal profile, EM-shower develops a transverse profile which represents the distribution of number of hit or energy deposition (corresponds to number of

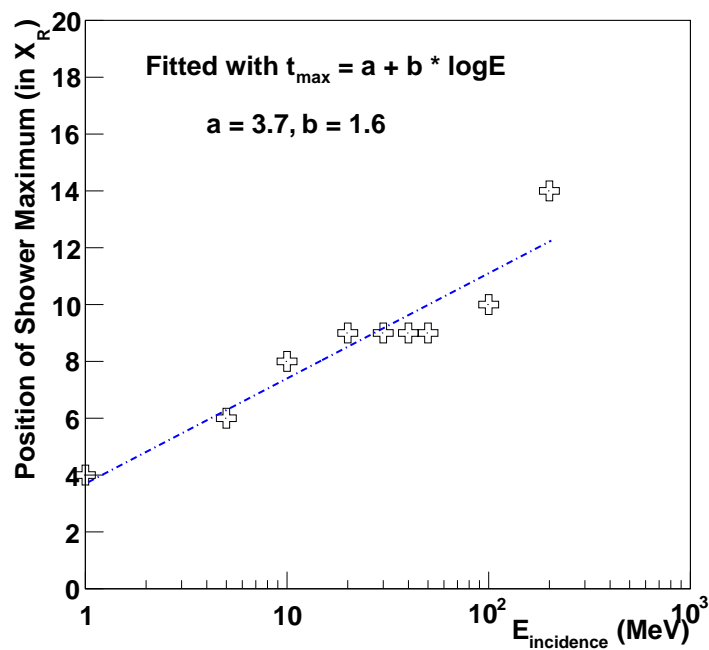


Figure 5.15: The plot represents the position of shower maximum ( $t_{max}$ ) as a function of incident energy for incoming photon. The position of shower maximum ( $t_{max}$ ), expressed in units of radiation length, varies linearly with the logarithmic of the incident energy. Importantly it hints about the depth of the calorimeter and the probable position of the highly granular layers for a specified energy range in designing a calorimeter.

shower particles) about the shower axis (as already explained). However, with LGL part of the calorimeter, it is hardly possible to reconstruct the transverse profile as the spread itself contained within an area of radius 1 cm (Moliere radius).

**Linearity for energy measurement:** Like in any general measurement strategy, the calorimeter should have linearity between the output signal and the incident energy. As has been discussed in the physics of calorimetry, the number of shower secondaries varies linearly with the incoming particle energy. However, the final output, involving two more steps: energy deposition by secondaries and production of measurable signal (light or charge), should follow linearity with the input. Because of statistical nature, the preciseness of  $E_{deposition/measured}$  will depend on the number of samples (corresponding to the number of layers) collected. In this study with 20-layers, total deposited energy was calculated from the simulation for a known set of incident energy of photons and is plotted in figure 5.16. It shows that the calorimeter is, indeed, behaving linearly within the expected incident energy range.

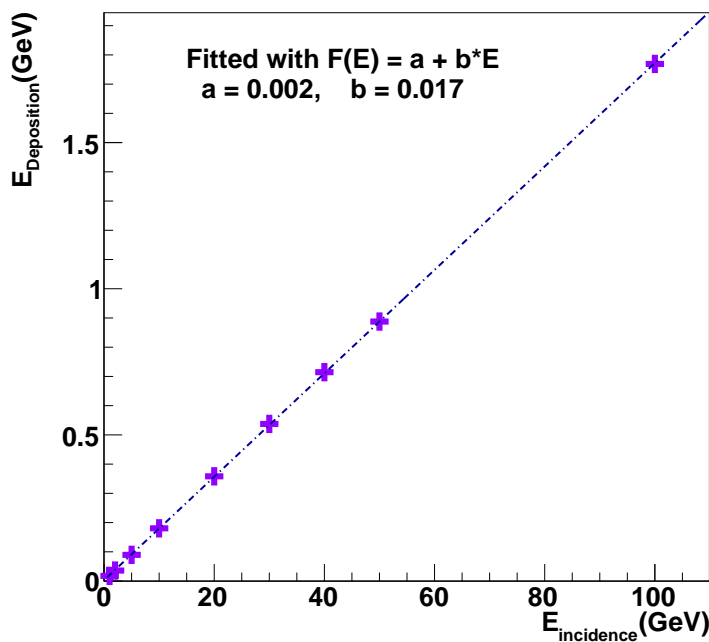


Figure 5.16: Calibration shows variation of total deposited Energy by the EM-shower triggered by inflowing Gamma with that of incident energy. It assures the the calorimeter is working in liner region indeed.

The figure 5.16, showing the relationship between deposited and the incident energies, is commonly known as calibration curve which provides the relationship which can be used to

calculate the unknown incident energy for particular measured energy. The results shows,  $E_{deposition}$  follow a linear equation  $E_{deposition} = 0.002 + 0.017 * E_{incidence}$  with an offset 0.002 which ideally must be zero.

**Energy Resolution:** Energy resolution ( $\frac{\sigma}{E}$ ), in general, can be defined as resolving power of an instrument in discriminating two closely spaced incoming particles in the energy spectrum. Calorimetry, being an energy measuring technique, should perform measurement with the desired energy resolution. The calorimeter under consideration is supposed to be operational under a moderately high particle density environment where a more or less continuum for the energy spectrum of incoming particles is expected. Before discussing details of the energy resolution, we will elaborate on the sources which are affecting the resolution in either way. Resolution can be thought of as an effect of physical processes which are statistical in nature and restrict introducing different type of fluctuations, inhibited in it. There are plenty of sources for such relevant fluctuations contributing to sampling type electromagnetic calorimeters and can be categorised as following

**1) Quantum Fluctuations** (which includes shower-fluctuations, photo-electron statistics) varies as  $\frac{1}{\sqrt{E}}$ .

**2) Shower Leakage** which depends on the calorimeter dimension. Usually, for a particular calorimeter, it is independent of energy. But longitudinal leakage needs much more attention as is more influential compared to lateral leakage for the energy resolution.

**3) Instrumental effects** like electronic noise and etc. This class of fluctuation depends on energy as  $\frac{1}{E}$ .

**4) Sampling fluctuation** is an issue which depends on the numbers of sampling layers and varies with energy as  $\frac{1}{\sqrt{E}}$ .

**5) Landau fluctuation** comes into the picture where thin active layers are used in the calorimeter. Within a thin active length, energy deposition is asymmetrically distributed which follows Landau distribution and varies with energy as  $\frac{1}{\sqrt{E}}$ .

**6) Track length fluctuation** which is effective due to the different path lengths traversed by different particles because of multiple scattering and depends on energy as  $\frac{1}{\sqrt{E}}$ .

Henceforth the generalised energy resolution of a sampling calorimeter is, considering all such contributions, can be represented by the following expression

$$\frac{\sigma(E)}{E} = a \oplus \frac{b}{\sqrt{E}} \oplus \frac{c}{E} + \mathcal{O}(E), \quad (5.9)$$

where symbol  $\oplus$  represents quadratic summation.

$a \rightarrow$  represents defects of the calorimeter of different types like non-uniformities (absorber

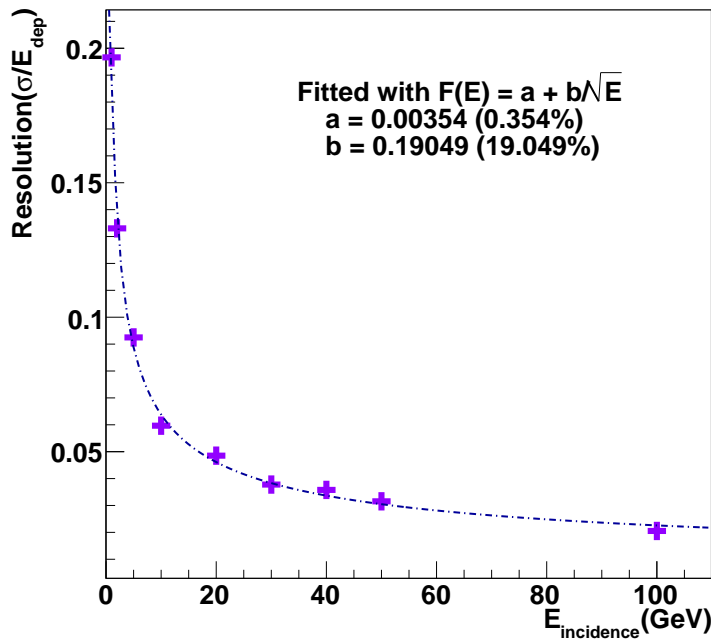


Figure 5.17: Energy resolution: represents the efficiency of the calorimeter in measuring the energy precisely of an inflowing particle. It is represented in terms of percentage of the incident energy that has been measured. Lesser the resolution ( $\frac{\sigma}{E_{in}}$ ) better will be the calorimeter. The dashed curve represents two-term resolution formula. The parameter associated with  $\frac{1}{\sqrt{E}}$  used to quote the resolution which is  $\approx 19\%$  in this case.

and active layers have irregular shapes), imperfections in the detector mechanical structure, temperature gradients, detector ageing, radiation damage, longitudinal leakage etc. Non-uniformities which might lead to periodic pattern in resolution can be cured in case they are originated from either detector geometry or readout electronics. On the other hand, mechanical imperfection affect the resolution in a random manner and difficult to cure.

$b \rightarrow$  stands for stochastic processes, representing fluctuations in signal generation, which depends on event-by-event fluctuation in case of sampling calorimeter and limit it to not so good like homogeneous calorimeters.

$c \rightarrow$  stands for the noise of readout electronics and depend on detector technique and readout circuit mostly.

Usually, in literature, values of  $a$  and  $b$  are quoted as the figure for energy resolution and thus the performance of a calorimeter.

Notably, the relative importance of different terms in the expression for resolution depends on the incident energy of the incoming particle. Therefore the optimised design for a

calorimeter can be different depending on energy ranges as might affect the resolution in different ways. Energy resolution may vary from an excellent  $\approx 2\%$  (for Homogeneous) to a compromising 30% and even worse depending on the choice of dimension, design, active/passive material combination, electronics etc. For the calorimeter under consideration, the resolution for incident energy range 1→200 GeV has been calculated and found to be  $0.354\% + 0.1905\%/\sqrt{E}$ , as is shown in figure 5.17, which is indeed quite inspiring for a sampling calorimeter.

## 5.5 Summary and scope

The different aspects of the design for a sampling calorimeter using a silicon detector and tungsten absorbers/converters have been discussed. A brief discussion about the requirements for the proposed FOCAL has been introduced in the beginning. A short note on the relevant calorimeter physics, regarding the passage of electromagnetic shower, was presented in the next. Details of geant4 simulation for FOCAL was done to help in optimising the geometry and to study the feasibility of the calorimeter. As one of the optimal choice,  $20 X_R$  thick calorimeter with 20 layers ( $1 X_R$  each) was considered as an option in this study. The calorimeter was optimised with a hybrid configuration having both HGL and LGL which made it an accommodative solution from both physics requirements and budget perspective. A detailed simulation regarding the performances of the calorimeter has been accomplished. The shower reconstruction using a fuzzy clustering method is adopted in this study. The applicability of the reconstruction technique was discussed for overlapping showers (hit patch at a layer) and found performing reasonably good for expected high particle density environment like in ALICE. The chapter ends with reconstruction response of the calorimeter to charged particles (MIP) and photons (triggering EM-shower) for wide incident energy. Simulation results, indeed, shows the potentiality of the designed calorimeter an acceptable option to pursue the physics interests under consideration.

The feasibility study of the calorimeter in simulation inspires to step forward for designing and developing the calorimeter will all its components. The details of hardware development for a series of prototype calorimeter, aiming for the proposed FOCAL, will be discussed in details in the next chapter.



# Chapter 6

## FOCAL: Detector Development, Fabrication and Tests

### 6.1 Introduction

After successful completion of the conceptual design for the calorimeter configuration, an effort was put in constructing prototype calorimeter as one of the major parts of the thesis work. The hardware development comprises of making of **silicon detector, large dynamic range readout electronics, detector and readout PCB board, mechanical structure, data acquisition** and etc. The main focus on FOCAL prototype development, for this study, will be on fabrication and test of a small scale calorimeter arrangement and analysis of results both for laboratory and high energy particle beam. As a first step towards detector development, we have started making a  $1\text{ cm}^2$ ,  $300\text{ }\mu\text{m}$  thin silicon detector elements and mounted them on a detector PCB. Although, this will invite a lot of dead space and can not be used in the actual experiment, it can provide important results regarding basic detector characteristics including noise and also explore the scope for further developments. Starting from such a simple prototype with physically isolated  $1\text{ cm}^2$  silicon sensors array as the detector, a series of prototype calorimeters were developed, fabricated and tested both with the radioactive source at the laboratory and with a high energy electron beam and published in [120]. Following a miniature version prototype test and its successful performances, a full depth prototype has been constructed which will be discussed in more details in this chapter. Analysis of test beam data, carried at both CERN-PS and CERN-SPS beamline facility, will be presented. Comparison of experimental data with that from simulation will also be analysed in subsequent sections. In the end, the scope for further progress and the final goal will be described.

## 6.2 Test of Si-detector with $\beta$ -source ( $Sr^{90}$ )

### 6.2.1 Experimental set-up

A detailed and extensive laboratory based test of each component like single pad detector, readout channels, mechanical arrangement, triggering unit etc. have been performed with radioactive  $Sr^{90}$   $\beta$ -source (with an endpoint energy of 0.546 MeV). The test set-up, as shown in photograph 6.1, comprises of a  $5 \times 5$  array of  $1 \text{ cm}^2$  silicon detector mounted on a PCB, two scintillators - as triggering unit,  $\beta$ -source for low energy electron beam, NIM-based electronics and etc. The optimum operating voltage, set for the detector, was 60 V which has been judiciously decided

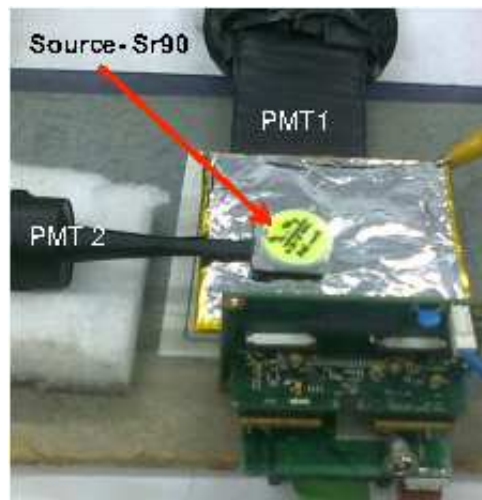


Figure 6.1: Experimental arrangement used to test the silicon detectors at VECC laboratory with the  $Sr^{90}$   $\beta$  source.

depending on the voltage scan (I-V characteristics) of the detectors. As per design, the detector, however, supposed to be depleted fully at  $70 \rightarrow 80$  volts with the capacitance of  $40 \text{ pF/cm}^2$ . The detector plane, as shown in the photograph 6.2, was interleaved in between two scintillator paddles which serve the purpose of triggering the detector by the method of coincidence.

The encapsulated  $Sr^{90}$  source was placed above the top scintillator paddles, as is shown in the experimental set up 6.1. The detector plane was wrapped with a thin aluminium sheet to protect against ambient EMI. The whole experimental arrangement was put inside a box, covered with black paper, to shield from light which otherwise increases the noise in the detector. Since the radioactive  $\beta$ -source emits a continuum spectra of the electron, it will deposit energy within the detector truncated at a maximum value, characterised by the

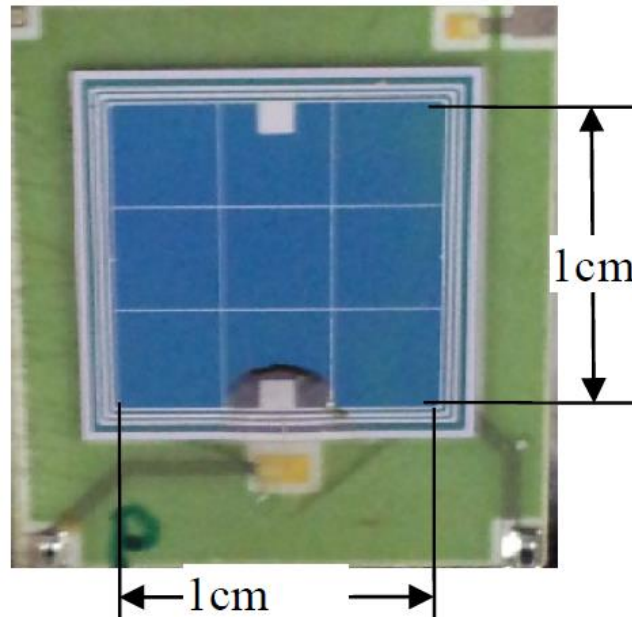


Figure 6.2: Photograph of a single  $1\text{ cm}^2$  silicon pad detector mounted on a PCB board.

end-point energy of the  $\beta$  spectrum. All the individual detector was checked during the experiment by adjusting the source position (xy-scanning) so that the radiation can hit a particular pad on the detector plane. However, to start, a run without any source is always performed to investigate the response of the detector to noise from different sources like from detector, readout electronics and experimental ambience and etc., which will set the reference during data analysis.

### 6.2.2 Discussion of laboratory test results

As discussed, the main aim of the laboratory test was to check the functionality of all individual detectors. The data from the test with  $\beta$ -source shows two clearly distinguished peaks corresponds to  $\beta$ -spectrum and the noise respectively which is described by the figure 6.3, depicting a reasonably good signal-to-noise ratio ( $\frac{S}{N}$ ). These results elucidate the good functionality of each element of the silicon detector array. However, for details of calorimeter response and energy loss profiles, the calorimeter prototype with both absorber and detector layers must be studied with high energy pion and electron beams which will be discussed next in this chapter.

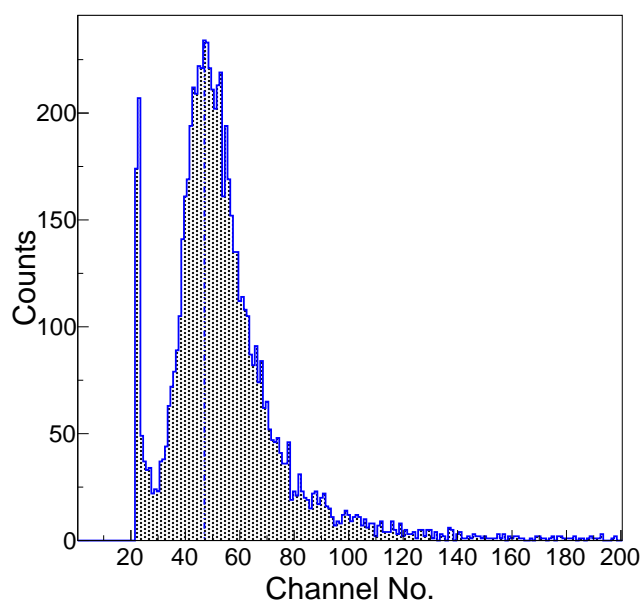


Figure 6.3: (Colour online). Response of a single silicon pad detector to  $Sr^{90}$ - $\beta$  source. A clear peak has been detected corresponding to  $\beta$  spectrum of with end point energy 0.546 MeV. The signal is well dispersed from the noise peak which is around the channel number 20.

## 6.3 Mini-Prototype

A miniature version for FOCAL prototype (mini-prototype) with only four layers of detectors and tungsten absorbers was fabricated as a next step. The test with mini-prototype was to put together all components along with the data acquisition system and to study the behaviour and characteristics of the detector. It will also help in estimating the requirements of readout electronics which can be feed for next step of developments. Though the mini-prototype is limited with four course layers, still basic characteristics like longitudinal shower profile, calibration of energy deposition, etc., can provide inputs to build the full length calorimeter. The details of the mini-prototype along with test beam results will be discussed in details in the next two sections.

### 6.3.1 Construction and test at CERN-PS

As discussed, a mini-prototpe, with active transverse area  $5\text{ cm} \times 5\text{ cm}$  and of the longitudinal dimension of  $\approx 4 X_R$ , has been constructed to study the response of pion and electron beams of various energies. Encouraging results from the tests of detectors at laboratory, miniature prototype, comprised of four-layers (Each layer  $= \approx 3.5\text{ mm}$  thick "W" +  $\approx 1\text{ cm}$  for detector and electronics together) of tungsten (converter/absorber) and  $5 * 5$  array of  $1\text{ cm}^2$  silicon detector planes, was constructed. Each layer is a combination of tungsten plate of dimension  $10\text{ cm} \times 10\text{ cm} \times \approx 1X_R \pm 0.03\text{ cm}$ , silicon detector array ( $5 * 5$ ) and front-end readout electronics. Physically isolated and each individual silicon pad detectors of dimension  $1\text{ cm}^2$ , as shown in figure 6.2, were assembled in a  $5 * 5$  array. the detector array was mounted on a  $0.08\text{ cm}$  thick 4-layer detector-PCB which is illustrated in figure 6.4. The PCB layers serve the purpose of both holding and connecting the detector to the front-end-readout electronics. There altogether four such composite layers (W+Si+electronics) which are contributing to the depth of  $4 X_R$  for the mini-prototype. The density and purity of the tungsten-plates, used as an absorber, was  $19.3\text{ gm/cm}^3$  and  $\approx 99.9\%$  respectively. There were two arrangements which have been used for the mini-prototype. Both the setups, as shown in figure 6.5, contains four layers of detectors. In Set-up-1, four layers of tungsten and silicon detector arrays were assembled alternatively. This gives the behaviour of incoming particles up to  $4 X_R$  in longitudinal depth. However, the Set-up-2 has two additional tungsten layers in front compare to Set-up-1 which could extend the depth up to  $6 X_R$ .

The either of the setup was used in a general scheme of the mini-prototype arrangement, as illustrated by the schematic diagram 6.6. Basically, the sketch explains the relative position of different parts during the actual experiment. The transverse granularity of the detector

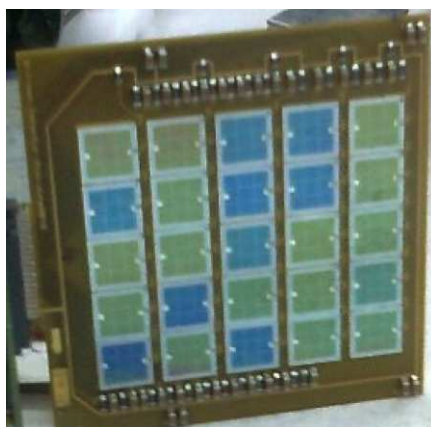


Figure 6.4: Sketch of the silicon detector array of dimension  $5 \times 5$  made of  $1 \text{ cm}^2$  physically isolated silicon pad detectors which are mounted on the detector PCB.

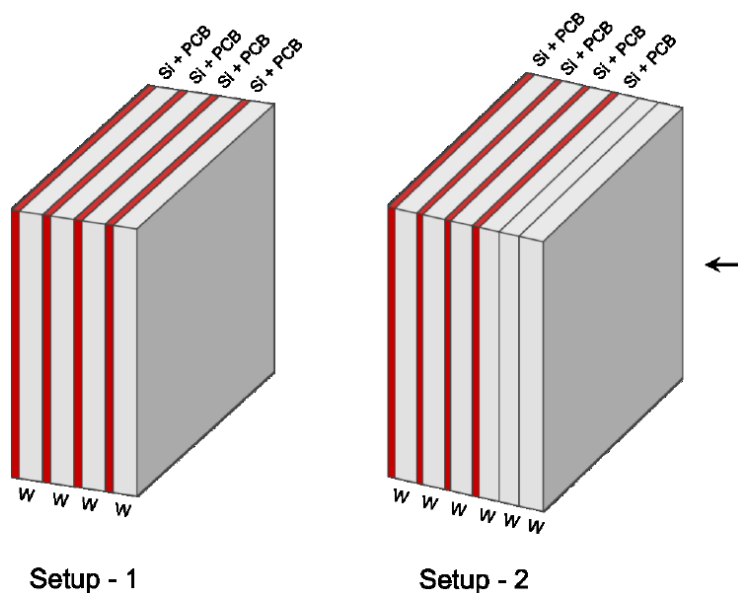


Figure 6.5: (Colour online) The figures represent sketches of two different setups of the Mini-prototype which had been used for the beam test at CERN-PS.

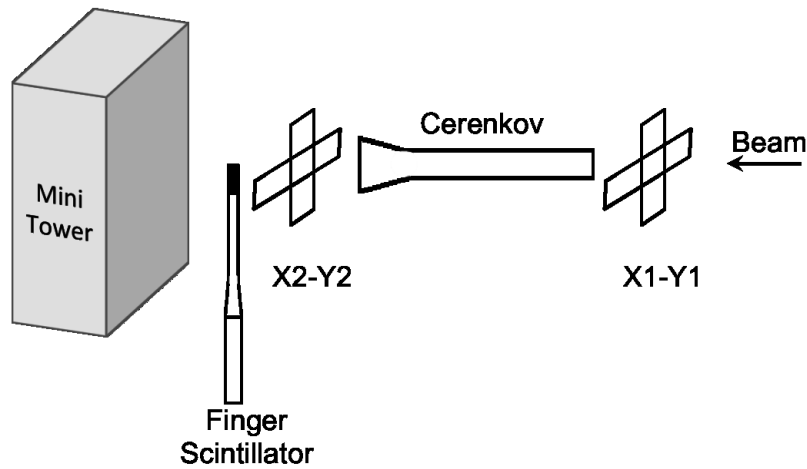


Figure 6.6: (Colour online) The figure represents the schematic of the mini-prototype with all different components in sequence as was arranged during the experiment.

plane, used in mini-prototype, was  $1\text{ cm} * 1\text{ cm}$  (similar to LGL of the proposed calorimeter) where  $320\ \mu\text{m}$  is thickness along the depth.

**Silicon detector:** The silicon detectors are fabricated on  $\langle 111 \rangle$  FZ n-type wafers with  $3 - 5\text{ k-}\Omega$  resistivity. The top pads are p+ while the bottom side is n+. The leakage current of the detectors is less than a few nA and breakdown voltage is above 250 V. Each pad detector is surrounded by a guard-ring which help in improving cross-talk among near-by detectors and make the field uniform inside the detector. All the detectors are appropriately biased. The silicon pads found to reach the full depletion at 60 V with detector capacitance of  $40\text{ pF/cm}^2$ . The detectors were attached to the 0.08 cm thin 4-layers PCB with silver conductive epoxy of resistivity  $0.006\ \Omega\text{-cm}$ . The top of the diode was coated with  $1\ \mu\text{m}$  thick Al and  $0.5\ \mu\text{m}$  thick phosphosilicate glass (PSG) passivation. Being physically isolated from each other, the probability of having a cross talk among adjacent silicon pad elements is ideally zero [120].

**Readout Electronics:** There were devoted Front End Electronics (FEE) boards which have been used to readout detector signal during experiments both at the laboratory and PS-Beam line. Two different kind of ASICs, namely, MANAS [131, 132] and ANUSANSKAR [133] were used for these purposes. Both of these ASICs have 16 pulse processing channels along with analogue multiplexed output. Each channel is subsumed of a Charge Sensitive Amplifier (CSA), second order semi Gaussian pulse shapers, track and hold (T&H) circuit and output buffer. For ANUSANSKAR, AMI Semiconductor  $0.7\ \mu\text{m}$  C07-MA technology has been used whereas for MANAS, SCL  $1.2\ \mu\text{m}$  C1D twin tub process has been adopted. The size

of the input transistor for both the ASICs is  $8000\mu\text{m} \times 1.5\mu\text{m}$ . In ANUSANSKAR, CSA design is based on conventional folded cascade architecture with a high value of feedback resistor, which is implemented through current conveyor method with improved linearity for large signals. As the input transistor plays a vital role in determining the noise performance of the whole amplifier, large area p-type MOS transistor is used as the input device to reduce the flicker noise. The input transistor is biased in subthreshold region with  $500\mu\text{A}$  bias current, ensures appropriate transconductance ( $g_m$ ) to reduce the contribution due to thermal noise. Semi-Gaussian shaping is implemented using 2<sup>nd</sup> order Sallen-key filter with wide swing Operational Transconductance Amplifier (OTA) and with a peaking time of  $1.2\mu\text{s}$ . However, semi Gaussian shapers inside MANAS are implemented through Gm-C filter topology. The baseline recovery is better than 1% after  $4\mu\text{s}$  in ANUSANSKAR can be achieved by tailoring the pole-zero locations by external DC voltage control. The T&H block is used to sample the peak information of the shaped signal. All the 16 channel outputs of both the ASICs can be read out serially via analogue multiplexer with a clock rate of 1 MHz. Brief performance summary of both the ASICs are given in Table 6.1 [120, 133].

Table 6.1: Specifications of the readout ASICS (MANAS and ANUSANSKAR) used in the mini-tower set-up and tests.

| Specification        | ANUSANSKAR                           | MANAS                                |
|----------------------|--------------------------------------|--------------------------------------|
| Noise at 0 pF        | 390 rms electrons                    | 500 rms electrons                    |
| Noise slope          | $7e^-/\text{pf}$                     | $11.6e^-/\text{pf}$                  |
| Linear dynamic range | +/- 600 fC                           | + 500 fC to -300 fC                  |
| Conversion gain      | 3.3 mV/fC                            | 3.2 mV/fC                            |
| Peaking time         | $1.2\mu\text{s}$                     | $1.2\mu\text{s}$                     |
| Baseline recovery    | 1% after $4\mu\text{s}$              | 1% after $5\mu\text{s}$              |
| VDD/VSS              | +/- 2.5 V                            | +/- 2.5 V                            |
| Analog readout speed | 1 MHz                                | 1 MHz                                |
| Power consumption    | $\sim 15\text{ mW/channel}$          | 9 mW/channel                         |
| Die area             | $4.6\text{ mm} \times 4.6\text{ mm}$ | $4.6\text{ mm} \times 2.4\text{ mm}$ |
| Technology           | $0.7\mu\text{m}$ standard            | $1.2\mu\text{m}$ standard            |
|                      | CMOS                                 | CMOS                                 |
| Package              | CLCC-68                              | TQFP-48                              |

**Trigger:** A dedicated trigger system consists of two pairs of scintillator paddles, a finger scintillator and a Cherenkov detector were used during the experiment. The arrangement of the trigger detectors with respect to the mini-tower is shown in figure 6.6. The two pairs of paddle scintillators are arranged to determine the x-y positions of the incoming beam within

1  $cm^2$  area, while the finger scintillator will pinpoint the position more precisely. The pion trigger is generated using the scintillator paddles along with a small finger scintillator of size 3 mm \* 3 mm, placed close to the mini-prototype, with the help of coincidence logic. In addition, a Cherenkov detector was used to trigger the electron signal. The gas pressure of the Cherenkov detector was so adjusted to obtain the highest purity of the electrons depending on the desired incident energy.

The mini-prototype was placed on a movable table to adjust the detector position with respect to the beam. The detector set-up, used in the PS-T10 beamline, is shown in figure 6.7. The silicon pad arrays, along with backplane PCBs are properly shielded against EMI and

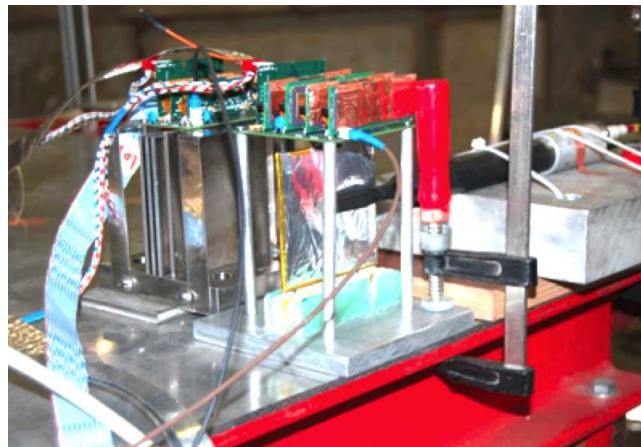


Figure 6.7: (Colour online) Photograph of the actual experimental set-up which was used at T10 PS Beam Line facility at CERN for the mini prototype test.

ambient light for better Signal-to-Noise ( $\frac{S}{N}$ ) ratio. The detector signals are readout using a FEE board and further processed by a MARC ASIC, which communicates with the Cluster Read Out Concentrator Unit System (CROCUS) [134, 135]. Finally, the CROCUS interfaces to the data acquisition system via fibre optic cable.

### 6.3.2 Test beam results and discussion

The details of test beam data with the mini-prototype at CERN-PS will be presented and discussed in details for different incident particles for wide incident energy in this section. The test beam results will also be compared to those from the simulation for competency. Every minute details of the actual experimental arrangement were taken into account within the simulation framework for one to one correspondence. The gap between consecutive tungsten layers was kept as 0.21 cm, out of which 0.03 cm was for the silicon wafer followed

by 0.08 cm thick four layer PCB and the rest 0.1 cm was left for associated electronics. The PCB and electronics parts were also included in the simulation with an equivalent-Z material, defined using geant4, of the same dimension.

During data analysis, performances of each layer of the detector had been computed by summing up all signals from each individual pad detectors. The Mini-prototype has been experimented with both pion and electron beams of energy range  $1 \rightarrow 6$  GeV during beam test at CERN-PS facility. Electron, having lighter mass and electromagnetic in nature, induced EM-shower and propagate through the layers of the prototype and leave its footprints for offline reconstruction. On the other hand, pions which is less likely to produce EM-shower within the extent of the mini-prototype depth, behave like minimum ionising particles (MIP). The energy deposition of the MIPs was fitted with Landau Distribution to extract the energy deposition profile characterised with MPV and RMS which has been discussed in details earlier.

Analysis revealed pions to act like MIP, as expected, with a most probable value (MPV) of 17 ADC, which is depicted in figure 6.8. There was conversion gain of 3.24 mV/fC of the readout ASIC (MANAS) incurred in the calculation. Comparison the results with that from,

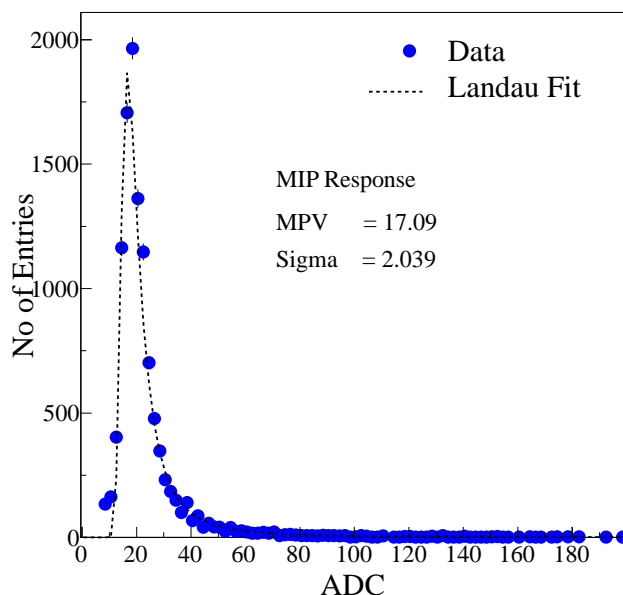


Figure 6.8: (Colour online). Response of silicon pad detector arrays to pions, showing the distribution similar to the minimum ionizing particles. The plot is shown in units of ADC.

as shown figure 5.13, indicate a clear resemblance to MIP spectrum with a MPV value of

83 keV.

On the other hand, from the earlier discussion about EM-shower formation and propagation, electrons is supposed to produce electromagnetic shower within the Mini-prototype, limited by the truncated depth of the mini-prototype. However, the shower shape and energy deposition in each silicon layer has a significance in terms of optimising the granularity as well as transverse and longitudinal leakage of energy in the calorimeter. Figure 6.9 provides the energy deposition of electromagnetic showers, produced after  $2 X_R$  depth, for three different incoming electron energies. Experimental results anticipate that, although the shower profile is not so well developed for 1 GeV electron and resulted smeared Gaussian, however, with the increase in incident electron energy, the distribution approaches more towards expected Gaussian profile. The mean of the distributions shifts steadily with incident energy, as shown in figure 6.9. Layerwise energy depositions were reconstructed for different incident energies of the electron, added over pad element over a detector array, and plotted as a function of longitudinal depth from  $1 X_R$  to  $6X_R$ . Longitudinal profile for EM-shower, as shown in figure 6.10, describes the mean energy deposition as a function of longitudinal depth within the extent of Mini-prototype. In this figure 6.10, with the increase of depth, the layer-wise energy deposition for given incident energy increases at first and then reaches a maximum, known as shower-maximum where further secondary particle production stops. Going further deeper in the depth, the profile downturns because of no further production of secondaries and the energy losses are mostly dominated by collision and ionisation. The limited depth of mini-prototype restricts the full longitudinal profile to be developed even for such lower incident energy range ( $1 \rightarrow 6$  GeV). In spite of that, the shower-max position was found to shift to larger depth with an increase in the incident energy of the particle. The shower profiles observed in the experimental data are complementary to the simulation as shown in figure 6.11 and was quite encouraging towards making the full-depth calorimeter. The energy depositions, taking all possible combinations of absorber thickness and beam energies, have been reconstructed and plotted with respect to that found from simulation, as shown in figure 6.12. The relationship, known as "conversion curve" with abscissa as energy deposition from simulated data and ordinate from experimental data, ensured a direct one to one harmonious relationships between data and simulation. In the absence of a calibration curve (limited by the lack of full energy reconstruction), it serves to study the linearity checks of the prototype calorimeter. Moreover, because of limited incident energy range, it was difficult to check the extent of linearity over a wide range of energy. Even though indirectly, but conversion curve assures the functionality of the calorimeter working in the linear domain safely. The electron data corresponding to each layer as well as the sum of

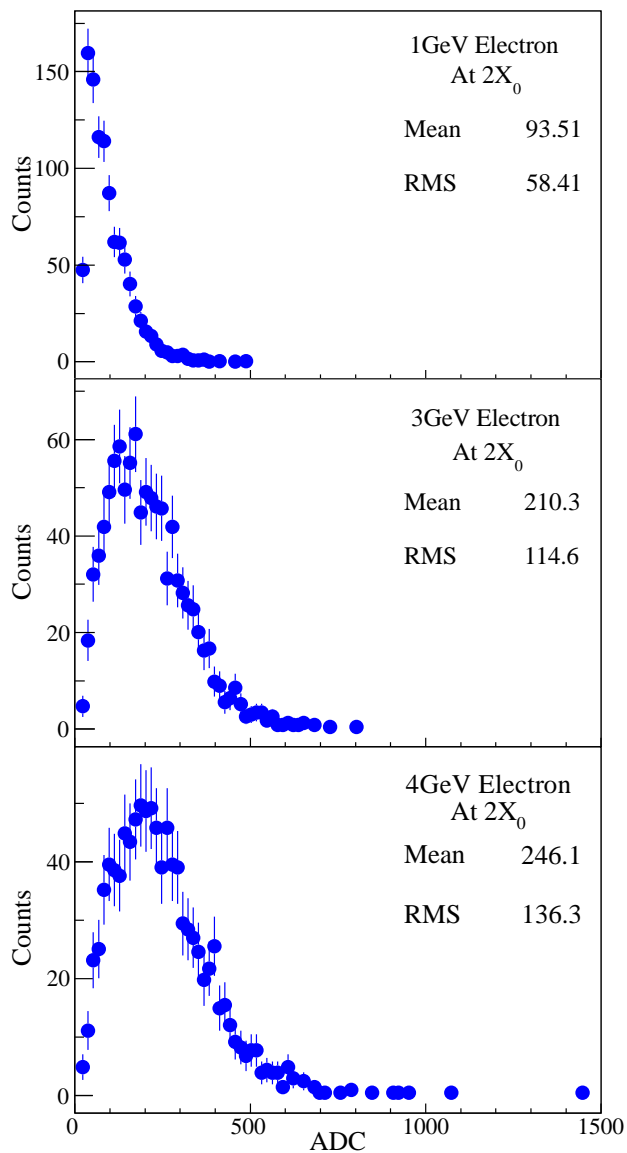


Figure 6.9: Response of silicon pad detector arrays, placed at the depth of  $2X_0$  of the mini-prototype, for electrons at three different energies.

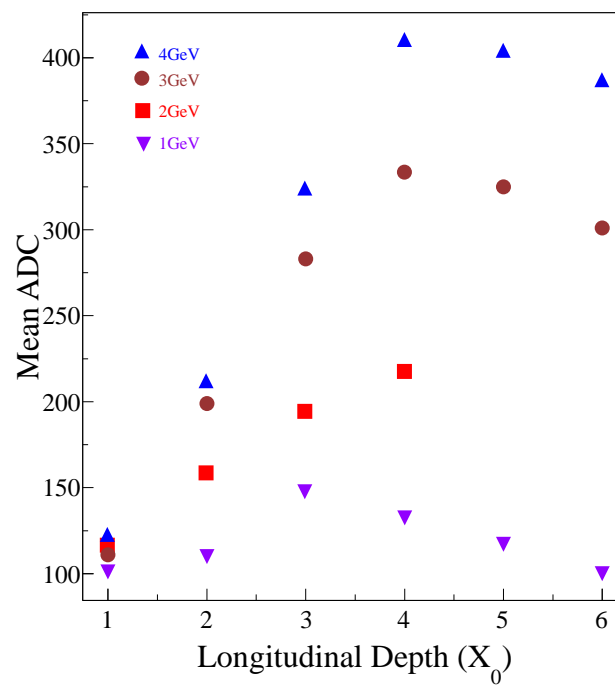


Figure 6.10: (Colour online) The plots represent the longitudinal shower profile which has been reconstructed from data using layer wise energy deposition of the incoming particle over a wide range of energy.

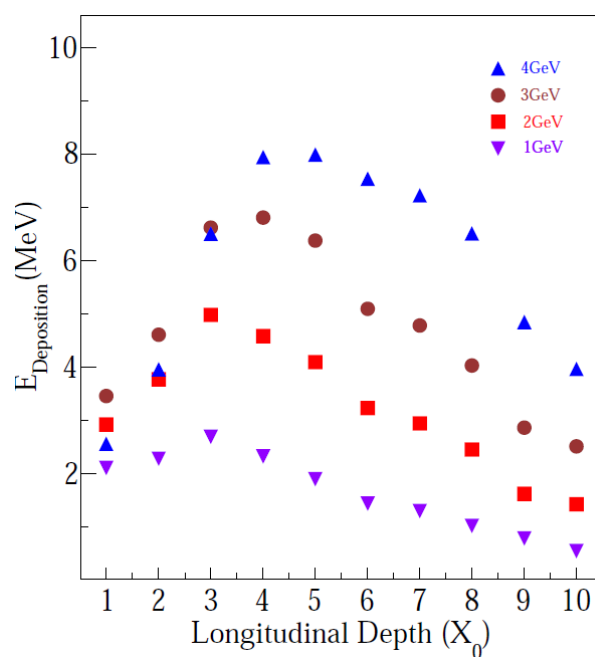


Figure 6.11: (Colour online) The plot shows longitudinal shower profile which has been reconstructed using simulated data with all details of mini-prototype set-up included in simulation package.

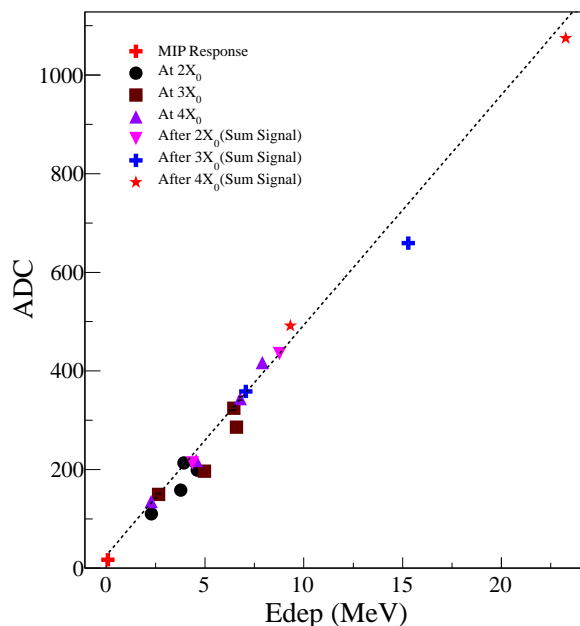


Figure 6.12: (Colour online) Conversion curve which compare between energy depositions within the calorimeter prototype which were reconstructed using experimental data (ADC) and the energy deposition from simulated data (MeV).

signals from different layers is presented in reconstructing the conversion curve in figure 6.12. The data for MIP, is also superimposed on the same figure as shown by the solid red cross marker. Linearity is observed over a wide range of energy depositions. A linear fit through the data points yields,  $ADC = 46.7 \times E_{dep} + 26$ , where  $E_{dep}$  is expressed in MeV. The offset is suspected to be contributed by electronics conversion and gain.

The success of the limited length mini-prototype test establishes "the proof for the working principle" of the calorimeter in terms of responses to MIP and EM-shower. This, indeed, set guidance for improving and developing a full depth prototype calorimeter which will be discussed in the next section.

## 6.4 Full-Depth prototype

In this section, we will discuss the construction of a full-length prototype calorimeter along with a brief description of the newly developed read-out electronics. Details of the prototype arrangement and installation at H6 beam line at CERN-SPS will be presented. The results from test beam data analysis will also be illustrated with emphasis on the discussion. Like in

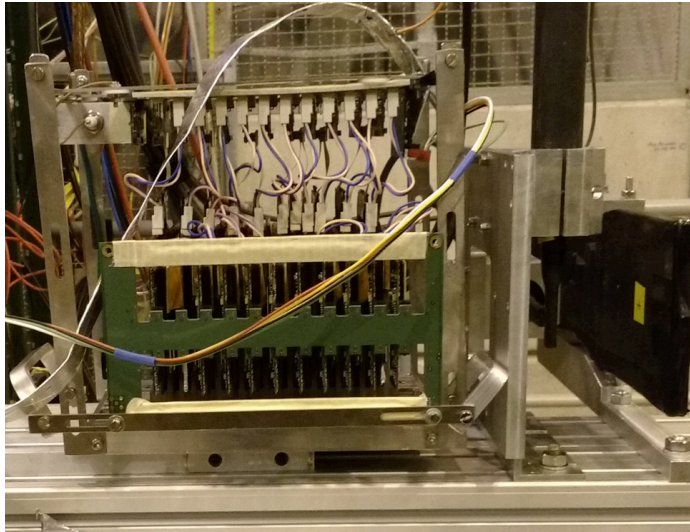


Figure 6.13: Experimental arrangement for the full-length Prototype with 19 layers of silicon pad detector arrays and tungsten plates along with all associated electronics for the test at CERN-SPS.

earlier, we have compared the experimental data with that of simulation for the full-length prototype as well.

### 6.4.1 Fabrication and beam test

With a wealthy TEST-BEAM with mini-prototype, we have earned experience to improve and step forward to the next level of prototype building. The successor in this series of prototype development was a full-depth ( $19X_R$  thick for this case) calorimeter, as shown in the figure 6.13, with silicon detectors and tungsten absorbers like earlier along with other components like Stainless steel metal frame, Back-Plane PCBs, readout electronics, data acquisition system etc. Unlike its miniature version, the detector layers, this time, is an array of  $6 \times 6$  of dimension  $1 \text{ cm} \times 1 \text{ cm} \times 300 \mu\text{m}$  silicon pad detectors on a single 4-inch n-type wafer.

**$6 \times 6$  silicon detector array:** A new set of silicon detector array had been designed and fabricated for the full depth focal prototype. Unlike earlier, the detector array is now on a single wafer, resembling toward the final requirement for the proposed FOCAL. Since the detectors are supposed to work under extreme operating conditions like very high luminosity and radiation environment, it has been designed with high breakdown voltage to avoid any possible polarity inversion which might occur due to constant operation. On the other hand, experiments in high particle density environment demand minimisation of dead area and fill

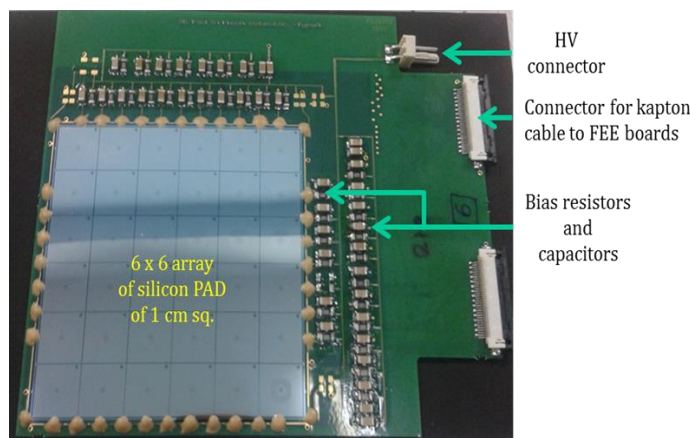


Figure 6.14: (Colour online) Sketch of the silicon detector array of dimension  $6 \times 6$  made of  $1 \text{ cm}^2$  silicon pad detectors which are fabricated on a single wafer and mounted on a detector PCB.

factor improvement. Design of silicon PAD was accomplished with multiple guard rings, optimised inter-pixel separation for reduced cross-talk, improved fill factor etc. Alignment sites were specifically designed and optimised for proper laser alignment of the stacked PAD detectors. The  $6 \times 6$  arrays of silicon PADs with  $1 \text{ cm}^2$  individual pixel size has been designed and developed with two different types of packaging options, firstly with conventional wire bonding and bump-bonding as a second option. The bump bonding is to be done using Under Ball Metallisation (UBM) technique which allows flip chip bonding and thereby enable 3D packaging. The highlight of the first design (wire bonding) was an interconnection and routing among the individual PADs with a single metal. Careful routing ensured minimum crosstalk among the PADs and also minimum dead area leading to maximum fill factor. An optimally spaced multiple Guard Rings (GRs) and inter Guard Rings have been incorporated in the design to assure uniform field inside, high enough breakdown voltage and reduced surface leakage current. The fabrication of the detectors was carried out on  $300 \mu\text{m}$  thin n-type FZ wafer with  $\langle 111 \rangle$  crystal orientation. The starting resistivity of the wafer is  $4\text{--}5 \text{ k}\Omega\text{-cm}$ . p n junctions were created by implanting p-type impurity from the top side. The fabricated silicon PADs are die-attached and mounted on a  $0.08 \text{ cm}$  thick four layer PCB followed by gold wire bonding to connect each pixel to PCB, as shown in following figure 6.14. The detectors were attached to the PCB with silver conductive epoxy of resistivity  $0.006 \Omega\text{-cm}$ . The fabricated and packaged detectors are then thoroughly tested in the laboratory. It has been found that the detectors have less than  $10 \text{ nA/cm}^2$  with a breakdown voltage more than  $500 \text{ V}$ . With a full depletion achieved around  $60\text{V}$ , each PAD detectors showed about

45 pF/cm<sup>2</sup>→50 pF/cm<sup>2</sup> detector capacitance. Each detector array was well wrapped with thin aluminium sheet and black paper against the EMI-protection.

**SPS-H6 beam line:** The beam test was carried out with H6 beamline at CERN-SPS [136]. H6, a secondary particle beam, part of SPS North Area located in EHN1, can provide hadrons, electrons or muons of energies between 10 and 205 GeV/c, depending on H8-Beam condition. A 450 GeV/c typical primary proton beam with intensity 10<sup>12</sup> per burst is extracted from the SPS and directed on the T4 primary target. The symmetry on the T4 target should be at least 80% for proper operation. Among the three secondary beams that are derived from T4 target, H6 beamline was used for the present prototype experiment. As momenta and polarities of the three beams are strongly correlated, the H6 beam always runs at the polarity of H8 beam and typically up to about 50% of the momentum chosen in H8. There are three modes (**High resolution, High transmission and Filter Mode**) of operation for the use of this H6 beam line. Filter-Mode of operation customarily serves the purposes for test-beam which can give different types of particles with a wide range of particle energy in a range of 5→205 GeV/c. In addition, it has several possibilities to provide tertiary beams in case required.

**Prototype at H6 beam line:** Before commissioning at SPS beamline, a meticulous check for all the components both separately and after assembling, was done with full Data acquisition in the laboratory. During the allotted time period, two consecutive prototype set-ups were placed at the beamline with an option to move the front-set-up (prototype under consideration) away from the beam. Primarily at the beginning, 11 layers of detectors were mounted in alternate layers with full absorber depth. After a successful test, the full configuration with all 19 detector layers was installed. The first set of data was taken with MANAS ASIC (experimentally proved working with HEP experiment ALICE) as readout electronics. After completion of data taking for all available energies (5→120 GeV/c), the **newly developed large dynamic range ASIC ANUSANSKAR** was mounted for few specific layers. Details of the test results will be discussed in the results section afterwards. The detector array along with the PCB is interleaved between two 10 cm× 10 cm×0.03 cm tungsten plates in the prototype and connected to the ASICs through patch-bus cable either from one side or from the top of the mechanical frame, specially developed made of stainless steel for this purpose. Proper one to one detector alignment from layer to layer was taken care during assembling of the prototype calorimeter. Two types of readout ASICs, for the prototype test, were used (MANAS and ANUSANSKAR). However, an ANU(INDRA) used here is a modified version of its successor used during mini-prototype test. In these

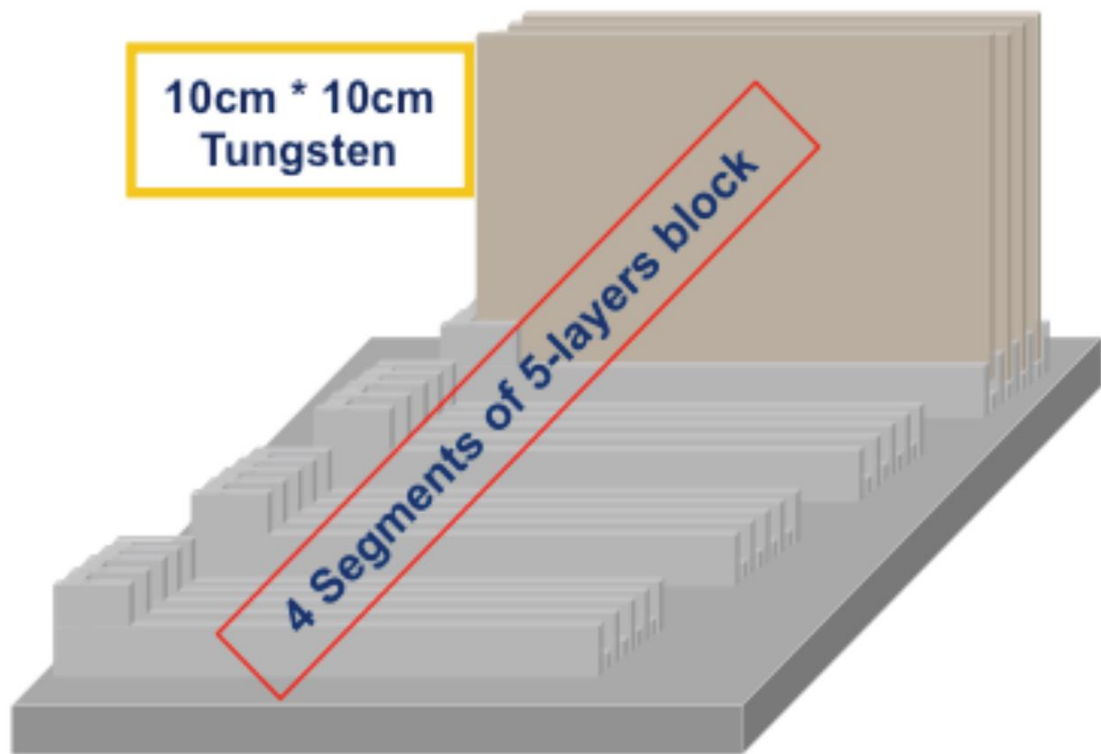


Figure 6.15: Schematic of the mechanical frame, designed and developed for the FOCAL prototype, is made of stainless steel. There are four movable segments, each of which can accommodate five detector and absorber layers. Option for electrical connections are kept both from either side or the top of the frame.

19 layers of arrangement, detectors were distributed among five longitudinally movable segments each with five layers in the mechanical arrangement as shown in figure 6.15. This movable segments can be adjusted such that another set of detector layers (e.g. HGL with MAPS) can be inserted at depth with multiple of five  $X_R$ . It kept an option for a test with Hybrid configuration with both LGL and HGL together. The prototype calorimeter was screwed firmly on a X-Y moving table (motor driven) taking z as the beam direction. This, in particular, helped for any necessary alignment of the prototype with respect to the beam line as well as keep provision for the experiment of another prototype behind it. During laboratory tests, there were few average/faulty PADs (channels) found for several detector layers and documented for any future reference. Proper positioning was maintained to allocate best detector layers around shower-max region, calculated for the available particle energy. A schematic of the full-length structure with hierarchical positioning of each component is shown in figure 6.16. For the prototype experiment, the first detector frame starts at 2.4 cm

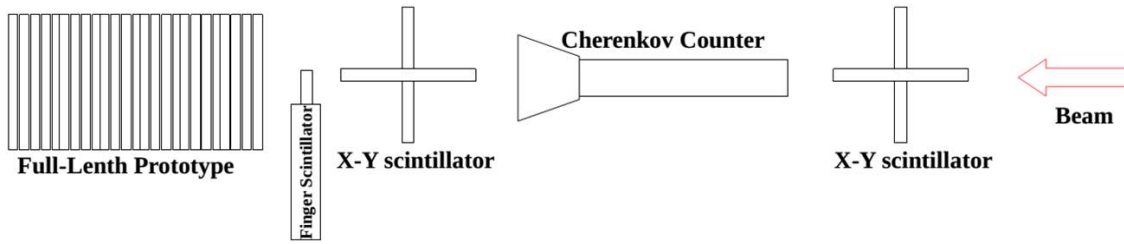


Figure 6.16: Schematic of the experimental setup for the full-depth prototype calorimeter which has been used at CERN-SPS. Different components of the experimental set -up are shown in the figure in a hierarchical order as positioned during the experiment.

away from the starting of the super base of the mechanical frame. All the PAD detectors were biased with a common operating voltage 45 volt. Other relevant low voltages applied to bias the readout electronics used in the experiment are listed as following -

$$LV = (V_{DD}, V_{SS}, V_{CC}) = (+2.5, -2.6, 3.3) \text{ V, with respect to Ground at } 0 \text{ V.}$$

And 3.3 V for CROCUS and corresponding Currents  $I = (0.83, 1.05, 0.26)$  Amp respectively.

**Trigger unit:** A dedicated trigger system having X-Y scintillator and finger scintillator was used. A Cherenkov counter in the upstream was there at beam line in SPS for selecting electron beams specifically. 3-fold (scintillator) trigger signal was used for  $\pi^\pm$  or  $e^-$  -data taking whereas a custom pulser signal feed during pedestal mode of data taking. A quick online analysis of data sample was used for quality assurance and other relevant instant actions like proper alignment of the detector with a beam, beam quality and position of the prototype with the beam for better acceptance etc. For better referencing, the pedestal has been taken before each and every data. As was expected a mere saturation effect was found for the higher side of the incident energies with MANAS ASIC because of its limited dynamic range. The details of the test beam performances will be discussed in the next sections.

## 6.4.2 Data analysis and performances

To start with the analysis of test beam data taken with the full depth prototype calorimeter, The first step could have been to study the combined response of noise both from detector and the readout channel which was measured in absence of beam. The background, commonly known as pedestal response, of the system for each detector channel in terms of mean and RMS of noise for the respective channel is shown in figure 6.17. Each 32 channel corresponds to a particular detector layer along the depth of the calorimeter. The mean was found about 250 ADC and is stable with time. The RMS (representing the noise) is found between 1.5

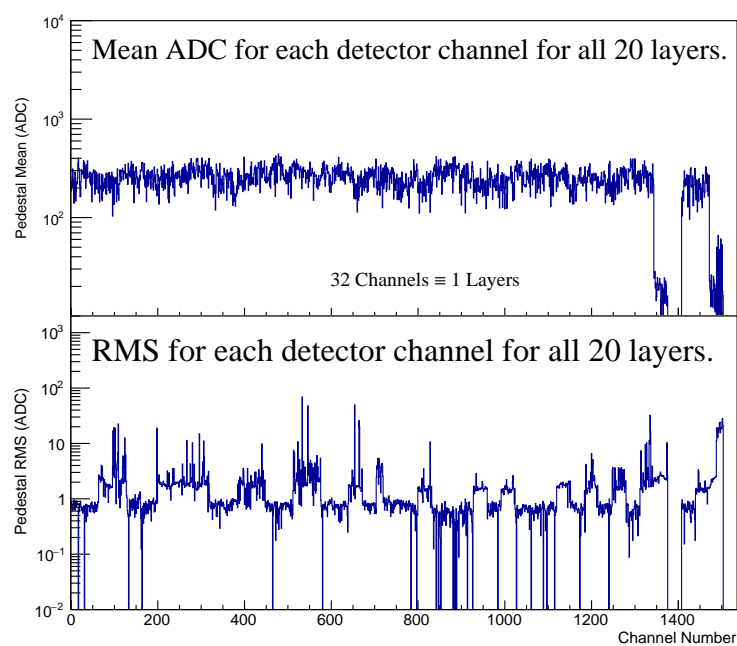


Figure 6.17: (Colour online). The figures show response of silicon pad detector in terms of the mean (upper) and RMS (lower) values of the pedestal as a function of electronic channel. Each 32 channels corresponds to one layer of the prototype calorimeter. In RMS plot, sharp drop to zero represent dead channels which was taken care during offline analysis.

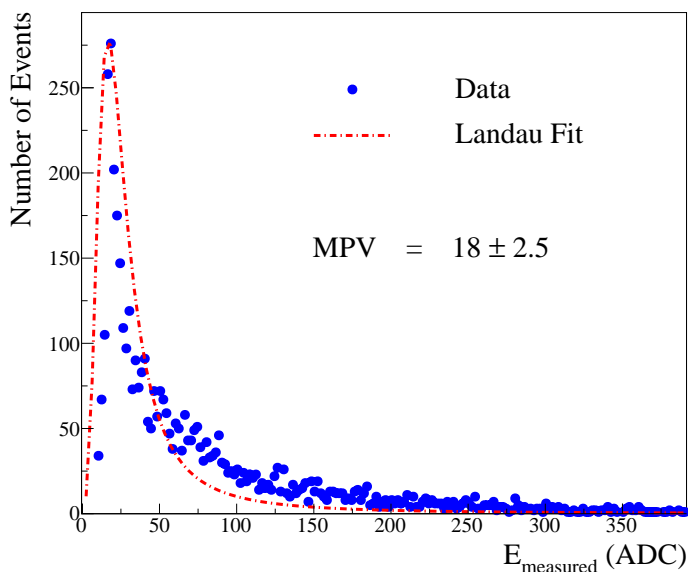


Figure 6.18: (Colour online). The plot shows the ADC distribution for pions as reconstructed from the prototype test data. The distribution reproduce the minimum ionising particles response.

to 2.5 ADC. Some fluctuations, however, have been found in RMS plot for few particular channels with either RMS shooting up (noisy channels) or to some larger value or touching zero (dead channels). Ideally, the dead and noisy channels should be counted during analysis. In our case, for counting of the signal of EM showers, these channels are assigned ADC values which are average of its adjacent channels.

The test beam results have been reconstructed and compared both with earlier mini-prototype test results and simulation for the sake of consistency. With SPS this time, the response and characterisation of the prototype could be accomplished much more elaborately with a wide range of available incident energies for different incoming particles, Undoubtedly, particles with relativistically high energy deposit minimum amount of energy, as was prescribed by Bethe-Bloch formula [137] and can be described by Landau distribution [130]. Depending on the detecting medium and associated electronics, the Most Probable Value (MPV) of the Landau-distribution fitted to the experimental data was extracted. Pion beams at an incident energy of 120 GeV were used to obtain the MIP energy deposition. The response of silicon PADs at  $2^{nd}$  layer (after  $2X_R$  depth) is shown in figure 6.18 in terms of the ADC values. The data is fitted well with a Landau distribution and provides most probable value (MPV) of  $18 \pm 2.5$  in units of ADC in compare to earlier results of 0.083 MeV

from simulation ( 5.13) and  $17.09 \pm 2.03$  ADC in CERN-PS test beam 6.8. The response for MIP was studied in earlier test beam with bare silicon pad detectors without any absorber plate in front [120]. The MPV of the ADC spectrum obtained in the present study is similar within the error bar. Though the measurement was taken with a  $2X_R$  material placed in front it hardly matters for the minimum ionising particle. A clear MIP signal for the calorimeter assures a better Signal to Noise ( $\frac{S}{N}$ ) discrimination capability.

**An electromagnetic shower** is originated either by bremsstrahlung or pair production, depending on the incident particle  $e^-$  or  $\gamma$ , and continues to grow along the depth till it reaches the critical energy ( $E_C(MeV)$ ) and then dissipates mostly by collision/ionisation processes. However as is discussed already, EM-shower from heavier particles like pions, protons etc. are less likely though there is a probability of hadronic-shower production. But Hadronic shower will start seldom within the extent of the present calorimeter depth. A wide range of incident energy for inflowing electron starting from 5 GeV to 60 GeV was used to characterise the full-depth prototype calorimeter to EM-shower. The shower shape in terms of energy deposition in each layer has been studied to understand the development of EM-shower both in longitudinal and transverse directions. This has been obtained by summing deposited energy in the unit of ADC for individual silicon PADs of each layer. For a particular incident electron energy, a number of silicon PADs are hit in each layer which is facing the transverse plane of the propagating shower. The deposited energy in all PADs of each layer are summed to obtain the total energy deposited in the particular layer. As an example, the summed energy deposition in units of ADC for the 7th layer of the prototype calorimeter is presented in figure 6.19 for six different incident energy electrons, 5, 20, 30, 40, 50 and 60 GeV respectively. The abscissa gives the total measured ADC, whereas the ordinate is expressed in terms of probability where the counts are normalised to the number of total events in each individual case. All the measured energy spectra are of Gaussian shape with the mean value shifted towards the right with an increase in incident energy. These results are used later on to obtain longitudinal shower profile, total energy deposition and energy resolution of the detector which will be discussed shortly.

As already shown in the previous section and discussed in details in [107], energy deposition profile, as a function of layer number (depth in the unit of  $X_R$ ), first rises to achieve shower-maximum and then falls gradually. For the full depth prototype under consideration,  $19 X_R$  thickness is enough to let the EM-shower develop completely for 5→60 GeV electron with nominal longitudinal leakage. The longitudinal profile reconstructed from data is fitted with the same empirical formula  $\frac{dE}{dX_R} = E_0 * t^a * e^{-b*t}$  with  $E_0$  as incident energy and "t" as thickness in unit of radiation length and shown in figure 6.20. A detailed analysis of

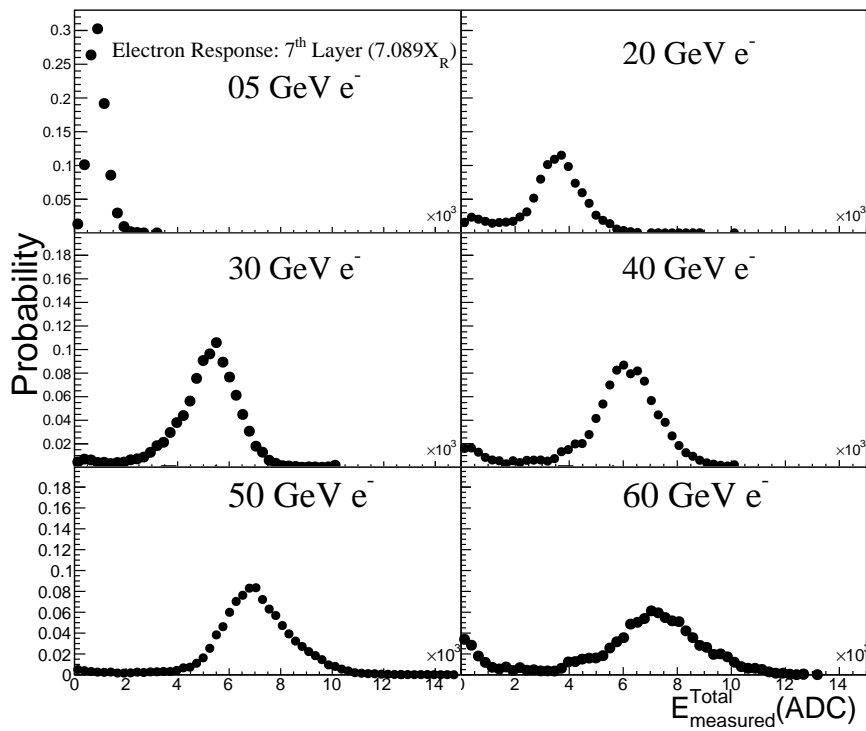


Figure 6.19: (Colour online). Energy deposition in unit of ADC at the 7th layer of the Si-W calorimeter prototype for incoming electrons of different energies (5, 20, 30, 40, 50 and 60 GeV). Gaussian fits to the curves give the mean ADC value of the spectra which are shifting to right gradually with the increase of incident energy.

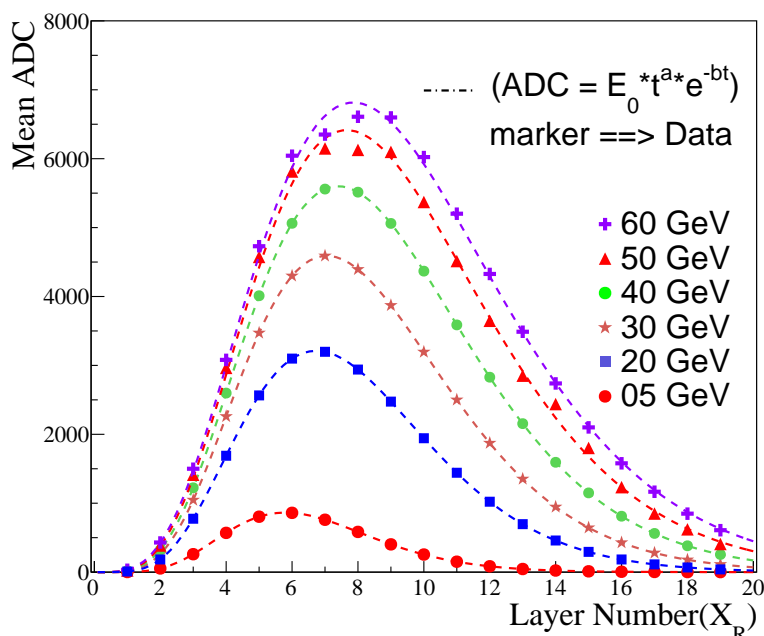


Figure 6.20: (Colour online) The figure illustrates the longitudinal shower profile which has been reconstructed using experimental data from full depth prototype test at CERN-SPS.

the longitudinal profile of EM-shower upto 40 GeV can reproduce the trend quite well as predicted by the empirical model but for higher energies, a flat region instead of a peak has appeared. The discrepancy at higher incident energies is suspected to be because of the limited dynamic range (lead to saturation in energy measurement) of the front-end-electronics (MANAS ASIC) used in the experiment. To have a comparative picture, response to electron-induced shower by the full prototype as a whole has been plotted in figure 6.21. Total energy deposition in the calorimeter is obtained by summing the deposited energies of all silicon PADs of all detector layers. Distribution of total measured energy in the unit of ADC over a large number of events represents the response of the incident electron. Figure 6.21 explains the behaviour of total measured energy for six incident electron energies. Gaussian shapes have developed at each energy and the distributions are well separated from each other. Peaks corresponding to different incident energies shift to the right with the increase of incident energy. Minor distortion has been found for 50 and 60 GeV electrons and expected to be attributed to the limited dynamic range of the readout ASICs, mixing of the hadronic shower in EM-shower or late produced  $\gamma$  by strong interaction within the calorimeter depth. Moreover, a slight bulging has been observed for 50 GeV electron which might arise because of contamination of low energy electrons. To be a decisive energy measuring instrument, the calorimeter should ensure linearity between incident energy and the respective measured

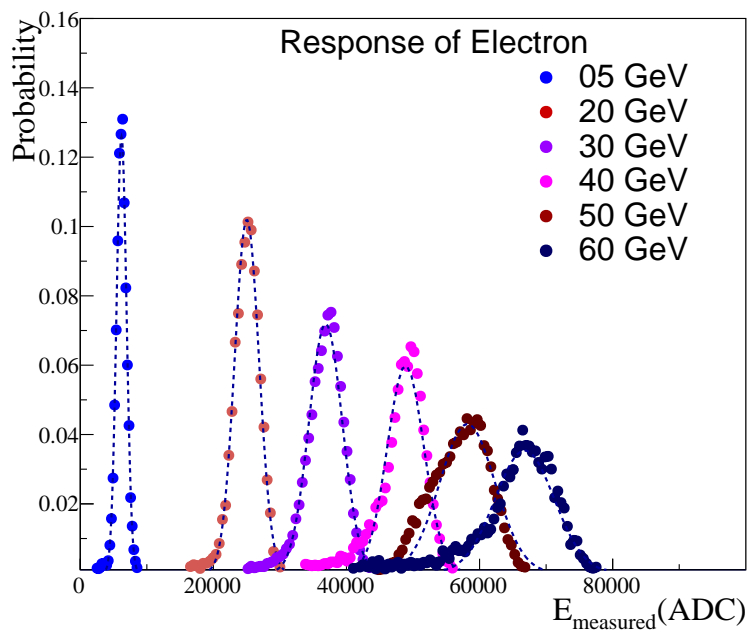


Figure 6.21: (Colour online). The plot shows the distribution of total energy deposition as measured by the full depth prototype calorimeter. The energy is expressed in unit of ADC as shown in the X-axis of the figure.

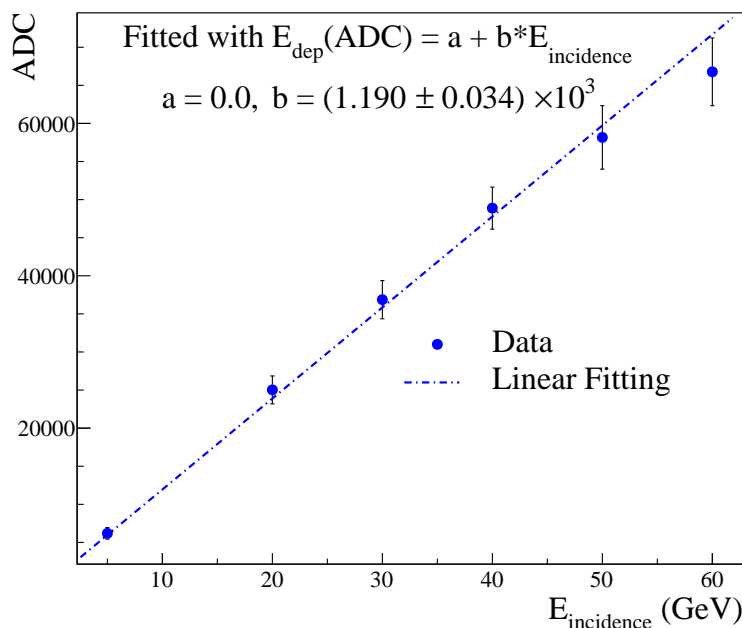


Figure 6.22: (Colour online) Calibration Curve from experimental data (ADC) to Incident energy of incoming particles (GeV).

energy. As only about 2% of the total deposited (in active layers only) energy is available for signal production and also an additional conversion factor to the electrical signal, a final calibration curve needs to be established between the measured energy and the incident electron energy. For this purpose, the mean value of the total measured energy profile for the calorimeter at each incident energy, obtained from figure 6.21. The calibration curve, as shown in figure 6.22, correlate total measured energy as a function of incident energy of electrons. The linearity between measured and the incident energy can be expressed quantitatively as:  $E_{\text{dep}}(\text{ADC}) = (1.190 \pm 0.034) \times 10^3 * E_{\text{incidence}}(\text{GeV})$ .

As a final and most important performance check, the energy resolution of the prototype calorimeter was investigated and reconstructed for the available incident energy range. For given incident energy, energy resolution is defined as the ratio of the  $\sigma$  to the mean of the distribution followed by the total deposited energy. Figure 6.23 represents energy resolutions as a function of incident energy, as obtained from the data. The resolution can be illustrated as a combinatorial effect of the structure for calorimeter, energy sampling efficiency, noise from detector and readout electronics and etc. The resolution of a calorimeter, usually

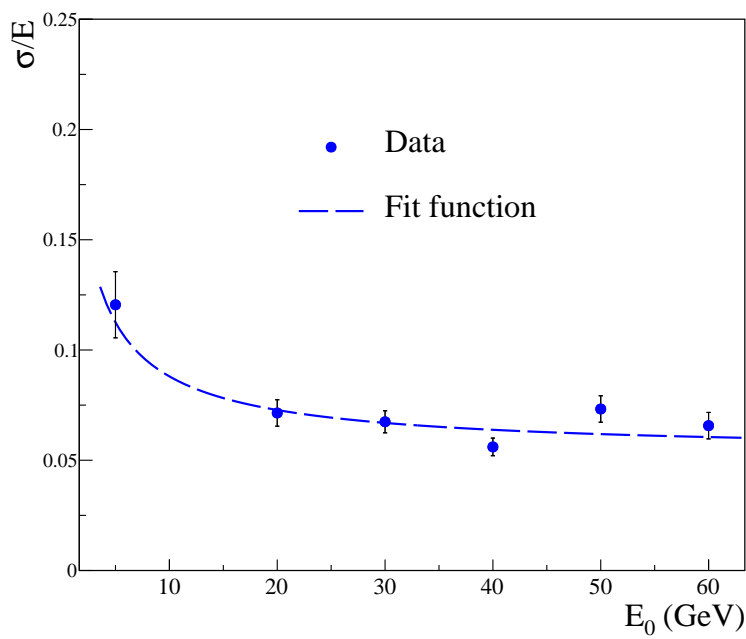


Figure 6.23: (Colour online) The figure presents the energy resolution as a function of incident energy of incoming electrons from experimental data. The data resulted resolution expressed with  $a = 0.053 \pm 0.005$  and  $b = 0.221 \pm 0.036$  which has been obtained from the fitting with  $\frac{\sigma}{E_{dep}} = a \oplus \frac{b}{\sqrt{E_0}}$  over the incident energy range of  $5 \rightarrow 60$  GeV .

parametrised in terms of an empirical formula [105]

$$\frac{\sigma}{E_{dep}} = a \oplus \frac{b}{\sqrt{E_0}}, \quad (6.1)$$

where,  $a$  and  $b$  are fit parameters, carrying definite physical importance. Fits to the data points yield,  $a = 0.053 \pm 0.005$  and  $b = 0.221 \pm 0.036$ , which can be considered to quote the energy resolution for the prototype under consideration. However, for sake of completeness, a different empirical formalism as expressed by following equation [105],

$$\frac{\sigma}{E_{dep}} = a \oplus \frac{b}{\sqrt{E}} \oplus \frac{c}{E_0}, \quad (6.2)$$

is also applied to understand the resolution. Here, the first term takes into account the contributions from the compactness of the calorimeter, the second term arises because of the stochasticity of the signal production process and the third term is related to the noise. Fits (not shown in the figure) using this formula, yields,  $a = 0.061 \pm 0.008$ ,  $b = 0.085 \pm 0.04$  and  $c = 0,48 \pm 22$ . If a part of the contribution to the energy resolution is accounted for electronic noise, this formula gives the contribution to the resolution of about 8.5% by the  $\frac{1}{\sqrt{E}}$  contribution which ensures the calorimeter to be as one of the best in its class. However, to be noted, the last two points (corresponding to 50 and 60 GeV) are sitting away from the trend. The reason might be partial because of the saturation effect of the readout electronics and due to shower leakage which might have worsened the resolution. In conclusion regarding the test beam experience for FOCAL prototype, the results, indeed, support the construction according to the conceptual design for the calorimeter, a feasible solution as well as the experimental ground for developing full-scale calorimeter in future.

## 6.5 Summary and Scope

Summarising in brief, the development, fabrication and test of a series of prototype calorimeter, starting from mini-prototype to full length, for proposed FOCAL have been discussed in this chapter. In short, mini-prototype establishes the proof of working principle for FOCAL in terms of basic calorimetric performances even with the limited depth. Reconstruction of responses for minimum ionising particle and EM-shower were described and discussed in regard to detector construction and characterisation. A full-depth silicon-tungsten prototype calorimeter, as a successor of a Mini-prototype, has also been fabricated and assembled to test at CERN-SPS beamline facility. Details of the construction of the prototype along with its each and every component were presented and discussed. The prototype consisted of

nineteen layers of silicon PAD detector arrays (on a single 4 inch n-type wafer) and several tungsten layers extending the effective depth of the calorimeter to be about  $19 X_R$ . The Prototype has been tested with 120 GeV pion and 5 to 60 GeV electron. The response of the prototype calorimeter to both MIP (pions) and EM-shower (electrons) has been reproduced and analysed. Clear development of the MIP signal shows an excellent S/N ratio. Widely separated EM-shower signal for different energies in the available energy range established a very good energy resolution of about 8.5% with three parameter fit. Linear behaviour of measured energy with that of incident energy ensures satisfactory calorimetric performances. Though an issue with saturation due to readout electronics was found but has been taken care of, with the development of a new large dynamic range ASIC as a next step for the calorimeter development. The development of the silicon detectors for the proposed calorimeter can be summarised pictorially by the following sketch 6.24 Because of the saturation effect found at higher energies of incident particle, a serious effort was put in developing dedicated readout electronics. A series of efforts are already in action. ANU chip with the help of BARC has reached a satisfactory level to handle such requirements of large dynamic range electronics. ANUSANAKAR have already been tested in this series but it has limited dynamic range as well but helped a lot in understanding the next level development. ANUINDRA on the other hand, the latest ASIC developed, have a dynamic range of 2.6 pC compared to its earlier version of 600 fC. Laboratory test results of the chip found to be hopeful in fulfilling the requirement. As a next check, another test with the upgraded electronics was put as next aim shortly.

In continuation of the physics motivation behind the proposed calorimetry for ALICE, we have studied the particle production in proton-proton collision at LHC energies which otherwise treated as baseline/reference for understanding particle production in heavy ion collision. In our study, particle production in pp collision found to have origin both from soft and hard scattering process. Moreover, probing the system produced in pp collision at LHC energies, revealed unexpected collectivity for high multiplicity events. As a natural consequence, pp collision, as a reference for heavy-ion collision, need to be used carefully. The details about particle production in terms of two-source model (NBD), search for collectivity in pp system with blast-wave model approach will be discussed rigorously in the next chapter. Moreover, a search for signal related to the degrees of freedom, governing the system formed in pp collision, has been formulated using Bjorken prescription. The details about Bjorken energy estimation for pp system will also be presented to understand the nature of collectivity (hadronic/partonic) found in small systems.

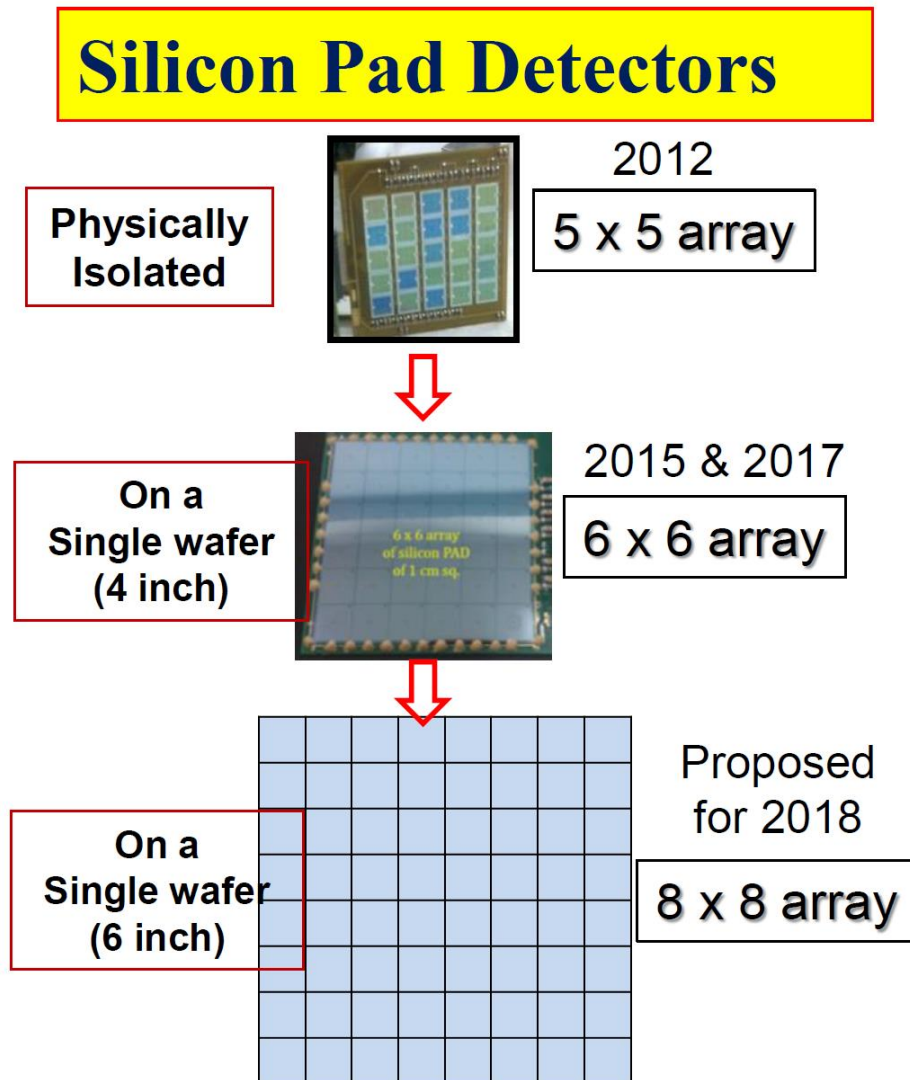


Figure 6.24: A series of detector development starting from the  $1 \text{ cm}^2$  physically isolated detectors to  $6 \times 6$  array of  $1 \text{ cm}^2$  on a single 4 inch wafer shown. The proposed final requirement for detector also shown in the sketch.



# Chapter 7

## High Multiplicity Proton-Proton Physics

### 7.1 Introduction

With the increase of incident energy of probing particles, the experimental techniques, mostly following Rutherford technique as is represented in equation 7.1, evolved at a steady pace to render physics interests starting from material science to finest structural concepts consist of coloured partons [8]. With the advancement of accelerator technology, collimated Tera electron Volt (TeV) energy is now a day available for an experiment in compare to early days naturally available MeV energies. The finer structure of nucleus and nucleons can be investigated to a length scale of femtometer following the de'Broglie hypothesis of wave-particle duality, as shown in table 7.1, where sub-nucleonic elements like quarks and gluons become relevant degrees of freedom. Depending on the available energy of scattering/collision and the choice of system, the physics reach could be of a different kind. for proton-proton, proton - heavy ion and heavy ion - heavy ion collision. Proton-proton collision illuminates the basics of hard scattering among partons whereas, nucleus-nucleus collision revealed the properties and evolution of a system which might have formed during the collision. The system formed in the nucleus-nucleus collision indicates the formation of a quark-gluon plasma state, as has been discussed in Introduction. Characterisation and quantification of various properties of the Quark-Gluon-Plasma (QGP) need a clean baseline understanding which is provided by proton-proton (pp) collision at the same energy. Before LHC era, pp collisions was strongly endorsed to yield particles which are the outcome of hard-scattering between partons followed by hadronisation. However, increase in centre-of-mass energy for pp collision, new speculation noticed regarding the behaviour of the system associated with a large number of particle production which could not be explained only by hard-scattering and found mimicking phenomenon more similar to heavy-ion-collision on small scale.

More specifically, a class of events (known as High Multiplicity (HM) events) in pp-collision was found which are found responsible in deviating pp system from its so far underlying nature. There are plenty of descriptions, such as hydrodynamic model, saturation model (Colour Glass Condensate: CGC) [40–46], Colour Reconnection (CR) model et.c, available in the literature [102–104] in understanding this anomalous aspect in pp collisions. Of course, no single model description can uniquely explain the phenomenon HM pp collision and associated with advantages and inadequacies of their own. In the present study, we will focus towards a hydrodynamic inspired model description for pp collision at LHC energies. Even though there can not be a smoking-gun signal/explanation till date to have a conclusive description, but it has been found that the particle production mechanism in pp collision is contributed by soft scattering and hard scattering partially which become more prominent at LHC energies. Not in all, rather pp events tagged with high multiplicity, demand for a new interpretation away from underlying physics interpretation. In the subsequent sections, first, a NBD model-based approach will be adopted to elucidate on probably more than one type particle production mechanism in pp collision. The understanding of the system formed in pp collision was studied using Blastwave model which assumes collectivity for the system under study. A positive search for collectivity in pp system appeals for harvesting the source for collectivity. In the last section in this chapter, an effort was made to understand the collectivity either coming from a partonic or hadronic form of matter using simple Bjorken formalism [138]. The study will be wrapped up with further possibilities and future scope in this direction.

$$\left(\frac{d\sigma}{d\Omega}\right) = \left(\frac{zZe^2}{2\mu v^2}\right)^2 \frac{1}{\sin^4 \frac{\theta}{2}}. \quad (7.1)$$

where  $\mu \rightarrow$  reduced mass,  $\theta \rightarrow$  scattering angle

## 7.2 Review and motivation of proton-proton physics

At ultra-relativistic high energies at LHC, proton-proton collision predicted the existence of long-awaited Higgs boson [10, 11], responsible for mass generation. On the contrary, pp collision serves more orderly in understanding each aspect of partonic interaction in terms of particle production. When a proton approaches a proton relativistically, constituent partons from both the proton interact strongly among themselves which is calculable using either perturbative Quantum Chromodynamics [139–141] or by non-perturbative model

Table 7.1: An overview of the dimension that can be probed with proton and electron of different beam energies using de’Broglie hypothesis.

| Energy  | $\lambda^{proton}(\text{fm})$ | $\lambda^{electron}(\text{fm})$ |
|---------|-------------------------------|---------------------------------|
| 1 MeV   | 28.6137                       | 871.9207                        |
| 10 MeV  | 090268                        | 118.0961                        |
| 100 MeV | 02.7888                       | 12.3356                         |
| 1 GeV   | 00.7310                       | 01.2392                         |
| 10 GeV  | 00.1138                       | 00.1239                         |
| 100 GeV | 00.0123                       | 0.01239                         |
| 1 TeV   | 00.0012                       | 0.31                            |
| –       |                               |                                 |
| 7 TeV   | 00.0002                       | –                               |

calculation depending on momentum transfer scale involved in the interaction. Eventually, scattered partons, can not stay in the coloured state due to colour confinement, will lead to various colourless particles like pion, kaon, proton, neutron and so on at the final stage. There exists models explaining hadronisation mechanisms (more popularly known as Fragmentation Function, FF) such as recombination [142–147], jet fragmentation [148–152] etc. Assuming factorisation [153], particle production in pp collision can be estimated using parton distribution, interaction cross-section and fragmentation function respectively. Till very recent breakthrough of High Multiplicity (HM) events in pp collisions [156], where an unexpectedly large number of particles has been produced as shown in figure 7.1, pp collision was essentially served baseline for more complex systems produced in heavy ion collisions (AA). The properties of a collective system produced in heavy ion (AA) collisions could be represented by a simple ratio, as is represented in equation 7.2. The particle production in AA collision can be scaled by the number of particles produced in pp collision along with a normalisation factor, defined by the number of the binary collision. Nevertheless, there had always been a different approach [157, 158, 71, 159] nourished which advocate for the possibilities of AA-like system on a small scale for pp collision as well. Early in SPS age, pp events in experiments [160, 161] impelled for the occurrence of high energy density events and an inspired quest for evidence of de-confined medium in pp collisions even at  $\sqrt{s} = 0.54$  TeV at SPS [157] and at  $\sqrt{s} = 1.8$  TeV [158, 71] at Tevatron, Fermilab.

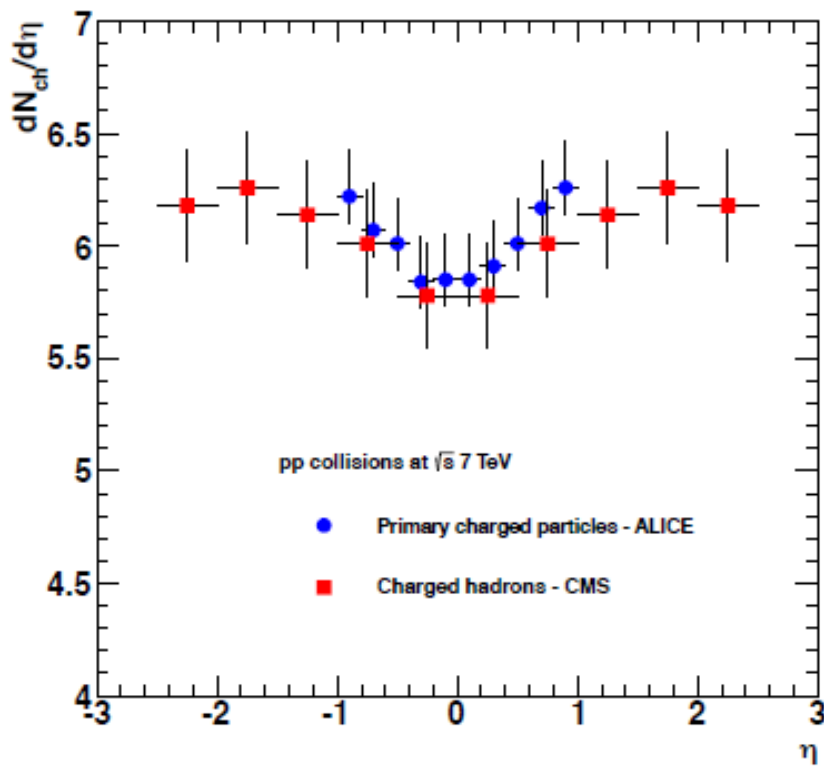


Figure 7.1: (Colour online). The plot shows the measured multiplicity density both by ALICE [154] and CMS [155] for proton-proton collision at  $\sqrt{s} = 7$  TeV. The value for the multiplicity density for pp collision reach to a limit where the possibility of medium formation is predicted energetically.

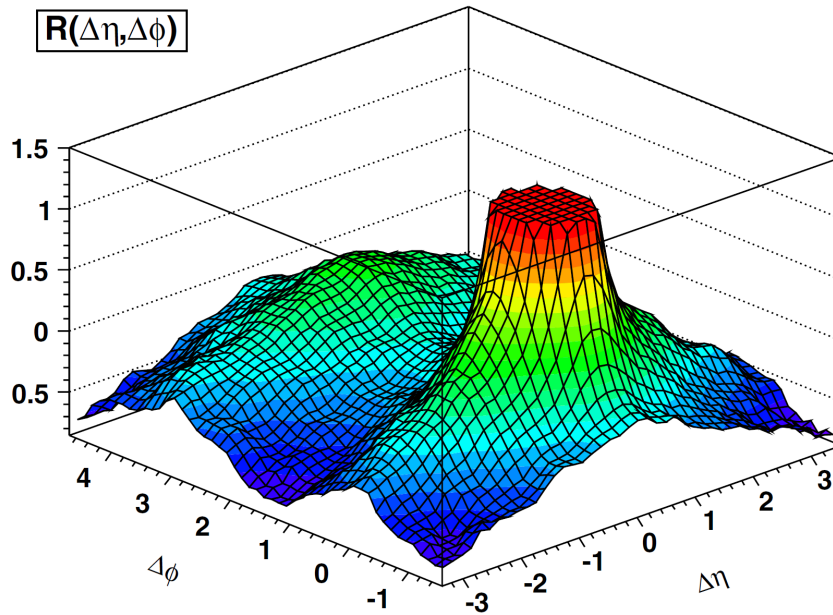


Figure 7.2: (Colour online). Ridge, structure found for particle correlation in  $\Delta\eta - \Delta\phi$  plane, attributed to hydrodynamical description in case of heavy-ion collision, has been found also in proton-proton collision recently.

$$\text{Scaled Particle production in AA-coll} = \frac{\left(\frac{dN}{dP_T dy d\phi}\right)_{AA}}{N\left(\frac{dN}{dP_T dy d\phi}\right)_{pp}}. \quad (7.2)$$

Studies of properties of final state particles, produced either in pp or in AA collision, are addressed and compared experimentally in terms of definite global variables [162, 163] like transverse momentum ( $p_T$ ) distribution, Pseudo-rapidity ( $\eta$ ) distribution, Multiplicity distribution etc and few more derived physics observables such as flow components, Nuclear shadowing, Double ratio, ridge etc. The pp collisions at LHC energies have resulted in a number of unexpected observations, mimicking on a small scale to the signals for a hydrodynamic system formed in relativistic heavy-ion collisions.

In the present context of the study, Particle production in pp collision at LHC energies has been reinstated using otherwise established model descriptions. There are recent physics observations in pp collision at LHC such as "ridge" [164] 7.2 in HM-pp events which strengthen the possibility of poking for AA-like system. Ridge, a structure found

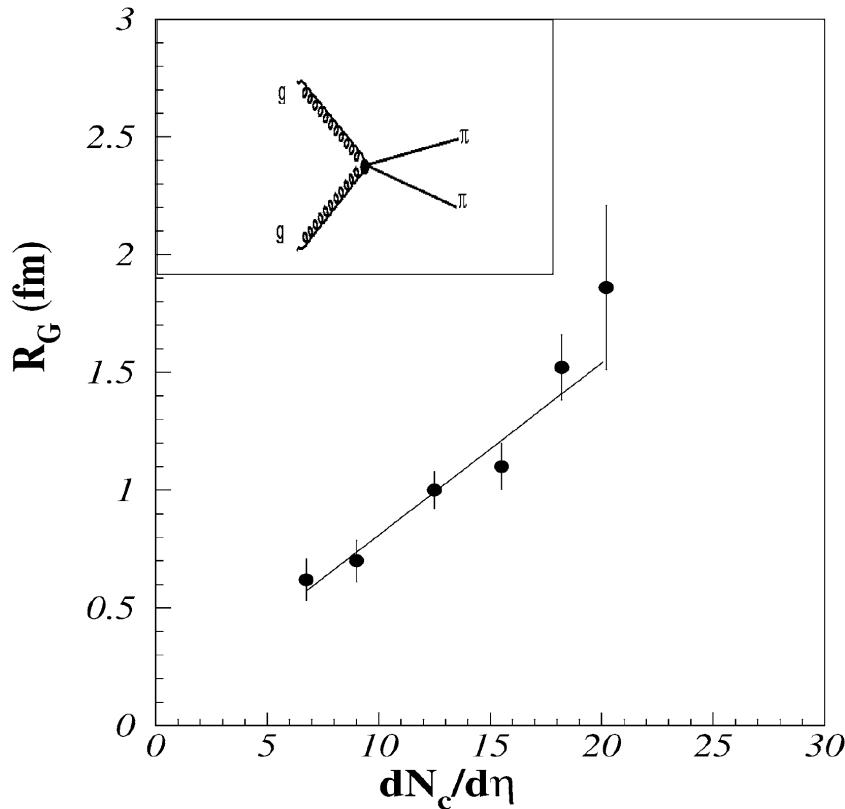


Figure 7.3: (Colour online). HBT radius ( $R_G$ ) of the fireball, produced in proton-proton collision at LHC energy, is shown as a function of charged particle multiplicity density  $\frac{dN_c}{d\eta}$  [71]. The dimension of fireball for high multiplicity proton-proton collision is quite indicative about the existence of a collective medium.

in particle correlation along  $\eta$  in  $\eta - \phi$  plane, is attributed [165] to the hydrodynamical evolution of the system formed in heavy ion collision at RHIC. In addition, the study of intensity interferometry [166], known as Hanbury-Brown-Twiss (HBT), as shown in figure 7.3 correlation, illustrate radii of the source of emission in HM-pp events depends on multiplicity or pair transverse momentum [167, 168] resembling as seen in heavy ion collision at RHIC which has been admitted [169] as the signature of collectivity. As a consequence of these surprising observations in pp collision, there have been numerous attempts [170–177] both to explain and predict collectivity in pp collision as a function of multiplicity, the centre of mass energy etc. The studies are endorsed by the availability of high-multiplicity 7.3, high energy density pp events 7.4 with satisfactory statistics at 7 TeV onwards. Moreover, there are other prescribed observables like direct photons at low  $p_T$  [175], strange baryon-to-meson ratio [176], transverse radial flow velocity [158, 179, 180] etc which indicate the existence

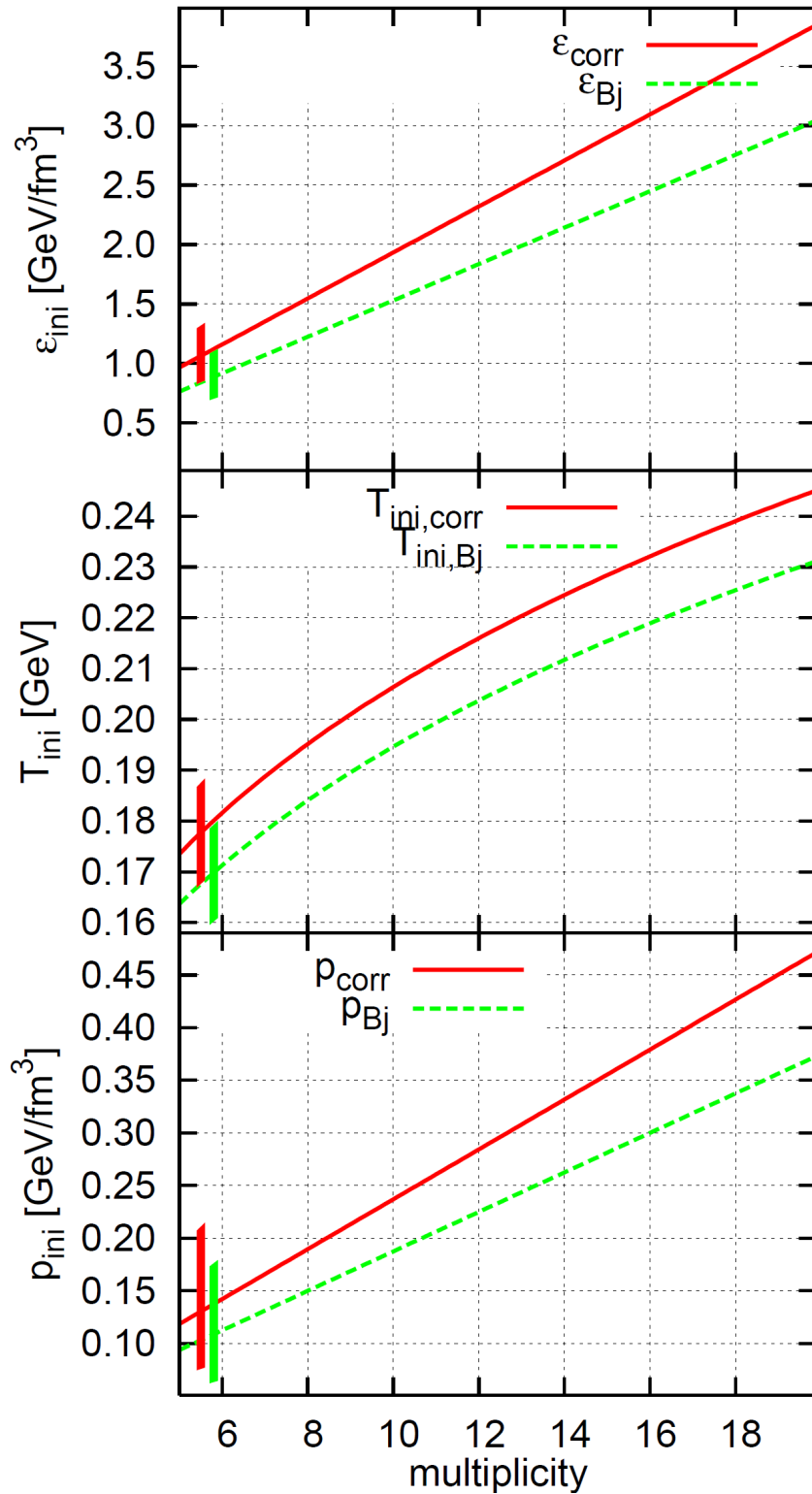


Figure 7.4: (Colour online). Theoretical prediction for initial energy density ( $\epsilon_{ini}$ ), temperature ( $T_{ini}$ ) and pressure ( $p_{ini}$ ) as a function of multiplicity of produced particles in pp collision [178] at 7 TeV centre of mass energy.

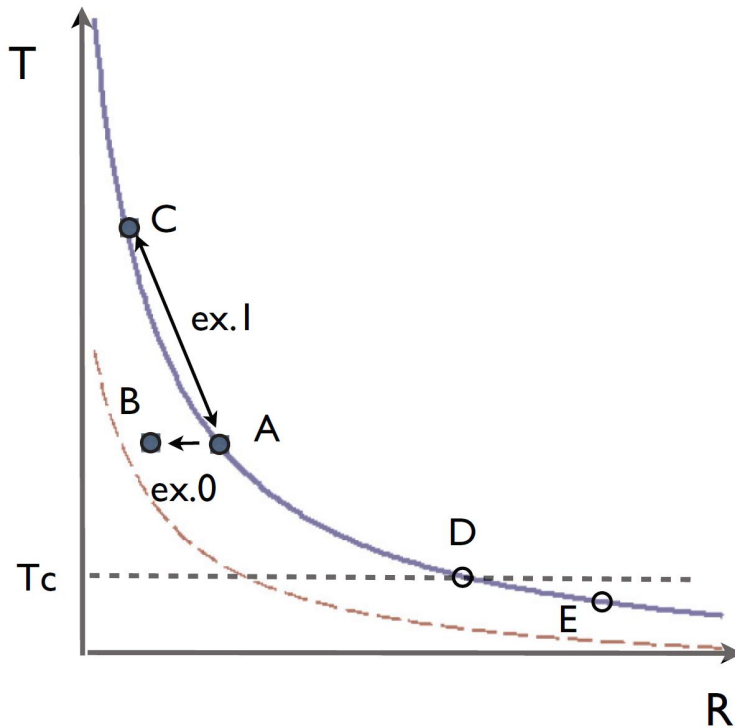


Figure 7.5: (Colour online). Theoretical prediction for the temperature of the fireball formed in small system like in proton-proton as a function of the size of the fireball [186].

of collectivity in a system. Further, significant theoretical approaches [181–183] support the applicability of relativistic hydrodynamics specifically for high multiplicity pp events assuming formation of a non-hadronic medium [181] which is 7.4 energetically possible in pp collisions at LHC energies.

A recent calculation shows that because of approximate scale invariance of sQGP, AA-like hydro can be expected in a smaller and hotter system like in larger and cooler system as explained in figure 7.5 [179]. A pertinent study [184] in search for the change in phase from hadronic to partonic in pp collisions, analysing a wide range of centre-of-mass energy, includes the LHC data also. Though a steady and substantial effort made to promote the liquid dynamical behaviour [173, 174] as a manifestation of the de-confined state of quarks, there has been other pictures available in literature such as colour glass condensate [185], colour reconnection [102–104] etc.

Primarily, relative flattening of the  $p_T$  spectra of identified particles of higher masses in pp collisions at LHC, as observed by the CMS (ref BW 31, 34), encourages to search for possible collective transverse radial flow in pp collisions at LHC. It is relevant in this context

that flattening of  $p_T$ -spectra of particles of heavy masses is attributed to the existence of a common transverse radial flow velocity and studied in heavy ion collisions starting from SPS to RHIC to LHC. Since LHC has potentially delivered centre of mass energy up to 14 TeV, the high-multiplicity events populated more frequently and extend the chance to achieve higher multiplicity classes more and more. Though not yet decisively established whether QGP has been formed in the proton-proton collision or alike small systems but it has opened a new area taking pp collisions more seriously than just for baseline studies.

## 7.3 Framework and models used for pp physics

In this section, we will discuss different models and frameworks those will be used for this study of particle production in the pp collision.

### 7.3.1 Negative Binomial Distribution (NBD)

Long back in 1713 [187], Jakob Bernoulli determined the probability of "k" outcomes in an "n" trials with the help of Binomial expression as expressed in equation 7.3. Since then, Binomial Distribution (BD) had been used abundantly and extensively in almost every field of science to understand and predict relevant properties of the system. Ideally BD, in the theory of probability and statistics, represents discrete distribution having two possible outcomes (true/false, yes/no, success/failure etc). The limiting condition for BD with a number of trial equal "1" is Bernoulli distribution.

$$Pr(k; n, p) = \binom{n}{k} p^k (1 - p)^{n-k}, \quad (7.3)$$

where "k" runs from 1, 0 . . . n and  $\binom{n}{k} = \frac{n!}{k!(n-k)!}$  and p represents the probability of  $k^{th}$  outcome. There can be several restrictions/conditions which can twist the BD to take a new form of distribution and make it usable for application to physical problems. For an example, the probability of the number of successes in a sequence of independent and identical Bernoulli trials before a specified number of failures (denoted by "r") can be represented by Negative Binomial Distribution (NBD). It can be expressed according to the equation 7.4

$$Pr(n, k) = \frac{\Gamma(k+n)}{\Gamma(k)\Gamma(n+1)} \left[ \frac{\bar{n}}{k+\bar{n}} \right]^n \left[ \frac{k}{k+\bar{n}} \right]^k. \quad (7.4)$$

Where  $\bar{n}$  is the average of the distribution and the parameter  $k$  can be related to the dispersion ( $D$ :  $D^2 = \overline{n^2} - \bar{n}^2$ ) as following

$$\frac{D^2}{\bar{n}^2} = \frac{1}{\bar{n}} + \frac{1}{k}. \quad (7.5)$$

In the present study, the Negative Binomial Distribution was used to understand multi-particle production in a relativistic proton-proton collision at LHC energies. Historically, particle production in either many baryonic or semi leptonic processes at relativistically high energies, Negative Binomial Distribution (NBD) found to describe particle production for both total multiplicities and for a restricted interval in phase space [188]. Though not yet clear about the applicability of NBD in explaining the multi-particle production, there were several attempts to understand the physical explanation behind it. The first appealing explanation by Van Hove and Giovannini was in 1987 with the introduction of clans of particle production [189, 190]. It had been shown that NBD is a natural outcome for cascade processes with particles, produced from independent clans. Moreover, though there are also attempts in understanding particle production in terms of Poisson distribution (assuming every single final state particle produced and emitted independently) which is again a limiting case of more general NBD where mean and variance of the distribution are same. In this connection, a very recent theoretical approach [191], Glasma flux tube model, has found the multiplicity distribution of multi-particle production could be interpreted as a convolution of a number of NBD functions which comes as a natural consequence of several impact parameters of the collisions. The model replicates the multiplicity distribution data of pp collisions in a small pseudo-rapidity window ( $\Delta\eta < 0.5$ ) at the LHC energies. It is important to mention that Poisson distribution or NBD in explaining multi-particle production in proton-proton collision is justifiable in lower  $p_T$  range where pQCD has limitation introduced by running coupling constant for strong interaction. The lack of a unique theory to explain the particle production for pp collision over the whole energy range demands phenomenological models for low energy region to pQCD in high energy regime. There have been several studies interpreting proton-proton data at the different centre of mass energies right from SPS to RHIC to LHC consistently. NBD, an one such successful model description, had sufficiently described charged particle "multiplicity distributions" in proton-antiproton ( $p\bar{p}$ ) collisions at  $S = 540$  GeV at SPS [192] at CERN both for full and limited pseudo-rapidity ( $\eta$ ) space intervals. But with the increase in the centre of mass energy, a single NBD is found not enough to represent the pp multiplicity distribution for full rapidity intervals but still can explain for small rapidity interval satisfactorily as is established by SPS for 900 GeV pp collision. Multiplicity distribution starts building substructures in it with an increase in

the centre of mass energy which can not be described by a single NBD. There had been a proposal and successful implementation of weighted superposition/convolution of more than one function including NBD [193–196] to illustrate the pp data with an assumption for each individual function representing a different mechanism for particle production. Such a substructure in multiplicity distribution found for pp collision at 900 GeV at SPS and 1800 GeV at Tevatron [197], was explained by a function convoluted from two NBDs as shown in equation 7.6.

$$P_n(\sqrt{s}, \eta_C) = \alpha_{soft}(\sqrt{s}) P_n[\bar{n}_{soft}(\sqrt{s}, \eta_C), k_{soft}(\sqrt{s}, \eta_C)] + [1 - \alpha_{soft}(\sqrt{s})] P_n[\bar{n}_{semi-hard}(\sqrt{s}, \eta_C), k_{semi-hard}(\sqrt{s}, \eta_C)], \quad (7.6)$$

where  $\alpha_{soft}$  is the fraction of "soft" events and is a function of  $\sqrt{s}$  only. The other parameters are bearing their usual meaning, as has already been discussed, for single NBD function. Significantly, particles, produced in pp collision, are differentiated with respect to their probable production sources as is mentioned in the equation 7.6 by "soft" and "semi-hard" respectively. Even if not possible to isolate particles of different production mechanisms, but still, it serves the existence of multi-mechanism particle production even at pp collision at sufficiently high centre of mass energy. According to the two-component model [194], the multiplicity distribution is a convolution of two classes of events, "semi-hard with mini-jets or jets" and "soft events without mini-jets or jets". It is very much relevant here to mention that there is an expectation for further modification to multiplicity distribution for particles produced in pp collision with further increase in the centre of mass energy like in LHC. A framework of the weighted superposition of NBDs representing different classes of events has been extended from the two-component to a three-component model in a recent study [198] with an expectation of a new physics at the LHC at  $s=14$  TeV. The additional component in the three NBD function is attributed to a new class of high multiplicity events, which appeared as an elbow structure in the tail of multiplicity distribution of the pp collisions at the highest LHC energy.

### 7.3.2 Blast Wave formalism (BW)

A blast wave (BW) is, in general, originated as increased pressure and flow from large energy localised in a very small volume in space. The flow field can be described in terms of a leading shock wave followed by a "self-similar" subsonic flow. In other ways, the leading shock wave expands supersonically from an explosive core (source) and always associated with a blast wind with a negative pressure which gulps things around back towards the

core [199]. Historically, the flow solution for the blast wave came during World War II by John von Neumann [199, 200] and Geoffrey Ingram Taylor [201, 202] independently. Shortly there was a similar effort for blast wave by three other people L. I. Sedov [203], R. Latter [204], and J. Lockwood-Taylor [205] respectively. Friedlander waveform [206], simplest representation for the blast wave, is one among available solutions depending on both theoretical and experimental approaches and can be expressed as shown in equation 7.7

$$P_t = P_s e^{-\frac{t}{t^*}} \left(1 - \frac{t}{t^*}\right). \quad (7.7)$$

where  $P_s$  is the peak pressure and  $t^*$  is a characteristic time which represents the interval after which the pressure drops to zero for the first time. In the beginning, the relevance to blast wave was restricted to understand the effects after the explosion and associated predictions which made the domain bounded within military applications only. Soon after, the essence of blast wave model understood in much more broader sense and extended to various field of science and engineering like calculation of blast load during building designing, outcome of supernova explosion in astronomy and more recently to the field of relativistic heavy ion collision to understand the evolution of a system mimicking the evolution of universe in small scale. In the present study, our aim is to understand the proton-proton data at LHC energy applying blast wave model. Understanding the system produced in a hadronic collision with blast wave description started long back in 1992 by Ekkard Schnedermann et al [157]. They have developed a phenomenological model assuming thermalisation as the basic criteria and applied to data successfully measured in central collisions of Sulphur-Sulphur at  $\sqrt{s} = 200$  GeV/A from the NA35 Collaboration at CERN. Taking collectivity into account, the model could describe almost all hadronic spectra. The success of the model explored a new technique in probing and extracting information for the system produced in the hadronic collision. In the subsequent section, we will be dealing blast wave model that has been introduced in ref [157] which can be expressed in terms of  $m_T$ -spectra as shown in equation 7.8

$$\frac{dN}{m_T dm_T} \propto \int_0^R r dr m_T I_0 \left( \frac{p_T \sinh \rho}{T} \right) K_1 \left( \frac{p_T \cosh \rho}{T} \right), \quad (7.8)$$

where  $\rho = \tanh^{-1}(\beta)$  with  $\beta$  represents flow velocity.  $I_0$  and  $K_1$  represent modified Bessel's functions. The transverse flow velocity distribution  $\beta(r)$  in the region  $0 \leq r \leq R$  by a self-similar profile, parametrised as 7.9

$$\beta(r) = \beta_s \left(\frac{r}{R}\right)^n, \quad (7.9)$$

with  $\beta_s$  as surface flow velocity and  $\left(\frac{r}{R}\right)$  stands for relative radial coordinate of the collective system. Using the above formulation, the average transverse flow velocity can be calculated and found to be  $\bar{\beta} = \left(\frac{2}{2+n}\right)\beta_s$ . It is important to note that the above formulation has some basic assumptions like *a) hard-sphere particle source, b) The source must be locally thermalised, c) there must exist a common outward transverse velocity (collective radial flow velocity), d) Particles undergo instantaneous common freeze-out, e) There exist a common kinetic freeze-out temperature.* Blastwave description of experimental data gives two important physical parameter  $\beta$  and  $T_{Kin}$  respectively for the collectively evolving system. To note,  $T_{Kin}$ , extracted from the BW-fitting to data is not the actual temperature of the system, rather it is a combined effect from both temperature and kinematics of the system and can be represented as  $T_{Kin} = T + f(\beta)$ .

As has been discussed already, blast wave formalism is not developed from 1<sup>st</sup> principle, rather it is a hydrodynamic inspired model taking Boltzmann-Gibbs entropy into account which has a successful domain to explain proton-proton data specifically in low  $p_T$  range. It is obvious that this assumption brings some limitation to the model description by themselves such as *i) applies only to very limited  $p_T$  range for momentum spectra (up to 1 GeV). ii) can not describe evolution from pp to peripheral to central heavy ion collision. iii) there is no such guideline for choosing the fitting range which sometimes brings arbitrariness in the results.* Nevertheless, blast wave description has been revived with the indication of collectivity even in pp collision which is so far understood as "one to one" binary collision. But at the same time, one has to be careful about the multiplicity in applying BW approach to pp data which otherwise might lead to an insufficient description. With the introduction of non-extensivity in the entropy introduced as by Tsallis [158] (which tends to BG entropy  $\sum_i p_i \ln p_i$  for  $q \rightarrow 1$ ), the use of the blastwave representation can be extended more in  $p_T$  up to 3 GeV or more. Blastwave with Tsallis modification is known as Tsallis blast wave and can be represented as shown in equation 7.10

$$\frac{d^2N}{2\pi m_T dm_T dy} = \int_{-y_b}^{+y_b} e^{\sqrt{y_b^2 - y_s^2}} m_T \cosh(y_s) dy_s \int_0^R r dr \int_{-\pi}^{\pi} \left[ 1 + \frac{q-1}{T} E_T \right]^{-\frac{1}{q-1}} d\phi, \quad (7.10)$$

where  $y_b = \ln\left(\frac{\sqrt{s_{NN}}}{m_N}\right)$ . and all other variables are carrying their usual meaning. In the present study we will keep Tsallis BW representation out of our discussion and concentrate only in BG-BW description.

### 7.3.3 Estimation of energy density

In this section, we will search and discuss observables which play an important role in indicating the phase change in a system. In general, the transition of a system during phase change can either be discrete or continuous depending on the nature of the physical parameter involved. According to Ehrenfest's classification [207], the type of a discrete phase transition might be of a different order. The order of phase transition is defined in terms of *order of the lowest differential of Gibb's free energy* ( $G: G=(E +PV - TS)$ ) showing a discontinuity with respect to the thermodynamic variable and can be generalised as shown in equation 7.11

$$\text{For } n^{\text{th}} \text{ order phase transition } := \Rightarrow \left( \frac{\partial G}{\partial r} \right)_{\text{Phase-I}}^n \neq \left( \frac{\partial G}{\partial r} \right)_{\text{Phase-II}}^n, \quad (7.11)$$

where "r" represents thermodynamic variables P, V, T with their usual meaning. For example, discontinuity in entropy and volume at the phase boundary of a system indicate to be 1<sup>st</sup> order phase transition. On the other hand, continuous phase transition, known as crossover transition, exhibits a smooth swing of the relevant physical parameter from one phase to the other. Commonly, a phase transition of a particular kind is characterised with an order parameter which has "zero" at one phase and "non-zero" for the other. Density function, for example, serves the purpose of the order parameter in liquid-gas phase transition. Practically, search for phase transition in an experiment has a primary constraint in terms of available measured observables. Usually in relativistic heavy ion collisions, global parameters like energy (E), transverse momentum ( $P_T$ ), Pseudo-Rapidity ( $\eta$ ), rapidity (y), azimuthal distribution ( $\phi$ ) etc. are measured directly. On the other hand, few more observables like flow, mass ordering, shadowing factor etc. can be reconstructed from these basic measured

quantities either by using first principle or model dependent relationships. In the present context of the study, the primary aim is to calculate the energy density ( $\epsilon$ ) of the system, produced in the proton-proton collision. The methodology we will discuss here is actually quite well established and familiar in case of the system produced in heavy ion collision. Though not applicable for proton-proton collision overall collision energies uniformly, but at the LHC energies pp collision tagged with HM have the potential to be treated differently. A simplistic 1-D model calculation, developed by Bjorken long back in 1982 [138], shows that the estimation of energy density can be expressed in terms of measured quantities like multiplicity density and the size of particle emitting source. There are some underlying assumptions like *a) rapidity independence of particle production, b) all relevant functions are homogeneous in transverse direction which interns assume the ion is infinitely extended in transverse direction and makes the calculation one dimensional along longitudinal direction., c) System is evolved towards thermalisation which let the landau prescription to be used in calculating energy density, pressure, temperature and etc.* According to Bjorken prescription, the energy density of the system produced in the relativistic collision can be expressed as shown in equation 7.12

$$\epsilon_{BJ} \simeq \frac{\frac{dN_{ch}}{d\eta} * \frac{3}{2} \langle P_T \rangle}{V}, \quad (7.12)$$

where "V" is the effective volume from where the particle is emitted. Theoretically, V can be represented as  $A * c * \tau$  with A as interaction area and  $\tau$  as the lifetime of the system. At this point, it is customary to discuss the importance of energy density of the system produced in high energy collision specifically in contrast to phase transition. The energy density for the system with hadrons gas (pion gas for simplicity and also practically pion contribute 80% of total particle production) can be expressed as 7.13

$$\epsilon_{\pi} = g_{\pi} \frac{\pi^2}{30} T^4, \quad (7.13)$$

where " $g_{\pi}$ " is the degeneracy of pion gas which is 3 for  $\pi^+$ ,  $\pi^0$ ,  $\pi^-$ . It can be used to calculate the pressure using  $P = \frac{1}{3} \epsilon$ . On the contrary, the energy density for system comprised of quarks and gluon only can be expressed as 7.14

$$\varepsilon_{qg} = g_{qg} \frac{\pi^2}{30} \left( g_g + \frac{7}{8} g_q \right) T^4, \quad (7.14)$$

where " $g_g$ " and " $g_q$ " are degeneracies for gluon and quarks. It is obvious from equations 7.13 and 7.14 that the value of energy density is different for pionic (hadronic phase) and partonic (quarks and gluon) phases, determined by the difference in the degeneracy of the system. Moreover, the degeneracy is a measure for the elementary constituents of the system for example pions of different kinds in the hadron phase and available type of quarks and gluons in partonic phase. A clear discontinuity in parameter  $\frac{\varepsilon}{T^4}$  (representation for the degeneracy in the system,) with respect to temperature can indicate for possible phase transition from partonic to hadronic or vice versa. An indication for phase change can be investigated in relativistic heavy ion or proton-proton collision using experimental data by exploring the degeneracy as a function of temperature. In this regards, calculation of the energy density from the experimental observables is of prime significance.  $\frac{dN_{ch}}{d\eta}$  is one the most basic and primary measured quantity for particle production in high energy collision. On the other hand, the cross-section "S" can be calculated using HBT-radius of the particle emitting source and assuming Bjorken picture for the system, produced just after the collision. the only caveat in the study is in finding the temperature of the system. The direct photon can be one of the cleanest probes to carry information about the temperature of the system produced in the collision as being not affected by the subsequent evolution processes of the strongly interacting medium. Experimentally, discrimination of direct photons from decay or thermal component is a challenging task and still require advancement for successful temperature estimation. Heavy flavour particles, reconstructed from their leptonic decay channel, are among other possible signatures for temperature because of the same reason of being not affected by the strong interaction. Even there are still simple and direct prescription to get imprecision temperature information of the system from the  $p_T$ -spectra of produced particles.  $p_T$ -spectra, being basic experimental observable, can be easily measured both for unidentified and identified particle by the existing experiments like SPS, RHIC, ALICE etc. over a wide range of centre of mass energy for different collision systems like proton-proton, proton-heavy ion, heavy ion- heavy ion etc. Specifically, the low  $p_T$  part of the  $p_T$ -spectra of produced particles from high energy collisions carry information on temperature along with the transverse expansion of the system. Even though disentangling the expansion part from the temperature is not so obvious, for an exclusive measure of temperature, experimental analysis deal with parameters that reflect the temperature of the system. Either the mean transverse momentum, ( $\langle p_T \rangle$ ), as proposed [208] by Van Hove, or

the slope of the transverse mass  $m_T$ -spectra, obtained from the  $p_T$ -spectra (for a particle of mass  $m$ ,  $m_T = (m^2 + p^2)^{1/2}$ ), can be used for comparing thermal states of the system. In the present study, an inclusive measurement of temperature from particle spectra and thus the energy density was reconstructed and studied as a function of  $\langle p_T \rangle$ , a representation for temperature, for the proton-proton collision at LHC energies. The details of the analysis and results will be discussed later part of this chapter.

## 7.4 Particle production in pp-collision with NBD and BW model

With the increase in the centre of mass energy of the proton-proton collision, particle production started indicating more than just about one-to-one hard scattering. Till recent results on proton-proton collision at LHC, particle production was conjectured as an outcome of hard scattering between strongly interacting partons which can be explained by Perturbative Quantum Chromodynamics (pQCD) satisfactorily. On the other hand, right from pp data at Tevatron at the centre of mass energy 630 GeV and 1800 GeV [209] a different trend has been found in particle production which lacks complete explanation using hard scattering phenomenon only. We have worked to understand particle production in proton-proton collision at LHC energies keeping other possibilities of particle production in mind during this study. Presuming particle production mechanism of a particular type can be represented by a Negative Binomial distribution function [188], we searched for the existence of mechanisms other than hard scattering in proton-proton collisions. Though the phenomenological study using NBD cannot disentangle particles produced from different mechanism it's success lies in illustrating the significant contribution of non-hard scattering even in proton-proton collisions which need more exhaustive analysis at LHC energies. In the following subsequent subsections, we will be discussing particle productions with the help of different distribution (model) functions and their relevant implications.

### 7.4.1 Particle multiplicity and NBD approach

As has been discussed in section 7.3.1, Negative Binomial distribution was a successful phenomenological model to understand the particle production since long. The charged particle multiplicity distribution in non single-diffractive  $p\bar{p}$  events at  $\sqrt{S}=540$  GeV energy at CMS-UA5 experiment found a scaling violation and was described using a two-parameter (mean and width) Negative Binomial Distribution (NBD) function for the first time [210]. The width of the distribution was found to decrease linearly with  $\ln(S)$ , in deviation of so

far energy independent width of the distribution as has been predicted by KNO scaling [51]. However, a deviation from NBD in explaining the multiplicity distribution has been found soon at higher energies at  $\sqrt{S}=900$  GeV and  $\sqrt{S}=1800$  GeV at UA5 and Tevatron respectively. The appearance of shoulder like structure in the multiplicity distribution called for a superposition of two NBDs representing two component of particle production as has been introduced by Giovannini and Ugoccioni in 1999 as soft and semi-hard component [194]. In our study, we have implemented the two-component approach to understand the pp data at LHC energies. Moreover, it is pertinent to mention that the framework of the weighted superposition of different particle source has been extended from the two to three component model [198] in conceding possible new physics at the LHC energies. The third component was accredited to explain the eventual appearance of a new elbow structure in the tail of multiplicity distribution of the pp collisions at the highest centre-of-mass energy at the LHC. As far as the present study is concerned, the multiplicity distributions for the pp collisions up to  $\sqrt{S}=7$  TeV were available and have no such elbow like new structure which has restricted the applicability of up to two NBD approach only. In our study, we have analysed LHCb data in terms of both single NBD and superposition of two NBDs, as has been prescribed by the two-component model of [194]. As has been discussed already, a two-component NBD-description for the multiplicity distribution of hadronic collisions can be seen as the weighted superposition of two events classes, "semi-hard with mini-jets or jets" and "soft" respectively. It is relevant to mention that the "semi-hard" events, hard parton-parton scatterings with high momentum transfer, resulting in QCD jets of high  $p_T$  above a certain threshold are also referred to as "hard-QCD" events. The LHCb experiment has measured [211] multiplicity distributions of primary charged particles for proton-proton collisions at  $\sqrt{S}=7$  TeV in the pseudo-rapidity ranges,  $-2.5 < \eta < 2.0$  and  $2.0 < \eta < 4.5$ , for two classes of events: minimum bias and the hard-QCD respectively. The criterion for selecting hard-QCD events from minimum bias events was to select those events which have at least one particle with  $p_T > 1$  GeV/c. A scan with the multiplicity distributions over pseudo-rapidity both with a small window of  $\eta = 0.5$  and wide  $\eta$ -range was done for each of the event classes. We have analysed all multiplicity distributions in the forward rapidity with NBD-approach which has been found to be successful in describing the same in the mid-rapidity region [212]. We have also compared our results with similar attempts at mid-rapidity.

## 7.4.2 Analysis and discussion

We have analysed multiplicity distribution for primary charged particles in proton-proton collision, published by LHCb experiment [194]. Data are available for five pseudo-rapidity windows of width  $\Delta\eta = 0.5$  in the  $\eta$ -range,  $2.0 < \eta < 4.5$ . There were two classes of events,

minimum-bias and Hard-QCD respectively, are available for both small  $\eta$ -windows and for the whole  $\eta$ -range. As a first attempt, we have fit minimum bias events with the single NBD function as given in Eq. 7.3. The single NBD fitting to multiplicity distribution for all five small  $\eta$ -windows for minimum bias proton-proton collision has been shown by solid lines in figure 7.6. Corresponding fit parameters are tabulated in table 7.2 along with  $\chi^2/ndf$ . As can be seen from  $\chi^2/ndf$  values, the single-NBD function is not sufficient in describing the multiplicity distribution for minimum bias data. Parameters from fitted NBD function show consistent dependence on the position of the  $\eta$ -window. Noticeably, the deviation for the single-NBD fits to the minimum bias data become more prominent as we go far in forward region. However, the average multiplicity ( $\langle n \rangle$ ) decreases whereas "k" parameter increases with the shift in  $\eta$ -window towards a more forward direction. Increasing "k" in turns indicates broadening of the multiplicity distribution for the pseudo-rapidity window in the more forward regions. However as can be seen from figure 7.6, the multiplicity distributions for the minimum bias events could be better explained by a weighted superposition of two NBD functions.

Table 7.2: Parameters as extracted from fitting with NBD functions to the multiplicity distributions for the primary charged particles for minimum bias events in pp collisions at  $\sqrt{S}=7$  TeV for five small  $\eta$ -windows.

| $\eta$ -Window     | k               | $\langle n \rangle$ | $\chi^2/ndf$ |
|--------------------|-----------------|---------------------|--------------|
| $2.0 < \eta < 2.5$ | $1.92 \pm 0.02$ | $3.49 \pm 0.03$     | 195.80/18    |
| $2.5 < \eta < 3.0$ | $1.98 \pm 0.02$ | $3.40 \pm 0.03$     | 231.59/18    |
| $3.0 < \eta < 3.5$ | $2.12 \pm 0.02$ | $3.26 \pm 0.03$     | 228.71/18    |
| $3.5 < \eta < 4.0$ | $2.35 \pm 0.03$ | $3.08 \pm 0.03$     | 233.34/18    |
| $4.0 < \eta < 4.5$ | $2.81 \pm 0.05$ | $2.88 \pm 0.03$     | 240.78/18    |

Although from the plots in figure 7.6 and the  $\chi^2/ndf$ , as tabulated in table 7.3, it is indicative that the weighted superposition of two NBDs can describe the minimum bias data better. At the same time, the fit parameters with large uncertainties for all these small rapidity intervals are not suitable to extract any systematic behaviour as far as the data trend is concerned. It is customary at this point to recollect that the multiplicity distributions of the charged hadrons produced in pp collisions at  $\sqrt{S}=7$  TeV [214] in overlapping pseudo-rapidity bins of different widths, also fit better [212] to the two-NBD function than a single-NBD function.

On the other hand, for hard-QCD events, it is significant to note that an event is called "hard" by LHCb experiment if "at least one particle with transverse momentum greater than 1 GeV/c" in the range  $2.5 < \eta < 4.5$ . The criteria of choosing "Hard" events has experimental support by a similar approach adopted [16] by the CDF experiment at the Tevatron, where

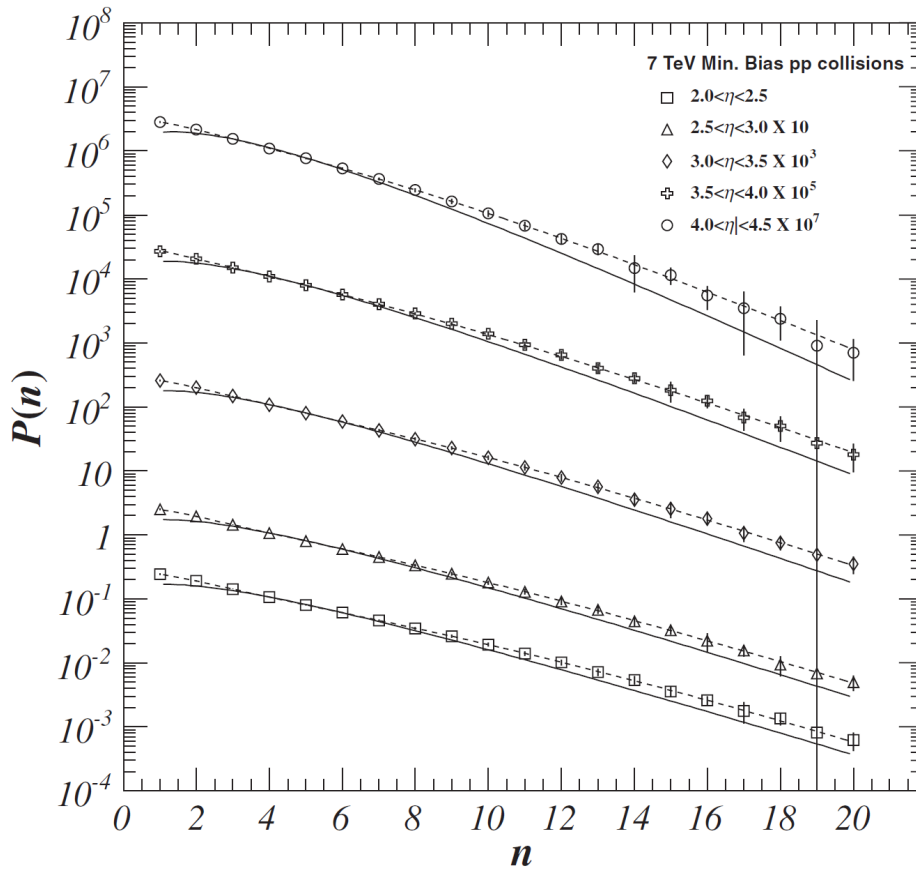


Figure 7.6: (Colour online). Primary charged particle multiplicity distributions for minimum bias events in pp collisions at  $\sqrt{S} = 7$  TeV for five different  $\eta$ -windows of width  $\Delta\eta = 0.5$  within the range  $2.0 < \eta < 4.5$ . The solid lines represent single NBD fitting along with the data points, while the dotted lines are for two-NBD fits. The error bars include both the statistical and the systematic uncertainties [213].

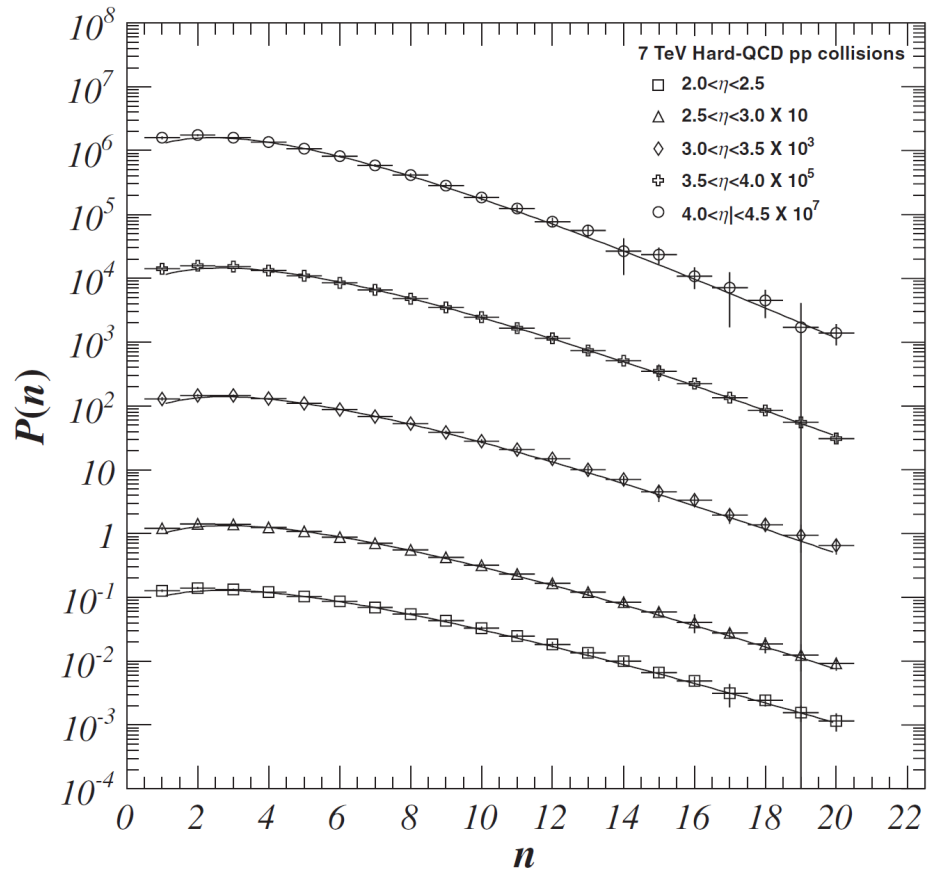


Figure 7.7: (Colour online). Primary charged particle multiplicity distributions for Hard-QCD events in pp collisions at  $\sqrt{S} = 7$  TeV for five different  $\eta$ -windows of width  $\Delta\eta = 0.5$  within the range  $2.0 < \eta < 4.5$ . The solid lines represent single NBD fitting along the data points, while the dotted lines are for two-NBD fits. The error bars include both the statistical and the systematic uncertainties [213].

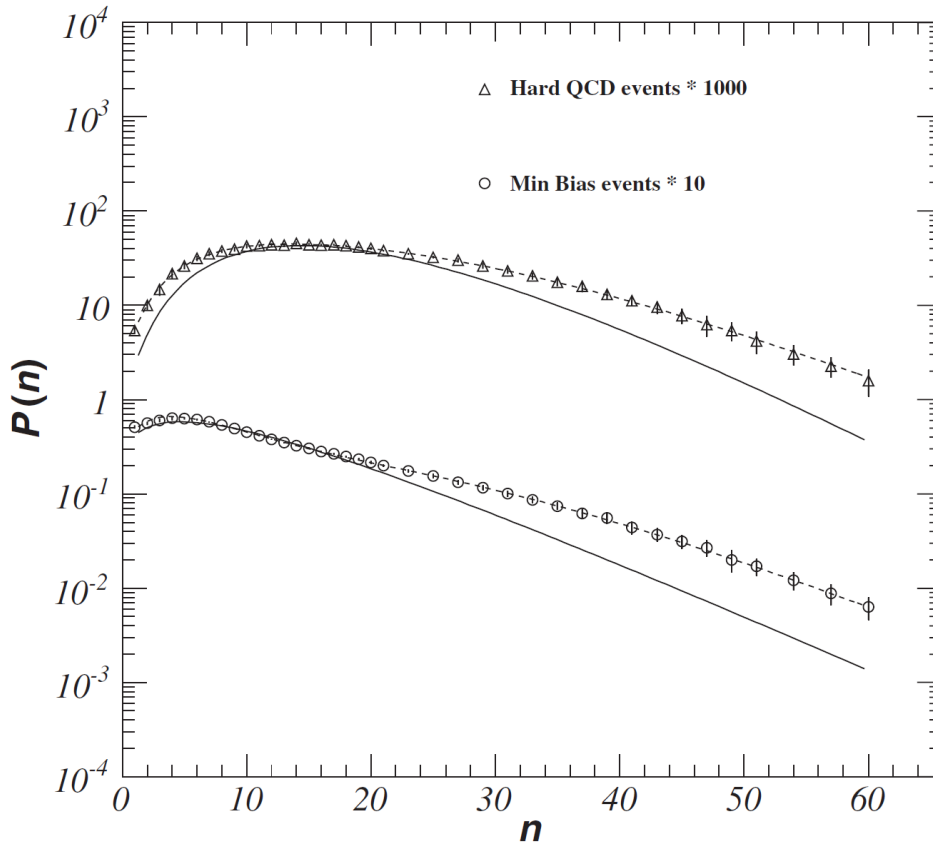


Figure 7.8: (Colour online). Primary charged particle multiplicity distributions for minimum bias and Hard-QCD events in pp collisions at  $\sqrt{S} = 7$  TeV for the entire  $\eta$ -range  $2.0 < \eta < 4.5$ . The solid and dotted lines are representing single and double NBD fitting respectively. The error bars include both the statistical and the systematic uncertainties [213].

Table 7.3: Parameters extracted from two NBDs fitting to the multiplicity distributions for the primary charged particles in minimum bias events in pp collisions at  $\sqrt{S}=7$  TeV for five  $\eta$ -windows, and shown in the table in the same order as in table 7.2.

| $\eta$ -Window     | $k_{soft}$      | $\langle n \rangle_{soft}$ | $k_{semihard}$  | $\langle n \rangle_{semihard}$ | $\chi^2/ndf$ |
|--------------------|-----------------|----------------------------|-----------------|--------------------------------|--------------|
| $2.0 < \eta < 2.5$ | $3.15 \pm 2.56$ | $5.14 \pm 2.06$            | $1.92 \pm 0.96$ | $1.53 \pm 0.80$                | 0.70/14      |
| $2.5 < \eta < 3.0$ | $2.72 \pm 2.23$ | $4.54 \pm 1.43$            | $2.31 \pm 2.25$ | $1.32 \pm 0.54$                | 0.47/14      |
| $3.0 < \eta < 3.5$ | $3.18 \pm 1.65$ | $4.63 \pm 2.01$            | $2.05 \pm 1.19$ | $1.43 \pm 0.83$                | 0.31/14      |
| $3.5 < \eta < 4.0$ | $1.98 \pm 0.54$ | $1.53 \pm 0.21$            | $3.99 \pm 2.99$ | $4.73 \pm 0.35$                | 0.29/14      |
| $4.0 < \eta < 4.5$ | $2.11 \pm 0.95$ | $1.30 \pm 0.47$            | $3.55 \pm 0.89$ | $3.93 \pm 0.80$                | 0.39/14      |

Table 7.4: Parameters as extracted from fitting with single NBD function to the multiplicity distributions for the primary charged particles for Hard QCD events in pp collisions at  $\sqrt{S}=7$  TeV for five small  $\eta$ -windows.

| $\eta$ -Window     | k               | $\langle n \rangle$ | $\chi^2/ndf$ |
|--------------------|-----------------|---------------------|--------------|
| $2.0 < \eta < 2.5$ | $2.83 \pm 0.05$ | $4.95 \pm 0.05$     | 29.14/18     |
| $2.5 < \eta < 3.0$ | $3.19 \pm 0.04$ | $4.86 \pm 0.05$     | 23.59/18     |
| $3.0 < \eta < 3.5$ | $3.39 \pm 0.05$ | $4.64 \pm 0.05$     | 87.69/18     |
| $3.5 < \eta < 4.0$ | $3.53 \pm 0.33$ | $4.45 \pm 0.02$     | 45.34/18     |
| $4.0 < \eta < 4.5$ | $3.82 \pm 0.06$ | $3.97 \pm 0.04$     | 27.47/18     |

two isolated sub-samples, soft and hard, were disentangled with a criterion "no particle of transverse energy,  $E_T > 1.1$  GeV, as soft events. Although, none of the other experiments at LHC has published multiplicity distribution for the so-called Hard-QCD events during the time of this work but the invariance of multiplicity distribution for soft events as a function of  $\sqrt{S}$  has been studied [212] with proton-proton data by CMS experiment [214] in terms of two NBDs. The presumptions of this study were a) the two-component model of particle productions in the proton-proton collision is valid also in the forward region. and b) the criteria for isolating the hard-QCD events is acceptable. The rest of the work with fitting multiplicity distributions for the hard-QCD events with a the single-NBD function will be in some sense straight forward. In this context, single-NBD function was used to fit the multiplicity distributions of the produced primary charged particles for the "Hard-QCD events" as published by LHCb experiments [215]. The in the minimum bias case, here also there were data available for multiplicity distribution for five small non-overlapping pseudo-rapidity windows. The relevant plots are shown in figure 7.7 for all five  $\eta$ -windows. As is shown in figure 7.7, the single-NBD function fits reasonably well and explain multiplicity distributions consistently.  $\chi^2/ndf$  for the respective plots in figure 7.7 are tabulated table 7.4. Two fitting parameters " $\langle n \rangle$ " and k, tabulated in table 7.4, show a systematic trend as is

Table 7.5: Parameters extracted from single NBD fitting to the multiplicity distributions for the primary charged particles in pp collisions at  $\sqrt{S}=7$  TeV for  $\eta$ -range 2.5 ( $2.0<\eta<4.5$ ) both for minimum bias and "Hard-QCD" events.

| Type of events | k               | $\langle n \rangle$ | $\chi^2/ndf$ |
|----------------|-----------------|---------------------|--------------|
| Minimum Bias   | $1.81 \pm 0.01$ | $11.63 \pm 0.06$    | 853.78/37    |
| Hard QCD       | $4.32 \pm 0.08$ | $19.35 \pm 0.15$    | 559.65/37    |

expected. " $\langle n \rangle$ " decreases whereas "k" increases with the shift of the  $\eta$ -window more toward forward rapidity. Altogether, the single NBD function performs acceptably in describing the multiplicity distributions for the hard-QCD events in small  $\eta$ -windows in the forward rapidity region. It was relevant at this point to study the NBD representation the multiplicity data for proton-proton collision for a wide range of  $\eta$ -coverage, eg  $\Delta\eta = 2.5$ , in the  $\eta$ -range  $2.0<\eta<4.5$  for both the event classes minimum bias and "Hard-QCD" events respectively. It is quite obvious from the plots in figure 7.8, that neither the minimum bias nor the "Hard-QCD" events can be described by the single-NBD functions which also understood from the  $\chi^2$  values for fitting to both the events classes as is listed in table 7.5. Figure 7.8 represents the primary charged particle multiplicity distributions for minimum-bias and "Hard-QCD" events along with corresponding best fit with a single-NBD function and with a weighted superposition of two NBDs. In the case of hard-QCD events, of course, one needs to be meticulous in adopting the terminology of "two-component model" for the weighted superposition of two NBDs. It rather will be relevant in taking the two NBD function just as a functional form far from two component model.

Table 7.6: Parameters extracted from two NBD fitting to the multiplicity distributions for the primary charged particles in pp collisions at  $\sqrt{S}=7$  TeV for  $\eta$ -range 2.5 ( $2.0<\eta<4.5$ ) both for minimum bias and "Hard-QCD" events.

| Type of events | $k_{soft}$      | $\langle n \rangle_{soft}$ | $k_{semihard}$  | $\langle n \rangle_{semihard}$ | $\chi^2/ndf$ |
|----------------|-----------------|----------------------------|-----------------|--------------------------------|--------------|
| Minimum Bias   | $2.23 \pm 0.15$ | $7.30 \pm 0.75$            | $4.11 \pm 1.00$ | $23.38 \pm 2.04$               | 16.31/33     |
| Hard QCD       | $4.04 \pm 0.62$ | $10.64 \pm 1.86$           | $4.20 \pm 0.85$ | $24.47 \pm 1.42$               | 4.62/33      |

In table 7.6, we have presented two components of the multiplicity distribution of both minimum bias and hard-QCD events with suffixes 1 and 2 respectively. The values of the fit parameters were obtained by the best fits in terms of  $\chi^2/ndf$  both the cases. In conclusion, the work revealed the fact that minimum bias proton-proton data at  $\sqrt{S}=7$  TeV can be well described with weighted superposition of two NBDs in accordance with the two-component model for particle production. On the other hand, "Hard-QCD" events for small  $\eta$ -windows can be explained using single NBD, accepting only hard partonic scattering process as a

mechanism for particle production. However, multiplicity distribution for "Hard-QCD" events for a wide  $\eta$ -window show deviation from single particle production mechanism and can be described well with double NBD function which indeed contradicts the concept of the discussed two-component model. The contradiction could be attributed either to biased selection criterion of the hard events or to the possibility of a different particle production mechanism in different phase space and need to be probed more deeply. It is noteworthy to mention here, that there were studies of minimum bias proton-proton data at LHC energies using weighted superposition of three NBD function [216]. However, understanding the presence of the third component is still not conclusive.

### 7.4.3 Collectivity in pp-collisions and Blast Wave Model

In continuation of the study of proton-proton collision with NBD model, which indicates, particle production in pp-collision is not governed only by pQCD, rather there exist some other particle production mechanism, resulting in softer part of the spectra. There is recent experimental evidence found in high multiplicity proton-proton collisions which are already there in case of heavy ion collisions and attributed to the hydrodynamical explanations. Ridge, a structure found in pair correlation study at  $\Delta\eta - \Delta\phi$  plane, was observed for the first time in heavy-ion collisions at RHIC [165] which was attributed to the hydrodynamical evolution of the system formed after collisions. Soon after, There was a similar kind of observation was noticed in proton-proton collisions at LHC(ref:bw16) for a special type of event class, called High-Multiplicity (HM) events. Hanbury-Brown-Twiss (HBT) correlations [166], intensity interferometry used to find the radius of a particle emitting source, is another important observations which show similar kind of event multiplicity or pair transverse momentum dependence for the radii of the particle emitting source both for pp collisions at LHC [167, 167] and heavy ion collisions at RHIC [169]. Interestingly, the dependence again was illustrated as a signature for collectivity for heavy ion collisions. Moreover, mass ordering, a dependence of Inverse slope parameter of  $p_T$ -spectra on particle type and a typical for a hydrodynamic description, was found for the first time in heavy ion collisions at RHIC. Later, a similar trend for mass ordering was also observed for small system produced in a proton-Lead collision at LHC energies 7.9 [217].

Very recently, a similar study [218] on mass ordering for HM proton-proton events was also found 7.10. The main motivation in revisiting the particle production in pp collision specifically at LHC energy in the present study was these above discussed experimental signatures that hint a possibility of forming heavy-ion-like hydrodynamical system even in pp collision at small scale. It is relevant to notice, with the availability of large statistics of high-multiplicity, high energy density pp events, particularly at  $s = 7$  TeV, there are

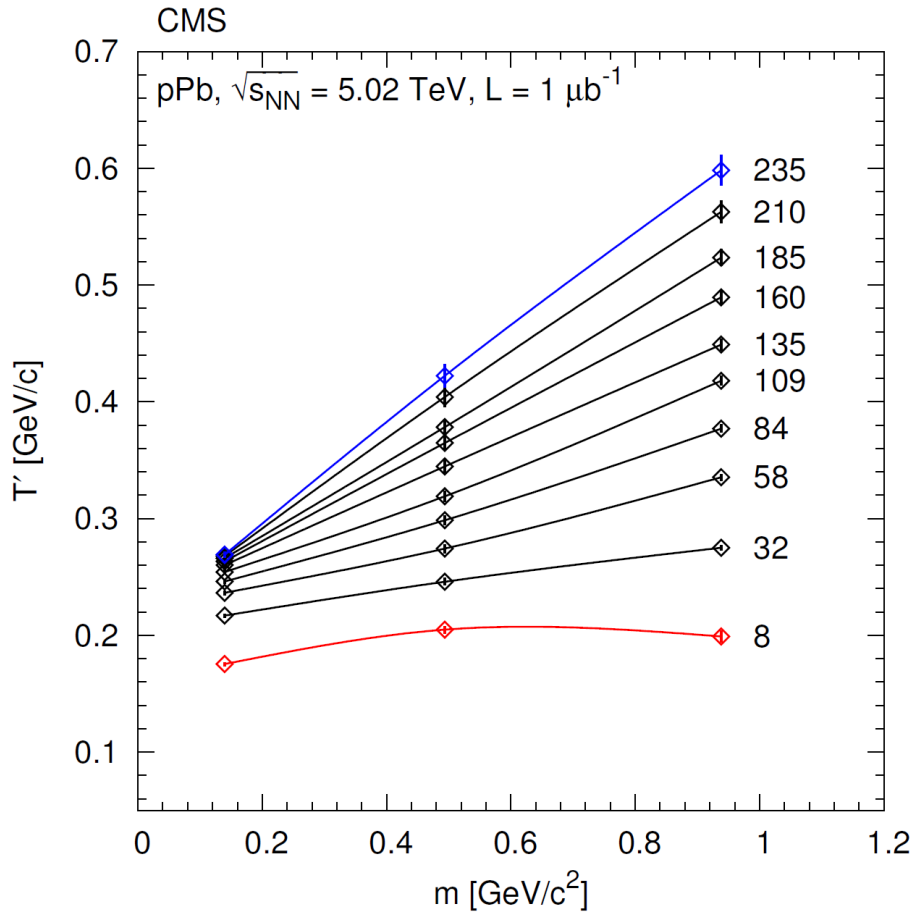


Figure 7.9: (Colour online). Mass ordering, variation of the inverse slope parameter as a function of particle species (mass  $m$ ), found for pPb collision at 5.02 TeV by CMS collaboration which is explained as a signature for collectivity of the system produced in the collision [217].

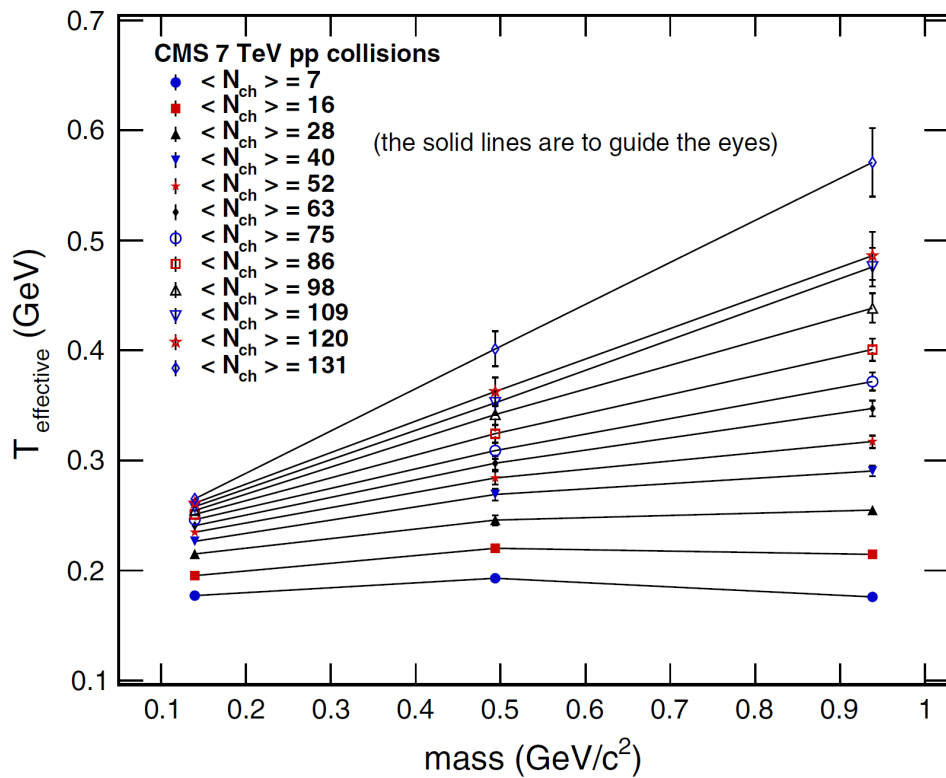


Figure 7.10: (Colour online). Variation of inverse slope parameter ( $T_{effective}$ ) as a function of particle mass, following almost same trend as has been found in pPb and PbPb collision which indicate the scope of applying hydrodynamic model to system produced in proton-proton collision as well [218].

several initiatives [170–177] to adopt different hydrodynamical inspired models in predicting collective phenomena in small systems produced in pPb and pp collisions at LHC energies. There are other experimental observables like direct photons at low transverse momentum [26], strange baryon-to-meson ratio [176], transverse radial flow velocity [158, 179, 180] etc. exists which are also used to probe the collective nature of the produced system in collisions. However, there are other contemporary frameworks like colour glass condensate [185] in the literature which explains the appearance of the "ridge" quite successful and does not accept the existence of hydrodynamical system formed in pp collisions. Nevertheless, recent results from CMS collaboration [219, 220] shows a relative flattening of the low- $p_T$  part of the  $p_T$ -spectra of identified particles with increasing mass in pp collisions at LHC which triggered for a search of collective transverse radial flow. Notably, a similar type of flattening of  $p_T$ -spectra in heavy-ion collisions at SPS, RHIC and LHC was explained assuming the existence of a common transverse radial flow velocity.

#### 7.4.4 Results and discussion

The study under the present scope has been done with published data for proton-proton collision at LHC. A wide range of data in terms of  $p_T$ -spectra for different identified particles with different detector coverages are available from different experiments at LHC. However, the phenomenological work, search for collectivity with blast wave approach, is limited by the relevance to the objective of the topic. There were published data for two different classes of particles which have been considered for the present work. Firstly, a class of particles [220, 221] with the commonly measured entities such as  $\pi^\pm$ ,  $K^\pm$ ,  $p(\bar{p})$  over the rapidity, ( $|y| < 1$ ) for the pp collisions at  $\sqrt{S} = 900, 2760$  and  $7000$  GeV which has been explored with blast wave approach. On the other hand, the second class of particles consisted with [219, 222] the strange particles of different degrees of strangeness (single, double etc),  $K_S^0$ ,  $\Lambda$  and  $\Xi$ , for NSD type pp collisions at  $\sqrt{S} = 0.9$  and  $7$  TeV. The data for  $p_T$ -spectra for different particles  $\pi^\pm$ ,  $K^\pm$ ,  $p(\bar{p})$  were accessible with event classes, tagged with "non-overlapping range of event multiplicity" which is assumed to contain the information of "centrality" in case of pp collision. An explicit blast-wave analysis could be performed with the CMS data [221, 222] which encourage to study the centre-of-mass energy, species and centrality-dependence of  $p_T$ -spectra produced in pp collisions at LHC and to compare the results with similar studies available for heavy ion (AA) and pA collisions. The fact to be mentioned at this point, that none of the event generators such as PYTHIA tunes was used in the study of the inclusive production of  $\pi^\pm$ ,  $K^\pm$ ,  $p(\bar{p})$  in pp collisions at  $s = 0.9, 2.76$  and  $7$  TeV [34] which can bring an acceptable overall description of data at the finer level such as the multiplicity (N) dependence of  $\langle p_T \rangle$  or  $E_{CM}$ ,  $\sqrt{S}$ -dependence of  $dN/dy$  or  $\langle p_T \rangle$  and

the particle yield ratios etc. Like in the case of non-strange particles, tuned event generators are far from explaining in case of strange particle as well in which the discrepancy increases with the increase in strangeness.

We have attempted to fit the blast-wave function (BGBW), as has been described in equation 7.8, to the  $p_T$ -spectra obtained from published data, as measured [219, 220] by CMS experiment. The fitting was done simultaneously for a class of particles ( $\pi^\pm$ ,  $K^\pm$ ,  $p(\bar{p})$ ) with all three fit parameters, kinetic freeze-out temperature ( $T_{kin}$ ), the radial flow velocity ( $\beta_S$ ) and the exponent (n) of flow profile, free as is shown in figure 7.11 for NSD pp-events with all strange and non-strange particles. The motivation was to obtain the best possible simultaneous or combined fits to the data which might shed light on the collective behaviour of the particle emitting source produced in pp collision. The value of  $\chi^2/ndf$ , using the MINUTE program in the ROOT analysis framework [55], was adopted as a sign of best fitting for the study. To start, we have fitted  $p_T$ -spectra simultaneously for  $\pi^\pm$ ,  $K^\pm$ ,  $p(\bar{p})$  with BGBW function for minimum bias pp collisions at  $\sqrt{S}=0.9, 2.76$  and 7 TeV respectively as shown in figure 7.11. Blast-wave model, however, could not describe the minimum bias data satisfactorily. We have explored the advantage of having centrality (multiplicity in case of pp collision) dependent  $p_T$ -spectra for pp collision which exhibits the fact that high-multiplicity pp events only carry the signatures, which could be attributed to the collectivity in pp collisions. The simultaneous BGBW fitting to the high multiplicity (more central) pp events was done for the search of collectivity in pp collision explicitly in this study.

Figures 7.12 represents the  $p_T$ -spectra for  $\pi^\pm$ ,  $K^\pm$ ,  $p(\bar{p})$  for highest multiplicity class  $N_{ch}$  for pp collision at 7 TeV as measured by CMS [220], fitted simultaneously with BGBW function. A similar exercise, simultaneous BGBW fitting as shown in figures 7.13 and 7.14, have been performed with highest available multiplicity classes ( $N_{ch}=98$  and 75) for two different centres of mass energies 2.76 and 0.9 TeV respectively. A rigorous blast-wave fit for all other multiplicity classes for different  $E_{CM}$  energies has been studied. However, BGBW fit to a certain multiplicity class was accepted for the signature of collectivity by the quality of simultaneous fitting depending on the values of  $\chi^2/ndf$ .

Apart from three free parameters,  $T_{kin}$ ,  $\beta_S$  and n, as have been discussed already, transverse radius (R) of the surface of particle emitting source at freeze-out plays a crucial role in BGBW fitting to  $p_T$ -spectra. The choice of R plays a crucial role in the fitting of  $p_T$ -spectra with the blast wave function. Selection of R in this context will be illustrated shortly. Ideally, the radius "R" could be obtained from the pair transverse momentum-dependent HBT radius for the source of particle production. Experimentally, HBT radius corresponding to the lowest value of pair transverse momentum ( $k_T$ ) which represents the radius of the source

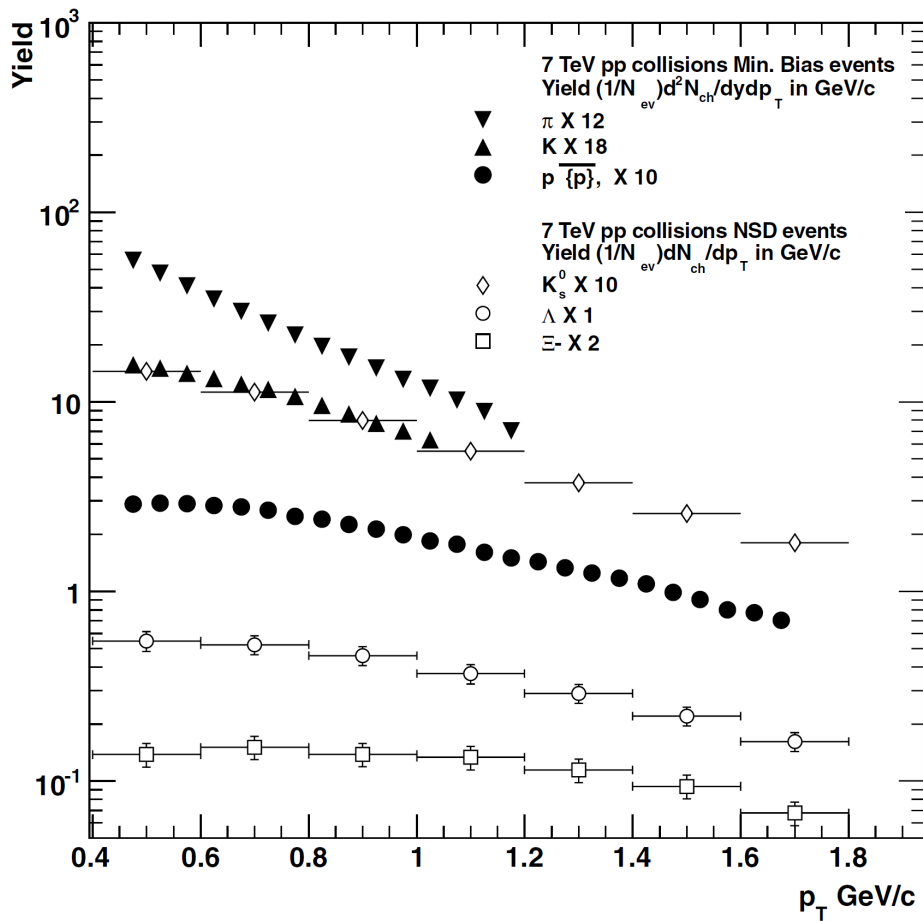


Figure 7.11: (Colour online). Transverse momentum ( $p_T$ ) spectra for  $\pi^\pm$ ,  $K^\pm$ ,  $p(\bar{p})$  within rapidity range  $|y| < 1$  for minimum bias pp collisions and for  $K_s^0$ ,  $\Lambda$  and  $\Xi$  within rapidity range  $|y| < 2$  for the non-single diffractive (NSD) events of pp collisions at  $\sqrt{S} = 7$  TeV as measured by CMS collaboration [219, 220] at LHC. Uncertainties shown, are obtained by adding statistical and systematic errors in quadrature [223].

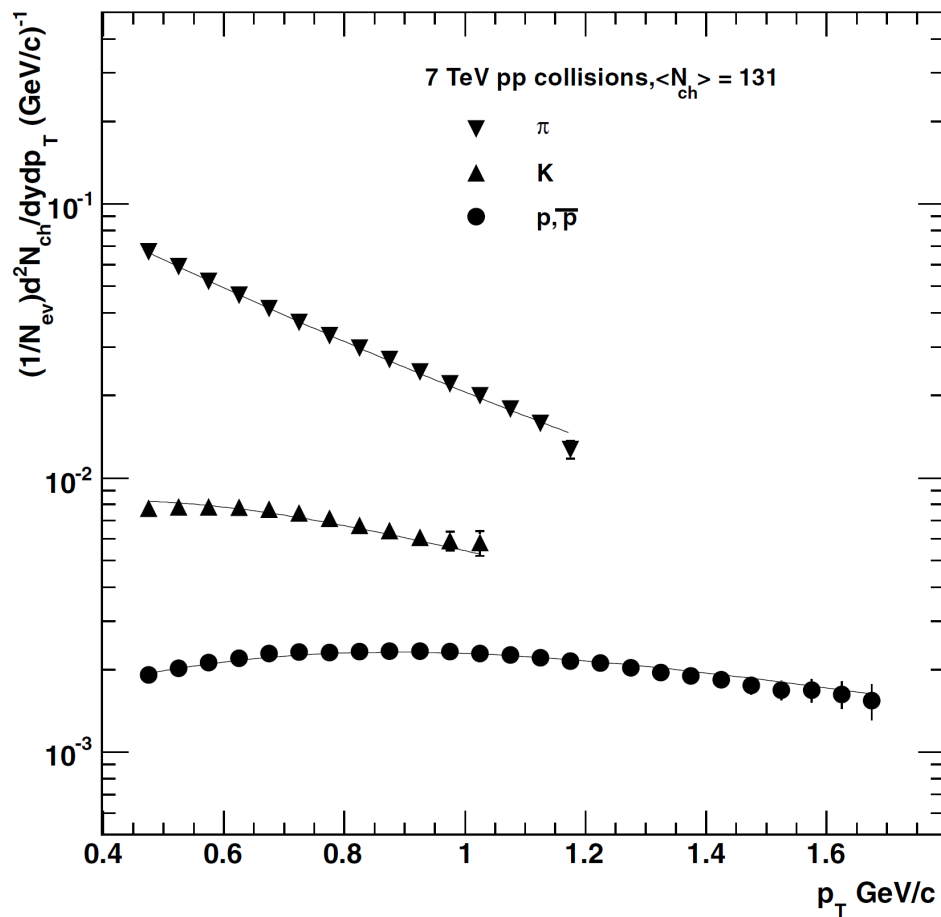


Figure 7.12: (Colour online). Transverse momentum spectra for  $\pi^\pm$ ,  $K^\pm$ ,  $p(\bar{p})$  as measured by CMS collaboration for proton-proton collision at centre of mass energy 7 TeV for multiplicity class 131 (highest multiplicity measure at 7 TeV) [223]. The solid lines represents the simultaneous blast-wave fitting to the data.

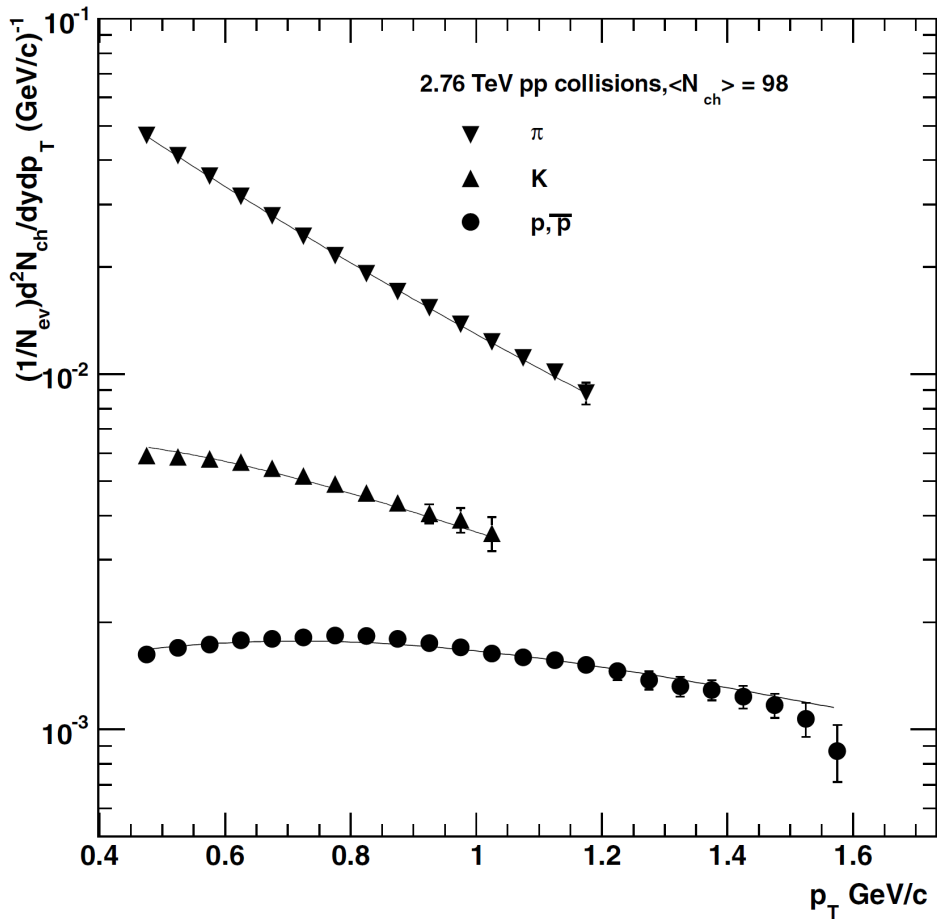


Figure 7.13: (Colour online). Transverse momentum spectra for  $\pi^\pm$ ,  $K^\pm$ ,  $p(\bar{p})$  as measured by CMS collaboration for proton-proton collision at centre of mass energy 2.76 TeV for multiplicity class 98 (highest multiplicity measure at 2.76 TeV) [223]. The solid lines represents the simultaneous blast-wave fitting to the data.

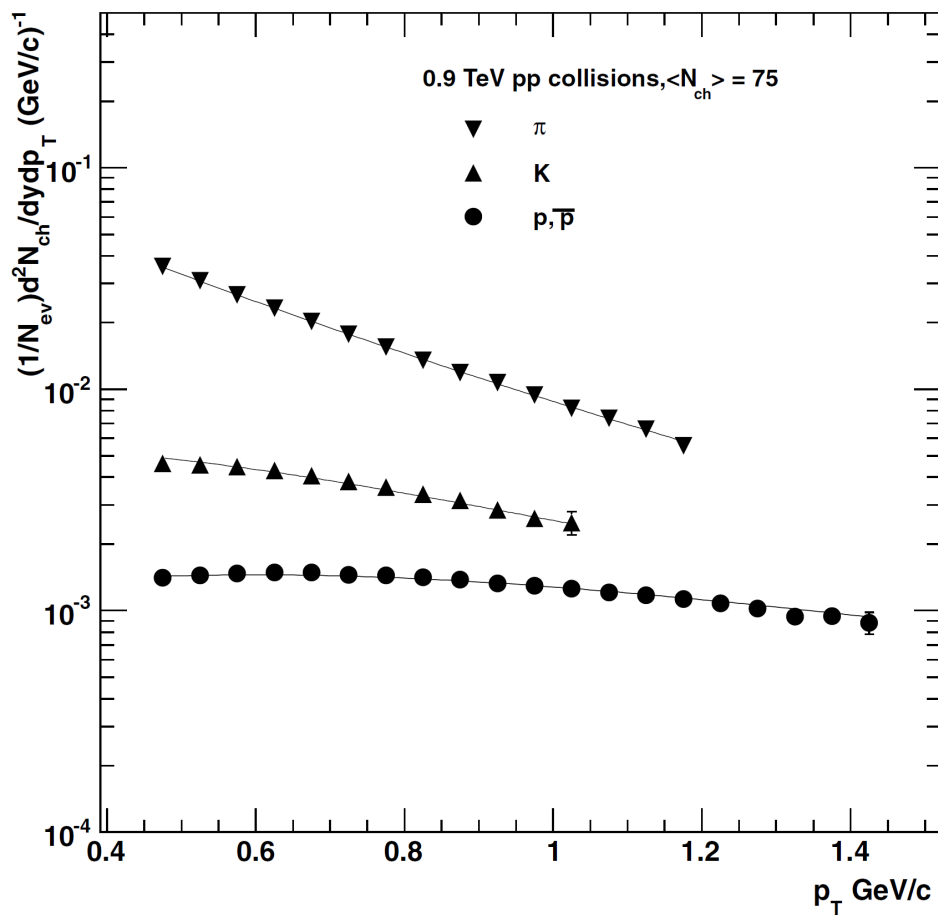


Figure 7.14: (Colour online). Transverse momentum spectra for  $\pi^\pm$ ,  $K^\pm$ ,  $p(\bar{p})$  as measured by CMS collaboration for proton-proton collision at centre of mass energy 0.9 TeV for multiplicity class 75 (highest multiplicity measure at 0.9 TeV) [223]. The solid lines represents the simultaneous blast-wave fitting to the data.

Table 7.7: Parameters of BGBW,  $T_{kin}$ ,  $\beta$  and  $n$ , have been extracted from the simultaneous fit to the published [53] spectra of  $\pi^\pm$ ,  $K^\pm$  and  $p(\bar{p})$  for pp collisions at  $\sqrt{S} = 0.9, 2.76$  and 7 TeV for different event classes depending on average multiplicity,  $N_{ch}$ , in the pseudo-rapidity range  $\eta < 2.4$ .

| $E_{CM}$ | $\langle N_{ch} \rangle$ | $T_{kin}(\text{MeV})$ | $\langle \beta \rangle$ | $n$               | $\chi^2/ndf$ |
|----------|--------------------------|-----------------------|-------------------------|-------------------|--------------|
| 0.9      | 75                       | $106.43 \pm 0.10$     | $0.745 \pm 0.004$       | $0.584 \pm 0.010$ | 0.29         |
| 2.76     | 86                       | $115.55 \pm 0.11$     | $0.742 \pm 0.005$       | $0.605 \pm 0.007$ | 1.25         |
| 2.76     | 98                       | $110.39 \pm 0.13$     | $0.769 \pm 0.005$       | $0.521 \pm 0.009$ | 0.43         |
| 7        | 98                       | $115.57 \pm 0.11$     | $0.766 \pm 0.004$       | $0.540 \pm 0.006$ | 1.02         |
| 7        | 109                      | $113.09 \pm 0.12$     | $0.779 \pm 0.004$       | $0.503 \pm 0.006$ | 0.61         |
| 7        | 120                      | $110.84 \pm 0.15$     | $0.790 \pm 0.004$       | $0.480 \pm 0.006$ | 0.34         |
| 7        | 131                      | $104.29 \pm 0.15$     | $0.809 \pm 0.005$       | $0.436 \pm 0.005$ | 0.44         |

of emission close to the freeze-out. There are results from both ALICE [168] and CMS collaboration for HBT radius for the particle emitting source in pp collision depending on pair transverse momentum and the event multiplicity which resembles results in case of a heavy-ion collision. However, due to lack of multiplicity classes for pp collisions like in heavy-ion, we have used a multiplicity dependent empirical formula ( $R(N_{ch}) = a \cdot N_{ch}^{1/3}$ ) for calculating the radius. Here, the parameter  $a = 0.597 \pm 0.009(\text{stat.}) \pm 0.057(\text{syst.})\text{fm}$  for 0.9 TeV and  $a = 0.612 \pm 0.007(\text{stat.}) \pm 0.068(\text{syst.})\text{fm}$  for 7 TeV was taken from results from CMS experiment [168]. However, because of the lack of data for "a" for 2.76 TeV, we have estimated the value by using the method of interpolation.

As has been discussed, a good simultaneous fitting of BGBW to the data for particles with different masses indicate the presence of some kind of collectiveness within the particle emitting source. To understanding the collectivity of the source produced in the collision, we have extracted the values of the BGBW fit parameters for different centre-of-mass energies ( $E_{CM}$ ), along with respective  $\chi^2/ndf$  which has been tabulated in table 7.7.

To understand the behaviour of the parameters, we need to look back the same kind of study both for heavy-ion (AA) collision and proton-ion (pA) collision which might provide some reference for pp collision. It has been found for heavy ion collision that for the particular centre of mass energy,  $T_{Kin}$  increases with the event multiplicities (or centrality) whereas, the average transverse radial flow  $\langle \beta \rangle$  decreases with increase in multiplicity. From our study for pp collision at 0.9, 2.76 and 7 TeV, it has been revealed that the parameters  $T_{Kin}$  and  $\langle \beta \rangle$  exhibit similar trend to what has been found in AA or pA collisions. Notably, the average radial flow velocity  $\langle \beta \rangle$  increases with  $E_{CM}$  for the highest multiplicity event class whereas and the kinetic freeze-out temperature  $T_{Kin}$  remains constant. The results for

pp collision has been compared with that of AA and pA collision and shown in figure 7.15 for  $\langle \beta \rangle$  and figure 7.16 for  $T_{kin}$ .

To understand the results from the phenomenological study, we need to recall that, in a hydrodynamic picture, the collective radial flow has resulted from the pressure gradient in the system which might be there due to a non-central collision. The resulted radial flow velocity for the system is more for larger pressure gradient. However, the pressure gradient evolves depending on initial energy density and the spatial size or the lifetime of the system formed during the collision. As obvious, higher initial energy density and the smaller size of the system leads to a larger pressure gradient and thus higher flow velocity. As a natural consequence, the smaller system produced in pp collision at LHC energies will hold larger pressure gradient as compared to both heavy-ion collision at SPS, RHIC and LHC and pA collisions at LHC with similar centrality (multiplicity) class. Consistent results for pressure gradient built depending on the collision energy and system size has already been established from experiments such as more for PbPb collisions at  $\sqrt{S_{NN}} = 2.76$  TeV is larger than that in AuAu at RHIC energies. Moreover, it is also evident, that the pressure gradient in pPb collisions at  $\sqrt{S_{NN}} = 5.02$  TeV is larger than PbPb collisions at  $\sqrt{S_{NN}} = 2.76$  TeV. Besides experimental evidence, there were recent theoretical attempts [186] which essentially predicts the flow velocity to be larger for smaller systems at same collision energies. Thus the plots shown in figure 7.15, is indeed consistent in terms of transverse radial flow velocity as a function of  $\sqrt{S}$ ,  $\frac{dN_{ch}}{d\eta}$  and the size of the system produced either in pp or pA or AA collision. Kinetic freeze-out temperature ( $T_{kin}$ ), extracted from simultaneous BGBW fitting to data and shown in figure 7.16, demonstrates a decreasing nature with an increase in centrality (multiplicity) for each individual case of pp, pA and AA collision. However, comparison among different collision systems shows, pPb system freezes out quickly (with larger  $T_{kin}$ ) compared to the AuAu or the PbPb systems whereas, an anomalous behaviour for pp system was found which indicates lower  $T_{kin}$  compare to both the pA and AA systems at comparable  $\frac{dN_{ch}}{d\eta}$ . The  $T_{kin}$ , found for high-multiplicity pp collisions is fairly comparable with that for the central AA collisions. However, a theoretical calculation by Shuryak et al. [186] shows for a particular  $T_{kin}$ , though absolute sizes and multiplicities are quite different for central AA and pp collisions, pp systems get more explosive in nature compare to AA system. As a result, according to the hydrodynamic picture, a larger  $\beta$  as a function of initial time "t" and system size "r" is observed for a smaller system like pp compare to AA.

After an elaborate study with BGBW model approach to  $\pi^\pm$ ,  $K^\pm$ ,  $p(\bar{p})$  for different multiplicity classes, we have attempted to apply BGBW model in describing  $p_T$ -spectra for strange particles like  $K_S^0$ ,  $\Lambda$  and  $\Xi$ . The data, used for this study, was taken from recent results



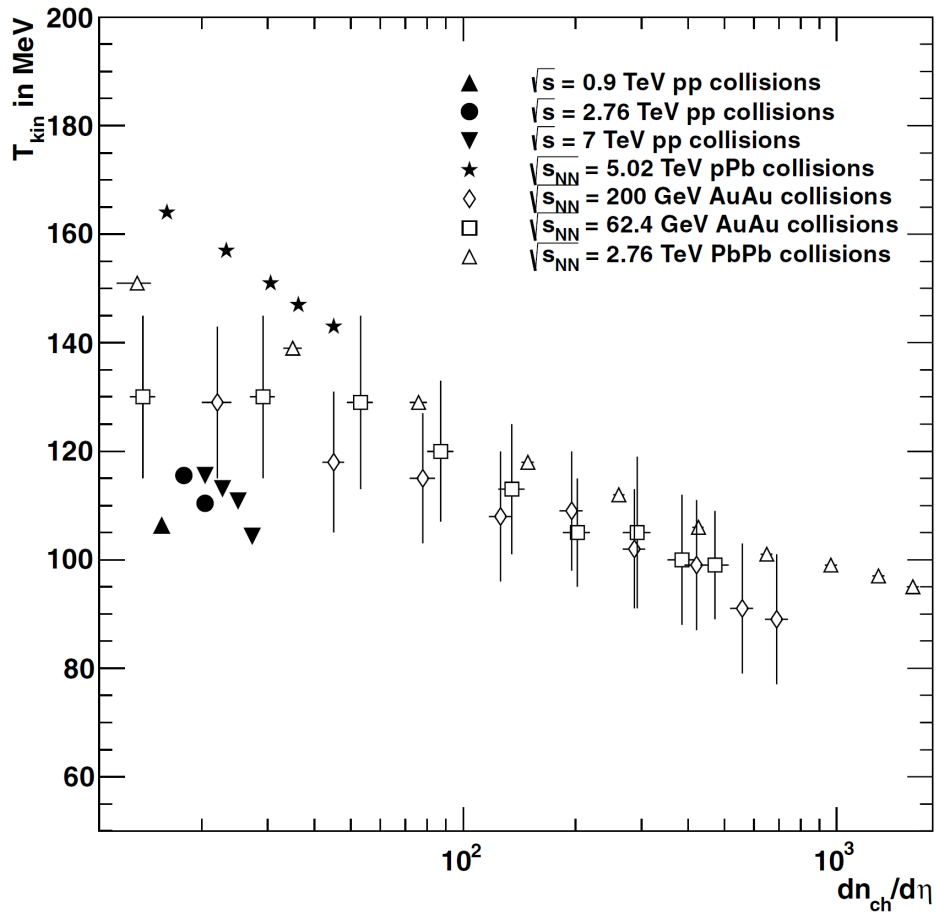


Figure 7.16: (Inverse slope parameter ( $T_{kin}$ : combined effect from flow and temperature) as a function of charged particle multiplicity density ( $\frac{dN_{ch}}{d\eta}$ ) for different centre of mass energies ( $\sqrt{S}$ ) as obtained from simultaneous blast wave fit to  $\pi^\pm$ ,  $K^\pm$ ,  $p(\bar{p})$  data for pp, pPb, and heavy ion collisions at LHC energies [223].

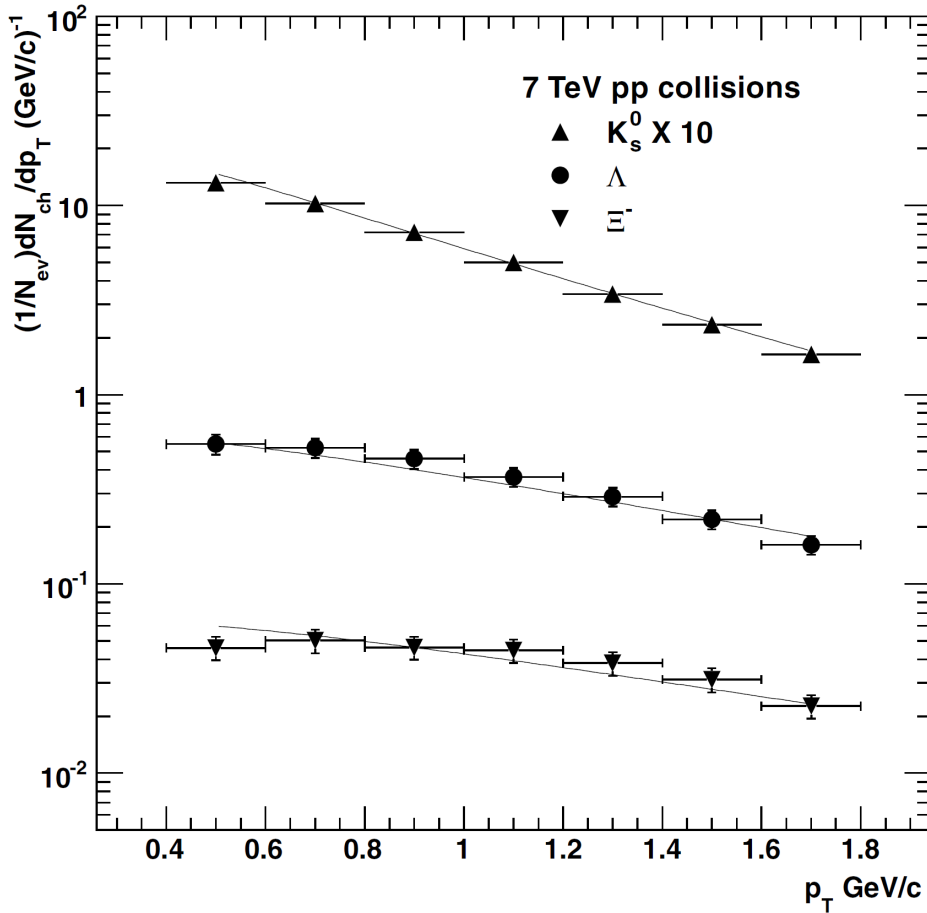


Figure 7.17: (Colour online). Transverse momentum spectra for strange particles  $K_s^0$ ,  $\Lambda$  and  $\Xi^-$  as measured by CMS collaboration for minimum bias proton-proton collision at 7 TeV centre of mass energy [223]. The solid lines are representing simultaneous blast-wave fitting to the family of strange particles.

from CMS collaboration [219, 222] for NSD pp events within the rapidity range  $|y| < 2$ . The strange particle spectra have been reconstructed from respective decays products (Strange meson  $K^0 \rightarrow \pi\pi$ , singly strange  $\Lambda \rightarrow p\pi$  and doubly strang  $\Xi \rightarrow \Lambda\pi$ ). As has been shown in figures 7.17 and 7.18,  $p_T$ -spectra with BGBW function could also be fitted satisfactorily with BGBW function for the  $p_T$ -range  $0.5 < p_T < 1.8$  GeV/c. The kinetic freeze-out temperature ( $T_{kin}$ ), the average radial flow velocity ( $\beta$ ) at the freeze-out surface and the exponent ( $n$ ) as extracted from simultaneous fitting along with respective  $\chi/ndf$  are tabulated in table 7.4.4.

The inspiration behind the studying strange particles, was to investigate the species dependence of blast-wave approach for pp collisions. Unfortunately, it is difficult to study one to one correspondence between strange and non-strange particles as the published spectra

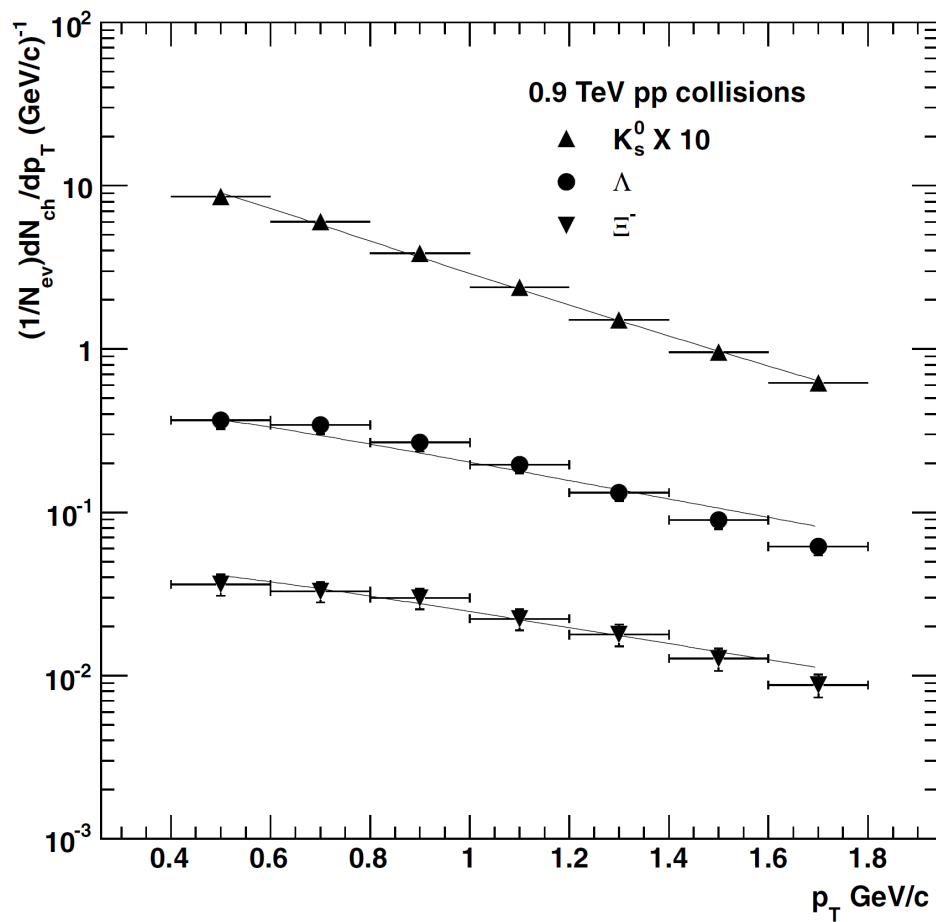


Figure 7.18: (Colour online). Transverse momentum spectra for strange particles  $K_s^0$ ,  $\Lambda$  and  $\Xi^-$  as measured by CMS collaboration for minimum bias proton-proton collision at 0.9 TeV centre of mass energy [223]. The solid lines are representing simultaneous blast-wave fitting to the data.

Table 7.8: Parameters of BGBW,  $T_{kin}$ ,  $\beta$  and  $n$ , have been extracted from the simultaneous fit to the published [31–54] spectra of strange mesons,  $K_S^0$ ,  $\Lambda$  and  $\Xi$  for pp collisions at  $\sqrt{S}=0.9$  and 7 TeV.

| $E_{CM}$ | $T_{kin}(\text{MeV})$ | $\langle \beta \rangle$ | $n$             | $\chi^2/ndf$ |
|----------|-----------------------|-------------------------|-----------------|--------------|
| 7        | $149 \pm 0.59$        | $0.62 \pm 0.006$        | $1.0 \pm 0.02$  | 0.85         |
| 0.9      | $140 \pm 0.53$        | $0.54 \pm 0.01$         | $1.27 \pm 0.12$ | 0.62         |

of for non-strange particles  $\pi^\pm$ ,  $K^\pm$ ,  $p(\bar{p})$  and strange particles  $K_S^0$ ,  $\Lambda$  and  $\Xi$  were measured in different kinematic-range. Moreover, the multiplicity dependent  $p_T$ -spectra are not available in case of strange particles which restrict the study for minimum bias data only. Nevertheless, the difference in BGBW description between strange and non-strange particles have also been observed in case of pp collision which is already there in heavy-ion collisions [224, 225].

Summarising in brief, the blast-wave approach in the search for collectivity in pp collision, revealed that the measured  $p_T$ -spectra of  $\pi^\pm$ ,  $K^\pm$ ,  $p(\bar{p})$  for the minimum-bias events of pp collisions at LHC at  $\sqrt{S}=0.9, 2.76$  and 7 TeV do not fit the BGBW, whereas, the spectra for  $K_S^0$ ,  $\Lambda$  and  $\Xi$  for NSD events at  $\sqrt{S}=0.9$  and 7 TeV pp collision could be well described by the blast-wave model. However, HM pp events can be well fitted with BGBW function which resemble similar results for AA collision, indicating the presence of collectivity even in pp collision.

## 7.5 Source of collectivity in pp collision.

The boost in centre of mass energy for pp collision at LHC had broadened the physics understanding beyond fundamental hard scattering and entered a new regime with special event classes, called high multiplicity, resembling properties found in the peripheral heavy-ion collision. We have found particle production in pp collision at LHC energies can be well described with two-component model (double NBD) indicating the presence of some other (soft) mechanism apart from hard scattering. Moreover, to understand the nature of system produced in pp collision including the softer part, BGBW model has successfully described the presence of collectivity in HM pp events which is specifically attributed to hydrodynamical nature of the system in case of a heavy-ion collision. In this context, it will be relevant to recall that, in the case of relativistic heavy-ion collisions, the local thermodynamic equilibrium is presumed to study the space-time evolution of the system using relativistic hydrodynamics [226]. On the other hand, as considered by most of the topical models, pp

collision do not endorse the formation of any medium. An obvious question regarding small system produced in pp collision is about achieving thermalisation to adopt hydrodynamical picture. Specifically, the mean free path of constituent particles in comparison to the system size along with the lifetime needs to cross-checked. However, a very recent study [227] about the system-size dependence of Knudsen number, a measure of the degree of thermalisation represented by the ratio of microscopic to the macroscopic property of the system, which illustrates that the system produced in AuAu collisions at RHIC and in high-multiplicity pp events at LHC, are similar which let hydrodynamical model to interpret the features of particle production in high-multiplicity pp events. Nevertheless, there are recent data of pp collisions, particularly for the HM events, published by different experiments at the LHC at CERN, unveiling features [228, 229], which are typical of the hydrodynamic medium formed in the relativistic heavy ion collisions. Immediately after, plenty of phenomenological studies with LHC pp data came up with the existence of [230–232] a collective medium which has been supported substantially by various theoretical approaches [183]. Estimation of initial energy density for HM pp events at LHC energies [181], showed that the system produced in pp collision is, indeed, energetically permissible to be comprised of partons instead of hadrons. In fact, Campanini and Ferri have shown in their work [184] regarding the change in phase for pp collision by analysing a wide range of data published by LHC experiments. From all above evidential observations in pp collisions, it is quite encouraging to follow the similar approach adopted in the search for the QGP in heavy-ion collisions with assuming local thermal equilibrium and search for signals for formation of partonic medium even in small systems like produced in pp collision. In our study, We have analysed pp data in the search of a signal of possible change of phase from hadron to parton or vice versa. The analysis is, however, completely data-driven and restricted with the availability of the kinematic range of the data, particles type, multiplicity classes etc.

### 7.5.1 Search for signal of phase change

As has been already discussed in earlier section that hadronic or partonic system are characterised with different degrees of freedom, namely pions (primarily) and partons (quark and gluons) respectively. Because of these obvious differences, we have put an effort in estimating the degrees of freedom, responsible for the system produced in a high multiplicity proton-proton collision. Estimation of energy density scaled with forth power of temperature, represents the number of degrees of freedom involved as is discussed in the subsection "Estimation of energy density", might give an important insight into the nature of the system produced in pp collision. We have calculated  $\frac{\epsilon}{T^4}$  or  $\frac{\sigma}{T^3}$  as a function of temperature, using available pp data for different multiplicity classes, as a signal for any possible phase change

as is predicted by the LQCD. Here,  $T$  represents temperature,  $\epsilon$  is the energy-density and  $\sigma$  is the entropy-density of the system under consideration. A sharp, step-like increase manifests the first order phase transition, whereas, a smooth but rapid rise indicates either the crossover or a second order phase transition. As of present scenario, latest LQCD calculations illustrate the transition as a crossover [233] in the QCD regime. At a temperature lower than the critical region of rapid rise, the system is populated mainly by pions, forming a hadron gas, however, the lattice calculation of  $\epsilon$  and  $\sigma$  is difficult as is exponentially suppressed [234]. On the other hand, At a temperature higher than the critical region, where the ideal gas limit of degrees of freedom is reached asymptotically, the system represents an ideal gas comprising of partons. However, due to the lack of a straightforward method of estimation of temperature from data, the predicted temperature dependence of  $\frac{\epsilon}{T^4}$  or  $\frac{\sigma}{T^3}$ , as a signal for the phase transition or the crossover is still a challenging task from experimental point of view. Moreover, the finite size effect [235, 236] of the system formed in the collision, may diffuse the signal which results smoothing of singularities in the LQCD-predicted dependence of the degrees of freedom.

Assuming non-viscous medium formed during the collision, the energy density can be calculated from the rapidity or the pseudo-rapidity density of the produced particles using relativistic hydrodynamics. High multiplicity pp data at  $\sqrt{S}=7$  TeV are available with enough statistics from CMS collaboration [237, 238]) which corresponds to the multiplicity density as large as  $\approx 30$  which is expected to be enough for the formation of non-hadronic medium. The main objective of this study was to investigate the dependence of  $(\frac{\epsilon}{T^4})$  on the temperature, not to evaluate the absolute value of the energy-density. Thus, we have adopted a simple 1-dimensional formalism [239] as proposed by Bjorken as has been discussed in equation 7.12 for the estimation of the energy-density. The low- $p_T$  part of the  $p_T$ -spectra, resulted from soft particle production mechanism in high energy collision, contains the information about the temperature as well as the transverse expansion of the system. As the contributions from temperature and the transverse expansion are twisted together not in an easy way, extraction of the temperature from the  $p_T$ -spectra is not possible unless otherwise exclusively experimentally measured. But, the mean transverse momentum, as proposed by Van Hove [208] or the slope of the transverse mass  $m_T$ -spectra could be used to as a signature of the thermal state of the system. Hence, in our study, we have probed the effective number of degrees of freedom in pp collisions in terms of the  $\langle p_T \rangle$ -dependence of  $\frac{\sigma}{\langle p_T \rangle^3}$ . It would be pertinent to mention that the inverse slope parameter ( $T_{eff}$ ), extracted from an exponential fit to the  $m_T$ -spectra, also contain both the information of thermal state and the transverse expansion of the system. The contributions are convoluted within the  $T_{eff}$

and can be written as  $T_{eff} = T + f(\beta)$ , where  $T$  and  $f(\beta)$  represent the temperature and the transverse expansion of the system respectively.

## 7.5.2 Analysis, results and discussion

The study under present scope has been carried out with published data by CMS collaboration [237, 238] for identified particles pions ( $\pi^\pm$ ), kaons ( $K^\pm$ ), and protons ( $p\bar{p}$ ) for pp collisions at  $\sqrt{S}=0.9, 2.76$  and  $7$  TeV respectively. The kinematic cuts for the available data were in terms of  $\frac{d\langle N_{ch} \rangle}{d\eta}$  for rapidity:  $|y| < 1$ , pseudo-rapidity:  $|\eta| < 2.4$ . Importantly, the data are available for a wide range of multiplicity ( $N_{ch}$ ) classes starting from 7 to 131 with reasonably good statistics. The measured transverse momentum ranges are different for different particle classes like  $1.0 \text{ GeV} \leq p_T^\pi \leq 1.2 \text{ GeV}$ ,  $0.2 \text{ GeV} \leq p_T^K \leq 1.05 \text{ GeV}$  and  $0.35 \text{ GeV} \leq p_T^{p\bar{p}} \leq 1.8 \text{ GeV}$  respectively. In fact,  $\frac{d\langle N_{ch} \rangle}{d\eta}$ -dependent data for identified particle give the opportunity to study for any possible change of phase in terms of degrees of freedom as a function of mean transverse momentum (representing temperature) experimentally. As is already discussed, the same data set has been used to search for collectivity in small system produced in pp collision at LHC energies [232] which resulted in a promising signature for collectivity. We have extended our study to reveal the source of the collectivity so found in pp collision. It is to be noted at this point that there is a model calculation which exhibits  $p_T$  as a function of temperature for identified hadron species, showing the change in shape of  $p_T$ -spectra due to transverse expansion indeed depend on particle mass like protons gain most in  $p_T$  while pions lose some  $p_T$ . Moreover, a model calculation [240] illustrates proton having a larger flow effect as an of late decoupling from the fireball compare to pions. On the other hand, pion has a lot of contamination specifically at lower  $p_T$  due to feeding down effects. As a result, Kaon, being weakly affected [241] by either re-scattering of hadrons or resonance decay, are considered to be a suitable candidate in the search for change in phase. Therefore, to avoid cumulative effect from transverse expansion of varying magnitude (different particles), we have considered individual  $p_T$ -spectra to extract the temperature dependent observable for the system. In this study, we have extracted  $\frac{\sigma}{\langle p_T \rangle^3}$  as a function of  $\langle p_T \rangle$  for charged pions and kaons produced in pp collision at  $\sqrt{S}=0.9, 2.76$  and  $7$  TeV separately. The radians, as appeared in Bjorken energy density 7.12, has been estimated using HBT-radius [242] which depend on the pair transverse momentum ( $kT$ ) and multiplicity. It is important to note here, that for a given  $\frac{dN_{ch}}{d\eta}$ , high- $kT$  indicates the early stage of the collision, whereas low- $kT$  is related to the final stage, close to the freeze-out. As the analysis aimed to estimate the energy density of the system produced

just after the collision,  $kT$  of relevance for our work is high- $kT$ , which has been taken as 0.5 to 1.0 GeV/c from CMS collaboration [229]). Since the study involves energy density as a function multiplicity ( $N_{ch}$ ), we have parametrised the radius of the interaction zone as a function of  $N_{ch}$  using  $R(N_{ch}) = a \cdot N_{ch}^{1/3}$  with  $a = 0.504 \pm 0.009$  fm. The entropy (energy) density for different multiplicity classes have been calculated both for pions and kaons and are shown in figures 7.19 and 7.20. In both, the cases, a definite and smooth but rapid rise in  $\frac{\sigma}{\langle p_T \rangle^3}$  with an increase in  $\langle p_T \rangle$  is found. This, indeed, indicates release of new degrees of freedom over a small change in  $\langle p_T \rangle$  in lower  $p_T$ -range. However, in the high  $p_T$  range, kaons and pions behave differently. No conclusive remarks about phase cannot be made because of lack of saturation in  $\frac{\sigma}{\langle p_T \rangle^3}$  in case of pions, whereas kaons at high  $p_T$  (high temperature) clearly points towards a saturation which corresponds to highest number of degrees of freedom for the possible partonic phase. The difference in pions and kaons behaviour is rather consistent as has explained in articles [243, 240, 241] at high  $p_T$ . The loss of  $p_T$  for pions [243] could be the reason for wearing away of the saturation effect for high multiplicity pp events. Also, the differential freeze-out of hadron species due to different elastic cross-sections [240–242] may lead to the early freeze-out for kaon in comparison to pion, which may describe the observed difference in response by the pions and the kaons. The reason behind kaon being less affected by the early freeze-out can be understood as the kaons are staying less with the system leading to less effect by the flow of the system. As a result, kaons are most retrain the temperature information of the system. However, it should be noted that the  $p_T$ , though, represents the temperature, but it can not give an absolute measure for  $T$ . Similar arguments stays for  $\frac{\sigma}{\langle p_T \rangle^3}$  as here also instead of  $T$ ,  $\langle p_T \rangle$  has been used. The fact of lack of experimentally measured temperature, the study, however, is limited with only qualitative aspects of LQCD-predicted signal for the change in phase of matter formed in pp collisions. Importantly, the nature of the signal for phase change from a data-driven approach matches satisfactorily to the results of the latest LQCD calculations predicting a crossover [233].

Though the multiplicity dependent study of pp collision with a data-driven, simplistic 1-D hydrodynamical Bjorken model reveals a new feature of possible indication for phase change, a comparison with the conventional Monte Carlo Event Generators is virtually obligatory. For our study, we have used standard event generators commonly used in the field. PYTHIA8.1 Tune 4C, explains [245] global properties like the  $p_T$ -dependence on  $N_{ch}$  in pp collisions as measured by ALICE, is relevant among various available versions. It is important at this point to note that PYTHIA along with colour reconnection [102–104], an alternative explanation for anomalous behaviour in pp data, can reproduce ALICE results satisfactorily of  $p_T$ -dependence on  $N_{ch}$  for the  $p_T$ -range up to 10 GeV/c whereas PYTHIA without CR

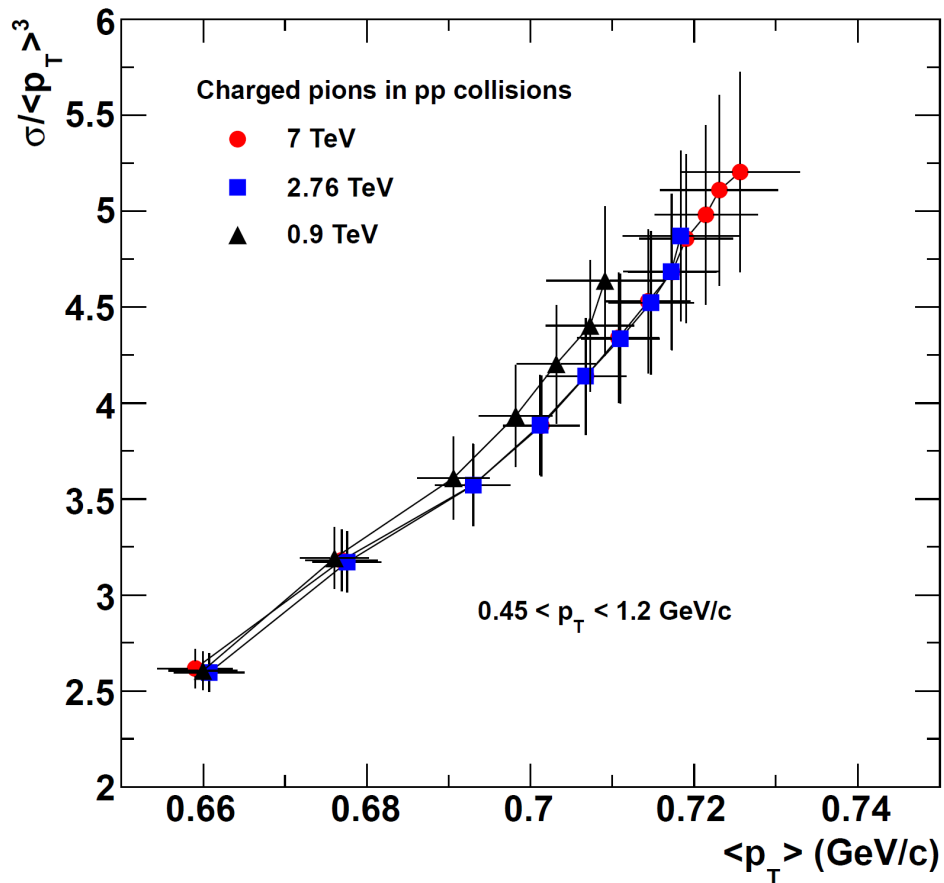


Figure 7.19: (Colour online). The figure represents the variation of entropy scaled with cube of transverse momentum ( $\frac{\sigma}{\langle p_T \rangle^3}$ ) as a function of average transverse momentum ( $\langle p_T \rangle$ ). Effectively, the figure shows the variation of degrees of freedom (DOF) for pions, obtained from the published pion-spectra data from CMS collaboration. The trend towards saturation at larger  $\langle p_T \rangle$  has been observed. The solid lines, joining data points, are to guide the eye. The error bars include both the statistical and systematic uncertainties [244].

can explain so. CR, a final state effect resulting traverse boost to the produced particle is manifested from multi-partonic interaction. We have generated pp events at  $\sqrt{S}=7$  TeV using PYTHIA8.1 Tune 4C event generator both with and without CR. The dependence of  $\langle p_T \rangle$  on  $N_{ch}$  were plotted and compared with data which has been shown in figure 7.21 for unidentified and figure 7.22 identified particles.

Although ALICE publishes data charged hadrons and compare with PYTHIA8.1 Tune 4C generated events in the  $p_T$ -range up to 10 GeV/c, but for our study, we have chosen the same kinematic range as has been used by the CMS collaboration [237]). We have plotted  $\langle p_T \rangle$  as a function of  $N_{ch}$ , as obtained from the CMS data [27, 28], for the pseudo-rapidity range ( $|\eta| < 2.4$ ) and the  $\langle p_T \rangle$ -ranges (0.1 to 1.2) GeV/c for  $\pi^\pm$ , (0.2 to 1.050) GeV/c for  $K^\pm$ ). As is clear from the figure 7.22, though the PYTHIA with CR gives the boost in the  $p_T$  of the produced particles, it is still far from the measured values for the kinematic ranges under consideration. The exercise, indeed, established the expected results regarding the mismatch between the data and the PYTHIA simulation. After finding the difference in  $\langle p_T \rangle$  as a function of  $N_{ch}$  for PYTHIA simulated events, we have calculated the entropy density ( $\frac{\sigma}{\langle p_T \rangle^3}$ ) as a function of  $p_T$  for the simulated data and compared with that of found from CMS published data, as is shown in figures 7.19 and 7.20.

It is significant in this context, that the temperature of a thermalised partonic medium, if formed, should in principle be reflected by the low- $p_T$  particles (usually  $p_T \leq 2$  GeV/c, as has been considered in heavy-ion collisions) and the CMS data can fulfil the desired requirement in this respect. As is always advisable, the prediction must be compared to established results for similar kind of the system. Though the existence of partonic medium is beyond doubt in the case of system produced in heavy ion collision, it is to be remembered that the extent of the system in AA collision is somewhat obvious. However, there exist results for a small system formed in proton-lead collision, which exhibits stronger evidence for collectivity

Perception about proton proton collision has unprecedented importance in understanding the particle production at relativistic high energy collision for different colliding system in terms of understanding of new physics processes, structural information inside nucleon, the baseline for the more complicated system and many more. With the advantage of accelerator technologies, the boost in  $E_{CM}$  lifted the proton-proton collision to a regime where it is expected to hold more than reflecting fundamental hard scattering phenomenon. Specifically, during LHC era, search for a small but more complicated system like in heavy-ion collision in pp ( $p\bar{p}$ ) collision reinstate the concept of the thermalised partonic matter even in pp collision. It is customary to mention that, prior to LHC, there have been several initiatives and studies [208, 246–250] which have addressed the de-confinement and formation of

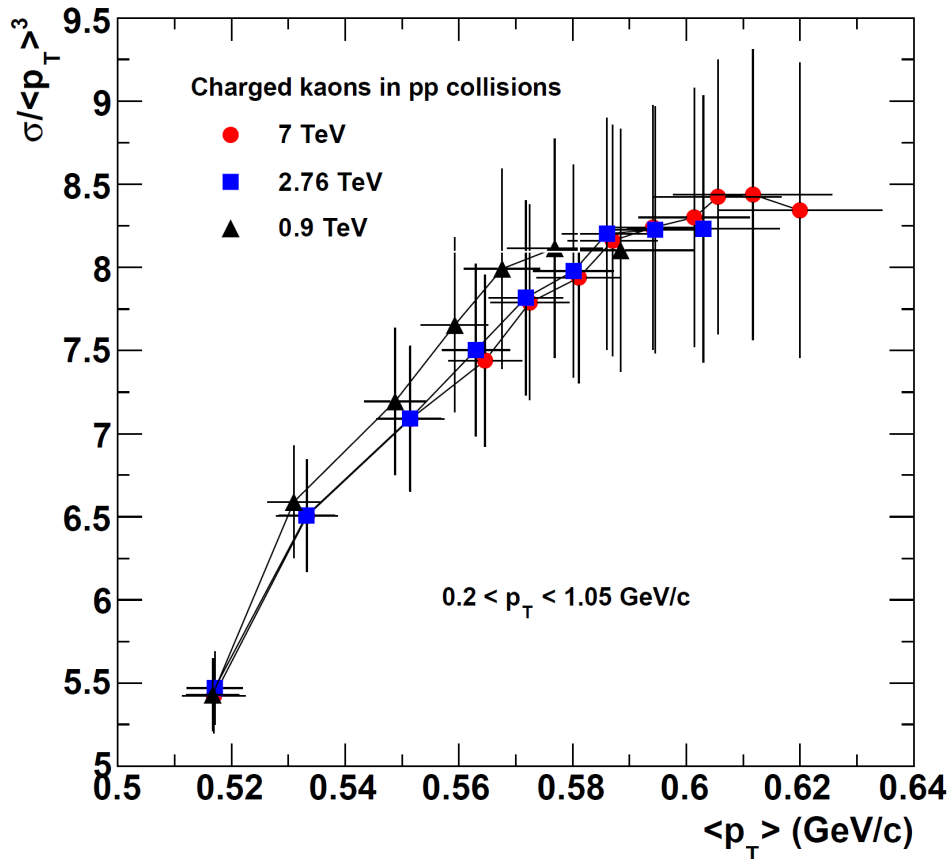


Figure 7.20: (Colour online). The figure represents the variation of entropy scaled with cube of transverse momentum ( $\frac{\sigma}{\langle p_T \rangle^3}$ ) as a function of average transverse momentum ( $\langle p_T \rangle$ ). Effectively, the figure shows the variation of degrees of freedom (DOF) for kaons, obtained from the published pion-spectra data from CMS collaboration. The trend towards saturation at larger  $\langle p_T \rangle$  has been observed. The solid lines, joining data points, are to guide the eye. The error bars include both the statistical and systematic uncertainties [244].

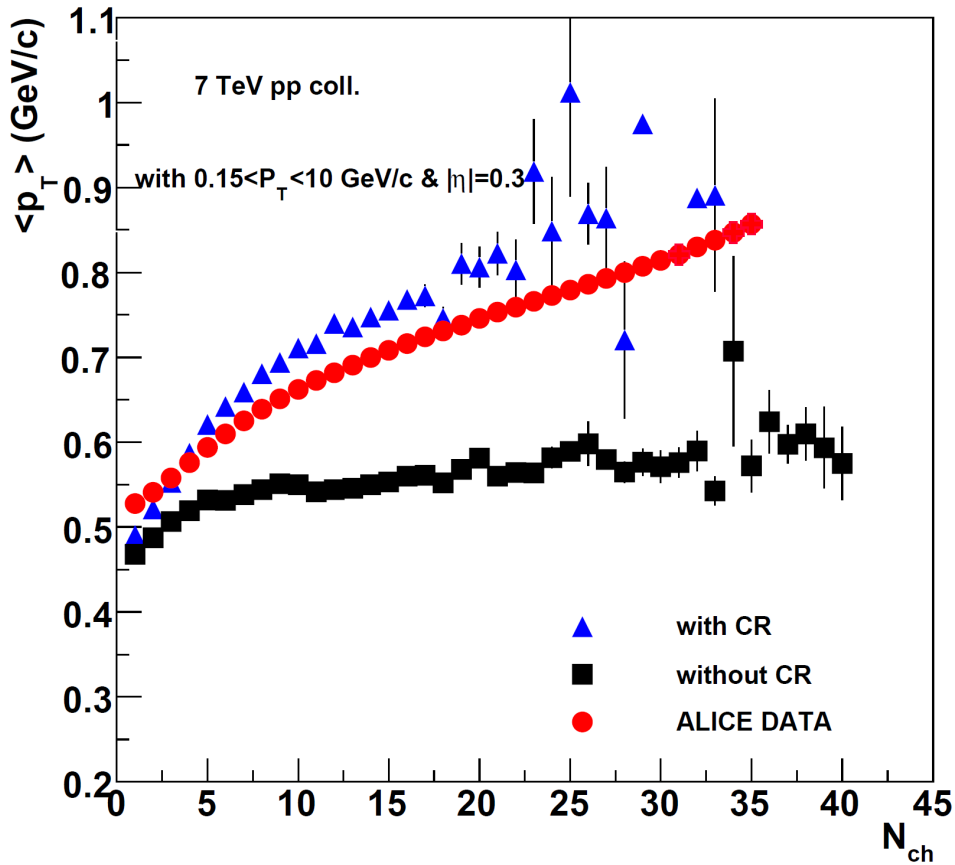


Figure 7.21: (Colour online). The figure shows average transverse momentum ( $\langle p_T \rangle$ ) as a function of charged particle multiplicity ( $N_{ch}$ ) for the  $p_T$ -range  $0 \rightarrow 10$  GeV and pseudo-rapidity range  $\pm 0.3$ . The data (solid red circle) has been taken from ALICE collaboration and was compared with the simulated events using PYTHIA8 Tune 4C event generator both with and without Colour Reconnection (CR) for pp collisions at 7 TeV. The error bars include both the statistical and systematic uncertainties [244].

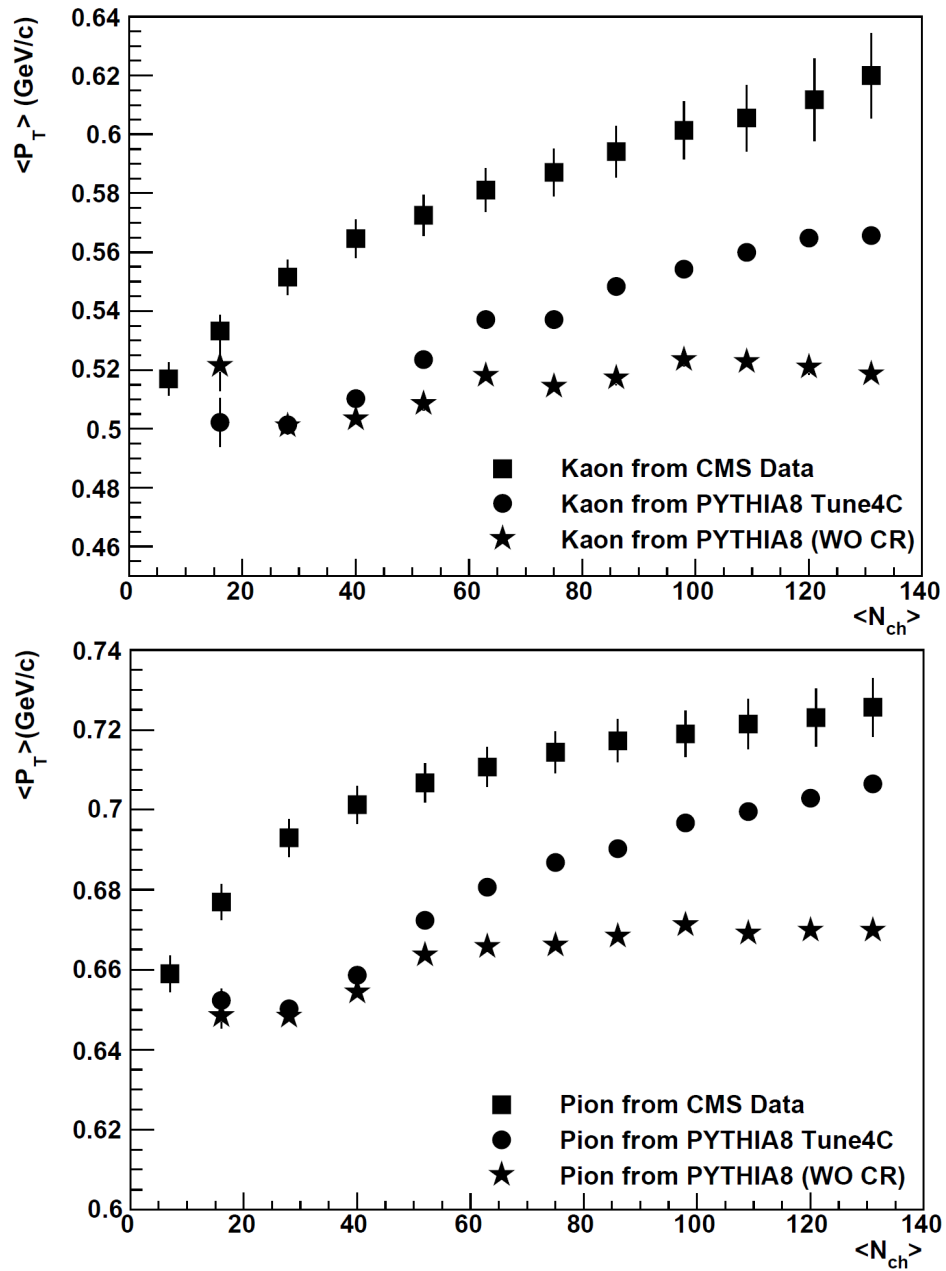


Figure 7.22: (Colour online). The figure shows the variation of average transverse momentum ( $\langle p_T \rangle$ ) as a function of charged particle multiplicity ( $N_{ch}$ ) for kaon (upper panel) and pion (lower panel) for proton-proton collisions at 7 TeV. . The data from was taken from ALICE collaboration and compared with the simulated events using PYTHIA8 Tune-4C both for colour reconnection on and off. The plots had been generated for the  $p_T$ -range up to 2 GeV both for kaon and pion. The error bars include both the statistical and systematic uncertainties [244].

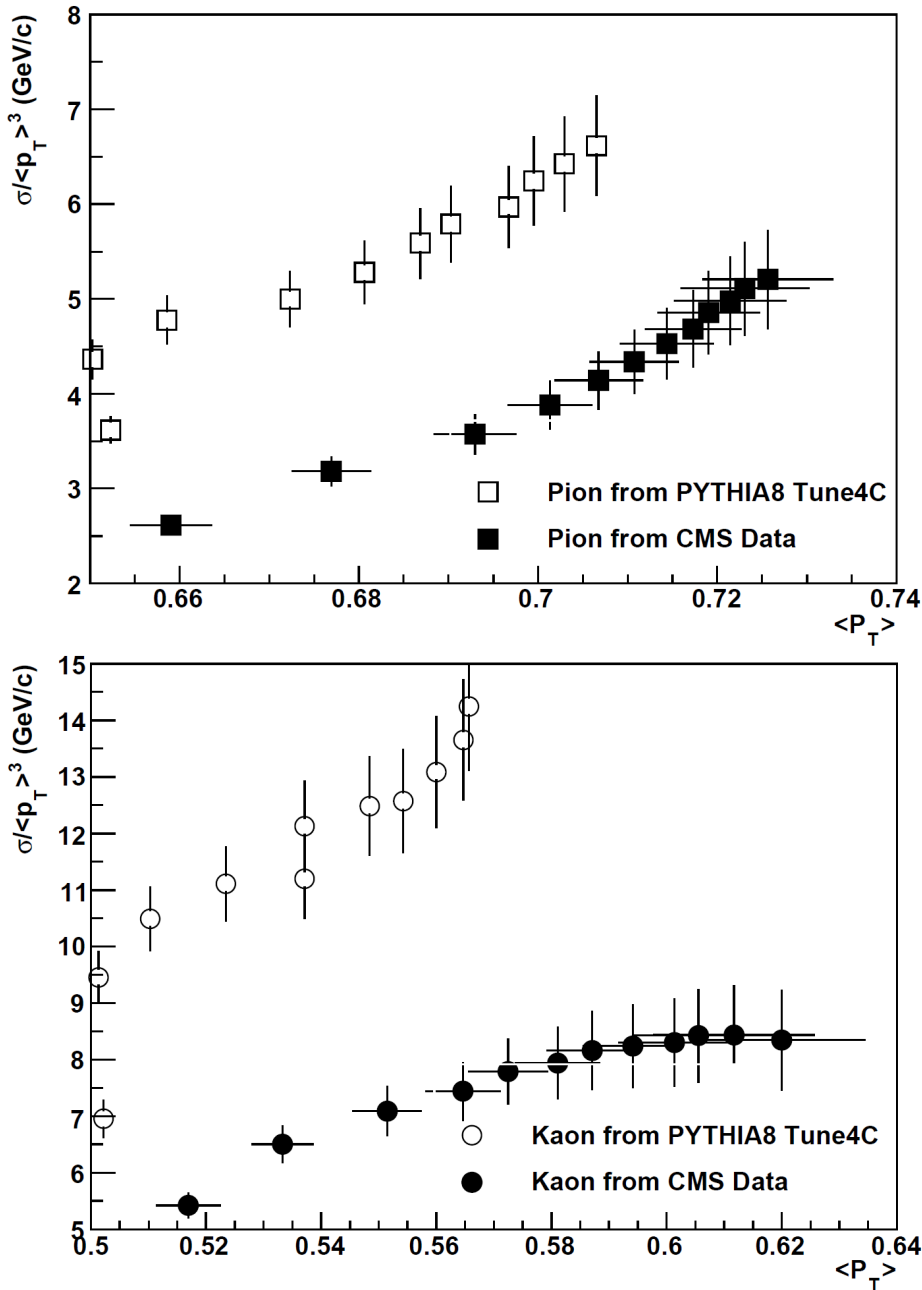


Figure 7.23: (Colour online). The figure shows the variation of  $\frac{\sigma}{\langle p_T \rangle^3}$  as a function of the mean transverse momentum ( $\langle p_T \rangle$ ) for pions (upper panel) and kaons (lower panel) for proton-proton collision at 7 TeV. The open squares represents simulated data from PYTHIA Tune-4C, whereas, solid squares are obtained from the measured [217] spectra data by CMS collaboration. The figures clearly shows differences between simulation and experiment as was expected. The error bars include both the statistical and systematic uncertainties [244].

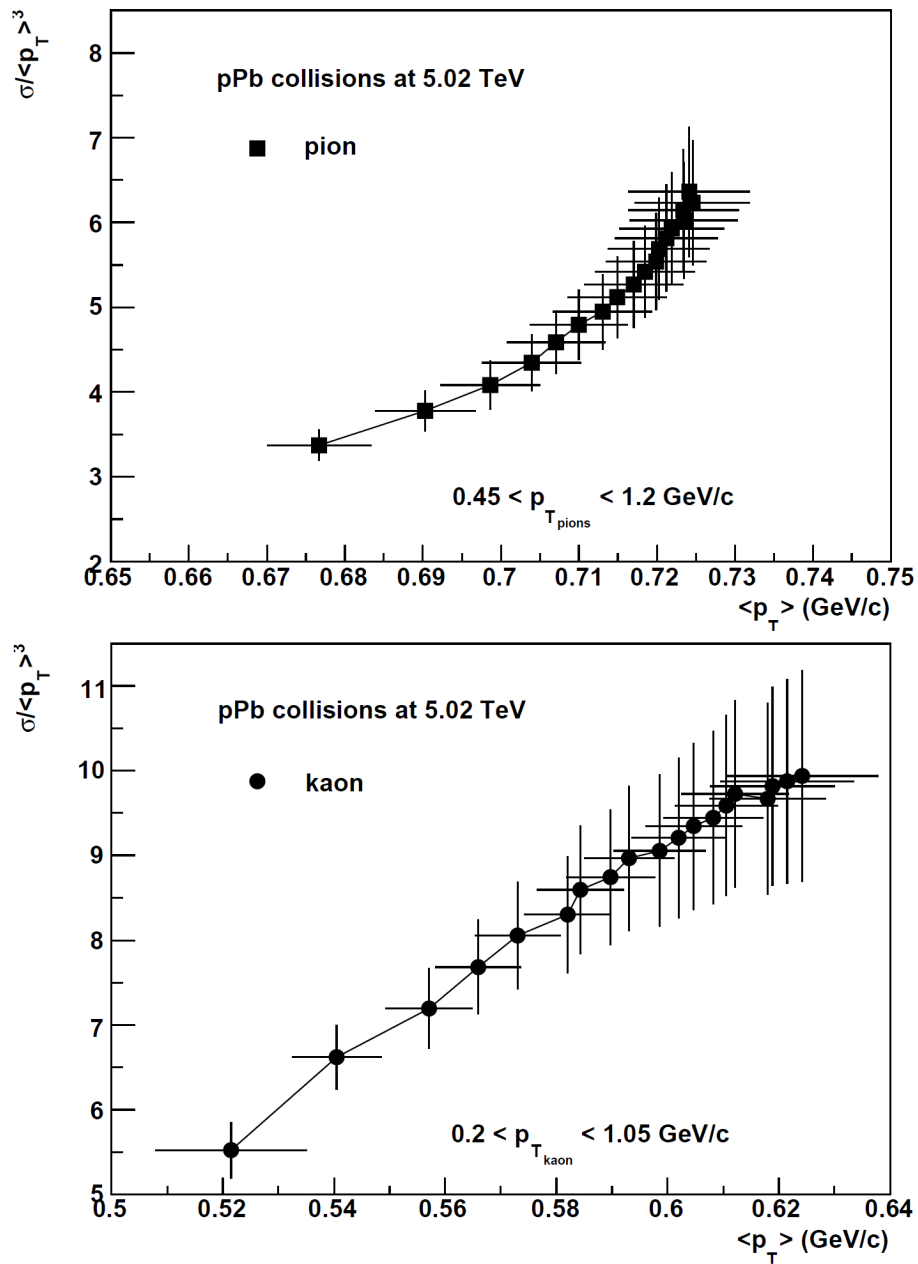


Figure 7.24: (Colour online). The figure illustrates the behaviour of  $\frac{\sigma}{\langle p_T \rangle^3}$ , extracted for proton-Lead collision at 5.02 TeV, as a function of the average transverse momentum ( $\langle p_T \rangle$ ) pion (upper) and kaon (lower). The open circles represent data from PYTHIA Tune-4C simulation, whereas, solid circles are obtained from the CMS collaboration [217]. The error bars include both the statistical and systematic uncertainties [244].

hydrodynamic medium in  $p\bar{p}$  collisions. In the same regards, we have revealed in our study an indication of a possible change of phase in pp collision in terms of the effective number of degrees of freedom represented by  $\frac{\sigma}{\langle p_T \rangle^3}$ . However, there is an obvious issue about acceptance of the thermal equilibrium for such a small system produced in pp collision. The concern can be explored with the fact that measured particle multiplicity in high-multiplicity pp collision at LHC energies is comparable to CuCu collision at  $\sqrt{S}=200$  GeV at RHIC [182]. We have studied in this work, the dependence of degrees of freedom on  $\langle p_T \rangle$  for multiplicity dependent event classes in pp collision. The study has perceived that the liberation of an effective number of degrees of freedom for a given pseudo-rapidity density and for a given  $p_T$ -range, depending on multiplicity (centrality) class and is independent of the centre-of-mass energy.

## 7.6 Summary

Summarising in brief, pp collision with minimum bias at LHC energies can be described with two-component model for a wide pseudo-rapidity window, indicating the possibility of particle production in pp collision is more than as understand as from hard scattering. Moreover, the phenomenological blast wave model description of pp data established a potential collectivity, more prominent for high multiplicity events. Though there is a lack of conclusive remarks about the so found collectivity in pp collision, but certainly, it provokes to dig more into the matter. At the end, we have adopted a data-driven analysis of the published data for pp collisions at the LHC, in terms of  $\frac{\sigma}{\langle p_T \rangle^3}$  (DOF) as function of multiplicity ( $\langle p_T \rangle$ ) which observe a smooth rise over small  $p_T$ -range for identified particles pion and kaon. LQCD predicted signal, for the change of phase, has been calculated experimentally adopting the same procedure that has been followed [14–17] in heavy-ion collisions by characterising the medium formed after collisions. Though at the same time the study can not claim that the experimental verification, for the change of phase in terms of change in degrees of freedom, is done convincingly. Moreover, the usefulness of the species-dependent response of the system, in search of a change in the effective number of degrees of freedom, found to be significant in this study and can enhance the relevance in heavy-ion collision. Still and all, the finding can not definitely clinch the signal as a "smoking gun" for a change of phase in pp collisions, but, it certainly reveals a new feature, significant enough to extend the study in search of collectivity and nature of collectivity in small systems produced in high multiplicity pp collisions.

# Chapter 8

## Summary

### 8.1 Summary and Future Scope

The present study comprised of two major topics, Forward-Calorimetry as an ALICE upgrade proposal and studying proton-proton collision at LHC energies with "out-of-the-box" explanation. The first part is aimed to enhance the present physics capabilities of ALICE experiment, specifically in forward rapidity region, with an extended physics interests starting from proton-proton to proton-nucleus to nucleus-nucleus collision. Whereas in second part, the physics potential of proton-proton collision with published data at LHC energies is explored which otherwise served for baseline for the more complex system like in Nucleus-nucleus collision. Here a brief discussion about the achievements and extent for further work will be presented for the sake of completeness of the study.

#### 8.1.1 Forward Calrimetry

The study started with an general introduction about the calorimetry, used in relativistic high energy collision. After brief survey of the field, the **Sampling type electromagnetic calorimeter** was discussed in more detail which suits the purpose of the study. As an primary requirement, the calorimeter was so choosed that it can measure photons for a wide range of energies up to  $p_T \leq 20 \text{ GeV}/c$  and it must be capable of disentangling different types of photons depending on their sources (e.g. prompt, thermal and decayed). The final physics motivation, however, is to probe the small- $x$  domain of parton distribution which supposed to reach a saturation scale ( $\Lambda_S$ ) for gluons at LHC energies leading to Color Glass Condensate. Moreover, the photon measurement at forward rapidity has also potential in understanding the parton energy loss and thus measuring the opacity of the partonic medium. To start with, an extensive simulation for geometry optimization for calorimeter was performed

using GEANT4 toolkit. 3.5 m along the beam line from the interaction point has been chosen as the position for the calorimeter at ALICE experiment which can cover 2.5 to 4.5 in pseudo-rapidity. However, an alternate position at 7 m away from the IP was also considered as an alternate position which will shift the rapidity coverage by unity. Specification for the calorimeter was optimised after a thorough simulation which resulted a sampling type,  $20 \times R$  depth calorimeter with full azimuthal coverage. There are 20 layers, comprised of tungsten as absorber and Silicon as detector along with relevant readout electronics, were considered. 6 cm and 80 cm were taken as inner and outer radius for the transverse dimension of the calorimeter. The granularity of the detector has been decided by taking input about particle density (No of particle/cm<sup>2</sup>) using HIJING event generators, that the calorimeter might face in high multiplicity density environment like in ALICE. The study gave an optimized solution with 17 low granular layer (LGL: detector size 1 cm<sup>2</sup>) and rest three high granular layer (HGL: detector size 0.1 cm<sup>2</sup>). The three HGL layers are interleaved at 4<sup>th</sup>, 8<sup>th</sup>, 12<sup>th</sup> layer to equally distribute the measurement efficiency of calorimeter for the wide range of incident gamma energy 1 to 200 GeV. Detailed calorimetric performances starting from Minimum ionising particle response, electromagnetic shower response, calibration of the deposited (simulated) energy with incident energy and finally energy resolution of the calorimeter have been completed. The calorimeter found response of 89 KeV as MPV to pion which behave like minimum ionising particle with nicely developed Landau distribution, as is expected for 300  $\mu$ m thin silicon detector. The depth of the calorimeter was found reasonably good to assure full energy containment for the desired incident gamma energy as is illustrated by both the longitudinal and cumulative energy deposition profile. The optimized configuration for the calorimeter resulted a energy resolution of  $\frac{\sigma}{E_{in}} = 0.035 \oplus \frac{0.1905}{\sqrt{E}}$ . To check the capability of the calorimeter in reconstructing the  $\pi^0$  from its two decayed photons, Invariant mass ( $M_{\pi^0 \leftarrow \gamma\gamma}$ ) of  $\pi^0$  has been calculated using FCM clustering algorithm and found satisfactory up to 100 GeV and need improvement beyond.

After a satisfactory performances with simulation, we have worked for development and fabrication for prototype calorimeter. At the beginning, a miniature version with four layers of detector, interleaved between 10 cm\*10 cm tungsten plates. 5\*5 array of physically isolated 1 cm<sup>2</sup> detector, mounted on detector PCB, was fabricated and tested initially with radioactive sources at laboratory and then with CERN-PS beam line facility. The results from the test beam were quite encouraging in terms MIP-response of 17 ADC which has been cross-checked taking detector and electronic parameters into consideration. Moreover, truncated longitudinal profile were also reconstructed for all available incident electron energies (1 to 6 GeV). The linearity of the measured energy to the incident energy of the mini-prototype calorimeter was also checked and found as expected which has been discussed in detailed in

the result section of the mini-prototype test.

Taking input from mini-prototype experience, further development for full depth prototype was planned and developed.  $6 \times 6$  array of  $1 \text{ cm}^2$  detector layer was designed and fabricated on a single 4 inch wafer and mounted on a detector PCB both to hold and connecting the detectors to the front end electronics. The same set of tungsten plates, as in mini-prototype, were used for the full depth prototype as well. For readout of the data, MANAS along with a newly developed ANUSANSKAR ASICS were used. Since the test beam with full depth prototype was planned with CERN SPS beam line facility where higher incident energy (5 to 60 GeV) for electrons are available. The analysis, as presented in chapter 2, shows expected performances of the prototype calorimeter both to pions (MIP) and electrons (EM-shower). As is presented, the calorimeter worked, indeed, in a good linearity and can produce smooth longitudinal profile for the available incident electron energies. interestingly, the prototype resulted an energy resolution of  $\frac{\sigma}{E_{in}} = 0.05 \oplus \frac{0.221}{\sqrt{E}}$  which close to the results from simulation. However, at the higher end of the incident energy range, with the present configuration, the prototype experience saturation in measuring energy which call for update in the readout electronics.

### **Future scope:**

As has been discussed already, with the present setups with both detectors and electronics, there is a need for upgradation to cope up larger energy deposition, expected for higher incident energies. Calculatulation shows, the dynamic range for the electronics required in final go need to be  $\approx 1000$  MIP (4 pC) which is presently  $\pm 500$ fC for MANAS ASIC. Moreover, in the present study, 4 inch wafer technology has been used for the silicon detector fabrication which need to be upgraded to 6 inch wafer technology. As has been discussed, the present study is only with LGC layers both in case of mini and the full depth prototype which has importance in establishing the proof of concept as well as basis calorimeter performnces. However, the future scope should entangle both LGL and HGL layers in the complete prototype and check for the final calorimeter and physics performances. After succesful completion of final prototype fabrication, resembling the proposed and designed calorimeter, an intense work for full size calorimeter aimed to be materialized.

## 8.1.2 Phenomenology with HM pp physics

In the 2<sup>nd</sup> part of the study, proton-proton collision has been reviewed differently against the regular understanding of particle production specifically at LHC energies. Proton-proton collision, before LHC era, used to serve the basic purposes of reference for more complex system like in nucleus-nucleus collision. Prediction from pQCD was found providing satisfactorily good description for particle production in pp collision where hard scattering among partons are supposed to be responsible for production mechanism. However, with the increase in centre of mass energies, pp collision observes a new class of events, known as High Multiplicity events, characterised by unexpectedly large particle production. The present study revealed the physics of proton-proton collision subject to available published data with phenomenological model approach to understand the global properties like multiplicity, collectivity and etc. Two component model, weighted superimposition of two Negative Binomial Distribution as discussed in section 3.3.1, was applied to multiplicity distribution for proton-proton collision at  $\sqrt{S} = 7$  TeV. The study was done for both small and large  $\eta$ -window of 0.5 and 2.5 respectively at forward rapidity with two events classes minimum bias and Hard-QCD events, based on criterion set by LHCb experiment at CERN. The study unveiled that the minimum bias data can be well described by two NBD model, indicating presence of particle production mechanism different from Hard scattering, while the Hard-QCD events can be explained with a single NBD. However, both the minimum bias and Hard-QCD events for wide  $\eta$ -window can be well described by double NBD. As a concluding remark, the study, indeed, explored the possibility of particles production mechanism (semi-Hard or soft) more than just hard-scattering even in proton-proton collision and need further critical investigation. Subsequently, with availability of pp data for different multiplicity classes, Blast-Wave model, a phenomenological model approach to understand the collective movement of an outbursting system, has been adopted for lower part of the  $p_T$ -spectra for different identified particles at centre of mass energies 0.9, 2.76 and 7 TeV respectively, as measured by CMS collaboration. Assuming the system formed in pp collision experience a collective nature, simultaneous fitting with BW function used to extract the common outward radial velocity ( $\beta$ ) as well as the kinetic velocity ( $T_{Kin}$ ) at freeze-out as a function of Multiplicity which serve the purpose of centrality in pp collision. Importantly, The  $\beta$  and  $T_{Kin}$  as a function of multiplicity behave similarly as nucleus-nucleus collisions, where collectivity due to de-confinement of quarks is established. The exercise with two different species of particles, strange and non-strange, resulted different set of values for  $\beta$  and  $T_{Kin}$  which can be understood as a result of successive freeze-out as a possible explanation. Importantly, simultaneous fitting with BW function could be done satisfactorily depending on  $\chi^2/NDF$  values for high multiplicity pp events only for all available centre of mass energies. The results about collectivity from this study

observe a theoretical agreement as has been discussed in section 3.4.4. Although, there is no clear evidence about the source (hadronic or partonic) of collectivity for system produced in pp collision, but there is obvious hints from similarities with heavy-ion collisions which illustrates possible formation of deconfined partonic system, responsible for non-perturbative particle production mechanism in proton-proton collision.

At the end, a data driven approach was explored to search for a direct evidence for possible phase transition (parton to hadron or vice versa) event at pp collision. A simplistic 1-D hydrodynamical calculation, following Bjorken model, was performed to extract the energy (entropy) density for system using published pp data by CMS collaboration. Due to unavailability of the temperature of the system formed in pp collision,  $\langle p_T \rangle$  has been used in place of temperature accepting the fact that it, indeed, contain flow contribution along with the temperature. Moreover, HBT-radius has been used in finding the volume of the pp system. Effective number of Degrees of Freedom (DOF), an LQCD predicted signal for change of phase, represented as  $\frac{\sigma}{\langle p_T \rangle^3}$  and responsible in characterising the system, was calculated as a function of  $\langle p_T \rangle$  (multiplicity) as discussed in detail in section 3.5. A smooth increase for DOF as function of  $\langle p_T \rangle$  has been observed both for pion and kaon. However, kaon shows saturating trend at high  $\langle p_T \rangle$  while pion lack so within the available maximum  $\langle p_T \rangle$ . Surely, even though the study can not demand the signal as the "smoking gun" for the change of phase in pp collisions, but it encourage for further exercise towards search and characterize the collective medium in pp collision.

### **Future scope:**

The study, inspired by a different thought for relativistic high energy proton-proton collision, explored systematic understanding about searching for soft particle production mechanism in pp collision and characterizing it assuming a existence of a collective medium. Though, there is no such unique confirmatory signal to endorse the collectivity and deconfined partonic phase as it's source, but, concurrently there are indications pointing towards possible phase transition even in small system like in pp collision. A recent result about strangeness enhancement [72] in pp collision, mimicking results from heavy-ion collision and attributed to Quark-Gluon-Plasma, create a new dimension in the field. However, as emerged from the study, there is a scope of reviewing global properties of pp-system as a function of multiplicity irrespective of centre of mass energy. Moreover, pp collision, as may lead to small scale partonic system, must be considered carefully during addressing and comparing results

from nucleus-nucleus and proton-nucleus collision to avoid any artifact that might be coming from pp-reference itself.

# Bibliography

- [1] S. Bethke *Prog. Part. Nucl. Phys.*, vol. 58, 2007.
- [2] “The united states at the lhc,” <http://united-states.cern/physics/standard-model-and-beyond>.
- [3] “Tapan nayak, heavy ions: Results from the large hadron collider,” <https://arxiv.org/pdf/1201.4264.pdf>.
- [4] T. Boeckel and J. Schaffner-Bielich *PHYSICAL REVIEW D*, vol. 85, p. 103506, 2012.
- [5] A. collaboration *Journal of Physics: Conference Series*, vol. 105, p. 252301, 2010.
- [6] “Tapan nayak, quark-gluon plasma: Present and future,” <https://arxiv.org/abs/0804.1368v1>.
- [7] “Particle data group,” <http://pdg.lbl.gov/>.
- [8] Heitler, “The quantum theory of radiation,” *Clarendon Press*, 1944.
- [9] <https://cds.cern.ch/record/2282027/plots>.
- [10] <http://inspirehep.net/record/827234/plots>.
- [11] L. D. McLerran and R. Venugopalan *Phys. Rev. D*, vol. 49, p. 3352.
- [12] L. D. McLerran and R. Venugopalan *Phys. Rev. D*, vol. 49, p. 2233.
- [13] L. D. McLerran and R. Venugopalan *Phys. Rev. D*, vol. 50, p. 2225.
- [14] A. Dumitru and J. Jalilian-Marian *Phys. Rev. Lett.*, vol. 89, p. 022301.
- [15] A. Dumitru and J. Jalilian-Marian *Phys. Lett. B*, vol. 547, p. 23.
- [16] F. Gelis and J. Jalilian-Marian *Phys. Rev. D*, vol. 66, p. 014021.
- [17] T. Peitzmann *et al.* *arXiv:1308.2585*, 2018.
- [18] A. collaboration *EPJC*, vol. 68, p. 345, 2010.
- [19] C. collaboration *Phys. Rev.Lett.*, vol. 105, p. 022002, 2010.
- [20] T. Alexopoulos *et al.* *Phys. Lett. B*, vol. 528, p. 43, 2002.

- [21] M. Csanad *et al.* *Universe*, vol. 3, p. 9, 2017.
- [22] E. Shuryak *et al.* *Phys. Rev. C*, vol. 88, p. 044915, 2013.
- [23] P. Ghosh *et al.* *PHYSICAL REVIEW D*, vol. 87, p. 094020, 2013.
- [24] S. Chatrchyan *Euro. Phys. J. C*, vol. 74, p. 2847, 2014.
- [25] S. Kar *et al.* *PHYSICAL REVIEW D*, vol. 95, p. 014016, 2017.
- [26] V. Khachatryan *et al.* *J. High Energy Phys.*, vol. JHEP05, p. 064, 2011.
- [27] V. Khachatryan *et al.* *Euro. Phys. J. C*, vol. 72, p. 2164, 2012.
- [28] P. Ghosh *et al.* *J. Phys. G: Nucl. Part. Phys.*, vol. 41, p. 035106, 2014.
- [29] P. Ghosh *et al.* *arXiv:1406.5811 [hep-ph]*.
- [30] “The history of atom,” <http://thehistoryoftheatom.weebly.com/democritus.html>.
- [31] “Maharshi Kanada – the propounder of atomic theory,” <http://firstip.org/legendary-scientists/maharshi-kanada-the-propounder-of-atomic-theory600-bce>.
- [32] E. Rutherford *Philosophical Magazine Series*, vol. 6, 21:125, p. 669—688, 1911.
- [33] J. Chadwick *Nature*, vol. Feb 27, p. 312, 1932.
- [34] M. GELL-MANN *PHYSICS LETTERS*, vol. 8, p. 214, 1964.
- [35] “An  $su_3$  model for strong interaction symmetry and its breaking,” <http://cdsweb.cern.ch/record/352337?ln=en>.
- [36] E. D. Bloom *et al.* *Phys. Rev. Lett.*, vol. 23, p. 930–934, 1969.
- [37] R. P. Feynman *et al.* *PHYSICAL REVIEW D*, vol. 3, 1971.
- [38] S. Chatrchyan *et al.* *Physics Letters B*, vol. 716, pp. 30–61, 2012.
- [39] G. Aad *et al.* *Physics Letters B*, vol. 716, pp. 1–29, 2012.
- [40] B. Alessandro *et al.* *Jour. of Phys. G: Nucl. and Part. Phys.*, vol. 32, p. 1295, 2006.
- [41] I. Arsene *Nucl. Phys. A*, vol. 757, pp. 1–27, 2005.
- [42] B. B. Back *Nucl. Phys. A*, vol. 757, pp. 28–101, 2005.
- [43] J. Adams *Nucl. Phys. A*, vol. 757, pp. 102–183, 2005.
- [44] K. Adcox *Nucl. Phys. A*, vol. 757, pp. 184–283, 2005.
- [45] R. Pasechnik and M. Sumbera <https://arxiv.org/pdf/1611.01533.pdf>, 2017.
- [46] “U.w. heinz and m. jacob; evidence for a new state of matter: An assessment of the results from the cern lead beam program,” *Theoretical Physics Division: Geneva, Switzerland*.

- [47] J. A. et al. *Nuclear Physics A*, vol. 757, pp. 102–183, 2005.
- [48] B. B. Back et al. *Nucl. Phys. A*, vol. 757, pp. 27–101, 2005.
- [49] K. Adcox et al. *Nucl. Phys. A*, vol. 757, pp. 184–283, 2005.
- [50] W. Busza, K. Rajagopal, W. van der Schee, K. Adcox, et al. *Ann. Rev. Nucl. Part. Sci.*, vol. 68, p. 1–49, 2018.
- [51] A. Collaboration *Nature Physics*, vol. 13, p. 535–539, 2017.
- [52] P. T. P. N. Itoh *Prog. Theor. Phys.*, vol. 44, p. 291, 1970.
- [53] C. P. P. Carruthers *Prog. Theor. Phys.*, vol. 1, p. 147, 1973.
- [54] A. D. Martin et al. *Eur. Phys. J.*, vol. 63, p. 189, 2009.
- [55] P. M. Nadolsky et al. *Phys. Rev. D*, vol. 78, p. 013004, 2008.
- [56] R. D. Ball et al. *Nucl. Phys. B*, vol. 809, p. 1, 2009.
- [57] R. D. Ball et al. *Nucl. Phys. B*, vol. 838, p. 136, 2010.
- [58] F. Aaron et al. *JHEP B*, vol. 1001, p. 109, 2010.
- [59] S. Alekhin et al. *Phys. Rev. D*, vol. 81, p. 014032, 2010.
- [60] M. Gluck et al. *Eur. Phys. J.*, vol. 53, p. 355, 2008.
- [61] V. N. Gribov vol. 15, p. 1218–1237, 1972.
- [62] L. N. Lipatov *Sov. J. Nucl. Phys.*, vol. 20, p. 94–102, 1975.
- [63] G. Altarelli *Nucl. Phys. B*, vol. 126, p. 298, 1977.
- [64] Y. L. Dokshitzer *Sov. Phys. JETP*, vol. 46, p. 641–653, 1977.
- [65] F. Gelis and J. Jalilian-Marian *Phys. Rev. D*, vol. 66, p. 094014.
- [66] Z.-B. Kang et al. *PHYSICAL REVIEW C*, vol. 92, p. 054911, 2015.
- [67] M. L. Miller et al. *Annu. Rev. Nucl. Part. Sci.*, vol. 57, pp. 205–243, 2007.
- [68] P. F. Kolb et al. *Nuclear Physics A*, vol. 696, p. 197–215, 2001.
- [69] P. Huovinen *AIP Conference Proceedings*, vol. 610, p. 571, 2002.
- [70] Z.KOBA et al. *Nucl. Phys. B*, vol. 40, pp. 317–334, 1972.
- [71] L. Landau *L. Landau and others SSSR*, vol. 17, p. 51, 1953.
- [72] A. Alexander and other *International Journal of Modern Physics E*, vol. 23, p. 1450083, 2014.
- [73] K. Saraswat et al. *J. Phys. Commun.*, vol. 2, p. 035003, 2018.

- [74] F. Jüttner *et al.* *Annalen Phys.*, vol. 339, p. 856, 1911.
- [75] G. Wolschin *Phys. Rev. C*, vol. 94, p. 024911, 2016.
- [76] I. G. Bearden and other *Phys. Rev.Lett.*, vol. 78, p. 2080, 1997.
- [77] <https://arxiv.org/pdf/1111.4188.pdf>.
- [78] G. E. Knoll, “Radiation detection and measurement,” *John Wiley Sons*, 1999.
- [79] W. Allison *Annual Review of Nuclear Science*, p. 30, 1980.
- [80] E. Longo *et al.* *Nucl. Instrum. Methods*, vol. 128, p. 283, 1975.
- [81] <https://www.nature.com/news/2008/080905/full/news.2008.1085.html>.
- [82] K. Aamodt *et al.* *JINST*, vol. 3, p. S08002, 2008.
- [83] P. F. for the ALICE Collaboration *Journal of Physics: Conference Series*, vol. 455, p. 012004, 2013.
- [84] A. Collaboration *nature Physics*, DOI: 10.1038/NPHYS4111, vol. 24 APRIL 2017, p. 535, 2017.
- [85] A. Collaboration *JINST*, vol. 3, p. S08002, 2008.
- [86] <https://cds.cern.ch/record/879894/files/lhcc-2005-030.pdf>.
- [87] L. N. Lipatov *Sov. J. Nucl. Phys.*, vol. 23, p. 338–345, 1976.
- [88] V. S. Fadin *Phys. Lett. B*, vol. 60, p. 50–52, 1976.
- [89] I. I. Balitsky and L. N. Lipatov *Sov. J. Nucl. Phys.*, vol. 28, p. 822–829, 1979.
- [90] J. Jalilian-Marian *et al.* *Nucl. Phys. B*, vol. 504, p. 415, 1997.
- [91] J. Jalilian-Marian *et al.* *Phys. Rev. D*, vol. 59, p. 014014, 1999.
- [92] H. Weigert *hep-ph/0004044*.
- [93] E. Iancu *et al.* *Nucl. Phys. A*, vol. 692, p. 583, 2001.
- [94] E. Iancu *et al.* *Phys. Lett. B*, vol. 510, p. 133, 2001.
- [95] A. Mueller *Physics Letters B*, vol. 523, p. 243–248, 2001.
- [96] A. Mueller *et al.* *Nuclear Physics B*, vol. 715, p. 440–460, 2005.
- [97] Z. Collaboration *Physics Letters B*, vol. 316, pp. 412–426, 1993.
- [98] J. Blumlein *et al.* *hep-ph/9609425*, vol. 20 Sep, 1996.
- [99] S. Gavin *et al.* *Phys.Rev.Lett.*, vol. 68, p. 1834, 1992.
- [100] R. Vogt *Phys.Rev.C*, vol. 61, p. 035203, 2000.

- [101] M. B. Johnson *et al.* *Phys.Rev.Lett.*, vol. 86, p. 4483, 2001.
- [102] B. Z. Kopeliovich *et al.* *Phys. Lett. C*, vol. 72, p. 054606, 2005.
- [103] I. Vitev *et al.* *Phys. Lett. C*, vol. 75, p. 064906, 2007.
- [104] R. Neufeld *et al.* *Phys. Lett. B*, vol. 704, p. 590, 2011.
- [105] X. N. Wang *et al.* *Nucl. Phys. A*, vol. A96, p. 788, 2001.
- [106] H. Xing *et al.* *Nucl. Phys. A*, vol. 879, p. 879, 2012.
- [107] M. P. McCumber *et al.* *J. Phys. G*, vol. 35, p. 104081, 2008.
- [108] J. Y. Jia *et al.* *J. Phys. G*, vol. 85, p. 155, 2011.
- [109] V. Khachatryan *et al.* *JHEP*, vol. 1009, p. 091, 2010.
- [110] G. Aad *et al.* *Phys. Rev. Lett.*, vol. 116, no.17, p. 172301, 2016.
- [111] B. Donigus *et al.* *Phys. Conf. Ser.*, vol. 800, no. 1, p. 012004, 2017.
- [112] S. J. Brodsky *et al.* *arXiv:1708.07173v3 [hep-ph]*, vol. 17 Oct, 2017.
- [113] T. Sjostrand *et al.* *Phys. Rev. D*, vol. 36, p. 2019, 1987.
- [114] A. O. Velasquez *et al.* *Phys. Rev. Lett.*, vol. 111, p. 042001, 2013.
- [115] I. A. M. Cervantes *et al.* *J. Phys. Conf. Ser.*, vol. 509, p. 012064, 2014.
- [116] C. W. Fabjan and F. Gianotti *Rev. Mod. Phys.*, vol. 75, p. 1243, 2003.
- [117] V. S. Murzin *Progr. Elem.Part.Cosmic Ray Phys.*, p. 34, 1967.
- [118] R. P. Sandhir, S. Muhuri, and T. K. Nayak *Nucl. Instr. and Meth. in Physics Research A*, vol. 681, p. 34, 2012.
- [119] G.Barbiellini *et al.* *Nucl. Instr. and Meth. in Phys. Res. A*, vol. 235, p. 55, 1985.
- [120] G.Barbiellini *et al.* *Nucl. Instr. and Meth. in Phys. Res. A*, vol. 236, p. 316, 1985.
- [121] G.Ferri *et al.* *Nucl. Instr. and Meth. in Phys. Res. A*, vol. 273, p. 123, 1988.
- [122] M. Bocciolini *et al.* *Nucl. Instr. and Meth. in Physics Research A*, vol. 370, p. 403, 1996.
- [123] G. Abbiendi *et al.* *Eur. Phys. J.*, vol. C14, p. 373, 2000.
- [124] J. Rouene *et al.* *Nucl. Instr. and Meth. in Physics Research A*, vol. 732, p. 470, 2013.
- [125] R. Cornat *Jour. of Phys. Conference Series*, vol. 160, p. 012067, 2009.
- [126] G. Mavromanolakis *Pramana - J. Phys.*, vol. 69, p. 1063, 2007.
- [127] C. Adloff *et al.* *Nucl. Instr. and Meth. in Physics Research A*, vol. 608, p. 372, 2009.

- [128] E. Kistenev *et al.* *Czechoslovak Journal of Physics*, vol. 55, p. 1659, 2005.
- [129] V. Bonvicini *et al.* *IEEE Trans. Nucl. Sci.*, vol. 52, p. 874, 2005.
- [130] D. Strom *et al.* *IEEE Trans. Nucl. Sci.*, vol. 52, p. 868, 2005.
- [131] S. Muhuri *et al.* *Nucl. Inst. and Meth. in Physics Research A*, vol. 764, pp. 24–29, 2014.
- [132] T. K. Nayak *et al.* *Nucl. Phys. A*, vol. 854, p. 230, 2011.
- [133] S. Agostinelli *et al.* *Nucl. Instr. and Meth. in Physics Research A*, vol. 506, p. 250, 2013.
- [134] J. Allison *et al.* *IEEE Transactions on Nuclear Science*, vol. 52, pp. 270–278, 2006.
- [135] W. Allison *Ann. Rev. Nucl. Part. Sci.*, p. 30, 1980.
- [136] <https://warwick.ac.uk/fac/sci/physics/staff/academic/gershon/gradteaching/warwickweek/material/detectors/calorimetry.pdf>.
- [137] M. Gyulassy *et al.* *Computer Physics Communications*, vol. 83, p. 307–331, 1994.
- [138] R. Nock *et al.* *IEEE Transactions on Pattern Analysis and Machine Intelligence*, vol. 28, p. 1, 2006.
- [139] J. Bezdek *et al.* *Pattern Recognition with Fuzzy Objective Function Algorithms*, Plenum, New York, vol. ISBN 0-306-40671-3, 1981.
- [140] N. Pal *et al.* *IEEE Transactions on Fuzzy Systems*, vol. 3, p. 370, 1995.
- [141] L. Landau *J. Phys. USSR*, vol. 8, p. 201, 1944.
- [142] P. Courtat *et al.* *ALICE Internal Note*, ALICE-INT-2004-026, 2004.
- [143] A. Collaboration *ALICE TDR 6*, CERN/LHCC 2003-038, 2003.
- [144] S. Mukhopadhyay *et al.* *Proceedings of the DAE-BRNS national symposium on nuclear instrumentation*, vol. 46, 2013.
- [145] P. Courtat *et al.* *ALICE Internal Note*, vol. ALICE-INT-2004-026, 2004.
- [146] A. Collaboration *ALICE TDR 6*, vol. CERN/LHCC 2003-038, 2003.
- [147] <http://sba.web.cern.ch/sba/BeamsAndAreas/h6/H6manual.pdf>.
- [148] H. Bethe and J. Ashkin *Experimental Nuclear Physics*, ed. E. Segre, J. Wiley, New York., p. 293, 1953.
- [149] J. D. Bjorken *Phys. Rev. D*, vol. 27, pp. 140–151, 1983.
- [150] G. Sterman *et al.*, “Handbook of perturbative qcd,” *The CTEQ Collaboration*, vol. Version 1.0, 1993.
- [151] Y. L. Dokshitzer *et al.*, “Basics of perturbative qcd,” *Editions Frontieres*, 1991.

- [152] Y. L. Dokshitzer *et al.*, “Perturbative qcd for beginners,” *Kluwer Academic Publishers*, 2001.
- [153] S. A. Bass *Journal of Physics*, vol. Conference Series 50, p. 279–288, 2006.
- [154] R. J. Fries *et al. Phys. Rev. Lett.*, vol. 90, p. 202303, 2003.
- [155] R. J. Fries *et al. Phys. Rev. C*, vol. 68, p. 044902, 2003.
- [156] S. A. Voloshin *Nucl. Phys. A*, vol. 715, p. 379, 2003.
- [157] C. Nonaka *et al. Phys. Lett. B*, vol. 583, p. 73, 2004.
- [158] K. Adcox *et al. Phys. Rev. Lett.*, vol. 88, p. 242301, 2002.
- [159] R. FIELD and R. FEYNMAN *Nuclear Physics B*, vol. 136, pp. 1–76, 1978.
- [160] T. SJOSTRAND *Computer Physics Communications*, vol. 39, p. 347–407, 1986.
- [161] A. V. A. Metz *Progress in Particle and Nuclear Physics*, vol. 91, p. 136–202, 2016.
- [162] P. K. for CMS collaboration *Nuclear Physics A*, vol. 904–905, p. 732c–735c, 2013.
- [163] A. Ali *et al. EPJ H*, vol. 36, p. 245, 2011.
- [164] J. C. Collins *et al. arXiv:hep-ph/0409313v1*, 2004.
- [165] V. Khachatryan *et al. J. High Energy Phys.*, vol. JHEP09, p. 091, 2010.
- [166] V. Hove *Phys. Lett. B*, vol. 118, p. 138, 1982.
- [167] P. Levai *et al. Phys. Rev. Lett.*, vol. 67, p. 1519, 1991.
- [168] R. M. Weiner *Int. J. Mod. Phys. E*, vol. 15, p. 37, 2006.
- [169] K. Alpgard *et al. Phys. Lett. B*, vol. 310, p. 107, 1981.
- [170] G. Arnison *et al. Phys. Lett. B*, vol. 320, p. 107, 1981.
- [171] B. Hippolyte *et al. Nuclear Physics A*, vol. 904–905, pp. 318–325, 2013.
- [172] M.V.Savina *et al. Kpamicue coodutewix OHHH N°5(9J)-98*, p. 65, 1998.
- [173] J. Adams *et al. Phys. Rev. Lett.*, vol. 95, p. 152301, 2005.
- [174] J. Adams *et al. Nucl. Phys. A*, vol. 757, p. 28, 2005.
- [175] G. Goldhaber *et al. Phys. Rev.*, vol. 120, p. 300, 1960.
- [176] K. Aamodt *et al. Phys. Rev. D*, vol. 84, p. 112004, 2011.
- [177] V. Khachatryan *et al. J. High Energy Phys.*, vol. JHEP05, p. 029, 2011.
- [178] J. Adams *et al. Phys. Rev. C*, vol. 71, p. 044906, 2005.

- [179] S. K. Prasad *et al.* *Phys. Rev. C*, vol. 82, p. 024909, 2010.
- [180] J. Casalderrey-Solana *et al.* *Phys. Rev. Lett.*, vol. 104, p. 102301, 2010.
- [181] D. d’Enterria *et al.* *Eur. Phys. J. C*, vol. 66, p. 173, 2010.
- [182] P. Bozek *et al.* *Eur. Phys. J. C*, vol. 71, p. 1530, 2011.
- [183] K. Werner *et al.* *Phys. Rev. Lett.*, vol. 106, p. 122004, 2011.
- [184] F. Liu *et al.* *Phys. Rev. Lett.*, vol. 106, p. 242301, 2011.
- [185] V. T. V *et al.* *Phys. Rev. C*, vol. 86, p. 044902, 2012.
- [186] K. Werner *et al.* *Phys. Rev. C*, vol. 82, p. 044904, 2010.
- [187] K. Werner *et al.* *Phys. Rev. C*, vol. 83, p. 044915, 2011.
- [188] M. Floris *et al.* *J. Phys.: Conf. Ser.*, vol. 270, p. 012046, 2011.
- [189] M. Csnad *et al.* *arXiv: 1307.2082v2*, 2013.
- [190] A. Kisiel *Phys. Rev. C*, vol. 84, p. 044913, 2011.
- [191] E. Shuryak *Phys. Rev. C*, vol. 88, p. 044915, 2013.
- [192] R. Campanini vol. 703, pp. 237–245, 2011.
- [193] “L. McLerran,” *arXiv:hep-ph/0104285v2*.
- [194] “Binomial distribution,” <https://www.britannica.com/science/binomial-distribution>.
- [195] J. CUGNO *Europhys. Lett*, vol. 4(9), pp. 1127–1131, 1987.
- [196] V. HOVE *Proceedings of the XVII International Symposium, Seewinkel, Austria, June 1986, edited by M. MARKYTAN et al. (World Scientific, Singapore)*, p. 561, 1987.
- [197] A. GIOVANNINI *Z. Phys. C*, vol. 30, p. 391, 1986.
- [198] P. Tribedy *et al.* *Nucl. Phys. A*, vol. 850, p. 136, 2011.
- [199] R. E. Ansorge *et al.* *Z. Phys. C*, vol. 43, p. 357, 1989.
- [200] G. N. Fowler *et al.* *Phys. Rev. Lett.*, vol. 57, p. 2119, 1986.
- [201] A. Giovannini *et al.* *Phys. Rev. D*, vol. 59, p. 094020, 1999.
- [202] T. Alexopoulos *et al.* *Phys. Lett. B*, vol. 435, p. 453, 1998.
- [203] W. D. Walker *et al.* *Phys. Rev. D*, vol. 69, p. 034007, 2004.
- [204] F. Turkot *et al.* *Nucl. Phys. A*, vol. 525, p. 165, 1991.
- [205] A. Giovannini *et al.* *Phys. Rev. D*, vol. 68, p. 034009, 2003.

- [206] Neumann *Collected Works*, edited by A. J. Taub, Vol. 6 [Elmsford, N.Y.: Pergamon Press, pp. 219–237, 1963.
- [207] Bethe *Los Alamos Report LA-2000*, vol. Ch. 2, 1947.
- [208] Taylor *Proceedings of the Royal Society A. 201 (1065): 159–174.*, p. 159–174, 1950.
- [209] Taylor *Proceedings of the Royal Society A. 201 (1065): 175–186. Bibcode:1950RSPSA.201..175*, p. 175–186, 1950.
- [210] Sedov *Journal of Applied Mathematics and Mechanics*, vol. 10, pp. 241–250, 1946.
- [211] Latter *Journal of Applied Physics*, vol. 26, pp. 954–960, 1955.
- [212] Lockwood-Taylor *Philosophical Magazine*, vol. 46, pp. 317–320, 1955.
- [213] Dewey *21st International Symposium on Military Aspects of Blast and Shock*, vol. Israel, 2010.
- [214] P. Ehrenfest, “The conceptual foundations of the statistical approach in mechanics,” *DOVER PUBLICATIONS, INC*, 1990.
- [215] L. V. Hove *Phys. Lett.B*, vol. 118, p. 138, 1982.
- [216] F.Rimondia and other *Nuclear Physics B*, vol. 92, pp. 114–121, 2001.
- [217] G. J. Alner *et al. Phys. Lett. B*, vol. 160, p. 199, 1985.
- [218] R. Aaij *et al. Eur. Phys. J. C*, vol. 72, p. 1947, 2012.
- [219] P. Ghosh *et al. Phys. Rev. D*, vol. 85, p. 054017, 2012.
- [220] V. Khachatryan *et al. J. High Energy Phys.*, vol. 01, p. 079, 2011.
- [221] G. Aad *et al. New J. Phys.*, vol. 13, p. 053033, 2011.
- [222] I. Zborovsky *et al. J. Phys. G*, vol. 40, p. 055005, 2013.
- [223] “The durham hepdata project,” <http://hepdata.cedar.ac.uk/view/ins1123117>.
- [224] “The durham hepdata project,” <http://hepdata.cedar.ac.uk/view/ins890166>.
- [225] H. V. Hecke *et al. Phys. Rev. Lett.*, vol. 81, p. 5764, 1998.
- [226] “O. barannikova (star collaboration),” *arXiv:nucl-ex/0408022v1*.
- [227] S. Z. Belenkij *Nuovo. Cim. Suppl.*, vol. 3S10, p. 15, 1956.
- [228] N. Sarkar *et al. PHYSICAL REVIEW D*, vol. 96, p. 044901, 2017.
- [229] V. Khachatryan *J. High Energy Phys.*, vol. 09, p. 091, 2010.
- [230] V. Khachatryan *J. High Energy Phys.*, vol. 05, p. 029, 2011.
- [231] P. Bozek *Eur. Phys. J.C*, vol. 71, p. 1530, 2011.

- [232] K. Werner *Phys. Rev. Lett.*, vol. 106, p. 122004, 2011.
- [233] S. M. P. Ghosh *J. Phys. G*, vol. 41, p. 035106, 2014.
- [234] Y. Aoki *Nature*, vol. 443, pp. 675–678, 2006.
- [235] F. Karsch *Nucl. Phys. A*, vol. 698, pp. 199c–208c, 2002.
- [236] H.-T. Elze *Phys. Lett. B*, vol. 179, pp. 385–392, 1986.
- [237] L. Palhares *J. Phys. G*, vol. 37, p. 094031, 2010.
- [238] V. Khachatryan *Euro. Phys. J. C*, vol. 72, p. 2164, 2012.
- [239] “The durham hepdata project,” <http://hepdata.cedar.ac.uk/view/ins1123117>.
- [240] J. D. Bjorken *Phys. Rev. D*, vol. 27, pp. 140–151, 1983.
- [241] D. Teaney *Phys. Rev. Lett.*, vol. 86, pp. 4783–4786, 2001.
- [242] *Phys. Lett. B*, vol. 567, pp. 175–178, 2003.
- [243] G. Goldhaber *Phys. Rev.*, vol. 120, p. 300, 1960.
- [244] S. A. Bass *Phys. Rev. C*, vol. 61, p. 064909, 2000.
- [245] B. Abelev *Phys. Lett. B*, vol. 727, p. 371, 2013.
- [246] K. Redlich *Phys. Rev. D*, vol. 33, pp. 3747–3752, 1986.
- [247] F. Karsch *Prog. Part. Nucl. Phys.*, vol. 62, pp. 503–311, 2009.
- [248] T. Alexopoulos *Phys. Lett. B*, vol. 528, p. 43, 2002.
- [249] P. Levai *Phys. Rev. Lett.*, vol. 67, p. 1519, 1991.
- [250] J. D. Bjorken *Fermilab Report No. FERMILAB-PUB-82-059-THY*, 1982.